DESIGN AND MATHEMATICAL MODELLING OF THE KINETIC SCULPTURE *BLADE*

S. D. Gooch

A thesis submitted for the degree of
Doctor of Philosophy
at the Department of Mechanical Engineering
University of Canterbury
Christchurch
New Zealand

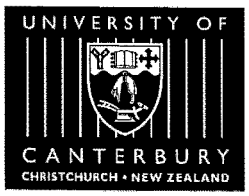

2001

Abstract

Christchurch born artist Len Lye (1901 – 1980) built the kinetic sculpture, *Blade (1965),* as a prototype for what he perceived to be a much larger work.

This thesis presents a study, which predicts the vibratory response of *Blade* and develops a design for the sculpture to be built at the largest practical economic size.

Len Lye's aesthetic requirements stipulate that the vibratory blade form of the scaled sculpture must be geometrically similar to the original work and that static similarity should exist between the original and the scaled blades.

Dimensionless formulae are derived and used to study the influence of design parameters and increasing size on structural properties such as natural frequencies, blade forces and moments, and system power requirements. For a solid metal blade of rectangular cross section it is found that the size, which *Blade* may be scaled, is limited by the magnitude of the bending stresses in the blade material.

Len Lye's specification imposes a set of requirements and constraints on the design, which in addition to economic constraints leads to a variational study which maximises the number of performances per dollar expended on blade materials with increasing size. As a result of this study a titanium alloy 6Al/4V is selected for the scaled blade with a nominal blade length is $3.355m$.

To test the validity of the design, frequencies and mode shapes were calculated and a numerical simulation performed. The exact solution for the natural bending frequencies and mode shapes for the blade and the *wand* are obtained using simple beam theory. The Rayleigh Ritz method is used to calculate the

plate frequencies and mode shapes for the blade. The calculated frequencies and mode shapes include the effects of the longitudinal gravitational loading. In this study they are the second and third blade bending frequencies and the third plate mode Len Lye described as the desirable vibrating *single* and *double harmonic* blade forms and the *shimmering* frequency respectively.

For the simulation a mathematical model is developed to describe the dynamics of the interaction of the blade and the wand. The model predicted a swinging phenomenon, which Lye observed in the performance of *Blade* at the prototype size and regarded as undesirable. A system configuration for the scaled *Blade* involving a lighter more flexible wand and modified ground motion characteristics predicted a significant reduction of this swinging phenomenon and is incorporated in the design.

Features in the design of the mechanism for the original sculpture were found to be unsatisfactory so a new improved mechanism concept was developed.

The complete design was produced and the system was manufactured and built. The performance of the scaled *Blade* is found to be consistent with the prediction from the mathematical model.

Acknowledgements

My sincerest thanks go to ***Professor John Raine*** who supervised this study. His careful attention to detail at project meetings, extensive engineering experience, and his flair for engineering design have been invaluable.

I am indebted to ***Professor Harry McCallion*** the co-supervisor for this work. His knowledge of engineering science, expertise in applied mathematics, and his talent as a teacher enabled me to tackle work I never thought possible.

Mr Evan Webb conscientiously acted as the *'aesthetic watchdog'* for this work. His experience in both creating and building sculpture was vital and is gratefully acknowledged.

Thanks to ***Dr Chris Damaren*** for his help and interest during the early stages of the analysis.

I am grateful to the ***Department of Mechanical Engineering*** and to ***John and Lynda Matthews*** for their sponsorship of the manufacturing costs and to ***Creative New Zealand*** who provided a scholarship for my support.

Thanks to ***Mr Scott Amies*** for an outstanding job in building the drive mechanism and the support structure for the scaled *Blade*.

The encouragement and interest from the ***staff and students*** at the ***Department of Mechanical Engineering*** is gratefully acknowledged.

Last but not least I thank my wife, ***Jo Gooch***, for her patience, encouragement, and support and to our daughter ***Coco*** for making it all worthwhile.

Publications

Gooch S.D. and Raine J.K., (2000) *The dynamics and limits on scaling of a flexible kinetic sculpture*, Proceedings of the Institute of Mechanical Engineers, Vol. 214, Part C, 537-548.

Raine J.K. and Gooch S.D., (1998) *Dynamic analysis and engineering design of kinetic sculptures*, IPENZ Transactions, Vol. 25, No. 1/Gen.

Gooch S.D. and Raine J.K., (1997) *A twice full scale 'Blade' - the engineering design of a kinetic sculpture, Proceedings of the IPENZ Annual Conference*, Wellington, New Zealand, 2, 247-252.

Raine J.K., Gooch S.D. and Webb E.A., (1997) *Artistic dreams, engineering limitations.* New Zealand Science Monthly, Vol. 8 Issue 9, South Pacific Information Services, Christchurch, New Zealand.

Gooch S.D., (1996) *Scaling Blade – a technical note for the engineering design of a kinetic sculpture,* IPENZ Proceedings of the Third New Zealand Conference of Postgraduate Students in Engineering & Technology, Canterbury University Press.

Table of contents

List of figures

List of tables

Nomenclature

Algebraic symbols

A	cross sectional area	(m^2)
a	blade length	(m)
b	*blade* width	(m)
d	*blade thickness*	(m)
C	equivalent damping constant	(Nm/sec)
C_{cb}	damping constant for the surface of the cork ball	(Nm/sec)
C_m	*blade* material cost per kg	(NZ$/kg)
C_w	damping constant for the *wand* stem	(Nm/sec)
c	damping constant	(Nm/sec)
D	a requirement that is a *Demand* and must be satisfied under all circumstances	
D	flexural rigidity of a thin plate	(Nm)
E	Elastic modulus	(N/m^2)
f	force	(N)
g	gravitational acceleration	(m/sec^2)
H	Distance from the surface of the blade to the surface of the cork ball	(m)

h	blade thickness	(m)
I	second moment of area	(m^4)
I_{cb}	moment of inertia for the cork ball	(kg-m^2)
i	unit for imaginary numbers such that $i^2 = -1$	
k_1, k_2 k_5, k_6	constants used in the development of the primary design equation for the optimal *Blade* solution	
k_3	ratio of the maximum blade displacement over length equal to R/l	
k_4	aspect ratio for the *blade* equal to b/l	
k_7	the ratio of input displacement to *blade* length, equal to Δ/l	
k_{cb}	stiffness of the surface of the cork ball	(N/m)
k_s	endurance limit modifying factor for the fixed end of blade	
l	*blade* length	(m)
M	equivalent mass	(kg)
M	bending moment	(Nm)
M_c	material cost for the blade	(NZ$)
M_{cb}	mass of cork ball	(kg)
MS	mild steel	
N_f	number of blade cycles to failure	
N_x, N_y, N_z	in plane blade forces	(N)

P	power	(watts)
P_f	number of blade performances to failure	
PLC	programmable logic controller	
P	load	(N)
P_l	axial end load	(N)
p	load much smaller than P	(N)
p	mode shape number for the lateral vibration of blade	
Q	shear force	(N)
q	generalised displacement	(m)
R	distance from fixed end of *blade* to the contact height	(m)
R_a	surface roughness	(μm)
r	wand sphere radius	(m)
S	equivalent stiffness	(N/m)
s	scale ratio (l_o/l_s)	
T_3	the length of time the *blade* operates at the third natural bending frequency	(sec)
T_e	kinetic energy	(J)
t	time	(sec)
U	number of performances per dollar expended	(NZ^{-1})
U_{sm}	dimensionless blade life parameter	

V	lateral blade displacement as a function of axial blade coordinate only	(m)
V_e	potential energy	(J)
v	lateral blade displacement as a function of axial *blade* coordinate and time	(m)
W	a requirement that is a *Wish* and is desirable but not essential for the success of the project	
W	lateral blade deflection	(m)
w	mass per unit length	(kg/m)
x	axial *blade* coordinate	(m)
xw	axial *wand* coordinate	
y	lateral blade coordinate	(m)

Greek symbols

Δ	offset for crank mechanism	(m)
δ	deflection	(m)
ε	deflection much smaller than δ	(m)
ϕ	constraint used in method of optimisation	
ϕ	characteristic shape function along length dimension of the blade	
γ	dimensionless stability factor	
η	loss coefficient	
μ	dimensionless frequency parameter	
ν	Poisson's ratio	
ρ	density	(kg/m^3)
σ	bending stress	(MPa)
σ_e	endurance limit	(MPa)

σ_f	mean fatigue strength	(MPa)
σ_u	ultimate tensile strength	(MPa)
σ_y	yield stress	(MPa)
Ω	blade base motion frequency	(rad/sec)
ω	frequency	(rad/sec)
ψ	functional requirement used in method of optimisation	
ψ	characteristic shape function along width dimension of the blade	

Suffixes

cb	refers to the cork ball
cr	critical
o	refers to the *'original'* size sculpture
p	refers to the *'prototype'* size sculpture
sc	refers to the *'scaled'* size sculpture
r, s,	letters corresponding to the first four blade bending
t, u	modes of vibration

1

Introduction

1.1 The purpose of this work

The purpose of this project is to investigate the possibility of producing a structure of the form of Len Lye's kinetic sculpture *Blade,* but at a much larger size.

1.2 Historical background

The aim of this section is to discuss briefly the historical background for the project and give some insight into the nature of the task.

1.2.1 Len Lye

Len Lye was born in Christchurch, New Zealand in 1901.

> *"The very first thing I remember is also the most vivid. I am kicking a large shiny square-sided kerosene can. Not quite four and in a tantrum I am turfed out of the house into a sunny backyard... I kicked that can around to make the most god awful racket... I can still feel the impact of my kicks on that can and hear an echo of tinny clashes. What is most clear is a great flash of quivering sunlight that came from the can. I stood stock still at it... We're all stopped short by wonder sometime..."*
> ***Len Lye*** *[From McCarthy & Leonard (1991)]*

From an early age Lye showed enthusiasm for motion. As a young art student he had a revelation.

> *"All of a sudden it hit me – if there was such a thing as composing music, there could be such a thing as composing motion. After all, there are melodic figures, why can't there be figures of motion? ..."* ***Len Lye***
> *[From Currow & Horricks (1984)]*

In the early 1920's, Lye moved to London where he pursued his interests in filmmaking and where he became one of the great pioneers of experimental filmmaking, particularly in the areas of animation and of direct film techniques. Lye completed his first film *Tusalava* in 1929. In his 1935 film, *Colour Box,* Lye painted directly onto clear film and in the 1958 film *Free Radicals,* he simply scratched lines onto the black celluloid. Both films were made without the use of a camera or by the 'direct' film technique.

Figure 1.1 *Len Lye in his New York studio*
[From Bouhours & Horrocks (2000)]

In 1944 Lye moved to New York where he lived until his death in 1980.

Lye's interest in motion is evident in his films, and his kinetic sculpture is an alternative medium for his showing what he called *"figures of motion"*. From 1958 – 1967, Lye put most of his energy into making sculpture.

> *"I realised that my particular sense of motion was tied in a lot with vibration"* ***Len Lye*** *[From Currow & Horricks (1984)]*

This realisation led to sculptures that consisted of motor powered, vibrating, light reflecting, highly polished steel strips and rods. Lye's sculptures were seen as more unpredictable in their movement & sound than other kinetic sculptures of the time which tended to be more technology based and regular in their motion.

> *"Perhaps I'm for magic carpets over flying saucers, and would rather be an heir to the Australian aboriginal with his boomerang and bullroarer than an heir to constructivism and mechanics."* ***Len Lye*** *[From McCarthy & Leonard (1991)]*

1.2.2 Len Lye's prototype for the kinetic sculpture Blade

The prototype for *Blade,* shown in Figure 1.2, was first exhibited at Lye's *'Bounding Steel Sculptures'* exhibition, Howard Wise Gallery, New York (March – April 1965).

The prototype, built in New York under Lye's supervision, consisted of a blade of cold rolled carbon steel strip measuring *1730 x 200 x 1.85mm (N.B. 100mm of the blade material is fixed in the base clamp).* The size of this *Blade*, evolved from the need to use of available materials. Lye used strip steel of the type commonly used for bandsaws in the timber industry. Lye's method of establishing the original length for the blade, was to extend the carbon steel strip vertically supported only at the base until it buckled under its own weight:

he then reduced this length until the material would just stand stably and vertical at rest. This determined the final height for the sculpture. [Webb (Jan 1996 – Dec 1998)]

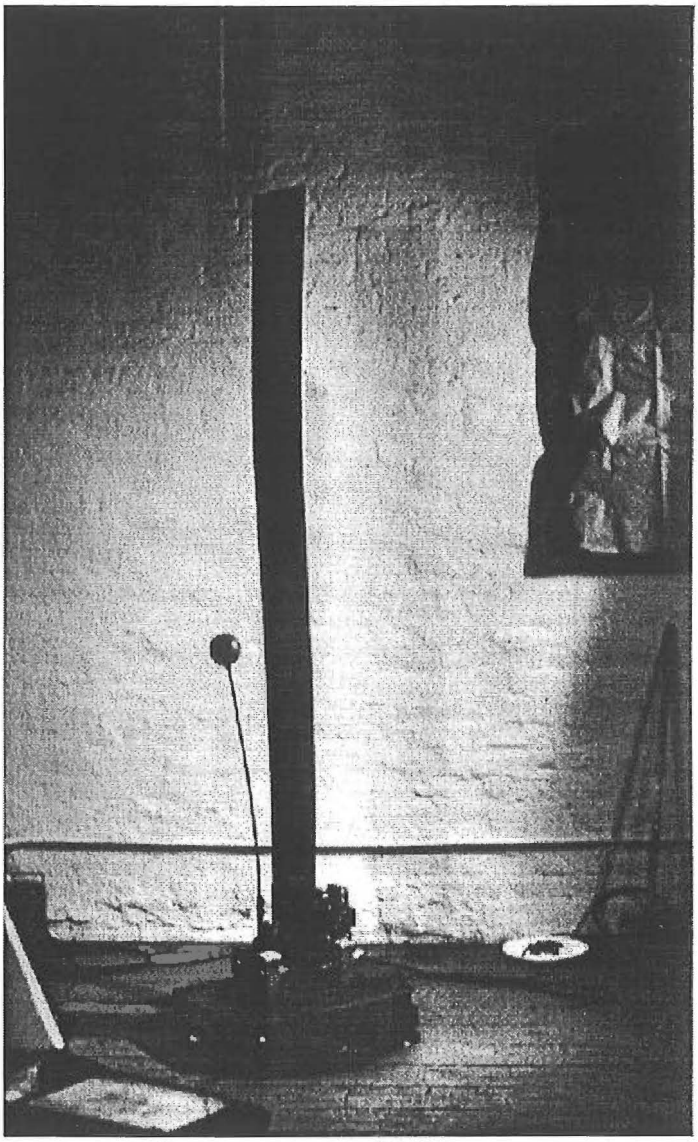

Figure 1.2 *Len Lye's prototype Blade*
[From Curnow (1980)]

The drive mechanism for the prototype *Blade* is shown in Figure 1.3. The base of the blade is fixed in a rigid clamp, the clamp is attached to a table, and the table slides in four 25mm diameter recirculating linear ball bearings. The clamp

is coupled to the drive through a 300mm long connecting rod and a crank mechanism. The drive motor is a Bodine 1/20th hp DC electric machine and incorporates a 5:1 gearbox reduction. The shuttle drive with the crank attachment provides a linear reciprocating base clamp motion. The connecting rod length is 300mm and the crank offset is 5.58mm. In front of the blade

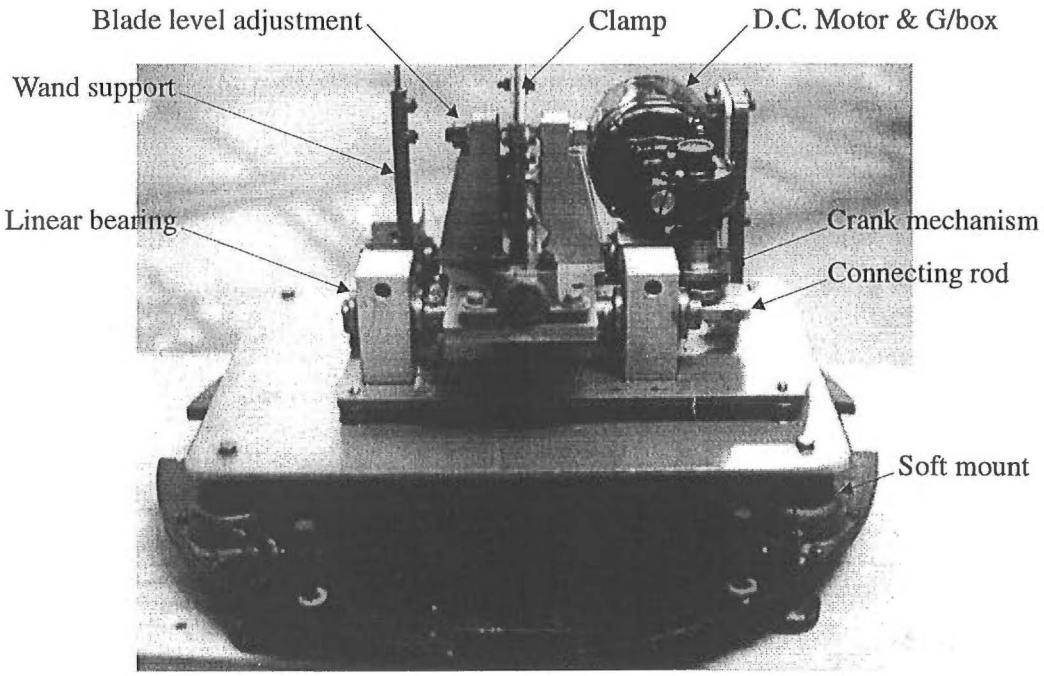

Figure 1.3 *The drive mechanism for Len Lye's prototype Blade [Courtesy of the Len Lye Foundation]*

stands a 500mm tall wand. The wand consists of a 75mm diameter cork sphere weighing 85g mounted on a 5mm diameter 316 stainless steel stem.

To operate the sculpture, Len Lye manually adjusted the speed of the D.C. machine by using a Veriac type rheostat. Lye found that at certain speeds the blade responded by vibrating in various modes and as the amplitude of vibration increased, the blade interacted with the wand to initiate a loud acoustic ringing. From these early experiments Len Lye left detailed notes of what he perceived the final performance of the work to be.

1.2.3 The completion of the Lye's prototype

Lye (1978) intended that the vibrating blade should also turn about its vertical axis, and that the work should reach the particular forms he had observed in a predetermined sequence. Lye stipulated that this sequence should happen unassisted by a concealed mechanism. The Len Lye Foundation undertook later modifications to the prototype *Blade*, after Lye's death, in accordance with his wishes. Figure 1.4 shows a schematic diagram of the *Blade* including the modifications to the drive system and the support structure, this work realises the completion of the Lye's prototype and will be referred to as the **original *Blade***

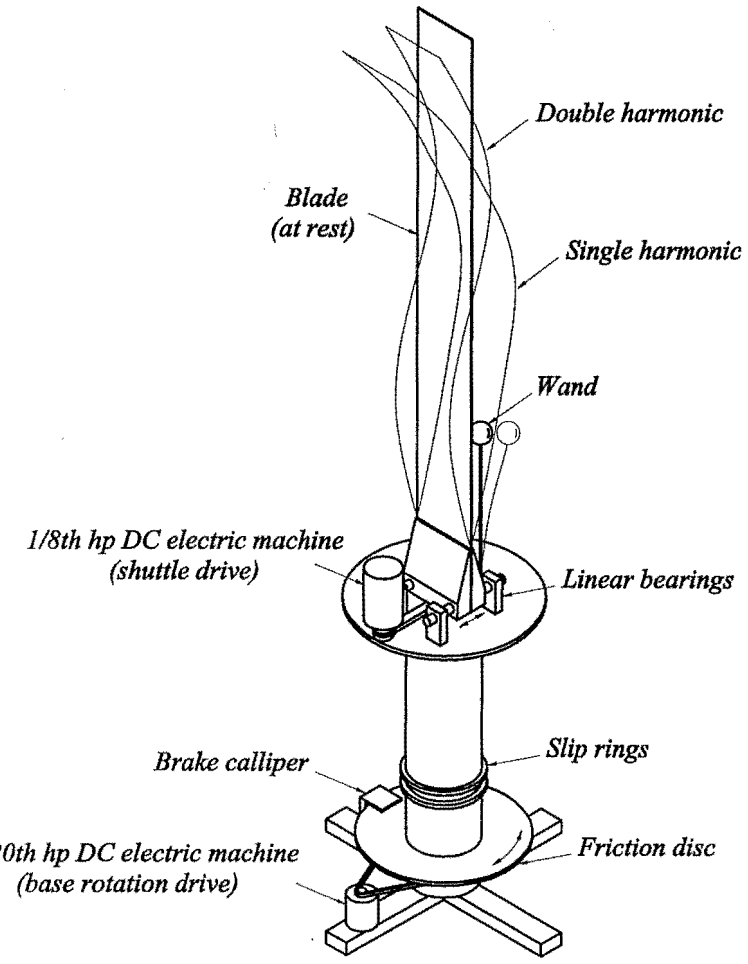

Figure 1.4 *Schematic diagram of the drive system and the support structure for the original Blade*

The blade material used for the prototype failed due to the development of a fatigue crack parallel with the width dimension of the blade and at the fixed end. A replacement blade was installed using a similar cold rolled high carbon steel strip or blade.

The shuttle drive of the prototype was not considered to have sufficient power. Modifications produced by the Len Lye Foundation were to re-power the shuttle mechanism using an $1/8^{th}$ hp permanent magnet D.C. electric machine.

An electronic control system was added to introduce a programmed performance routine for the original *Blade.* The shuttle motor is controlled using a D.C. motor speed controller *(rectifier with variable output voltage and current).* The shuttle motor/gearbox output shaft is fitted with a rotary speed encoder providing positive feedback for the speed controller. The control system uses a programmable logic controller to perform basic timing and switching functions.

After some modification, the mechanism was mounted on a steel column. The steel column houses two deep groove ball bearings and the mechanism and column assembly rotate on a fixed central axle. The central axle is welded to the base frame.

Power to the shuttle drive, and the encoder signal, are transmitted from the stationary base frame to the rotating table using copper slip rings and carbon brushes. The slip ring arrangement has since proven problematic because the brushes are prone to bouncing on the slip rings interrupting the speed feedback signal.

The base rotation drive uses the original shuttle drive motor from the prototype to transmit rotary motion though a gearbox and chain drive reduction.

To reduce unwanted vibration *(i.e. for a smooth base rotation motion)* due to out of balance forces, a mechanical spring actuated disc brake provides a friction damping function to reduce the tendency of the chain drive to whip.

The *Blade* mechanism and the support structure are concealed within in a black cylinder. The original *Blade,* shown in Figure 1.5, is an indoor kinetic sculpture, regularly exhibited at the Govett Brewster Art Gallery, New Plymouth, New Zealand and at selected international exhibitions.

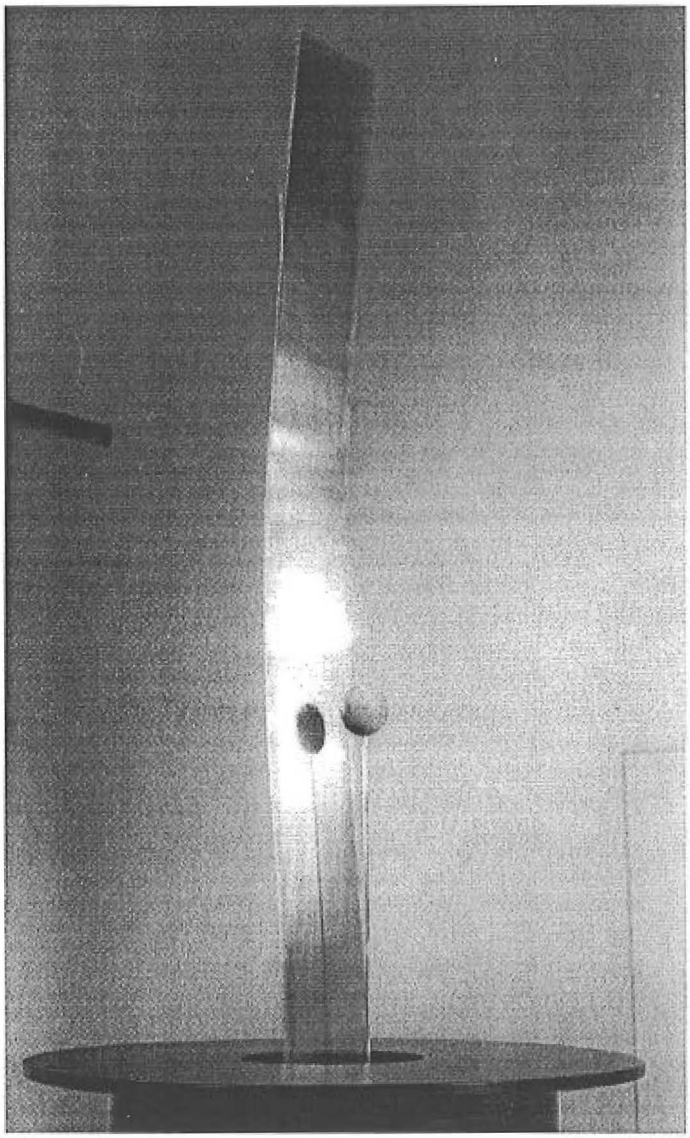

Figure 1.5 *The original Blade [From McCarthy & Leonard (1991)]*

1.2.4 Characteristics in the performance of the original Blade

The performance of the original *Blade,* shown in Figure 1.5, begins with the blade rotating slowly *(0.13Hz)* about its vertical axis.

After ten seconds of base rotation motion, the shuttle drive starts the reciprocating harmonic clamp motion. The clamp frequency ramps from rest to a frequency of *3.26Hz* at which the blade responds by forming a shape referred to as a ***single harmonic*** [Lye (1978)]. At this frequency there is light intermittent interaction between the blade and the wand. This part of the performance lasts for sixty seconds and is referred to as ***kissing*** [Webb (Jan 1996 – Dec 1998)].

After *kissing,* the reciprocating clamp frequency increases to *3.43Hz* which results in the maximum amplitude of the *single harmonic* and a correspondingly heavier and more regular interaction between the blade and the wand. This part in the performance of *Blade* is shown schematically in Figure 1.4: it lasts for thirty seconds, and is referred to as the ***full amplitude single harmonic*** [Webb (Jan 1996 – Dec 1998)].

Following the *full amplitude single harmonic,* the shuttle speed increased to *9.34Hz* when the blade began to shimmer. Thus, the name given to this part of the performance is ***shimmering*** [Webb (Jan 1996 – Dec 1998)] and it lasts for thirty seconds. The amplitude of vibration at the *shimmering* frequency is relatively small in comparison with the other modes: the motion appears to have a torsional component, and there is generally no interaction with the wand.

After *shimmering* for thirty seconds the shuttle frequency increases to *9.95Hz*, and the blade suddenly bursts into a ***double harmonic*** [Lye (1978)]. The *double harmonic* is shown schematically in Figure 1.4 and is the most spectacular part of the performance of the original *Blade.* The *double harmonic* lasts for twenty seconds before suddenly diminishing as the shuttle frequency is decreased back to rest. As the speed passes through the second mode, the

blade forms the *single harmonic* and hits the ball one or two times before settling again and coming to rest.

The base rotation motion continues for a further ten seconds. Figure 1.6 shows the time history for the shuttle and base rotation motors on the original *Blade*.

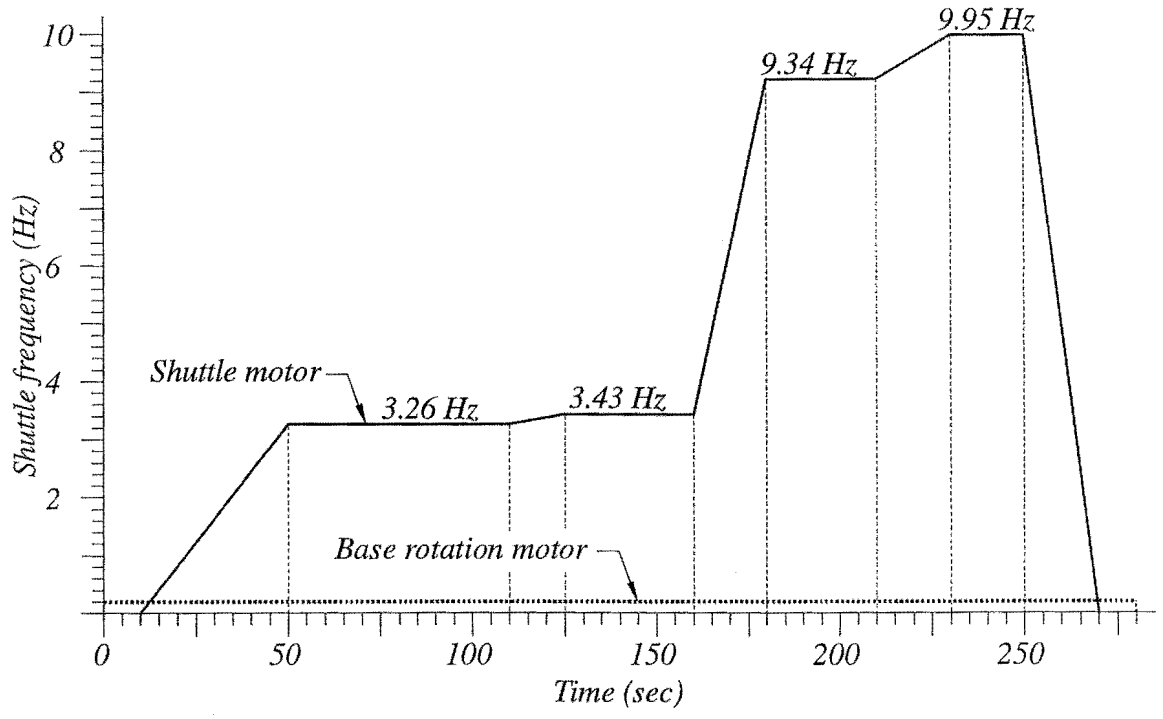

Figure 1.6 *Motor speed / time history for the original Blade*

It is interesting to note that when the original *Blade* is at the *double harmonic* frequency, the drive motor can be heard to be labouring: it does not appear to have sufficient power to overcome the blade inertia forces. This is intentional and typical of many of Lye's kinetic works, where ***'the tail appears to wag the dog'*** [Webb (Jan 1996 – Dec 1998)] giving a certain amount of unpredictability to the performance. The interaction between the wand and the blade is also irregular and hence cannot be anticipated by the observer.

1.2.5 Lye's vision

Len Lye made his kinetic sculpture without ever allowing technology to upstage the aesthetic qualities of his art. He found that technical and cost factors restricted the scale at which his sculpture could be implemented. To this end, he built modest sized works that were precursors to much larger works designed to have far greater impact.

> *"When I get the kinetic side of a figure of motion sorted out, then comes the scale question. Its mostly the bigger the better; for example, when a three foot shrub falls, so what? Where's the tie-in of bodily empathy? But when it's the accelerating rush of the three-hundred-foot redwood, Kurrrrash-empathy, I'm with thee.* ***Len Lye*** *[From pg 88 Currow & Horricks (1984)]*

Lye left detailed notes and drawings, so that his ambition of building monumental size kinetic sculpture [Essay by Webb & Hurrell pp 214-216 of Bouhours et al. (2000)] could be realised after his death, anticipating the availability of new technical processes and materials.

Lye intended *Blade* at the size shown in Figure 1.2, to be one of a number of *Blades* built at various sizes, and exhibited simultaneously as a larger outdoor work called *Steel Henge*. *Steel Henge* comprises twelve *Blades* arranged to in a circular pattern similar to the Wiltshire Stone Henge.

> *" ... Aztec monument to the sun ... all pulsating like a giant, kinetic Stone Henge ..."* ***Len Lye*** *[From McCarthy & Leonard (1991)]*

Len Lye's original *Blade* was intended to be the smallest *Blade (blade length 1.63m)* in *Steel Henge* and the largest *Blade* was intended to be over five times the original size *(blade length 9.14m).* Len Lye's original sketch of the *Steel Henge* is shown in Figure 1.7. Other records [Lye (1978)] indicate that Lye intended *Blade* to be built at the monumental size of 100ft tall.

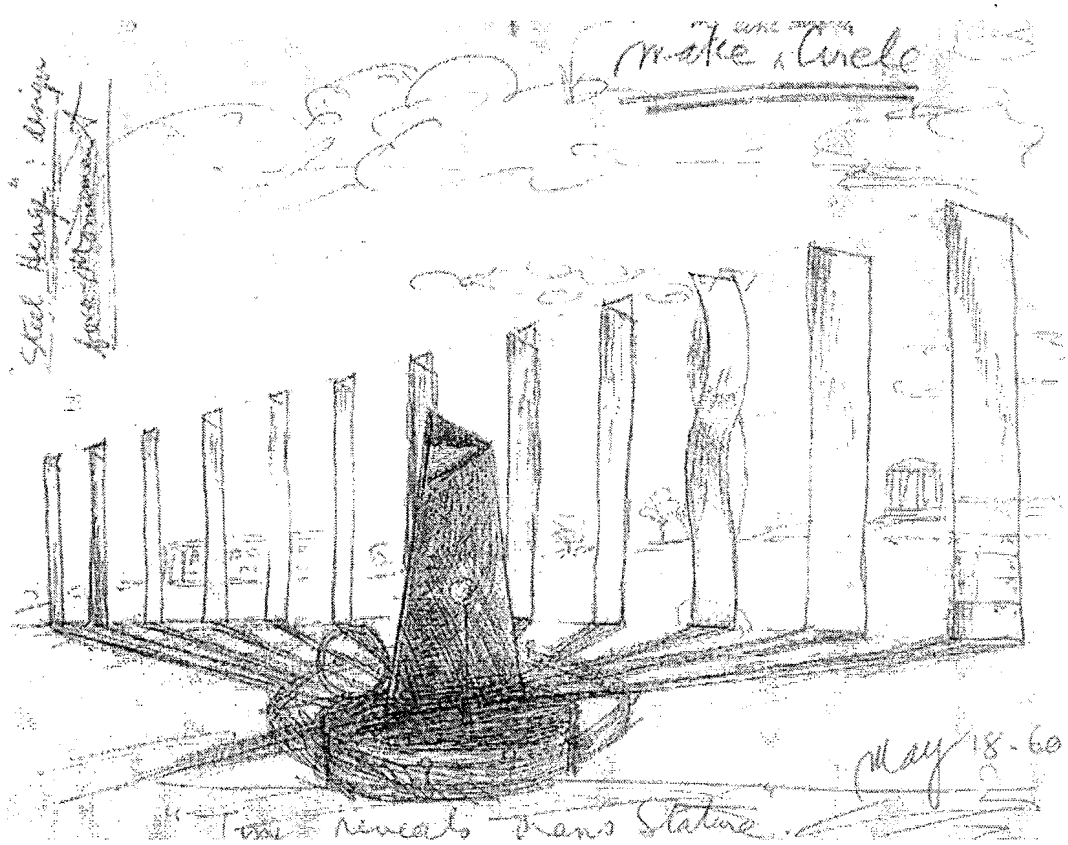

Figure 1.7 *Len Lye's Steel Henge [kindly supplied by Rodger Horricks]*

1.3 The scope and structure of this thesis

The aim of this work is to study the influence increasing the size of *Blade* on structural properties, system dynamics, life, and cost. This study will be used to evolve a new embodiment design for the sculpture at the largest practical size.

> ***The scope of this thesis is to develop a mathematical model that predicts the significant characteristics in the kinetic performance of Blade. The mathematical model will be used to implement the design features that achieve the most satisfactory performance of the larger work.***

It is intended that the sculpture be built at the largest practical size and that the work be tested and later commissioned at a public exhibition.

Chapter 2 of the thesis specifies the scaling rules for increasing the size of *Blade* and studies the influence that scale has on the structural properties of the work.

In Chapter 3, the artist's intentions for the work are formulated in a design requirement specification. Feasibility of the scaled *Blade* is then addressed and an optimum design solution pursued.

In Chapter 4 the exact natural bending frequencies of the blade and the wand are calculated. The blade and the wand stem are treated as thin vertical cantilever beams in a gravitational acceleration field.

In Chapter 5 a second vibration analysis is conducted to predict the lateral plate frequencies for the blade. An energy method is used and the gravitational acceleration field is included.

Chapter 6 presents a mathematical model for the forced damped vibration of the blade and the wand. This model includes the interaction of these two components and discusses the influence of design variables affecting the kinetic performance.

Chapter 7 presents the design study required to build the mechanism and the support structure for the sculpture.

Chapter 8 reports the observations of the building and testing stages for the scaled *Blade*.

Finally, in Chapter 9 the key research findings are summarised and recommendations are made for further work.

2

Similarity and the influence of size on structural properties

2.1 Introduction

The purpose of this chapter is to develop an approach to increasing Blade size that best satisfies the artist's intentions for the work. Furthermore, the aim is to study the influence of increasing size on the forces, bending moments, natural frequencies, and power requirements. The results of this study are to be used in the design of the drive mechanism and the support structure.

Changing the size of *Blade*, whilst preserving the visual qualities of this work [Webb (Jan. 1996 – Dec. 1998)], would require geometric similarity of the blade width to length ratio, and geometric similarity of the displaced blade shape at the maximum amplitude of vibration. That is, geometric similarity between the *'original'* and the *'scaled'* sizes.

2.2 Relevant quantities in changing *Blade* size

In formulating the scaling laws for mechanical structures such as *Blade*, Buckingham's π theorem may be applied [Dieter (1983)]. This study will follow the general approach to dimensional analysis as presented by [Massey (1989)]. The relevant quantities of interest, as discussed in Section 2.1 above, are listed

in Table 2.1, along with the exponents of the reference magnitudes in their dimensional formulae.

Table 2.1 *Properties involved in scaling the blade*

Properties	Symbol	Dimensional formulae		
		[M]	[L]	[T]
length	l	0	1	0
width	b	0	1	0
lateral displacement at x	$V(x/l)$	0	1	0
mass per unit length	w	1	-1	0
natural frequency	ω	0	0	-1
gravitational acceleration	g	0	1	-2
second moment of area	I	0	4	0
elastic modulus	E	1	-1	-2
bending moment	$M(x/l)$	1	2	-2
shear force	$Q(x/l)$	1	1	-2

Considering the geometric scaling requirements, the aspect ratio of blade width to length and ratio of lateral blade deflection to blade length are two dimensionless groups of interest. After considering the form of the equation of motion for the blade, Equation (4.7), other groups of variables of interest are

$$EI; \qquad wg; \qquad w\omega^2 \tag{2.1}$$

Dividing the first two quantities through by l and assembling the combinations from (2.1), Table 2.1 takes the form

Table 2.1 *(cont.)*

Symbol	Dimensional formulae		
	[M]	[L]	[T]
b/l	0	0	0
$V(x/l)$	0	1	0
IE	1	3	-2
wg	1	0	-2
$w\omega^2$	1	-1	-2
$M(x/l)$	1	2	-2
$Q(x/l)$	1	1	-2

From inspection, the dependence of the last four quantities on [M] & [T] may be removed by dividing through by EI, thus

Table 2.1 *(cont.)*

Symbol	Dimensional formulae		
	[M]	[L]	[T]
b/l	0	0	0
$V(x/l)$	0	1	0
wg/IE	0	-3	0
$w\omega^2/IE$	0	-4	0
$M(x/l)/EI$	0	-1	0
$Q(x/l)/EI$	0	-2	0

Finally the dependence on [L] is removed by multiplying the last four quantities through by appropriate powers of [L]. Thus the 10 dimensional variables with three fundamental dimensions M, L, & T, as listed in Table 2.1, are arranged into the seven dimensionless groups shown in Table 2.2.

Table 2.2 *Dimensionless groups for the blade*

Dimensionless group	Dimensional formulae		
	[M]	[L]	[T]
b/l	0	0	0
$V(x/l)/l$	0	0	0
wgl^3/IE	0	0	0
$w\omega^2 l^4/IE$	0	0	0
$M(x/l)l/EI$	0	0	0
$Q(x/l)l^2/EI$	0	0	0

2.3 Geometric similarity

Preserving the visual qualities of this work requires geometric similarity, hence the first two dimensionless parameters from Table 2.2 are held constant between in the original and scaled works giving

$$\left(\frac{b}{l}\right)_o = \left(\frac{b}{l}\right)_s \tag{2.2}$$

&

$$\left(\frac{V(x/l)}{l}\right)_o = \left(\frac{V(x/l)}{l}\right)_s \tag{2.3}$$

It was agreed that some tolerance on the blade thickness, d, could be tolerated [Webb (Jan. 1996 – Dec. 1998)].

2.4 Static similarity

Static similarity implies a geometrically similar deflection of a vertical blade under self weight [Dieter (1983)]. In this case the third dimensionless ratio from Table 2.2 includes the self-weight load *'wg'* and is therefore the ratio that must be held constant for static similarity, namely

$$\left(\frac{wgl^3}{EI}\right)_o = \left(\frac{wgl^3}{EI}\right)_s \qquad (2.4)$$

The elastic stability of a vertical cantilever beam has been the subject of many previous investigations. The approximate solution for the critical weight at the onset of buckling was first given by A.G. Greenhill in 1881 [Frish-Fay (1961)] as

$$\frac{wgl_{cr}^3}{EI} = 7.84 \qquad (2.5)$$

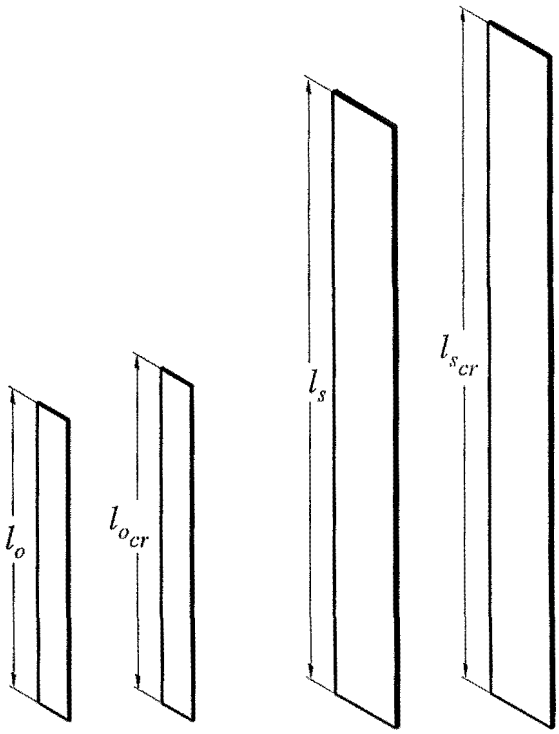

Figure 2.1 *Ratio of the length l to the critical length l_{cr}*

The constant 7.84 in Equation (2.5) is the numerical value for stability parameter, γ, at the onset of buckling under self weight. Len Lye used the value 5.65 for γ to be below the buckling threshold. The problem of elastic stability of a vertical cantilever has been the subject of more recent investigations, and has since been solved exactly, for which [Timoshenko & Gere (1961)] give a solution. [Naguleswaran (1991)] & [Frish-Fay (1961)] also confirm Greenhill's approximate solution to the first two decimal places.

Maintaining a constant stability parameter ensures that the ratio of the blade length l to the length at the onset of buckling l_{cr} remains constant, that is

$$\left(\frac{l}{l_{cr}}\right)_o = \left(\frac{l}{l_{cr}}\right)_s \tag{2.6}$$

Equation (2.6) would be expected to hold true using Lye's experimental method; hence static similarity will be the governing scaling criterion.

2.4.1 Blade thickness for static similarity

Considering the blade geometric and material properties, Equation (2.4) may be written in the form

$$\left(\frac{12\rho bdgl^3}{Ebd^3}\right)_o = \left(\frac{12\rho bdgl^3}{Ebd^3}\right)_s \tag{2.7}$$

and with some rearrangement, Equation (2.7) may be expressed as the ratio of blade thicknesses, i.e.

$$\frac{d_o}{d_s} = \sqrt{\frac{\rho_o l_o^3 E_s}{\rho_s l_s^3 E_o}} \tag{2.8}$$

For the particular case where the same materials are used for the blade, the ratio of the thicknesses becomes

$$\frac{d_o}{d_s} = \sqrt{\frac{l_o^3}{l_s^3}} \qquad (2l_o = l_s,\ E_o = E_s,\ \rho_o = \rho_s) \tag{2.9}$$

From Equation (2.9), for an exactly double size blade, using the same materials, results in an increase in blade thickness by a factor of $2\sqrt{2}$. The original blade thickness is $1.85mm$, therefore for the blade with a length exactly twice the size of the original requires a thickness is $5.23mm$.

2.4.2 The effect of increasing blade size on bending moment and shear force

The effect of increasing blade size on bending moment in the blade material may be investigated by considering the dimensionless bending moment parameter from Table 2.2. Equating the dimensionless bending moment parameter for the original blade with that for the scaled blade gives

$$\left(\frac{M(x/l)l}{EI}\right)_o = \left(\frac{M(x/l)l}{EI}\right)_s \tag{2.10}$$

Rearranging Equation (2.10) in terms of the ratio of the bending moments leads to

$$\frac{M(x/l)_o}{M(x/l)_s} = \frac{E_o I_o l_s}{E_s I_s l_o} = \frac{E_o b_o d_o^3 l_s}{E_s b_s d_s^3 l_o} \tag{2.11}$$

and noting that for geometric similarity, the aspect ratio from Equation (2.2) for the blade is constant, .ie. $b/l = k_4$, Equation (2.11) becomes

$$\frac{M(x/l)_o}{M(x/l)_s} = \frac{E_o k_4 l_o d_o^3 l_s}{E_s k_4 l_s d_s^3 l_o} = \frac{E_o d_o^3}{E_s d_s^3} \tag{2.12}$$

For static similarity, the ratio of the thicknesses is given by Equation (2.8). Therefore substituting Equation (2.8) into (2.12) gives

$$\frac{M(x/l)_o}{M(x/l)_s} = \frac{E_o}{E_s}\left(\frac{\rho_o l_o^3 E_s}{\rho_s l_s^3 E_o}\right)^{\frac{3}{2}} = \left(\frac{\rho_o}{\rho_s}\right)^{\frac{3}{2}}\left(\frac{E_s}{E_o}\right)^{\frac{1}{2}}\left(\frac{l_o}{l_s}\right)^{\frac{9}{2}} \tag{2.13}$$

The effect of increasing blade size on shear force in the blade material may be investigated by equating the dimensionless shear force parameter for the original blade with that for the scaled blade from Table 2.2, namely

$$\left(\frac{Q(x/l)l^2}{EI}\right)_o = \left(\frac{Q(x/l)l^2}{EI}\right)_s \tag{2.14}$$

Applying the same treatment to Equation (2.14) as applied to the bending moment, Equation (2.10), gives the ratio of the shear stresses as

$$\frac{Q(x/l)_o}{Q(x/l)_s} = \frac{E_o d_o^3 l_s}{E_s d_s^3 l_o} \tag{2.15}$$

Substituting in the blade thickness relationship for static similarity from Equation (2.8) gives

$$\frac{Q(x/l)_o}{Q(x/l)_s} = \frac{E_o l_s}{E_s l_o}\left(\frac{\rho_o l_o^3 E_s}{\rho_s l_s^3 E_o}\right)^{\frac{3}{2}} = \left(\frac{\rho_o}{\rho_s}\right)^{\frac{3}{2}}\left(\frac{E_s}{E_o}\right)^{\frac{1}{2}}\left(\frac{l_o}{l_s}\right)^{\frac{7}{2}} \tag{2.16}$$

For the case where the scaled blade has a blade length of exactly double the size of the original work and the same materials are used, the bending moment and shear force ratios may be simplified to

$$\frac{M(x/l)_o}{M(x/l)_s} = \left(\frac{l_o}{l_s}\right)^{\frac{9}{2}} = \frac{1}{(2)^{\frac{9}{2}}} = \frac{1}{16\sqrt{2}} \qquad (2l_o = l_s,\ E_o = E_s,\ \rho_o = \rho_s)$$

&

$$\frac{Q(x/l)_o}{Q(x/l)_s} = \left(\frac{l_o}{l_s}\right)^{\frac{7}{2}} = \frac{1}{(2)^{\frac{7}{2}}} = \frac{1}{8\sqrt{2}} \qquad (2l_o = l_s,\ E_o = E_s,\ \rho_o = \rho_s) \tag{2.17}$$

2.4.3 The effect of increasing blade size on bending stress

From basic mechanics of materials [Hibbler (1991)], the ratio of the bending stresses in the original blade to the bending stresses in the scaled blade may be arranged in the form

$$\frac{\sigma(x/l)_o}{\sigma(x/l)_s} = \frac{M_o d_o}{2I_o} \frac{2I_s}{M_s d_s} \tag{2.18}$$

Substituting Equation (2.11) into Equation (2.12) gives

$$\frac{\sigma(x/l)_o}{\sigma(x/l)_s} = \frac{E_o I_o l_s}{E_s I_s l_o} \frac{d_o}{I_o} \frac{I_s}{d_s} = \frac{E_o l_s d_o}{E_s l_o d_s} \tag{2.19}$$

For static similarity, the ratio of the blade thicknesses from Equation (2.8) may be substituted into Equation (2.19) to give

$$\frac{\sigma(x/l)_o}{\sigma x/l_s} = \frac{E_o l_s}{E_s l_o} \sqrt{\frac{\rho_o l_o^3 E_s}{\rho_s l_s^3 E_o}} = \sqrt{\frac{\rho_o E_o l_o}{\rho_s E_s l_s}} \tag{2.20}$$

From Equation (2.20), it may be noted that for a material with a lower value of the product of elastic modulus and density $(E \times \rho)$, the blade will be expected to have a lower bending stress. However, if the same materials are used then increasing the size of the blade while maintaining static similarity will result in an increase the bending stress in proportion to the square root of the scale ratio s.

For the case where the same materials are used and the *scaled* work is exactly double the size of the *original*, then Equation (2.20) becomes

$$\frac{\sigma(x/l)_o}{\sigma(x/l)_s} = \sqrt{\frac{l_o}{l_s}} = \frac{1}{\sqrt{2}} \qquad (2l_o = l_s,\ E_o = E_s,\ \rho_o = \rho_s) \tag{2.21}$$

hence, for the particular case described by Equation (2.21), bending stress increases by a factor of $\sqrt{2}$.

2.4.4 The effect of increasing blade size on natural bending frequencies

The effect of increasing size on natural bending frequencies for the blade may be investigated by equating the dimensionless frequency parameter *(the fourth term in Table 2.2)* for the original blade that for the scaled work, namely

$$\left(\frac{w\omega^2 l^4}{EI}\right)_o = \left(\frac{w\omega^2 l^4}{EI}\right)_s \tag{2.22}$$

Considering the blade geometry and material properties, Equation (2.22) takes the form

$$\left(\frac{12\rho bd\omega^2 l^4}{Ebd^3}\right)_o = \left(\frac{12\rho bd\omega^2 l^4}{Ebd^3}\right)_s \tag{2.23}$$

Rearranging Equation (2.23) in terms of the ratios of the natural bending frequencies gives

$$\frac{\omega_o}{\omega_s} = \frac{d_o l_s^2}{d_s l_o^2}\sqrt{\frac{\rho_s E_o}{E_s \rho_o}} \tag{2.24}$$

For static similarity, the ratio of the thicknesses from Equation (2.8) may be substituted into Equation (2.24) to give

$$\frac{\omega_o}{\omega_s} = \sqrt{\frac{\rho_o l_o^3 E_s}{\rho_s l_s^3 E_o}}\frac{l_s^2}{l_o^2}\sqrt{\frac{\rho_s E_o}{E_s \rho_o}} = \sqrt{\frac{l_s}{l_o}} \tag{2.25}$$

In the case of Equation (2.25), frequency is independent of material properties because stability was considered in the thickness relationship, Equation (2.8)

For the case where the blade length for the *scaled* work is exactly double the size of the original and the static stability criteria are satisfied, the result will be a decrease in the natural frequencies by a factor of $2^{-1/2}$, i.e.

$$\frac{\omega_o}{\omega_s} = \sqrt{2} \tag{2.26}$$

2.4.5 The effect of increasing size on system power requirements

The system power requirements are a significant consideration in the design of the mechanism for the scaled work. If the damping ratio for the forced blade vibration is assumed to be constant, then the input displacement at the fixed end will change directly as the scale ratio s [Stiedel (1989)]. In this case the ratio of power requirements of the original sculpture divided by the power requirements for the scaled work will take the form

$$\frac{P_o}{P_s} = \frac{\omega_o Q_o(0) k_7 l_o}{\omega_s Q_s(0) k_7 l_s} \tag{2.27}$$

$$where \quad k_7 = \frac{\Delta}{l}$$

Substituting in the *blade* geometry and material properties from Equations (2.16) and (2.25) into Equation (2.27) gives

$$\frac{P_o}{P_s} = \sqrt{\frac{\rho_o^3 E_s}{\rho_s^3 E_o}} \left(\frac{l_o}{l_s} \right)^4 \tag{2.28}$$

Therefore, for an exactly double size *Blade* using the same blade materials, the system power requirements will be a factor of 16 times the power requirements for the *Original Blade*.

2.5 Kinematic similarity

Kinematic similarity *(similarity of motion)* implies similarity of lengths *(geometric similarity)* and in addition similarity of time intervals [Massey (1989)]. For *Blade*, this requires that the vibrating original size blade be geometrically similar to the vibrating scaled blade at corresponding points in time, thus requiring the vibrating blade frequency to remain constant when increasing blade size. In this case the left hand side of Equation (2.24) may be set to unity and the ratio of the thicknesses becomes

$$\frac{d_o}{d_s} = \frac{l_o^2}{l_s^2}\sqrt{\frac{\rho_o E_s}{E_o \rho_s}} \tag{2.29}$$

The ratio of the bending stresses, Equation (2.19), takes the form

$$\frac{\sigma(x/l)_o}{\sigma(x/l)_s} = \frac{l_o}{l_s}\sqrt{\frac{E_o \rho_o}{E_s \rho_s}} \tag{2.30}$$

For the case where both the original and scaled blades are made from the same materials, the thickness increases as the square of the scale ratio s, and the bending stress increases directly as s.

2.6 Scaling for constant stress

Blade may be scaled for constant stress under various rules governing blade thickness.

For the case where the blade thickness is set to give static similarity i.e. satisfying Equation (2.8), the maximum bending stress may be limited by

limiting the maximum amplitude of vibration. In a damped system this is easily achieved by limiting the amplitude of the input displacement.

From basic mechanics of materials, the bending stress - curvature relationship for small deflections is of the form [Benham & Crawford (1987)]

$$\sigma(x)=\frac{Ed}{2R(x)} \tag{2.31}$$

Holding Equation (2.31) constant between the original and scaled works, and substituting blade thickness using the static stability condition, Equation (2.8), the ratio of the curvatures becomes

$$\frac{R_o(x/l)}{R_s(x/l)}=\sqrt{\frac{\rho_o E_o l_o^3}{\rho_s E_s l_s^3}} \tag{2.32}$$

From Equation (2.32) the radius of curvature increases as $(l_s/l_o)^{3/2}$ with increasing blade size and the corresponding maximum blade displacement will be lower in the ratio $(l_s/l_o)^{-3/2}$.

If, however, it is required to maintain constant stress while also achieving the geometric similarity of the displaced blade shape, the static stability criteria must be relaxed. From Equation (2.31), and considering the relationship between curvature and blade length from Equation (2.32), the ratio of the thicknesses takes the form

$$\frac{d_o}{d_s}=\frac{E_s l_o}{E_o l_s} \tag{2.33}$$

The blade thickness must now vary directly as the scale ratio l_s/l_o *(rather than* $(l_s/l_o)^{3/2}$*).*

2.7 Summary of results

The two cases of particular interest are the exactly double size steel blade and the final-specification titanium alloy blade from the optimisation study in Chapter 3. The results of the application of the static similarity rules developed in Section 2.4 are summarised in Table 2.3

Table 2.3 *Comparison of the results of applying static similarity conditions to the exactly double size steel blade and the final-specification titanium alloy blade*

Parameter	***original blade***	***double size steel blade***	***final specification***
scale factor	$s = 1$	2	2.1
thickness	d_o	$2.8\, d_o$	$3.1\, d_o$
bending moment	M_o	$22.6\, M_o$	$16.8\, M_o$
shear force	Q_o	$11.3\, Q_o$	$7.9\, Q_o$
bending stress	σ_o	$1.4\, \sigma_o$	$0.8\, \sigma_o$
natural bending frequency	ω_o	$0.7\, \omega_o$	$0.7\, \omega_o$
system power req.	P_o	$16\, P_o$	$11\, P_o$

The values of the blade parameters listed in Table 2.3 are plotted for the scale ratios ranging from 1 to 5 in Figure 2.2 for the cases of the alloy steel and titanium alloy blades.

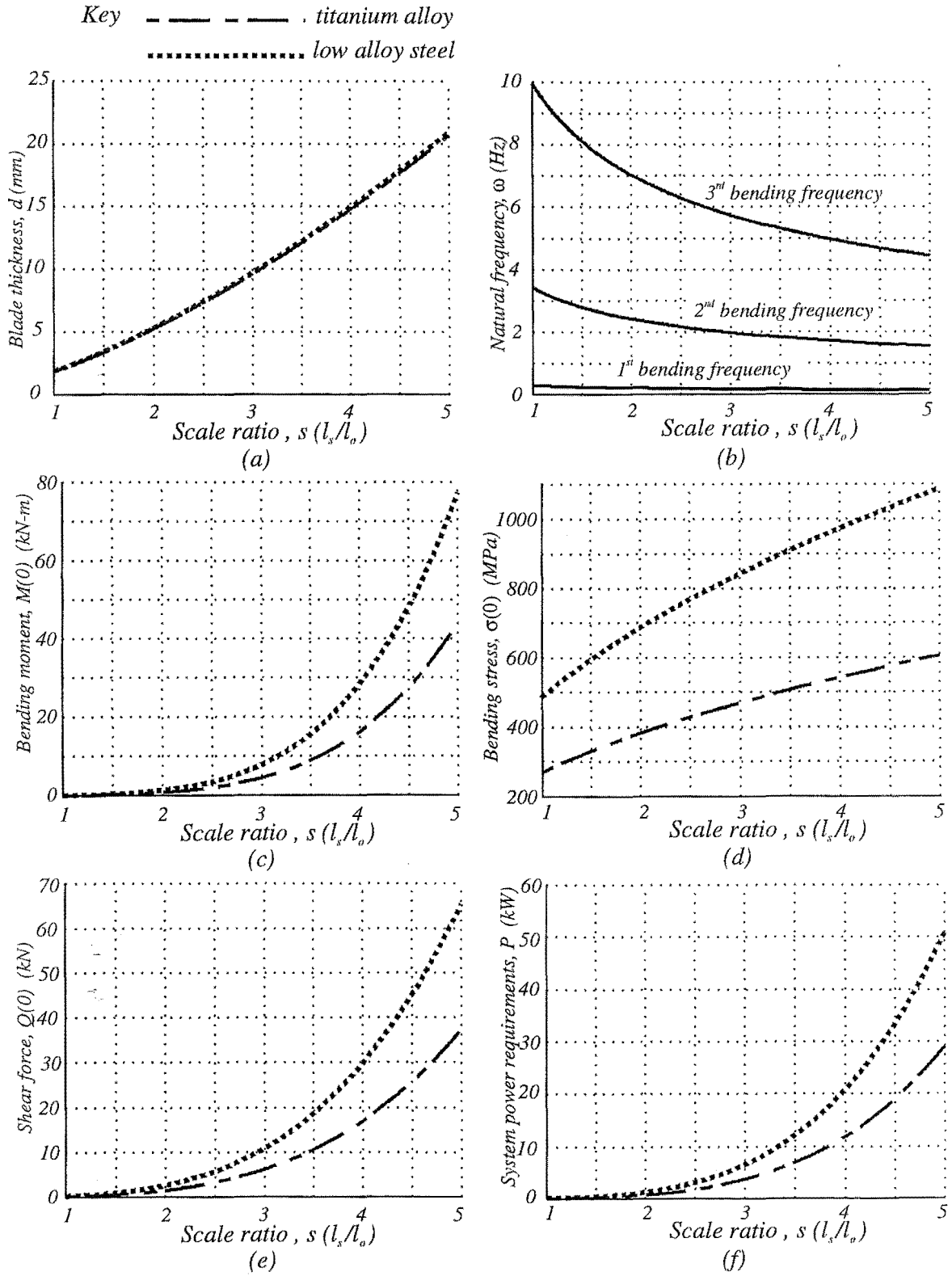

Figure 2.2 *The influence of blade size on structural properties (for static similarity case only)*

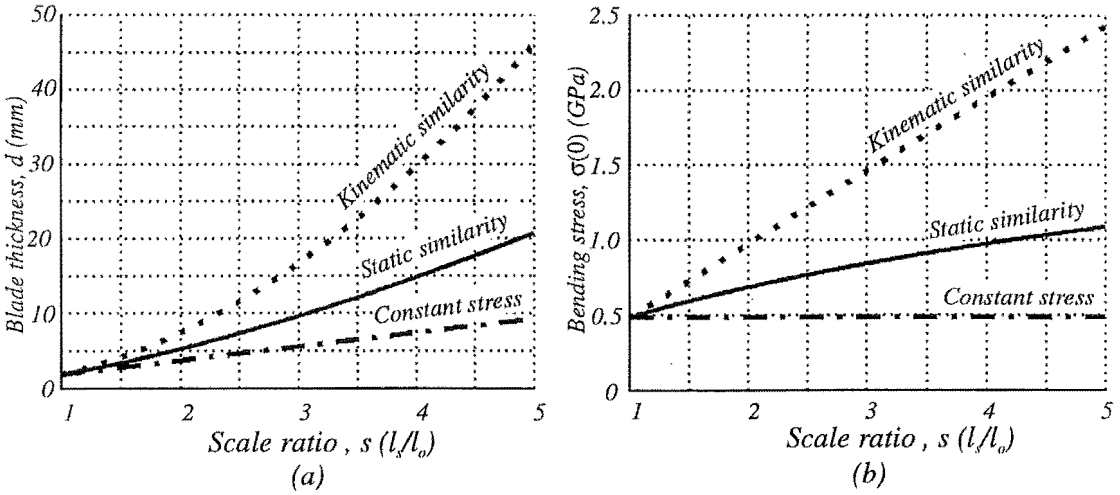

Figure 2.3 *The influence of size using each of the three scaling methods*
(a) on blade thickness (b) on bending stress
(NB. For the constant stress case in (a) the static similarity criterion is relaxed)

2.8 Discussion

The blade thickness relationship, Equation (2.8), requires an increasing blade thickness with increasing blade length. From Figure 2.2a, the increase in thickness for the titanium and alloy steel materials is at a similar rate. From the shaded region on Figure 2.4, it is interesting to note that the ratio E/ρ for engineering materials such as steel, aluminium alloys, and titanium alloys varies within the range 24×10^6 to 34×10^6 *Nm/kg*. Therefore the ratio of blade thicknesses, Equation (2.9), holds approximately true for a change in blade size *(or scale ratio s)* using different these engineering materials.

Figure 2.2b shows the relationship between natural frequency and scale ratio for the first three bending modes. From inspection of Table 2.2, the magnitude of elastic modulus and density are the same for the dimensionless stability and frequency parameters. Therefore, for the case where the dimensionless stability parameter is held constant, the frequency scale relationship shown in Figure 2.2b will be the same for all materials considered.

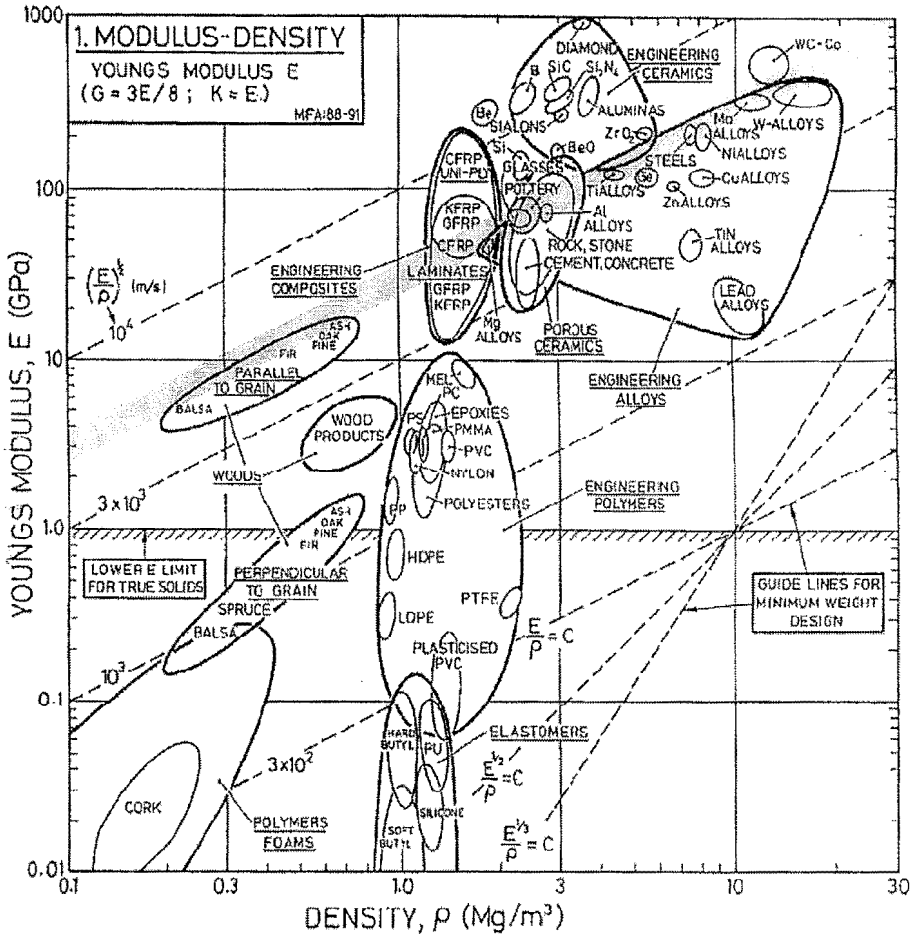

Figure 2.4 *The relationship between elastic modulus and density for a range of engineering materials [after Ashby (1992)]*

The bending moment, shear force, and power relationships plotted against scale ratio s in Figures 2.2c, 2.2e, & 2.2f show an increasing rate of change in magnitude with increasing s. From Table 2.3, an increase in scale by a factor of two using the same blade material results in a bending moment increase by a factor of *22.6*. The implication for design, is that on blade replacement, a small increase in blade thickness due to use of available materials will result in a significant increase in force, bending moment, and power requirements.

Figure 2.2d shows the expected increase in bending stress in the blade with increasing scale ratio s. From Table 2.3, the final specification titanium alloy blade will be expected to have a lower bending stress than for the original size steel blade. From Equation (2.20), this is a direct result of the lower elastic

modulus and density of the titanium alloy material. On first inspection the lower bending stress in the titanium alloy blade looks to be a most favourable result, however further consideration of the tensile strength and fatigue properties is required to select a true optimum material. The scale at which this work may be built has been found to be bending stress limited. If the bending stress is found to be above the materials endurance limit, then the blade will have a finite working life.

Intuitively, the first approach to increasing the scale of a kinetic work such as the *Blade* might be to apply kinematic similarity rules. For the case where the vibrating *blade* is scaled for kinematic similarity, the static stability criterion must be relaxed, the structure becomes relatively stiffer with increasing size, and from Figure 2.3b, bending stress becomes unacceptably high. Kinematic similarity was not expected between the original and scaled sculptures, as it is expected that the frequency of the vibrating blade would be reducing with increasing scale [Webb (Jan. 1996 – Dec. 1998)].

Increasing blade size using a constant stress criterion would be ideal from a strength of materials perspective, as this would remove the stress-related limit on maximum achievable size for sculpture. The constant stress condition, setting Equation (2.20) equal to unity, and the static similarity criteria Equation (2.7) may be satisfied simultaneously by limiting the maximum *blade* amplitude. For an exactly double size steel blade the maximum blade displacement would in this case be reduced from *150mm (for geometric similarity)* to *26.5mm* for the constant stress case. This would be unacceptably small from the aesthetic viewpoint [Webb (Jan. 1996 – Dec. 1998)].

A second approach to increasing blade size using the constant stress model allowed for blade thickness to be set by the constant stress criteria. In this case the increase in blade thickness is shown in Figure 2.3a, and while this approach will give geometric similarity of the displaced blade shape, the stability criteria will not be satisfied. As *Blade* is scaled up, it becomes too slender and reaches

its critical buckling length at a scale factor of γ_{cr}/γ, or *1.387:1* i.e. the blade will buckle under its own weight.

2.9 Conclusion

The conditions for similarity between the original and scaled sculpture have been defined and follow Len Lye's original experimental method for establishing the blade length.

> ***Similarity conditions require that static similarity exist between the original blade and scaled blade. Static similarity is satisfied if the blade thickness relationship, Equation (2.8) holds true.***
>
> ***Similarity conditions require that the shape of the blade at its maximum amplitude of vibration be geometrically similar between the original and scaled works. Geometric similarity for the vibrating blade (a damped system) can be achieved by adjusting the amplitude of the reciprocating harmonic ground motion.***

Increasing *Blade* size results in an increasing bending stress in the blade material. There will be a upper limit on *Blade* size due to the maximum allowable reversed bending stress in the blade. Further consideration of blade material properties is needed to allow for fatigue failure modes.

As *Blade* size increases, the magnitudes of the drive forces and the bending moments at the fixed end increase at an increasing rate. Assuming that a suitable blade material is available, there will be an upper limit on *Blade* size constrained by the ability of the mechanism to provide sufficient power and support for the blade.

3

The monumental Blade – limitations on the realisable size

3.1 Introduction

The objective of this chapter is to investigate the size limit to which a scaled Blade is realisable using currently available materials and technology.

Although the influences of size on structural properties were identified in Chapter 2, neither the artist's requirements nor the feasibility of producing the scaled *Blade* was addressed.

Len Lye's intentions in the performance of *Blade* primarily concern the aesthetic and acoustic characteristics of the work, as experienced by the audience. On the other hand he required the drive mechanism and the support structure to be concealed within a cylindrical base cover.

For the purpose of formally discussing the artist's intentions for *Blade*, and for identifying attributes influencing feasibility, a *Blade* performance requirement specification was developed [Webb (Jan. 1996 – Dec. 1998)]. These requirements are formulated as a list of demands & wishes in accordance with the design procedure of Pahl & Beitz (1996), which was updated during the course of the project. The final form of the *Blade* performance requirement specification is recorded in Table 3.1.

Table 3.1 *Blade performance requirement specification*

Demand Wish	***Blade performance requirement specification 'the artists aesthetic and acoustic requirements' (in order of importance)***
D	blade length at least double the prototype size $(l_s \geq 3.26m)$
D	minimum *Blade* life of one performance
D	static similarity to be preserved in changing blade size
D	*double harmonic* to feature in the *Blade* performance
D	sound quality for the blade material of better than would be expected from a mild steel blade $(\eta < 2 \times 10^{-3} @ 30°C)$
D	bright steel-like colour for the blade *(equivalent to, or better than would be expected from a polished aluminium)*
D	running costs for a nominally $2 - 2.5$ times prototype size blade to be less than $500\ NZ\$/performance$
D	polished surface finish for the blade *(surface roughness* $R_a < 0.8\ \mu m)$
D	mechanism to be concealed in black cylinder *(maximum outside diameter* $= 0.6 \times l_o$ *and maximum height* $0.375 \times l_o)$
W	geometric similarity of the vibratory form to be preserved in changing blade size
W	running costs of less than $50\ NZ\$/performance$

Table 3.1 *(cont.)*

W	for the case where the blade has a finite life then use a readily available blade material *(acquirable within 12 month lead time)*
W	preserve the sound qualities of the original *Blade* *(η for the* blade *material $< 10^{-4}$ @ 30°C)*
W	*Blade* to be resistant to attack by salt water and U-V radiation
W	bright highly reflective steel-like surface finish for the blade *(e.g. refer to Len Lye quote pg 1)*
W	infinite design life for the blade
W	low noise emission from the drive mechanism *(< 50 dB-A [pg 1209 Oberg et al. (1992)])*

A study in Chapter 7 developed conceptual solutions for a proposed drive mechanism and support structure. After considering the system loads and power requirements calculated in Chapter 2, it was evident that a mechanism could be built to provide sufficient power and support for the blade while operating within the specified space constraints. While the operating environment and noise emission requirements for the mechanism require special consideration, they are not considered to be factors limiting the size of the monumental *Blade*. Thus the mechanism and support structure for the monumental *Blade* could be built using available materials and bought-out components to perform the prescribed duty in the specified environment.

The design constraints for the blade only, may be summarised and considered under into the four sub headings given in Figure 3.1.

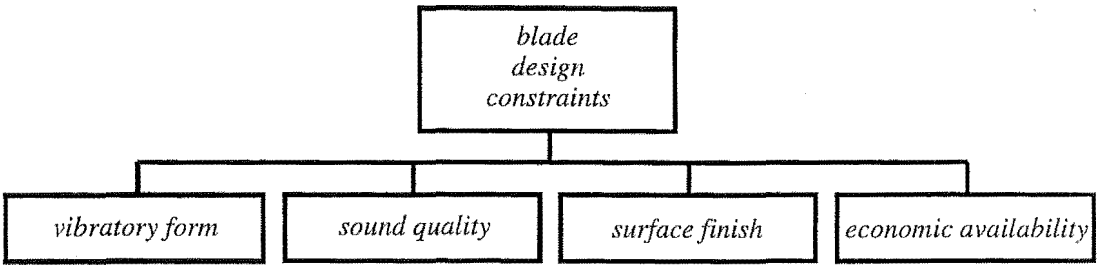

Figure 3.1 *Design constraints for Blade*

As the mechanism is considered realizable to a blade size of at least 5m, the performance requirements for the characteristic groups identified in Figure 3.1 are in this case a function of blade material properties only. That is, the solution expected to give the optimum design in terms of meeting the performance requirements for the blade, will lead to the solution that is an optimum in meeting the requirements of the complete work, *Blade*.

The approach to design adopted in this Chapter is the *'method of optimum design'* [after Johnson (1980)].

> ***The optimum solution will yield the maximum realisable Blade size within the limits imposed by the design requirement specification, Table 3.1.***

3.2 Method of optimal design for the monumental *Blade*

Using the *'method of optimum design'*, satisfaction of the design constraints of Figure 3.1 may be pursued. The constraints will be considered under two headings, ***equality constraints*** being conditions that must be met for the project to be successful and ***inequality constraints*** being the factors that have upper or lower limits.

3.2.1 The vibratory form

Equality constraints require that geometric similarity of the vibratory blade form exist between the original and scaled sculptures. From Equation (2.3), the equality constraint ψ_1 for geometric similarity may be defined as

$$\psi_1 = V\left(\frac{x}{l}\right)_p - \frac{l_p}{l_m} V\left(\frac{x}{l}\right)_m = 0 \tag{3.1}$$

If Equation (3.1) holds true, it follows that the slope at corresponding points on the original and scaled blades should be the same, i.e.

$$\psi_2 = \left(\frac{dV\left(\frac{x}{l}\right)}{dx}\right)_p - \left(\frac{dV\left(\frac{x}{l}\right)}{dx}\right)_m = 0 \tag{3.2}$$

similarly the work will require

$$\psi_3 = \left(\frac{d^2V\left(\frac{x}{l}\right)}{dx^2}\right)_p - \frac{l_m}{l_p}\left(\frac{d^2V\left(\frac{x}{l}\right)}{dx^2}\right)_m = 0 \tag{3.3}$$

From the design rules developed in Chapter 2, equality constraints require static similarity to be preserved as *Blade's* size increases. Static similarity *(i.e. a similar degree of static stability)* is achieved by setting blade thickness d to give the required stability factor γ in Equation (2.5), hence the equality constraint ψ_4 for stability is

$$\psi_4 = d - \sqrt{\frac{12\rho g l^3}{\gamma E}} = 0 \tag{3.4}$$

Considering the blade frequency relationship from Equation (2.22), if Equation (3.4) is satisfied an equality constraint ψ_5 for blade frequency implies that

$$\psi_5 = \mu - \frac{\gamma l \omega^2}{g} = 0 \tag{3.5}$$

where μ is the dimensionless frequency parameter equal to $w\omega^2 l^4/EI$. μ was evaluated *(in C3Prog1.m)* as *3.46, 436.68, 3666.03,* & *14328.90* for the 1^{st} 2^{nd}, 3^{rd}, & 4^{th} blade bending frequencies respectively.

The lower limit on the blade length for the scaled sculpture forms an inequality constraint ϕ_1, namely

$$\phi_1 = \frac{l_s}{l_o} \leq 2 \tag{3.6}$$

Satisfying Equations (3.3) and (3.4) result in a blade curvature and thickness for a given blade length and material type. Curvature R and thickness d imply a bending stress in the blade material [Benham & Crawford (1978)] i.e.

$$\sigma = \frac{dE}{2R} \tag{3.7}$$

For the purpose of this analysis, elastic modulus E will be assumed to be a property of the blade material only. There will however be an upper limit or inequality constraint ϕ_2 on bending stress, namely

$$\phi_2 = \frac{dE}{2R} \leq \sigma_y \tag{3.8}$$

The performance requirement specification stipulates that *Blade* should survive a minimum of one performance *($P_f \geq 1$),* however this minimum life will not be achieved unless Equation (3.8) is satisfied.

From the results of Chapter 6, the worst-case scenario for the assumed vibratory form, using Equation (4.32), is assumed to be a superposition of the first and third blade bending modes *(with a maximum blade displacement of 0.435 & 0.150m for the first and third modes respectively)*. This worst-case scenario, shown in Figure 3.2, is used for strength of materials calculations.

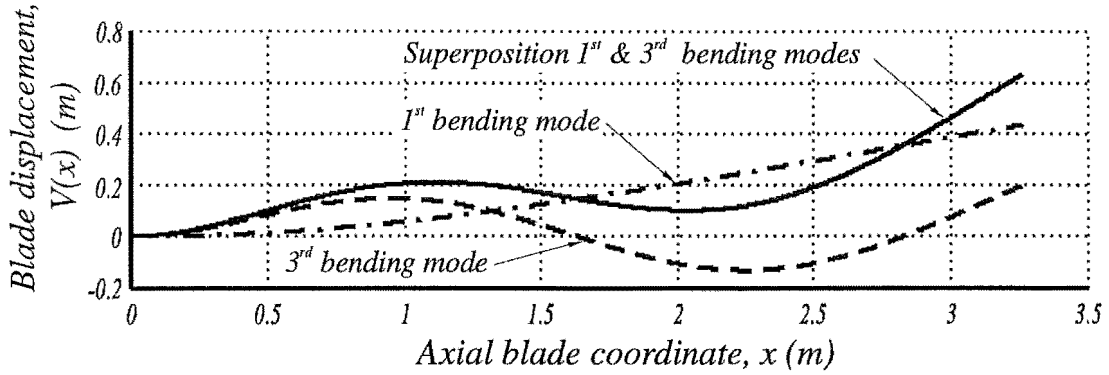

Figure 3.2 *The assumed vibratory blade form used in strength of materials calculations*

The minimum radius of curvature and corresponding maximum bending stress for the combined vibratory form in Figure 3.2 is at the fixed end *($x = 0$)* of the blade. The analytical form of the modes is discussed in Chapter 4, in particular Equations (4.32) which may be differentiated with respect to x to give the maximum bending stress *(as calculated in C3Prog1.m)* namely

$$\sigma(0) = \frac{dE}{2R(0)} \tag{3.9}$$

$$where \quad \frac{1}{R(0)} = \left(\frac{d^2V_1(0)}{dx^2} + \frac{d^2V_3(0)}{dx^2} \right)$$

Table 3.2 lists the calculated maximum blade bending stresses, calculated from Equation (3.9) for a number of the higher strength candidate materials from Figure 3.3.

Table 3.2 *Bending stress prediction for candidate blade materials*

Material	E (GPa)	ρ (kg/m^3)	d (m)	η $(\times 10^{-3})$	σ_u	σ (MPa)	σ_y (MPa)	σ_e' (MPa)	σ_e (MPa)
[4]CFRP	110	1550	3.19	4	-	218	-	350	223
[3]Titanium Alloy (6Al/4V)	114	4429	5.3	0.3	1000	374	914	550	350
[5]Stainless Steel (414)	207	7850	5.2	0.7	807	671	1480	310	197
[2]Bisalloy 500	207	7850	5.2	0.4	1585	671	1480	737	469
[1]Aluminium Alloy 7050	70	2850	5.42	0.5	572	235	455	159	101
Glass S_1O_2	69	2500	5.11	0.015	-	218	-	113	72
[1]Spring Brass C2600	110	8530	7.48	0.04	650	510	490	160	104

N.B. The effects of the stress concentration at the clamp exit have not been considered for the static stress case. An estimate of the endurance limit modifying factor was applied to the endurance limit of all materials considered ($\sigma_e = 0.636\sigma_e'$)

[1] [ASM Metals Handbook (1992)], [2] [Bunge Industrial Steels Pty Limited], [3] [President Titanium], [4] [Savage (1993)], [5] [Deutschman et al. (1975)]

Equation (3.9) predicts that for all of the materials considered, with the exception of CFRP, the maximum bending stress is above the modified endurance limit. Therefore, because the blade is operated at its third order bending frequency, a reversed bending stress will be imposed at a level expected to result in a finite working life for the blade.

3.2.1.1 Preliminary blade life investigation

Fatigue data for particular materials is often difficult to obtain or must be acquired by experimental means [Collins (1993)]. Therefore, in an attempt to make the optimisation process more efficient, the number of candidate blade materials is reduced before gathering detailed fatigue information. Accordingly, this analysis considers the amplitude of the blade bending stress in relation to the endurance limit for the candidate blade materials listed in Table 3.2; a blade life parameter U_{sm} is defined as

$$U_{sm} = \frac{Endurance\ limit}{bending\ stress} = \frac{\sigma_e}{\sigma} \tag{3.10}$$

The value σ in the ratio σ_e/σ is a failure stress at a number of stress cycles to failure on an S-N diagram for a candidate material. Substituting the bending stress equation, Equation (3.9), into Equation (3.10) gives

$$U_{sm} = \frac{2\sigma_e R}{dE} \tag{3.11}$$

Including the equality constraint for blade thickness from Equation (3.4), the blade life parameter becomes

$$U_{sm} = \frac{\sqrt{\gamma}\sigma_e R}{\sqrt{3\rho g E l^3}} \tag{3.12}$$

Equation (3.12), may be factorised into three independent groups, as described by Johnson (1980) and Ashby (1992), giving

$$U_{sm} = \frac{1}{\sqrt{3}}\left(\frac{\gamma}{g}\right)^{\frac{1}{2}}\left(\frac{R}{l^{\frac{3}{2}}}\right)\left(\frac{\sigma_e}{\rho^{\frac{1}{2}}E^{\frac{1}{2}}}\right) = maximum \qquad (3.13)$$

blade stability index ***blade shape parameter*** ***blade material properties index***

The *blade stability index* and *shape parameter* in Equation (3.13), contain variables from the equality constraint equations and are fixed. The variables that may be changed are the material properties *(i.e. the material properties index).* For a maximum value of the blade life parameter the best solution will require a blade material with the highest *blade material properties index.* For the materials considered, Table 3.3 lists these values in order

Table 3.3 *The blade material properties index*

material	***blade material properties index***
CFRP	*26.8*
Titanium Alloy 6Al/4V	*24.5*
High Carbon / Alloy Steels	*18.3*
7050 Aluminium Alloy	*11.3*
Glass	*8.6*
Stainless steel (414)	*7.7*
Spring Brass	*5.2*

3.2.2 Sound qualities

Like a good bell or percussion instrument, the blade must have good reverberant qualities and requires a material with low intrinsic damping or internal friction. Intrinsic damping is an important property when structures vibrate and is characterised by the loss coefficient η. Figure 3.3 shows the loss coefficient η plotted against elastic modulus for a range of engineering materials. The high carbon steel blade used on the original sculpture has a particularly low loss coefficient, ($\eta = 10^{-4}$), as do copper alloys and glass which have been traditionally used as bell materials. Titanium alloy, alloy steel, and

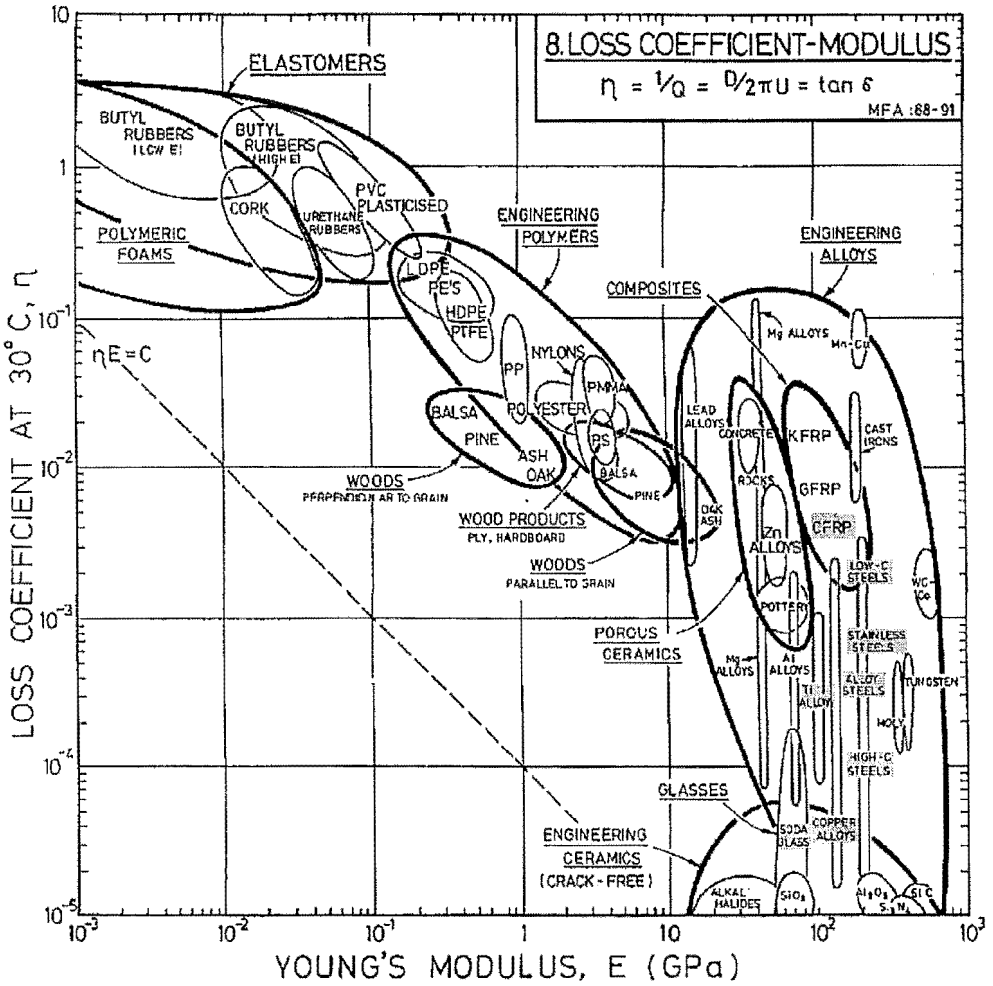

Figure 3.3 *Loss coefficient η [from Ashby (1992)]*

(NB. highlighted materials are of particular interest)

aluminium alloy, have a higher loss coefficient than high carbon steel, thus a deterioration in sound quality would be expected for the sculpture using a blade made from these materials.

An experimental investigation was conducted to study the acoustic characteristics of a blade made from titanium alloy 6Al/4V at the original size. The sound pressure level was measured after releasing a pendulum to strike the original high carbon steel blade and then the test repeated with a similar sized titanium alloy blade. The results of this experiment, shown in Figure 3.4, are that the initial disturbance to the sound pressure level was greater in the case of the titanium alloy blade.

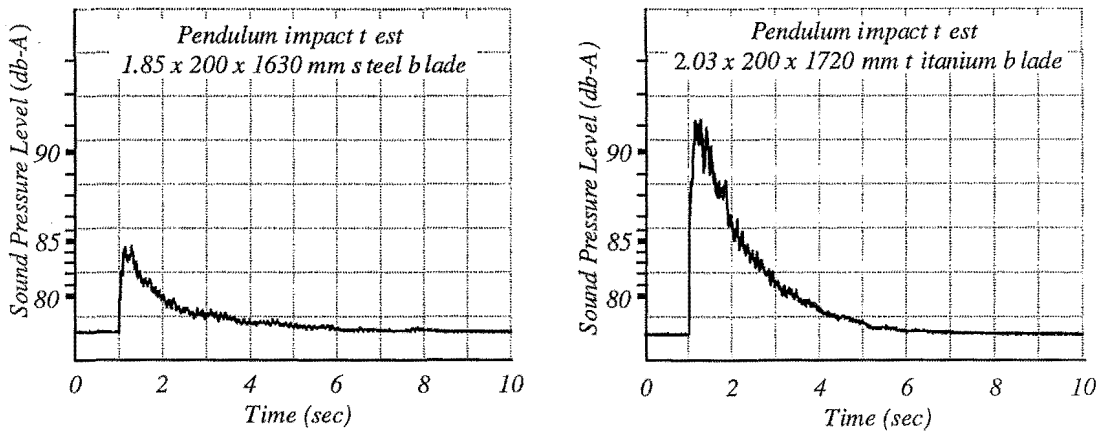

Figure 3.4 *Sound pressure level following a pendulum impact test*

The maximum amplitude of displacement observed for the impact test was greater for the titanium blade and thus is consistent with Figure 3.4. These higher blade disturbances were ascribed to the titanium having a lower elastic modulus and density.

From Figure 3.4, it is observed that the time for the sound pressure level to attenuate from *84 db-A* to an ambient level, is *4.8 seconds* for the carbon steel blade and *3.75 seconds* for the titanium alloy blade. Hence this titanium alloy appears to be more damped, which is consistent with the lower loss coefficient η in Figure 3.3.

After considering the results of the impact test, and the materials selection chart Figure 3.3, it was decided to set an upper limit on the damping coefficient of candidate blade materials. The upper limit defined is the sound quality that would be expected from a mild steel blade material [Webb (Jan. 1996 – Dec. 1998)], thus from Figure 3.3 the *inequality constraint* ϕ_3 is

$$\phi_3 = \eta \leq 2\times10^{-3} \tag{3.15}$$

3.2.3 Surface finish

Ideally the surface finish for the blade is to be highly reflective and steel-like in colour *("... a large shiny square-sided kerosene ... a great flash of quivering sunlight ..." [from Len Lye quote pg 1]).* Agreed inequality constraints in this case [Webb (Jan. 1996 – Dec. 1998)], were that the blade should have a surface *colour* comparable with or more steel-like than dull grey aluminium and that the blade surface roughness R_a be finer than $0.8\mu m.$

The scaled *Blade* is to be permanently exhibited at an outside location within 1km of the sea. Corrosion resistance, and in particular the resistance to attack by a salt water and U-V light are significant considerations for selecting candidate blade materials.

Corrosion resistance was not set as a formal constraint to the design because it was decided [Webb (Jan. 1996 – Dec. 1998)] that while undesirable, the blade could have a protective coating applied between performances.

Figure 3.5 shows the comparative ranking of the resistance of the blade materials considered so far, to attack by salt water and U-V radiation. Glass and titanium are expected to offer excellent resistance to attack by salt water followed by the CFRP that has excellent to good resistance and followed by aluminium alloy, alloy steels, and carbon steel which are expected to be good, poor, and bad respectively. All materials with the exception of CFRP have excellent resistance to U-V light.

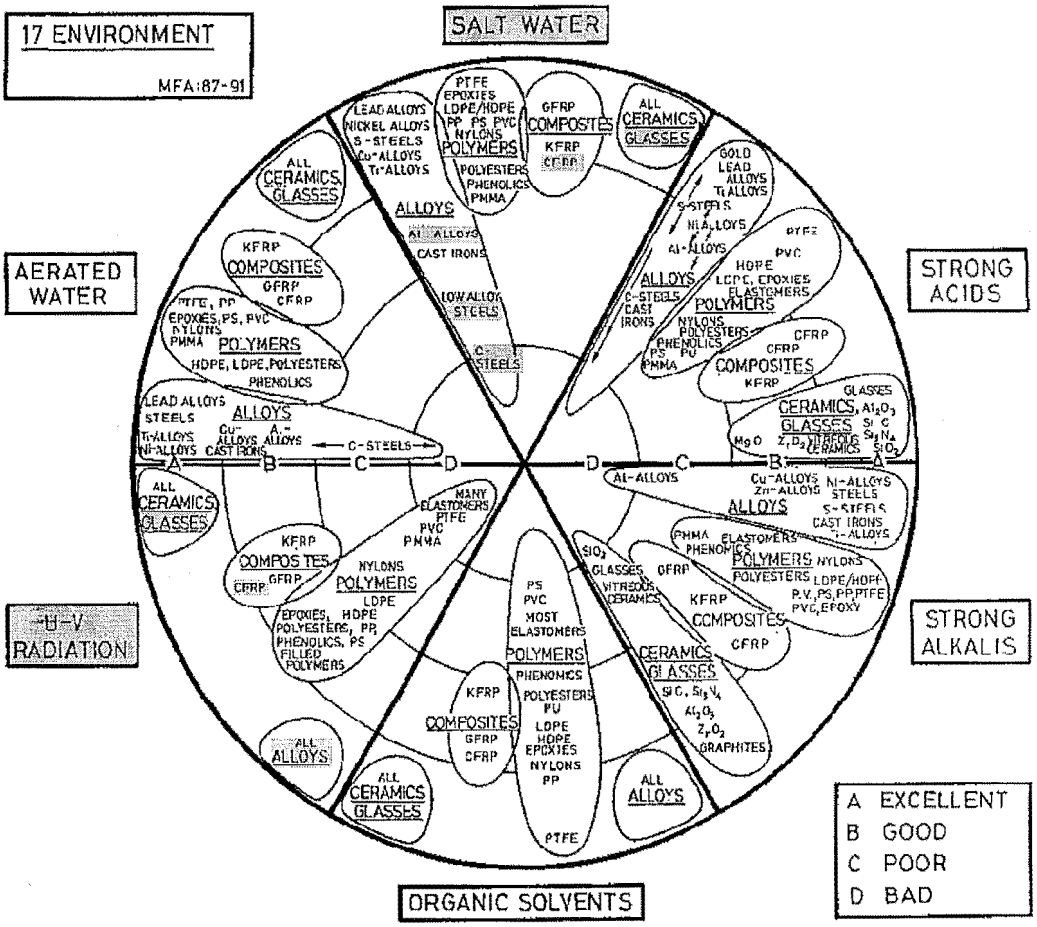

Figure 3.5 *Resistance of materials to attack by some corrosive environments [from Ashby (1992)] (NB. highlighted materials and environments are of particular interest)*

3.2.4 Economic availability

Early investigations found that the original cold rolled high carbon steel was not available in a thickness of over *3mm* due to limitations of the cold rolling process.

A high strength low alloy steel, Bisalloy 500 [Bunge Industrial Steels], while not generally available at the required length, was likely to be available at a suitable size if requested before a mill run.

High strength titanium alloys such as those listed in [Duncan & Hanson (1980)] were found to be difficult to obtain in the dimensions required for a blade. After extensive discussions representatives of titanium alloy suppliers and mills, including Diyanni (Jan. – May 1996) and Hudson (Jan. – May 1996), it was decided that the most suitable grade of titanium, likely to be available at the required size, is Ti6Al/4V. Ti6Al/4V is produced in small batch runs, obtaining a suitable piece for *Blade* is likely to require a worldwide search of potential suppliers and mills.

Finding suitable materials for the flexible components in Len Lye's kinetic sculptures have in the past been a limiting factor governing the maximum size [Raine et al. (1996)].

Inequality constraints on economic availability were defined for a nominally double-original size sculpture. These upper limits require a blade material cost of less than *NZ$500 per performance* and an availability within a 12 month lead time [Webb (Jan. 1996 – Dec. 1998)]. For *Blade* at the monumental size *(l_s > 30ft)* further consideration would be required to establish potential income from a paying audience.

3.2.5 Reducing the number of candidate materials

The most promising candidate blade materials were selected for further consideration based on their ability to meet the constraints derived in Section 3.2.2. Figure 3.6 illustrates the initial material selection process.

Materials selection chart

Selection of candidate 'blade' materials

Sheet 1 of 1

Material	*Vibration and sound qualities ($\eta < 0.001$)*	*Vibratory form ($\sigma < \sigma_y$)*	*Material properties index (Equation 3.14 > 12)*	*Economic availability (U^1 < 500NZ$ & lead time < 12 mths when $s \approx 2$)*	*Colour (more steel-like than dull a aluminum)*	*Resistance to attack by salt water and U-V light*	*Comments*	*Score*	*Develop further*	*Eliminate*	*Get information*
1	x x	√ √	√ √	√ √	x	√	***Pros*** *- infinite working life* ***Cons*** *- poor reverberant qualities* ***Ideas*** *- use a hidden device to create sound*	4		√	
2	√	√ √	√	√	√	√ √	***Pros*** *- excellent corrosion resistance properties* *- better sound quality than for low alloy steel* *- material has extra element of interest for audience*	7	√		
3	√	√ √		√	√	x √	***Pros*** *- may be available at larger sizes if requested at time coinciding with bigger mill run* ***Cons*** *- poor resistance to attack by salt water*	5	√		
4		√ √		x	√	x √	***Cons*** *- not available in required thickness 'blade' made by laminating two thin sheets* *- poor resistance to attack by salt water*	2		√	
5	√	√ √	x x	?	√	√ √	***Pros*** *- excellent corrosion resistance properties* ***Cons*** *- low material properties index*	4		√	
6	√	√ √	x	?		√ √	***Cons*** *- low material properties index*	3		√	
7	√ √	√ √	x x	?	x	√ √	***Pros*** *- excellent reverberant qualities (used for bells)* ***Cons*** *- brittle failure may be dangerous to viewer* *- low material properties index*	3		√	
8	√ √	√ √	x x	?	x	√	***Pros*** *- good reverberant qualities (traditionally used for bells)* ***Cons*** *- low material properties index*	3		√	

Materials considered

1. *C.F.R.C.*
2. *Titanium Alloy*
3. *Low alloy steel*
4. *Cold rolled high carbon steel*
5. *Stainless steel*
6. *Aluminum alloy*
7. *Glass*
8. *Spring brass*

Key: (√) positive +1, (x) negative -1, ( ) neutral 0, (?) not enough information

Figure 3.6 *Materials selection chart [adapted from Pahl & Beitz (1996)]*

3.3 Final material selection

The selection process in Figure 3.6 resulted in reducing the number of candidates to consider only the alloy steel and titanium alloy materials.

While the choice of material may be made purely in terms of the blade life parameter, the decision as to whether the sculpture is viable at a certain scale is also an economic one.

The objective of this analysis is to investigate the cost per performance with increasing scale for a blade made from either titanium alloy or low alloy steel when subject to the design constraints identified in Section 3.2.

Using the *'method of optimum design'* it is useful to formulate a *'primary design equation'* [Johnson (1980)] to maximise or minimise. In this case the *primary design equation parameter U,* to be maximised, is the number for *Blade* performances for a given expenditure i.e.

$$U = \frac{Number\ of\ performances\ to\ failure}{material\ cost} \quad (NZ\$^{-1}) \tag{3.16}$$

If P_f & C_m are defined as the number of performances to failure and the material cost per kg respectively, then the primary design equation, Equation (3.16) takes the form

$$U = \frac{P_f}{C_m \rho b d L} \tag{3.17}$$

The relationship between the number of cycles to failure N_f, the mean failure strength σ_f, and the endurance limit σ_e, may be represented using an S-N diagram. Typical S-N curves for ferrous and titanium alloys exhibit a steep drop in the high

cycle fatigue life range *(typically from 10^3 – 10^6 cycles)* and levelling off to approach a stress asymptote *(the fatigue limit)* at longer lives [Collins (1993)]. For high cycle fatigue *(beyond 10^3 cycles of stress)* investigations on fatigue strength of wrought steels recommend that a line on the log S - log N chart joining $0.8\sigma_u$ at 10^3 cycles and σ_e at 10^6 cycles could be used to define the mean fatigue strength corresponding to any life between 10^3 and 10^6 cycles [Shigley (1986)]. Based on this analogy, the S–N diagram for a typical steel or titanium alloy is modelled in Figure 3.7. *(N.B. Figure 3.7 has been adjusted to include the fatigue strength modifying factor k_s this is calculated in C3ProgA1)*

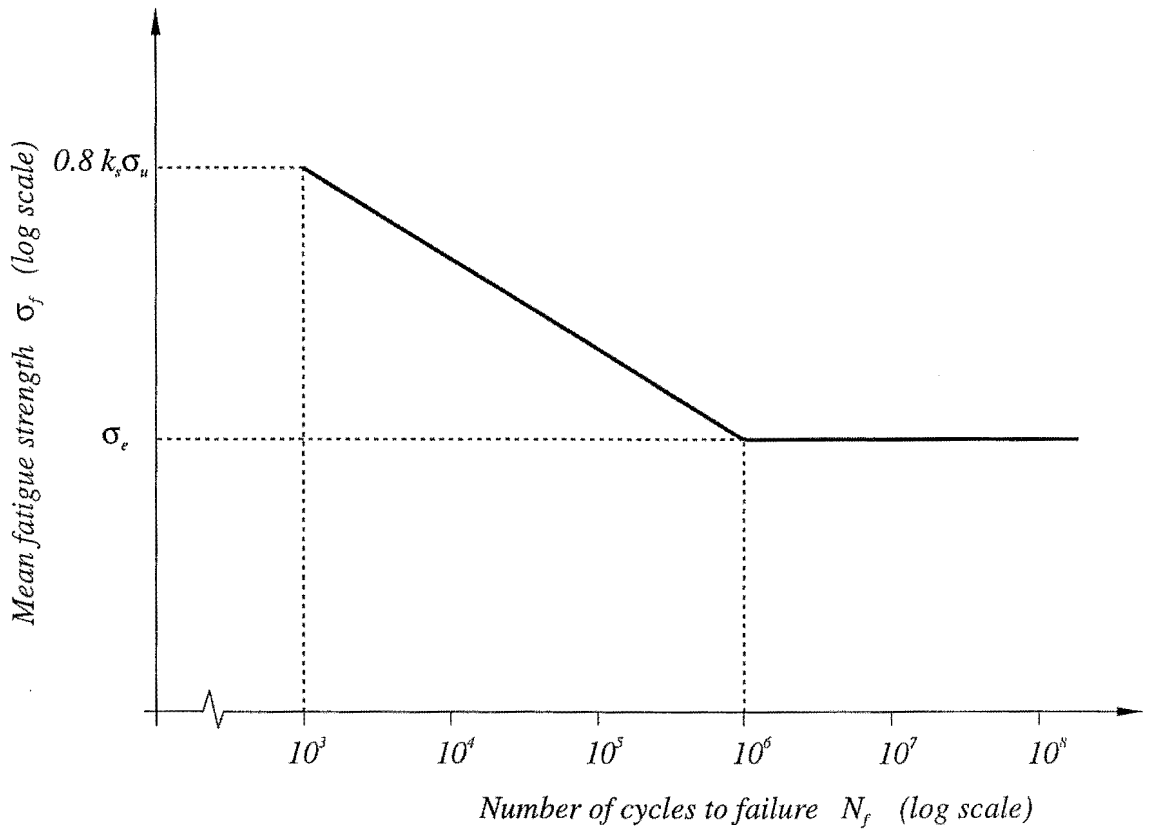

Figure 3.7 *Assumed form of the S–N curve for a typical low alloy steel or titanium alloy*

The line from $10^3 - 10^6$ cycles in Figure 3.7 is defined by the relationship

$$log(\sigma_f) = -\frac{1}{3} log \frac{0.8k_s\sigma_u}{\sigma_e} log(N_f) + log \frac{(0.8k_s\sigma_u)^2}{\sigma_e} \qquad 10^3 < N_f < 10^6 \tag{3.18}$$

Substituting in the thickness d from the equality constraint, Equation (3.4) into the bending stress equation, Equation (3.7), Equation (3.18) may be arranged in the form

$$N_f = 10^{\left(\frac{\log\frac{(0.8k_s\sigma_u)^2}{\sigma_e}}{\frac{1}{3}\log\frac{0.8k_s\sigma_u}{\sigma_e}}\right)} \left(\sqrt{\frac{3E\rho gl^3}{\gamma}}\frac{1}{R}\right)^{\left(\frac{-3}{\log\frac{0.8k_s\sigma_u}{\sigma_e}}\right)} \qquad 10^3 < N_f < 10^6 \tag{3.19}$$

For the case where the ratio of the ultimate strength to endurance limit is assumed to be constant, the constants k_1 and k_2 may be introduced, giving

$$N_f = k_1 \left(\sqrt{\frac{3E\rho gl^3}{\gamma}}\frac{1}{R}\right)^{k_2} \qquad 10^3 < N_f < 10^6$$

$$where\ k_1 = 10^{\left(\frac{\log\frac{(0.8k_s\sigma_u)^2}{\sigma_e}}{\frac{1}{3}\log\frac{0.8k_s\sigma_u}{\sigma_e}}\right)} \ \&\ k_2 = \frac{-3}{\log\frac{0.8k_s\sigma_u}{\sigma_e}} \tag{3.20}$$

If the length of that part of a performance of *Blade* vibrating at the third bending frequency is T_3 seconds, then the number of important stress cycles per performance is $T_3\omega_3/(2\pi)$, and the number of performances to failure is

$$P_f = \frac{2\pi N_f}{\omega_3 T_3} \tag{3.21}$$

To allow for reducing blade frequency with increasing blade length, the dimensionless frequency from Equation (3.5) may be applied. The inverse of a representative frequency introduced in Equation (3.21) above, recognises that the life of a blade of given size will be a finite number of stress reversals and will reduce as the average vibration frequency during a *Blade* performance increases. The inverse of frequency ω, is included by transposing Equation (3.5). On this basis

$$\omega_3 = \sqrt{\frac{\mu_3 g}{\gamma l}} \tag{3.22}$$

This frequency corresponds to the third order natural bending vibration that causes the high fatigue stress, and includes the dimensionless frequency constraint, μ_3. Substituting Equation (3.22) into (3.21) gives

$$P_f = \frac{2\pi N_f}{T_3}\sqrt{\frac{l\gamma}{g\mu}} \tag{3.23}$$

Finally, it is necessary to include the cost of the blade material. Cost M_c is introduced by multiplying the material cost per kg C_m by the blade mass ρdbl. Substituting for d from Equation (3.4) leads to

$$M_c = 2C_m b\sqrt{\frac{3l^5\rho^3 g}{\gamma E}} \tag{3.24}$$

Substituting Equations (3.23) & (3.24) into (3.16) results in an expression for the *'primary design equation' (number of blade performances per dollar cost)* as

$$U = \frac{\frac{2\pi}{T_3}\sqrt{\frac{\gamma}{g\mu}}k_1\left(\sqrt{\frac{3E\rho g l^3}{\gamma}}\frac{1}{R}\right)^{k_2}}{2C_m b\sqrt{\frac{3l^5\rho^3 g}{\gamma E}}} \qquad 10^3 < N_f < 10^6 \tag{3.25}$$

For the same aspect ratio between the original and scaled blades, then $b = (k_4 \times l)$. Applying the equality constraint equation for the blade curvature relationship, Equation (3.3), R in Equation (3.9) is proportional to blade length l. Defining the constant $k_3 = R / l$. Making these substitutions in Equation (3.25) gives

$$U = \frac{\frac{\pi}{T_3}\sqrt{\frac{\gamma}{g\mu}}k_1\left(\sqrt{\frac{3E\rho g l^3}{\gamma}}\frac{1}{k_3 l}\right)^{k_2}}{C_m k_4 l\sqrt{\frac{3l^5\rho^3 g}{\gamma E}}} \qquad 10^3 < N_f < 10^6 \tag{3.26}$$

Defining two new constants

$$k_5 = \frac{\pi k_1 3^{\frac{1}{2}(k_2-1)}}{k_4 k_3^{\,k_2}} \quad \& \quad k_6 = 1 - \frac{k_2}{2} \tag{3.27}$$

The number of performances to failure per dollar cost, Equation (3.26) becomes

$$U = k_5\left[\frac{\gamma^{k_6}}{\mu^{\frac{1}{2}} g^{k_6} T_3}\right]\left[\frac{1}{l^{(k_6+2)}}\right]\left[\frac{1}{E^{\left(k_6-\frac{3}{2}\right)}\rho^{\left(k_6+\frac{1}{2}\right)}C_m}\right] \tag{3.28}$$

stability & freq. parameter ***blade shape parameter*** ***blade material properties index***

Note: Constants k_5 & k_6 are +ve

Calculations show that the relationship given by Equation (3.28) has the effect of increasing the advantage of the ratio σ_e/σ in Equation (3.10) that titanium offers by comparison with steel. The values of the *'primary design equation' U,* for a double size *Blade* were calculated to be 0.027 & 0.004 for titanium alloy and alloy steel respectively. Results of this analysis *(calculated using C3Prog1)* are listed in Table 3.4

Table 3.4 *Predicted performances to failure and material cost per performance for an exactly double size blade*

Material	***Number of performances to failure***	***Material cost per performance***
Titanium alloy 6Al/4V	*217*	*37*
Low alloy steel	*9*	*221*

From Equation (3.30), it may be noted that the number of performances per dollar expended on the blade material varies inversely as $l^{(k_6+2)}$, and the cost per performance of *Blade* will increase exponentially with increasing scale. Figure 3.8 shows the calculated number of performances to failure for the two cases where either high strength titanium alloy or high strength alloy steel materials are used for the blade. Figure 3.8 illustrates the rapid reduction in life with increasing scale. A scale ratio of 1 refers to the original 1630 mm high blade. The theoretical limiting scale is reached when the sculpture will complete not more than one performance before failure. For the case of the titanium alloy and alloy steel materials, the limit on blade length was calculated; results are listed in Table 3.5.

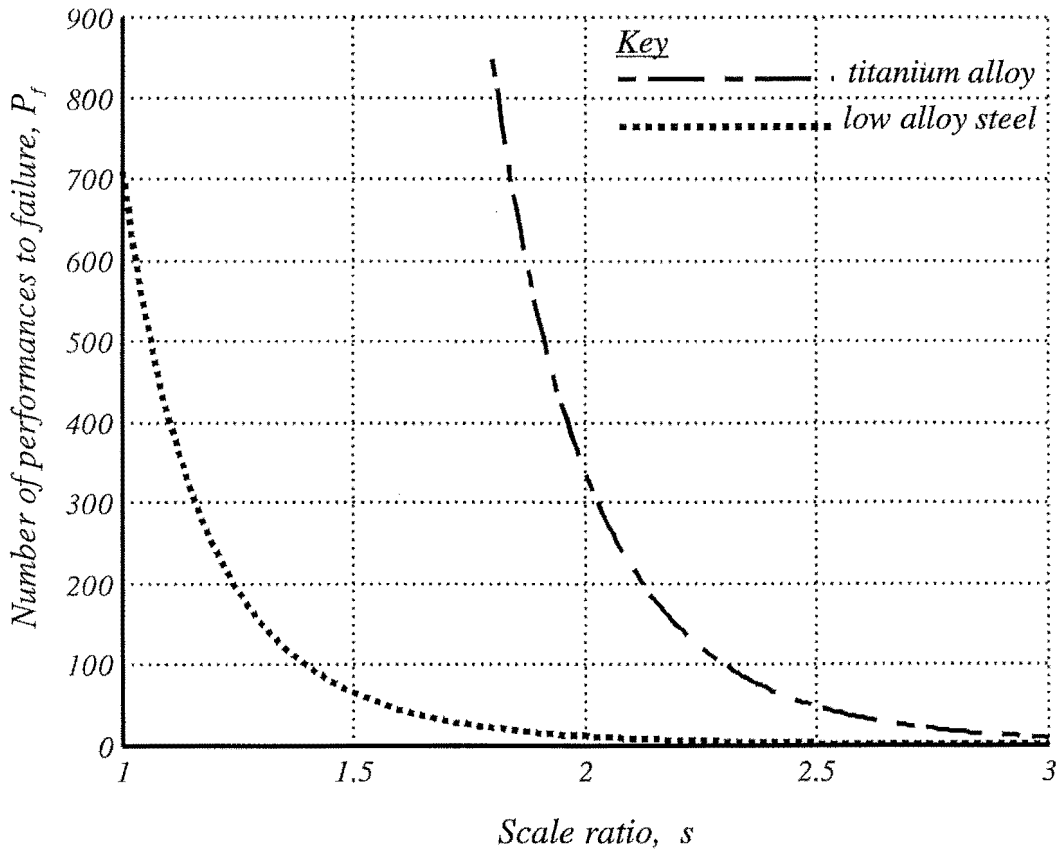

Figure 3.8 *Performances to failure, P_f, with increasing scale, s*

At the theoretical limiting scale the maximum bending stresses in the blade are approaching the yield stress, and the blade will not be expected to last a second performance despite satisfying the buckling stability criterion.

Table 3.5 *The theoretical limiting scale*

Material	**theoretical limiting scale**	***cost for one performance (NZ$)***
Titanium alloy 6Al/4V	*3.7 (l = 6.0m)*	*68000*
Low alloy Steel	*2.9 (l = 4.7m)*	*7000*

If cost and availability were not considered as constraints the theoretical limiting scale and associated performance costs would be as listed in Table 3.5

Figure 3.9 illustrates the rapid increase in cost per performance with increasing scale. While cost rapidly becomes prohibitive, the limit on cost per performance *(NZ$500)* was not found to be the limiting factor. The optimum solution is constrained by availability of materials.

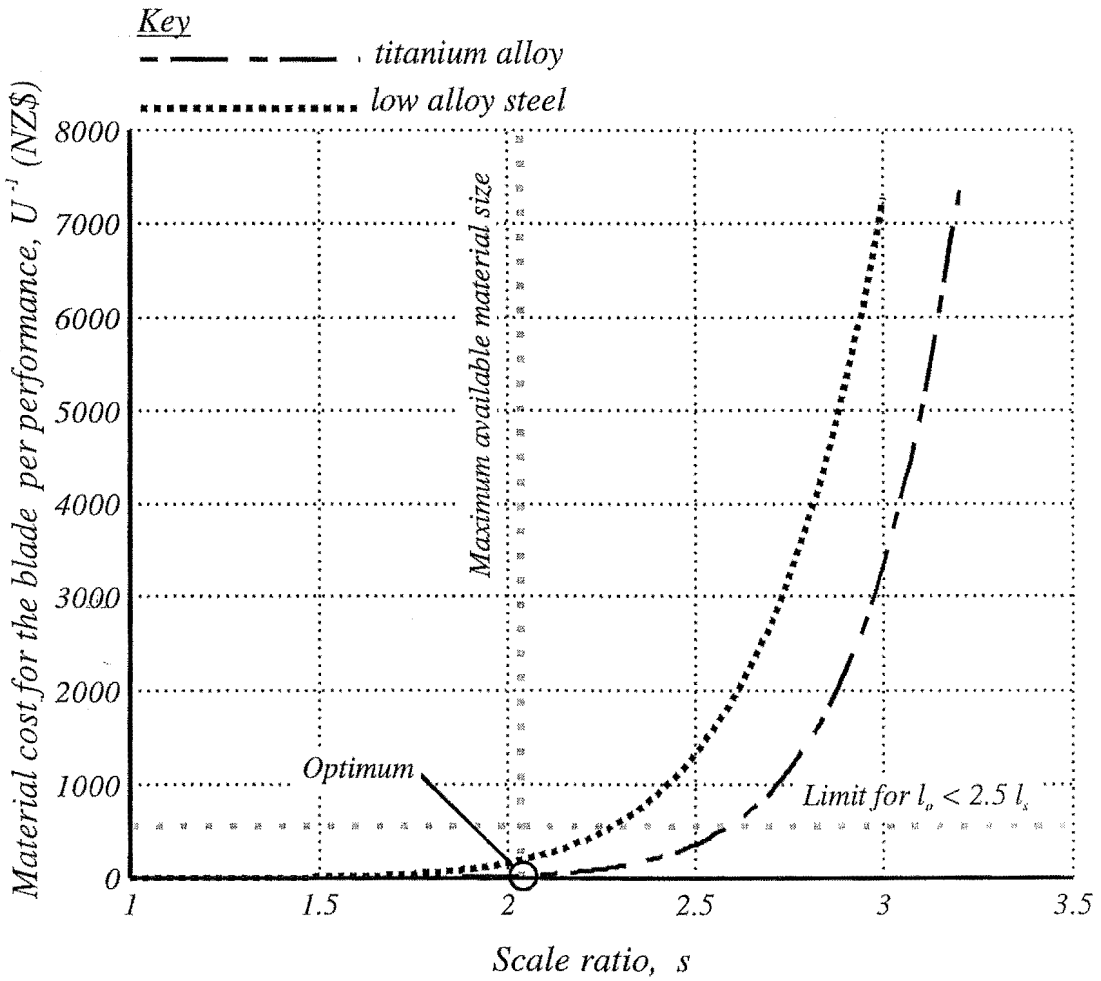

Figure 3.9 *Blade material cost per performance U^{-1} with increasing scale s*

3.4 Specification for the optimal design solution

The specification of components for the optimum design solution for the kinetic sculpture *Blade* consists of the material specification for the blade. The selected material is titanium alloy 6Al4V and the specification is listed in Table 3.6.

The surface of the titanium blade material was finished using a belt sanding process. The blade was clamped flat onto a table and passed under a revolving flat belt sander in a similar way to a planning machine. New belts were used to reduce the risk of contamination. The resulting surface roughness was $0.8\mu m$ and the machining grain ran along the length dimension of the blade.

The blade thickness after the surface finishing process was $5.533mm$. The equality constraint for stability, Equation (3.4), results in a blade length l *(i.e. length from the clamp exit point to the free end)* of $3.355m$. Because of the expense of this material, and considering that the blade is expected to fail at the clamp exit *(i.e. the fixed end),* the specified nominal blade length l is $3.455m$. *(NB. $200mm$ of the blade is fixed in the rigid clamp and the actual length of material cut is l + $200mm$)* In this case, after the first failure, providing the material has failed as expected, the blade can be shortened by $200mm$, turned end for end, and a second life used. *(NB. turning the blade end for end ensures the maximum possible second life. This is because the free end from the previous use will have endured lower mean alternating bending stresses.)*

Hemple & Hillnhagen (1969) give the S-N curve for flat Ti6Al/4V specimens in the annealed condition as shown in Figure 3.10. The chemical composition and material properties for the material test in Figure 3.10 are very similar to the material acquired for the blade, hence the Figure 3.10 was used to predict the number of cycles to failure for the scaled blade. The two uppermost dashed

lines in Figure 3.10 show the data range for the flat annealed test specimens. The green line is the assumed mean curve, the red line includes the modifying factor of fatigue stress at the clamp exit and was used for blade life predictions. The maximum calculated reversed bending stress at the clamp exit was $383MPa$ (39kg/mm^2) and the corresponding number of cycles to failure is 2.05×10^5. 2.05×10^5 cycles gives ***261*** performances to failure and a blade material cost of ***NZ$36*** per performance.

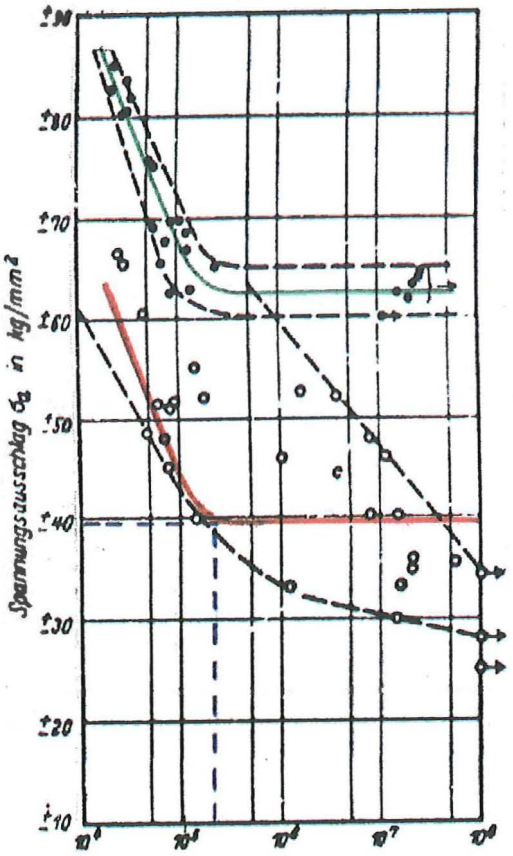

Figure 3.10 *Fatigue test data for titanium alloy 6Al4V annealed. [after Hemple & Hillnhagen (1969)]*

Table 3.6 *Final material specification for the blade*

Description	Specification
blade material	*Ti6Al4V*
US military specification	*MIL-T-9046_J*
material condition	*Annealed ½ hr @ 1400F AC*
chemical composition [Timet]	*0.009C, 0.225Fe, 0.008N, 4.449Al, 4.070V, 0.130O,avg %weight & 88H2 ppm*
elastic modulus, E [President titanium]	*114 GPa*
density, ρ [President titanium]	*4429 kg/m^3*
tensile strength, σ [Timet]	*985 MPa*
yield strength, σ_y [Timet]	*931 MPa*
endurance limit, σ_e [Hemple & Hillnhagen (1969)]	*614 MPa*
surface finish & roughness	*Belt sanded to 0.8 μm*
length, l	*3.455 m*
width, b	*0.43 m*
thickness, d	*0.00553 m*
predicted number of performances to failure, P_f	*261*

Table 3.6 *(cont.)*

predicted cost per performance, U^{-1}	*NZ$ 36*
material cost, M_c	*NZ$ 9396*
country of origin	*Russia*
supplier	*Tiernay Aerospace Services,* *2600 Marine Ave,* *Redondo Beach,* *CA 90278 U.S.A.*

3.5 Discussion

CFRP was the most promising material in terms of meeting the strength of materials requirements for a blade. If the amplitude of the first order swinging effect, as discussed in Chapter 6, stays within the assumed limits in Figure 3.2, then a double size sculpture would be expected to have an infinite working life. Unfortunately CFRP was found to be unsuitable due to poor reverberant qualities.

From a sound quality perspective, the best material group investigated was glass. While glass was eliminated using the life parameter *(due to a low material properties index)* further consideration of this material is warranted when building similar sculptures. The specified titanium alloy was found to have slightly better reverberant qualities than alloy steel, hence better meets the acoustic qualities for the sculpture.

The fatigue life for the scaled sculpture has been investigated using two independent data sources. The S-N curve, Figure 3.7, yielded a similar result to the prediction using experimental results from Hemple & Hillnhagen (1969). If

the *double harmonic* were not a feature in the performance of *Blade*, the blade would be expected to have an infinite life.

The specified titanium alloy blade material has excellent corrosion resistance due to the fact that it is intrinsically very reactive [Duncan & Hanson (1980)]. Whenever fresh titanium alloy is exposed to an environment containing oxygen, it immediately acquires a thin tenacious oxide film.

The colour of the titanium alloy 6Al4V is a light shade of grey and considered to be more steel-like in colour than the minimum requirement *(dull aluminium)* [Webb Jan. 1996 – Dec. 1998]. This material is also expected to retain a polish in the outdoor environment.

3.6 Conclusion

The best possible solution satisfying the design requirement specification *(including specifications from Len Lye)* for the kinetic sculpture *Blade* has been obtained by the selection of an optimal blade material.

The two best candidate material groups identified for the blade material were found to be high strength titanium alloy and alloy steel. A life parameter based on the ratio σ_e/σ, showed titanium alloy to be preferable to alloy steel. A variational study of the number of performances per dollar expended for these two materials gave a more quantitive measure and showed that the titanium alloy was almost six times cheaper for a nominally double size work when considered on a cost per performance basis.

The optimal design of the kinetic sculpture Blade, within the artists brief, requires the sculpture to have a titanium alloy (6Al/4V) blade with a nominal blade length of $3.355m$

The scaled *Blade* is expected to fail due to reversed bending fatigue at the fixed end after *260* performances. This blade life corresponds to a blade material cost per performance of *NZ$36*.

The selected titanium alloy has good reverberant properties and is expected to result in the acceptable sound qualities for the sculpture.

The selected titanium alloy has particularly good resistance to attack by the salt air and will have a self-repairing quality if scratched in place.

Availability of a suitable blade material was found to be the constraint limiting the realisable size of *Blade*.

4

The vibratory form – beam modes

4.1 Introduction

Visual qualities in the performance of the kinetic sculpture, *Blade,* are principally due to the shapes formed by the vibrating blade and wand, and by the interaction of these two components. Preliminary observations of the vibration of the blade on the original sculpture established that Lye's single and double harmonic shapes were consistent with the second and third bending modes of vibration for a uniform cantilever beam [McCallion (1972)]. These shapes are shown in Figures 4.1a, and 4.1b.

> ***The purpose of this chapter is to accurately calculate the natural bending frequencies and to define the vibratory form for the blade and the wand. The blade and wand stem are considered as thin uniform beams subject to a gravitational acceleration field.***

This analysis is extended in Chapter 5 where the plate modes are considered and in Chapter 6 where the interaction between wand and blade will be studied.

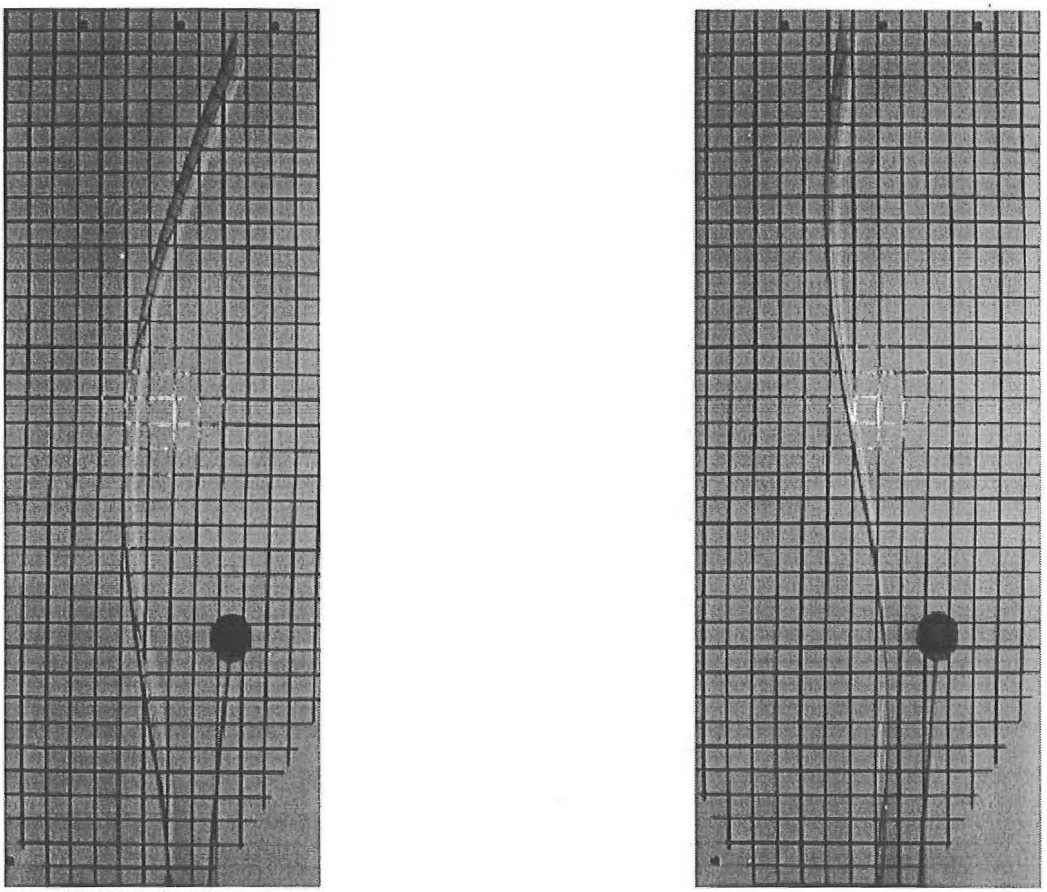

(a) (b)

Figure 4.1 *Vibratory form for the blade and the wand on the original sculpture*
(a) second bending mode (b) third bending mode
(NB. grid background is used for experimental observations only)

4.2 Exact solution for the free lateral vibration of the blade and the wand

The lateral vibration of uniform cantilever beams subject to an axial acceleration has been investigated before [Naguleswaran (1991)] [Newland (1989)]. Naguleswaran (1999) gives an exact solution for the case where the cantilever has an end mass.

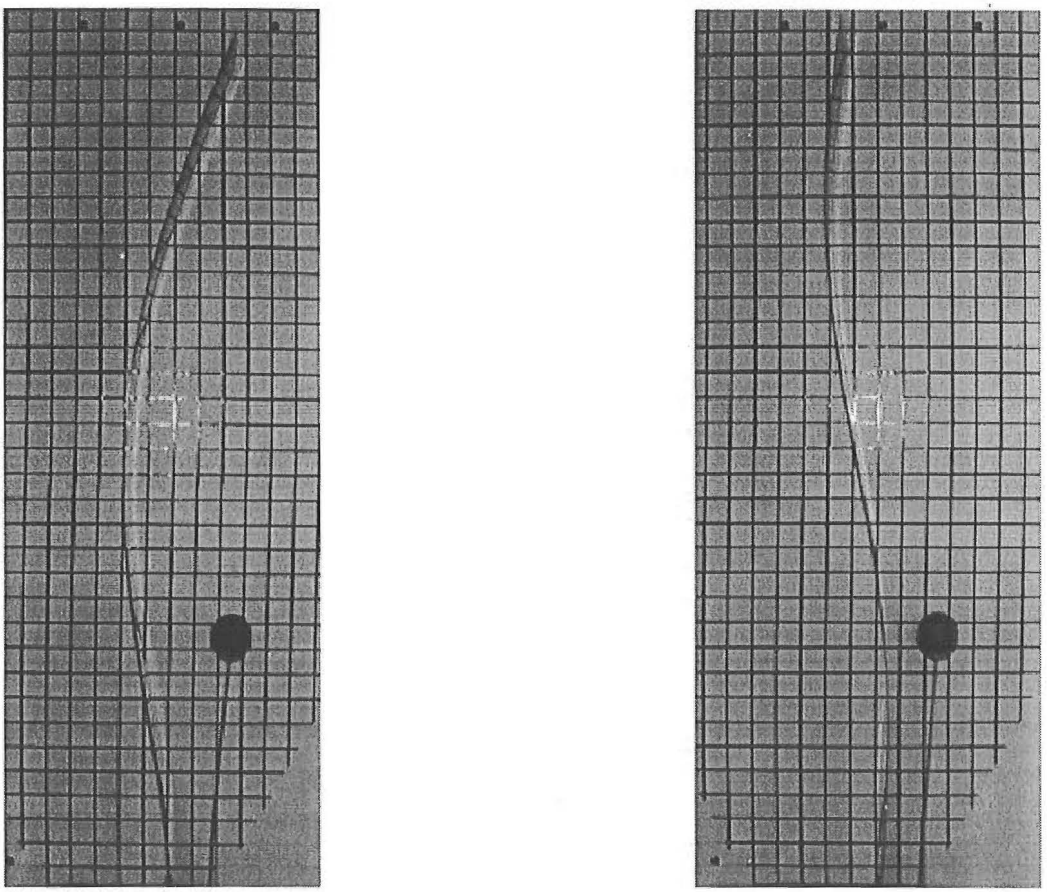

(a) (b)

Figure 4.1 *Vibratory form for the blade and the wand on the original sculpture*
(a) second bending mode (b) third bending mode
(NB. grid background is used for experimental observations only)

4.2 Exact solution for the free lateral vibration of the blade and the wand

The lateral vibration of uniform cantilever beams subject to an axial acceleration has been investigated before [Naguleswaran (1991)] [Newland (1989)]. Naguleswaran (1999) gives an exact solution for the case where the cantilever has an end mass.

4.2.1 The equation of motion

The geometry and mass properties of the assumed form of the vertical cantilever beam are shown schematically in Figure 4.2a.

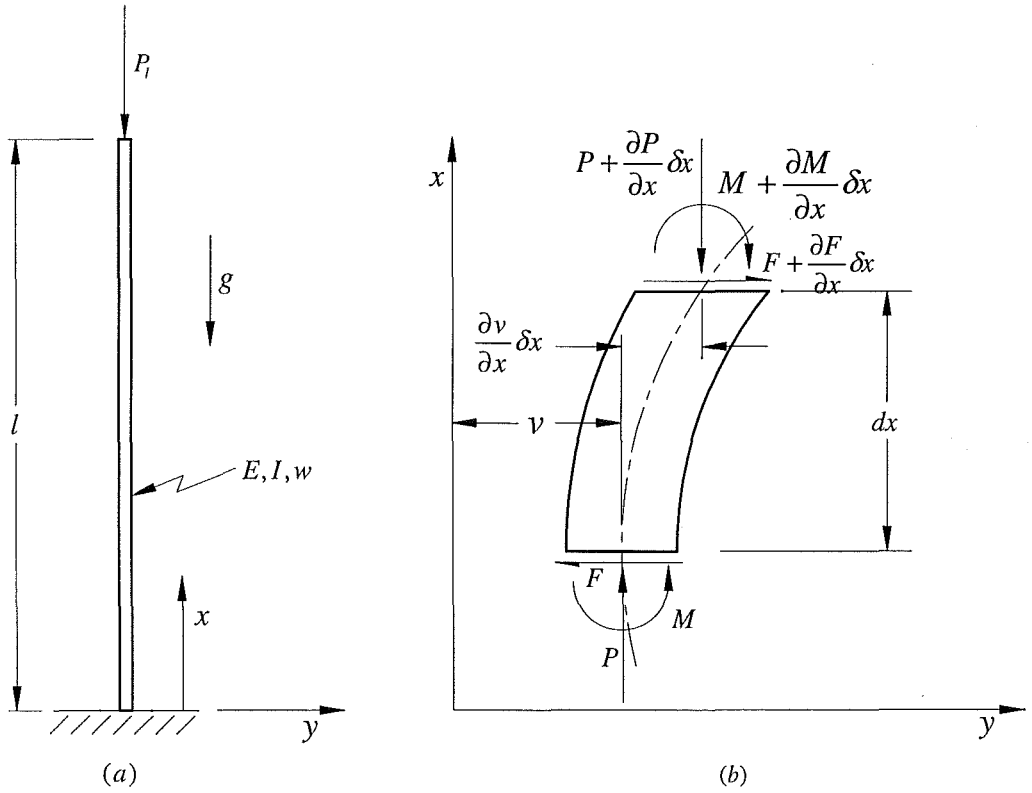

Figure 4.2 *The coordinate system and sign convention used in the beam vibration analysis (a) coordinate system for a vertical cantilever beam subject to an axial acceleration g (b) Positive sign convention for a beam element*

Consider the free body diagram of the beam element shown in Figure 4.2b. Summing forces *(using Newton's second law),* the equation of motion for the translation motion in the y direction is

$$-F(x,t)+F(x,t)+\frac{\partial F(x,t)}{\partial x}\delta x = w\delta x\frac{\partial^2 v(x,t)}{\partial t^2}$$

$$\frac{\partial F(x,t)}{\partial x} = w\frac{\partial^2 v(x,t)}{\partial t^2} \tag{4.1}$$

and similarly for rotation motion *(neglecting rotary inertia and taking moments about the top end of the beam element)*

$$-M(x,t)+M(x,t)+\frac{\partial M(x,t)}{\partial x}\delta x + F(x,t)\delta x + P(x)\frac{\partial v(x,t)}{\partial x}\delta x = 0$$

$$F(x,t) = -\frac{\partial M(x,t)}{\partial x} - P(x)\frac{\partial v(x,t)}{\partial x} \tag{4.2}$$

Substituting Equation (4.2) into Equation (4.1) gives the equation of motion for the free lateral vibration of the beam

$$\frac{\partial^2 M(x,t)}{\partial x^2} + \partial\left(P(x)\frac{\partial v(x,t)}{\partial x}\right)\Big/\partial x + w\frac{\partial^2 v(x,t)}{\partial t^2} = 0 \tag{4.3}$$

From basic mechanics of materials, the moment curvature relationship for a thin beam is *(note: M +ve because slope increases in the +ve v direction)*

$$M(x,t) = EI\frac{\partial^2 v(x,t)}{\partial x^2} \tag{4.4}$$

The axial force at any point along the length of the beam due to self-weight is

$$P(x) = P_t + (l-x)wg \tag{4.5}$$

Substituting Equations (4.4) & (4.5) into Equation (4.3), and for the particular case where E & I remain constant, then the equation of motion becomes

$$EI\frac{\partial^4 v(x,t)}{\partial x^4}+P_l\frac{\partial^2 v(x,t)}{\partial x^2}+\partial\left((l-x)wg\frac{\partial v(x,t)}{\partial x}\right)\Big/\partial x+w\frac{\partial^2 v(x,t)}{\partial t^2}=0 \tag{4.6}$$

Expanding the third term in Equation (4.6), using the separable solution $v(x,t) = V(x)T(t)$, differentiating with respect to x and t, and simplifying gives the mode shape differential equation

$$EI\frac{d^4V(x)}{dx^4}+\left(P_l+wg(l-x)\right)\frac{d^2V(x)}{dx^2}-wg\frac{dV(x)}{dx}-w\omega^2V(x)=0 \tag{4.7}$$

4.2.2 Solving the mode shape differential equation

The mode shape differential equation, Equation (4.7), is a fourth order linear partial differential equation with a variable coefficient. Exact solutions to Equation (4.7) are difficult to obtain. Consider a series solution to Equation (4.7) of the form

$$F(X,c)=\sum_{n=0}^{N}a_{n+1}(c)x^{c+n} \tag{4.8}$$

where c is an undetermined exponent and the coefficients $a_{n+1}(c)$ are functions of c, γ, and μ. Using the differential operator $D = d/dx$, differentiating Equation (4.8) with respect to x, and substituting into the first term in Equation (4.7) gives

$$\begin{aligned}EID^4F(x,c)=EI\big[&(c-3)(c-2)(c-1)ca_1(c)x^{c-4}+(c-2)(c-1)c(c+1)a_2(c)x^{c-3}\\&+\ \ldots\ldots\ldots\quad (c+N-2)(c+N-1)(c+N)(c+N+1)a_N(c)x^{c+N-4}\big]\end{aligned} \tag{4.9}$$

Differentiating Equation (4.8) with respect to x, and substituting into the second term in Equation (4.7) gives

$$\begin{aligned}(P_l + wg(l-x))D^2F(x,c) = (P_l + wg(l-x))\big[&(c-1)ca_1(c)\left(x^{c-2} - x^{c-1}\right) \\ &+ c(c+1)a_2(c)\left(x^{c-1} - x^{c}\right) \\ &+ \ \ldots\ (c+N-1)(c+N)a_N(c)\left(x^{c+N-2} - x^{c+N-1}\right)\big]\end{aligned} \tag{4.10}$$

similarly the third term in Equation (4.7) becomes

$$-wgDF(X,c) = -wg\left[ca_1(c)x^{c-1} + (c+1)a_2(c)x^{c} + \ \ldots\ldots\ldots (c+N)a_N(c)x^{c+N-1}\right] \tag{4.11}$$

and the forth term in Equation (4.7) is

$$-w\omega^2F(x,c) = -w\omega^2\left[a_1(c)x^{c} + a_2(c)x^{c+1} + \ \ldots\ldots\ldots\ a_N(c)x^{c+N}\right] \tag{4.12}$$

Summing Equations (4.9) to (4.12) *(in the form of Equation (4.7))*, setting the lead coefficient equal to unity, and equating the coefficients of x^{c-3} and all higher powers of x to zero results in the coefficients

$$a_1(c) = 1 \qquad a_2(c) = 0 \qquad a_3(c) = -(wgl + P_l)\Big/EI[(c+1)(c+2)]$$

$$a_4(c) = wgc\Big/EI[(c+1)(c+2)(c+3)] \tag{4.13}$$

and the recurrence relationship *[after Naguleswaran (1991)]*

$$a_{n+5}(c)=\frac{-(wgl+P_l)(c+n+1)(c+n+2)a_{n+3}(c)+wg(c+n+1)^2a_{n+2}(c)+w\omega^2a_{n+1}(c)}{EI[(c+n+1)(c+n+2)(c+n+3)(c+n+4)]} \tag{4.14}$$

The resulting power series is

$$F(x,c)=x^c-{(wgl+P_l)}/{EI[(c+1)(c+2)]}x^{c+2}+{wgc}/{EI[(c+1)(c+2)(c+3)]}x^{c+2}+\sum_{n=0}^{N}a_{n+5}(c)x^{c+n+4} \tag{4.15}$$

Substituting Equation (4.15) into Equation (4.7) and noting that all coefficients of x^{c-4} and higher are set to zero leads to

$$EID^4F(x)+(P_l+wg(1-x))D^2F(x)-wgDF(x)-w\omega^2F(x)=c(c-1)(c-2)(c-3)x^{c-4} \tag{4.16}$$

The R.H.S. of Equation (4.16) will vanish if c is a root of the indicial equation

$$c(c-1)(c-2)(c-3)=0 \tag{4.17}$$

The first four solutions are therefore

$$F(x,0);\quad F(x,1);\quad F(x,2);\quad F(x,3) \tag{4.18}$$

and the general solution is

$$V(x)=C_1F(x,0)+C_2F(x,1)+C_3F(x,2)+C_4F(x,3) \tag{4.19}$$

For the purpose of computation it is convenient to express $F(x,c)$ in the form

$$F_1(X,c)=x^c, \qquad F_2(X,c)=0, \quad F_3(X,c)=-(wgl+P_l)x^{c+2}/EI[(c+1)(c+2)]$$

$$F_4(x,c)=wgcx^{c+3}/EI[(c+1)(c+2)(c+3)] \tag{4.20}$$

The remaining terms are

$$F_{n+5}(x,c)=\left[-(P_l+wgl)(c+n+1)(c+n+2)F_{n+3}(x,c)+wg(c+n+1)^2F_{n+2}(x,c)x \right.$$
$$\left.+w\omega^2F_{n+1}(x,c)x^2\right]x^2/EI[(c+n+1)(c+n+2)(c+n+3)(c+n+4)] \tag{4.21}$$

Differentiating Equation (4.21) with respect to x, with some simplification, gives

$$DF_{n+5}(x,c)=F_{n+5}(x,c)\frac{[c+n+4]}{x} \tag{4.22}$$

The second derivative of Equation (4.21) respect to x, again after some simplification, yields

$$D^2F_{n+5}(x,c)=F_{n+5}(x,c)\frac{[(c+n+3)(c+n+4)]}{x^2} \tag{4.23}$$

The third derivative of Equation (4.21) with respect to x is

$$D^3F_{n+5}(X,c)=-\frac{(wgl+P_l)DF_{n+3}(x,c)}{EI}+\frac{wg(c+n+1)F_{n+2}(x,c)}{EI}+\frac{w\omega^2F_{n+1}(x,c)x}{EI(c+n+1)} \tag{4.24}$$

The fourth derivative of Equation (4.21) with respect to x is

$$D^4F_{n+5}(X,c) = -\frac{(wgl+P_l)D^2F_{n+3}(x,c)}{EI} + \frac{wg(c+n+1)DF_{n+2}(x,c)}{EI} + \frac{w\omega^2F_{n+1}(x,c)x}{EI} \tag{4.25}$$

Substituting Equations (4.20) & (4.21) into Equations (4.18) gives the first four solutions as

$$F(x,0) = 1 - \frac{(wgl+P_l)x^2}{2EI} + \sum_{n=0}^{N} F_{n+5}(x,0) \tag{4.26}$$

$$F(x,1) = x - \frac{(wgl+P_l)x^3}{6EI} + \frac{wgx^4}{24EI} + \sum_{n=0}^{N} F_{n+5}(x,1) \tag{4.27}$$

$$F(x,2) = x^2 - \frac{(wgl+P_l)x^4}{12EI} + \frac{wgx^5}{30EI} + \sum_{n=0}^{N} F_{n+5}(x,2) \tag{4.28}$$

$$F(x,3) = x^3 - \frac{(wgl+P_l)x^5}{20EI} + \frac{wgx^6}{40EI} + \sum_{n=0}^{N} F_{n+5}(x,3) \tag{4.29}$$

4.2.3 Boundary conditions at the fixed end

At the fixed end $(x = 0)$ the displacement is equal to zero giving

$$V(0) = C_1F(0,0) + C_2F(0,1) + C_3F(0,2) + C_4F(0,3) = 0 \tag{4.30}$$

$$\therefore \; C_1 = 0$$

similarly the slope at the fixed end is zero giving

$$DV(0) = C_1 DF(0,0) + C_2 DF(0,1) + C_3 DF(0,2) + C_4 DF(0,3) = 0$$
$$\therefore \; C_2 = 0 \tag{4.31}$$

Hence after considering the boundary conditions at the fixed end the general solution, Equation (4.19), may be reduced to

$$V(x) = C_3 F(x,2) + C_4 F(x,3) \tag{4.32}$$

4.2.4 Boundary conditions at the free end of the blade

The bending moment at the free end $(x = l)$ of the blade is zero, therefore substituting the second derivative of Equation (4.32) with respect to x into Equation (4.4) gives

$$M = EID^2 V(l) = EI\left[C_3 D^2 F(l,2) + C_4 D^2 F(l,3)\right] = 0 \tag{4.33}$$

and similarly the shear force at the free end of the blade is zero. By substituting the third derivative of Equation (4.32) with respect to x into Equation (4.2), and noting that $P(l) = 0$ for the blade, gives

$$F = -EID^3 V(l) = -EI\left[C_3 D^3 F(l,2) + C_4 D^3 F(l,3)\right] = 0 \tag{4.34}$$

Equations (4.33) & (4.34) may be assembled in the standard matrix form

$$\begin{bmatrix} D^2F(l,2) & D^2F(l,3) \\ D^3F(l,2) & D^3F(l,3) \end{bmatrix} \begin{bmatrix} C_3 \\ C_4 \end{bmatrix} = \begin{bmatrix} 0 \\ 0 \end{bmatrix} \tag{4.35}$$

Applying Cramer's rule, the frequency equation for the free vibration of the blade is therefore

$$f(\omega) = D^2F(l,2)D^3F(l,3) - D^3F(l,2)D^2F(l,3) = 0 \tag{4.36}$$

4.2.5 Boundary conditions at the ball end of the wand stem

The boundary conditions at the ball end of the wand stem may be derived by considering the free body diagram of the ball as shown in Figure 4.3

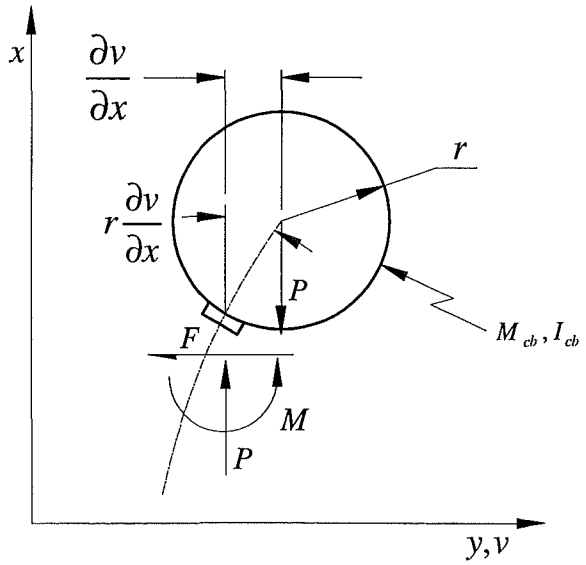

Figure 4.3 *Free body diagram of the ball*

From Newton's second law for motion of the ball in the y direction *(neglecting vertical motion of the centre of mass of the ball)*

$$-F(l,t) = M_{cb}\left(\frac{\partial^2 v(l,t)}{\partial t^2} + \frac{\partial^2\left(r\dfrac{\partial v(l,t)}{\partial x}\right)}{\partial t^2}\right) \tag{4.37}$$

Substituting Equation (4.37) into Equation (4.2)

$$\frac{\partial M(l,t)}{\partial x} + P(l)\frac{\partial v(l,t)}{\partial x} = M_{cb}\left(\frac{\partial^2 v(l,t)}{\partial t^2} + \frac{\partial^2\left(r\dfrac{\partial v(l,t)}{\partial x}\right)}{\partial t^2}\right)$$

$$\therefore \left(P_l + M_{cb}\omega^2 r\right)\frac{dV(l)}{dx} + EI\frac{d^3V(l)}{dx^3} + M_{cb}\omega^2 V(l) = 0 \tag{4.38}$$

Considering Equation (4.32) and derivatives of Equation (4.32) with respect to x, Equation (4.38) may be re-written as

$$\begin{aligned}\left(P_l + M_{cb}\omega^2 r\right)&\left[C_3 DF(l,2) + C_4 DF(l,3)\right] \\ &+ EI\left[C_3 D^3 F(l,2) + C_4 D^3 F(l,3)\right] \\ &+ M_{cb}\omega^2\left[C_3 F(l,2) + C_4 F(l,3)\right] = 0\end{aligned} \tag{4.39}$$

From Newton's second law for rotation motion of the ball about its centre of mass

$$F(l,t)r + P(l)r\frac{dv(l,t)}{dx} - M(l,t) = I_{cb}\,\partial^2\left(\frac{dv(l,t)}{dx}\right)\Big/\partial t^2 \tag{4.40}$$

substituting Equation (4.2) into Equation (4.40) gives

$$\left(-P_l\frac{dV(l)}{dx} - EI\frac{d^3V(l)}{dx^3}\right)r + P_l r\frac{dV(l)}{dx} - EI\frac{d^2V(l)}{dx^2} = -\omega^2 I_{cb}\frac{dV(l)}{dx}$$

$$-EIr\frac{d^3V(l)}{dx^3} - EI\frac{d^2V(l)}{dx^2} + \omega^2 I_{cb}\frac{dV(l)}{dx} = 0 \tag{4.41}$$

Considering Equation (4.32) and derivatives of Equation (4.32), Equation (4.41) may be re-written as

$$\begin{aligned} &-EIr\left[C_3D^3F(l,2)+C_4D^3F(l,3)\right] \\ &-EI\left[C_3D^2F(l,2)+C_4D^2F(l,3)\right] \\ &+\omega^2I_{cb}\left[C_3DF(l,2)+C_4DF(l,3)\right]=0 \end{aligned} \tag{4.42}$$

Equations (4.39) & (4.42) may be assembled in the standard matrix form

$$\begin{bmatrix} EID^3F(l,2) & EID^3F(l,3) \\ +\left(P_l+M_{cb}\omega^2r\right)DF(l,2) & \left(P_l+M_{cb}\omega^2r\right)DF(l,3) \\ +M_{cb}\omega^2F(l,2) & +M_{cb}\omega^2F(l,3) \\ -EIrD^3F(l,2) & -EIrD^3F(l,3) \\ -EID^2F(l,2) & -EID^2F(l,3) \\ +\omega^2I_{cb}DF(l,2) & +\omega^2I_{cb}DF(l,3) \end{bmatrix} \cdot \begin{bmatrix} C_3 \\ C_4 \end{bmatrix} = \begin{bmatrix} 0 \\ 0 \end{bmatrix} \tag{4.43}$$

It is convenient to express Equation (4.43) in the form

$$\begin{bmatrix} coef(1,1) & coef(1,2) \\ coef(2,1) & coef(2,2) \end{bmatrix} \cdot \begin{bmatrix} C_3 \\ C_4 \end{bmatrix} = \begin{bmatrix} 0 \\ 0 \end{bmatrix} \tag{4.44}$$

The natural frequencies for the wand may be calculated by calculating the zeros of the determinant of the coefficient matrix in Equation (4.44), that is

$$f(\omega)=coef(1,1)coef(2,2)-coef(2,1)coef(1,2)=0 \tag{4.45}$$

4.2.6 Results of calculations

The natural frequencies for the blade and the wand were calculated using the numerical procedure described in Appendix A. For the case of a beam with a free end *(the blade),* the numerical procedure was checked by setting the dimensionless gravity parameter γ equal the values as given by Naguleswaran (1991). Results of this analysis are tabulated in Table 4.1.

Table 4.1 *Checking the numerical procedure for blade bending frequency calculations*

Test	γ	Ω_1	Ω_2	Ω_3
1	*-5*	*2.11489*	*21.02928*	*60.76619*
2	*10*	*5.29178*	*23.91200*	*63.68155*
3	*100*	*12.86874*	*36.50917*	*78.98033*

Results in Table 4.1 compared exactly with those tabulated by Naguleswaran (1991). For the case where $\gamma = 100$, it was necessary to increase the number of terms in the power series, equations (4.20) & (4.21), to around 55 (i.e. *'nmax=50'*) to get the required accuracy.

For the case of a beam with an end mass *(the wand),* the procedure was checked by calculating system mass and geometry using the dimensionless variables δ, Δ, γ, & ε, as defined by Naguleswaran (1999). Three beam configurations investigated are listed in Table 4.2

Table 4.2 *Checking the numerical procedure for wand bending frequency calculations*

Test	δ	Δ	γ	ε	$\Omega_1^{1/2}$	$\Omega_2^{1/2}$	$\Omega_3^{1/2}$
1	0.25	0.25	1	0	1.3328	2.3302	5.1777
2	0.5	0.5	1	0.1	1.3529	2.2662	5.1677
3	1.0	0.5	5	0.1	1.4021	2.1814	5.1296

Results in Table 4.2 compared exactly with those tabulated by Naguleswaran (1999).

The mode frequencies for the blade and for the wand were calculated for the two cases where gravitational acceleration was firstly neglected and then included. Figure 4.4 shows results of calculations for the original and scaled blade and wand for the case where gravitational acceleration is included.

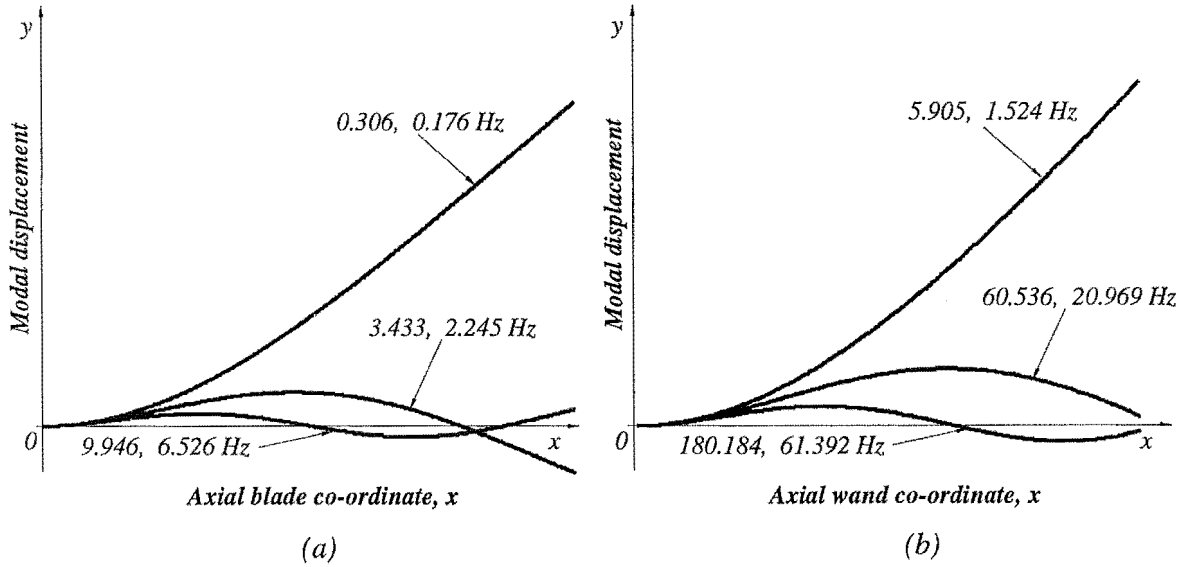

Figure 4.4 *Mode shapes and corresponding natural frequencies for the original and scaled sculptures respectively.*
(a) the blade (b) the wand

4.3 Experimental observations

A resonance test was conducted to measure the bending frequencies for the blade at the original size. This procedure involved fitting the original sculpture with a manual speed control and a digital speed display. The blade motor speed was set to excite each of the first three bending frequencies and the motor speed recorded.

A second method, the impact test, involved placing an accelerometer on the blade, striking the blade to create a disturbance, and then recording the resulting frequency spectrum using a fast Fourier transform (FFT) analysis. Figure 4.5 shows the results of this test.

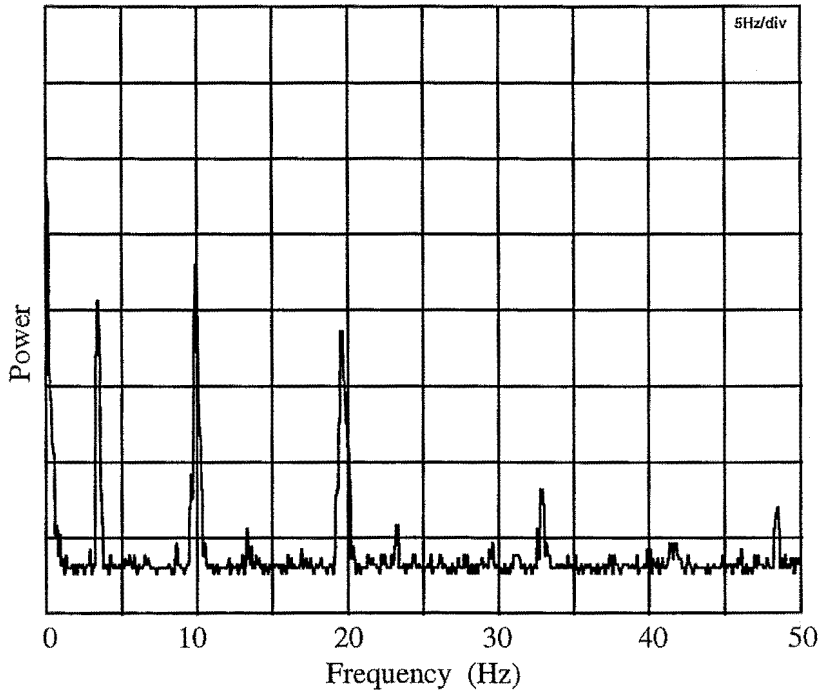

Figure 4.5 *Frequency response spectrum using FFT analysis*

The measured frequencies using experimental procedures are listed in Table 4.3.

4.4 Summary of results

Results of calculations and experimental observations are tabulated below.

Table 4.3 *Summary of results of calculations and experimental observations for the bending vibrations of the blade and the wand*

Analytical treatment of *Blade*	Lateral mode frequencies (Hz)			
	First	Second	Third	Fourth
Excluding effects of gravitational acceleration				
Exact solution for the original blade	*0.578*	*3.620*	*10.135*	*19.861*
Exact solution for the original wand	*5.915*	*60.549*	*180.201*	*361.927*
Exact solution for the scaled blade	*0.380*	*2.379*	*6.662*	*13.055*
Exact solution for the scaled wand	*1.535*	*20.987*	*61.413*	*123.160*
Including effects of gravitational acceleration				
Exact solution for the original blade	*0.306*	*3.433*	*9.946*	*19.663*
Exact solution for the original wand	*5. 905*	*60. 536*	*180.184*	*361.907*
Exact solution for the scaled blade	*0.176*	*2.245*	*6.526*	*12.913*
Exact solution for the scaled wand	*1.524*	*20.969*	*61.392*	*123.133*
Results of experimental observations of the original blade *(using the resonance test)*	***0.30***	***3.3***	***9.2***	-
Results of experimental observations of the original blade *(FFT using the impact test)*	-	***3.4***	***9.9***	***18.7***

4.5 Discussion of results

The mode frequencies were calculated for two cases with and without the inclusion of the gravitational acceleration field. Results show that the most significant difference is for the first mode frequency for the blade. This is because at higher frequencies the kinetic energy of the vibrating blade/wand and the strain energy due to bending are much greater than the strain energy due to self-weight. This could be easily quantified further by considering the magnitude of the terms generated by the Rayleigh-Ritz analysis [Gooch and Raine (2000)].

The calculated exact small amplitude mode frequencies were in good agreement with results obtained from the impact test. The relative modal blade displacement observed in the impact test was very small compared with the resonance test. Therefore the influence of non-linear effects was expected to have some bearing on the resonance test results. The frequencies measured using the resonance test, were lower than the predicted frequencies, and lower than the measured frequencies from the impact test. This disparity in results is consistent with the non-linear forced vibration response of a system with a softening spring. This effect is illustrated in Figure 4.6. The softening spring effect is a function of the radius of curvature of the beam. Considering the exact relationship between the bending moment and the geometry of a curved beam [Benham and Crawford (1987)], Equation (4.4) may be more precisely written as

$$M = \frac{EI\, d^2v/dx^2}{\left[1+(dv/dx)^2\right]^{\frac{3}{2}}} \tag{4.46}$$

From Equation (4.46) it is clear that the beam becomes softer with increasing slope. A second interesting observation, also associated with a softening spring, was a step in amplitude as the frequency of the clamped end of the blade was slowly increased towards either the second or the third mode frequencies. This behaviour is commonly known as the non-linear jump phenomenon [Nayfeh and Nayfeh (1992)].

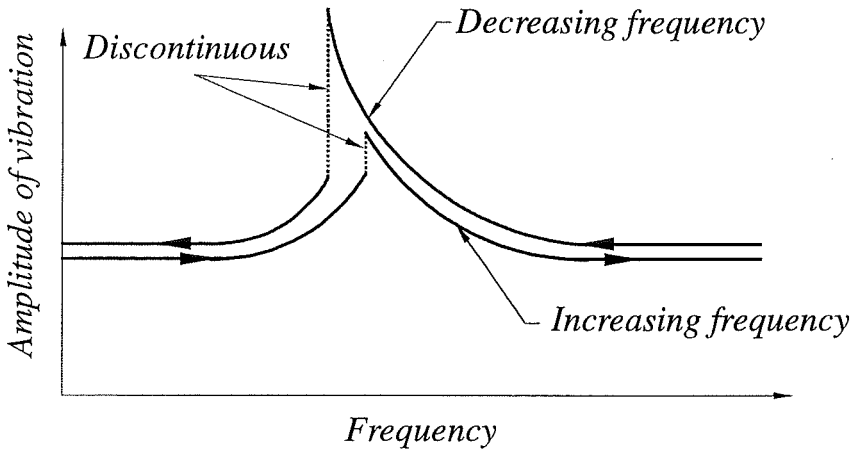

Figure 4.6 *Non-linear softening spring effect and jump phenomenon*

This non-linear jump in blade amplitude was very small in the run up to the second blade mode frequency, but it was much more marked in the run up to the third mode frequency for the blade. This more marked non-linear behaviour in the run up to the third mode frequency is consistent with Equation (4.46) and with the increased slope expected at higher modes. Although the artists did not understand the mechanics of the jump phenomenon, they regard it as a desirable aspect in the performance of the sculpture [Webb (Jan. 1996 Dec. 1998)].

During the course of experimental procedures using the original sculpture, it was observed that the motor tended to be labouring under load and did not appear to have sufficient power to overcome blade feedback forces.

4.6 Concluding comments

The mode frequencies for the free vibration of the blade and wand have been calculated. The results of this analysis have been found to be in good agreement with results from the literature, experimental observations, and have been confirmed using more approximate methods

Lye's 'kissing' and 'single harmonic' frequencies correspond to the second bending mode of vibration for the blade while the double harmonic frequency corresponds to the third bending mode of vibration.

Non-linearities have been found to be an important factor affecting the performance of the blade, particularly in the third bending mode of vibration. The blade was found to get softer as the amplitude of vibration increases, this coupled with the non-linear jump phenomenon means that in order to achieve a maximum blade displacement at either the second or third modes of vibration it is necessary to ramp the clamp frequency past the mode frequency and then reduce the frequency to get the maximum blade displacement. This characteristic is an important consideration when selecting control system components.

A second observation made was a first order swinging effect of the blade while exciting the third mode of vibration. This effect appeared to be less significant when the wand is removed. Aesthetically, from the artists perspective [Webb (Jan. 1996 Dec. 1998)], this is an undesirable effect. First order swinging is also likely to result in high bending stresses, which may cause the blade to yield at the larger scale. These observations have identified the need to investigate the interaction between the wand and the blade, which will be the topic of Chapter 6.

5

The vibratory form – plate modes

5.1 Introduction

Lye's *single harmonic,* and *double harmonic* vibratory forms have been identified as corresponding to the second and third bending modes of vibration respectively. *(NB. Lye's kissing is of the same form as the single harmonic but with a lower amplitude of vibration)* Given the geometry of the blade, the *shimmering* characteristic is suspected to correspond to a torsional plate mode of vibration.

> ***The purpose of this chapter is to calculate the natural frequencies for the free vibration of the blade considering the blade as a thin plate.***

Leissa (1969) conducted a comprehensive survey of the literature giving a summary of all known results for the frequencies and mode shapes for the free vibration of plates. Exact solutions are known for rectangular plates which are simply supported on all four edges or simply supported on a pair of opposite edges. For the case of a cantilevered plate, exact solutions are difficult to obtain and it is convenient to obtain an approximate solution using the Rayleigh-Ritz method.

The nomenclature used in this chapter is adopted from Young (1950) and Leissa (1973). The coordinate system for the blade is shown schematically in Figure 5.1.

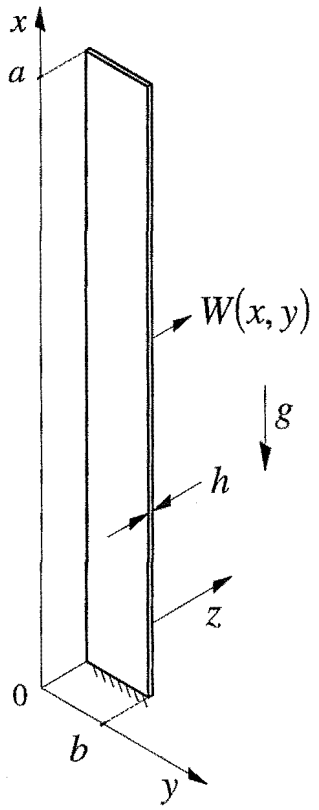

Figure 5.1 *Coordinate system used in plate analysis*

5.2 The Rayleigh-Ritz method

In using the Rayleigh-Ritz method it is necessary to make assumptions as to the vibratory form along the length and width dimensions of the plate. The frequencies corresponding to each plate modes are then calculated by considering the energy of the system.

For a plate vibrating harmonically with amplitude $W(x,y)$ and angular frequency ω, the maximum potential/strain energy is

$$V(W)=\frac{D}{2}\int_0^b\int_0^a\left[\left(\frac{\partial^2 W}{\partial x^2}\right)^2+\left(\frac{\partial^2 W}{\partial y^2}\right)^2+2\nu\frac{\partial^2 W}{\partial x^2}\frac{\partial^2 W}{\partial y^2}+2(1-\nu)\left(\frac{\partial^2 W}{\partial x\partial y}\right)^2\right]dxdy$$
$$+\int_0^b\int_0^a\left[N_x\left(\frac{\partial^2 W}{\partial x^2}\right)+N_y\left(\frac{\partial^2 W}{\partial y^2}\right)+N_{xy}\frac{\partial^2 W}{\partial x\partial y}\right]dxdy \tag{5.1}$$

The blade is subjected to an in-plane gravitational acceleration, Figure 5.1, causing an in-plane stress due to the inertial body force *ρg per unit volume*. Assuming that the stress in x due to gravitational loading does not vary as the plate vibrates and the stresses do not vary through the thickness of the plate, the in-plane forces may be calculated. Hence, for the blade we may define

$$N_x=(x-a)\rho gh$$
$$N_y=N_{xy}=0 \tag{5.2}$$

The maximum kinetic energy of the vibrating plate is

$$T(W)=\frac{\rho h\omega^2}{2}\int_0^b\int_0^a W^2 dxdy \tag{5.3}$$

Assuming no losses in energy we may equate Equations (5.1) and (5.3) giving

$$\omega^2=\frac{2V(W)}{\rho h\int_0^b\int_0^a W^2 dxdy} \tag{5.4}$$

The natural frequencies correspond to expressions for W that minimizes Equation (5.4). Using the Rayleigh Ritz method the transverse blade deflection *(with respect to time)* may be defined using a series of characteristic functions of the form

$$W(x,y)=\sum_m\sum_n A_{mn}\phi_m(x)\psi_n(y) \tag{5.5}$$

$\phi(x)$ and $\psi(y)$ in Equation (5.5) describe the mode shapes along the width and length dimensions of the blade respectively. Each member of the assumed series of functions in Equation (5.5) must be admissible i.e. must satisfy the kinematic boundary conditions of the cantilevered plate. For convenience Equation (B1), Appendix B, shows Equation (5.5) in its expanded form. Equations (B2a) to (B2h) give the products of Equation (5.5) and derivatives of Equation (5.5) as defined inside the integrals in Equations (5.1) and (5.3).

Substituting the series approximation for $W(x,y)$ from Equation (5.5) into Equation (5.4), the right hand side becomes a function of the coefficients A_{mn}. This is minimized by taking the partial derivatives with respect to each coefficient and equating to zero i.e.

$$\frac{\partial V}{\partial A_{ik}} - \frac{\rho h \omega^2}{2} \frac{\partial}{\partial A_{ik}} \int_0^b \int_0^a W^2 dxdy = 0 \qquad (5.6)$$

Evaluating Equation (5.6) with respect to A_{ik} *(for convenience the derivatives of each of the components in Equation (5.6) are listed in Equations (B3a) to (B3h) Appendix B)* and applying the conditions given in Equation (5.2) gives

$$\begin{aligned} A_{mn} \Big\{ & D \int_0^b \int_0^a [\phi_m'' \psi_n \phi_i'' \psi_k + \phi_m \psi_n'' \phi_i \psi_k'' + 2\nu(\phi_m'' \psi_n \phi_i \psi_k'' + \phi_m \psi_n'' \phi_i'' \psi_k) \\ & + 2(1-\nu)\phi_m' \psi_n' \phi_i' \psi_k'] dxdy + \rho g h \int_0^b \int_0^a [(x-a)\phi_m' \psi_n \phi_i' \psi_k] dxdy \\ & - \rho h \omega^2 \int_0^b \int_0^a \phi_m \psi_n \phi_i \psi_k dxdy \Big\} = 0 \end{aligned} \qquad (5.7)$$

5.3 Characteristic functions

An important consideration in the application of the Rayleigh Ritz method is the selection of appropriate admissible functions for the series $W(x,y)$. Four commonly used types of characteristic functions are

- characteristic beam functions
- simply supported plate functions
- degenerated beam functions
- characteristic orthogonal polynomials

5.3.1 Characteristic beam functions

Young (1950) and Simons and Leissa (1971) use characteristic beam functions in conjunction with the Rayleigh Ritz method to calculate the natural frequencies of vibrating cantilever plates. Characteristic beam functions for clamped-free beam modes are [Young (1950)]

$$\phi_m(x) = \cosh\left(\frac{\lambda_m x}{a}\right) - \cos\left(\frac{\lambda_m x}{a}\right) - \alpha_m\left(\sinh\left(\frac{\lambda_m x}{a}\right) - \sin\left(\frac{\lambda_m x}{a}\right)\right) \tag{5.8}$$

λ_m may be calculated by finding solutions to the characteristic frequency equation for a clamped free beam, namely

$$\cosh\lambda_m \cos\lambda_m = -1 \tag{5.9}$$

The first eight values of λ_m were calculated using the Newton-Raphson extrapolation method [Griffiths and Smith (1991)] in *C5Prog1.m*.

The constant α_m in Equation (5.8) may be calculated using [Simons & Leissa (1971)]

$$\alpha_m = \frac{\cosh \lambda_m + \cos \lambda_m}{\sinh \lambda_m + \sin \lambda_m} \tag{5.10}$$

The first eight values of λ_m and α_m are listed in Table 5.1

Table 5.1 *Constants for characteristic beam functions - clamped/free modes*

m	λ_m	α_m
1	*1.87510407*	*0.73409551*
2	*4.69409113*	*1.01846732*
3	*7.85475744*	*0.99922450*
4	*10.99554077*	*1.00003355*
5	*14.13716828*	*0.99999855*
6	*17.27876015*	*1.00000006*
7	*20.42034993*	*1.00000000*
8	*23.56194562*	*1.00000000*

Figure 5.2 shows the first four characteristic functions for the clamped free modes plotted using Equation (5.8).

The characteristic beam functions for a free/free beam are of the form [Young (1950)]

$$\psi_1 = 1 \tag{5.11a}$$

$$\psi_2 = \sqrt{3}\left(1 - \frac{2y}{b}\right) \tag{5.11b}$$

$$\psi_n(y) = \cosh\left(\frac{\mu_n y}{b}\right) + \cos\left(\frac{\mu_n y}{b}\right) - \beta_n\left(\sinh\left(\frac{\mu_n y}{b}\right) + \sin\left(\frac{\mu_n y}{b}\right)\right) \quad n > 2 \tag{5.11c}$$

μ_n may be calculated by finding solutions to the characteristic frequency equation for a clamped free beam, namely

$$\cosh \mu_n \cos \mu_n = 1 \tag{5.12}$$

The constant β_n is calculated using [Simons & Leissa (1971)]

$$\beta_m = \frac{\cosh \mu_n - \cos \mu_n}{\sinh \mu_n - \sin \mu_n} \tag{5.13}$$

The first eight values of μ_n and β_n are listed in Table 5.2

Table 5.2 *Constants for characteristic beam functions - free /free modes*

n	μ_n	β_n
1	*0*	*0*
2	*0*	*0*
3	*4.73004074*	*0.98250221*
4	*7.85320462*	*1.00077731*
5	*10.99560779*	*0.99996645*
6	*14.13716545*	*1.00000145*
7	*17.27876028*	*0.99999994*
8	*20.42241022*	*1.00000000*

Figure 5.3 shows the first four characteristic functions for the clamped free modes plotted using Equations (5.11a) to (5.11c).

5.3.2 Simply supported plate functions

Dickinson (1981) investigated the use of *'simply supported plate functions'* in the Rayleigh-Ritz method. These were found to offer some improvement in accuracy for frequency calculations where plates have all edges supported, however for a plate with free edges they were found to be less than

satisfactory. Hence, from the results of Dickinson's study, simply supported plate functions will not be used in the Rayleigh-Ritz treatment of blade.

5.3.3 Degenerated beam functions

Bassily and Dickinson (1975) developed a set of *'degenerated beam functions'* which were shown to improve accuracy of calculations for plates with free edges. In later developments Dickinson and Di Blasio (1986) found simpler polynomial functions to give a degree of accuracy equivalent to degenerated beam functions, but they will not be investigated further here.

5.3.4 Characteristic orthogonal polynomials

Bhat (1985a) (1985b) (1985c) proposed the use of characteristic orthogonal polynomials to calculate the natural frequencies of rectangular plates.

Given a starting polynomial $\phi_1(x)$ an orthogonal set of polynomials over the interval a - b can be generated by the Gram-Schmidt process [Burden et al. (1981)] as follows

$$\phi_1(x) = Starting\ Function \tag{5.14a}$$

$$\phi_2(x) = (x - B_2)\phi_1(x) \tag{5.14b}$$

$$\phi_k(x) = (x - B_k)\phi_{k-1}(x) - C_k\phi_{k-2}(x) \tag{5.14c}$$

$$B_k = \frac{\int_a^b x\, w(x)\phi_{k-1}^2(x)\,dx}{\int_a^b w(x)\phi_{k-1}^2(x)\,dx} \tag{5.14d}$$

$$C_k = \frac{\int_a^b x\, w(x)\phi_{k-1}(x)\phi_{k-2}(x)\,dx}{\int_a^b w(x)\phi_{k-2}^2(x)\,dx} \tag{5.14e}$$

'w' is a weighting function equal to unity for uniform beams. The starting function, Equation (5.14a), must satisfy the boundary conditions for the plate. In this case the starting function for clamped free modes *(along the length dimension of the blade)* is [after Bhat (1985)]

$$\phi_1(x) = a_1\left(6x^2 - 4x^3 + x^4\right) \tag{5.15}$$

and similarly for free/free modes

$$\psi_1(x) = b_1 \tag{5.16}$$

where a_1 and b_1 are constants of the orthogonal mode functions and are derived in Appendix B.

In program *C5Prog2.m* the first two polynomials are defined for the clamped-free and free-free boundary conditions respectively and the higher order terms are calculated using the recurrence relationships given by Equations (5.14a) (5.14b) & (5.14c). Calculations compared exactly with the results tabulated by Bhat (1985b), the constants for the polynomials described by Equations (5.14) are listed in Tables 5.3 and 5.4.

Table 5.3 *Constants for orthogonal polynomials – clamped/free modes* $\phi_p(x) = \sum_{q=1} a_{pq} x^{q+1}$

	$a_{p,q}$						
	$q=1$	$q=2$	$q=3$	$q=4$	$q=5$	$q=6$	$q=7$
$p=1$	3.9468	-2.6312	0.6578	0	0	0	0
$p=2$	20.0501	-38.3606	20.0042	-4.1656	0	0	0
$p=3$	62.4439	-225.0335	259.3606	-115.0232	21.114	0	0
$p=4$	152.1058	-868.7596	1733.288	-1512.983	591.07	-97.9188	0
$p=5$	317.6653	-2613.846	7900.0815	-11320.00	8147.96	-2861.11	433.74

Table 5.4 *Constants for orthogonal polynomials – free /free modes*

$$\psi_p(x) = b_{p=1,q=1} + \sum_{q=2} b_{pq} y^{q-1}$$

	$b_{p,q}$				
	$q = 1$	$q = 2$	$q = 3$	$q = 4$	$q = 5$
$p = 1$	1.0000	0	0	0	0
$p = 2$	1.7321	- 3.4641	0	0	0
$p = 3$	2.2361	-13.4164	13.4164	0	0
$p = 4$	2.6458	-31.7491	79.3725	-52.9150	0
$p = 5$	3.0000	-60.0000	270.0000	-412.0000	210.0000

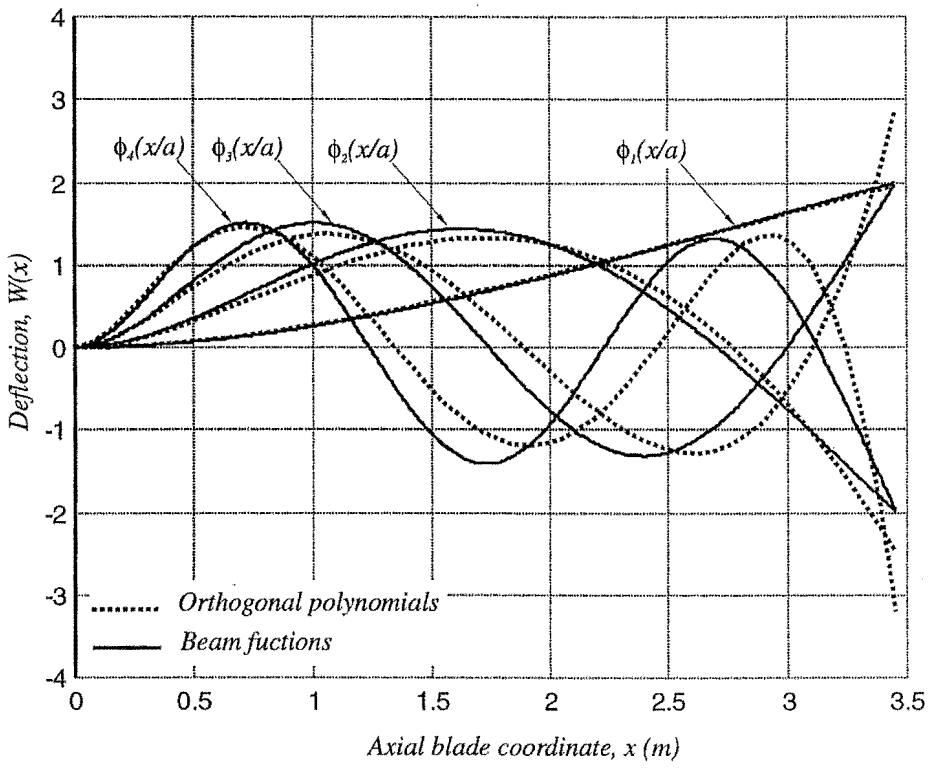

Figure 5.2 *Characteristic functions for clamped-free modes*

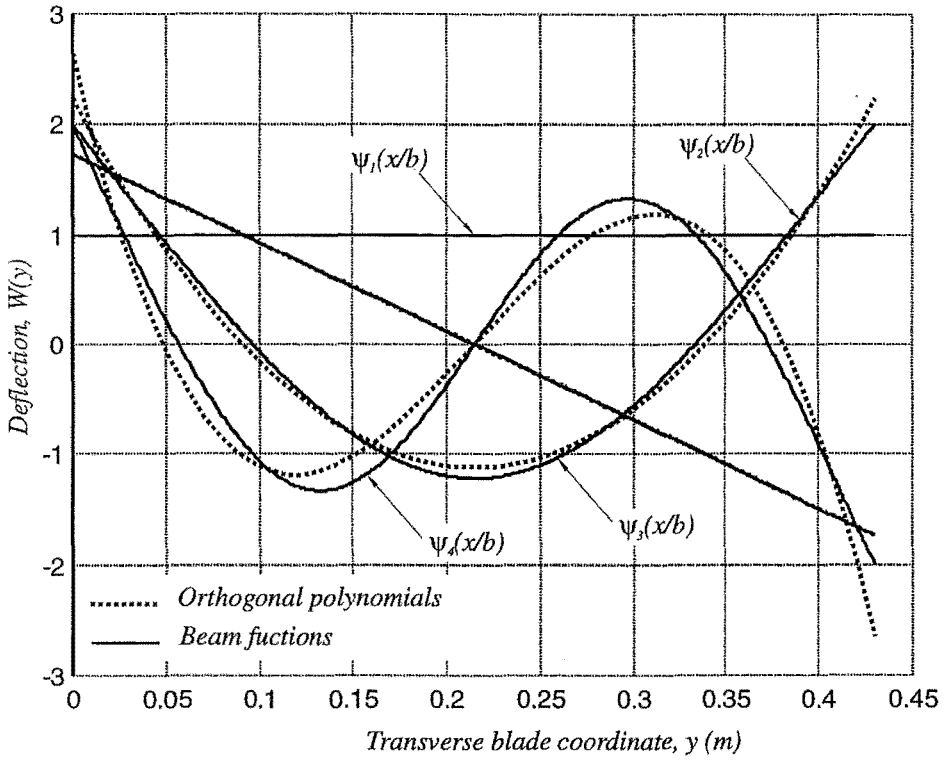

Figure 5.3 *Characteristic functions for free-free modes*

5.4 Integrals of characteristic functions

As both the characteristic beam functions and orthogonal polynomials are orthogonal, the following relationships hold true

$$\begin{aligned} \int_0^a \phi_m \phi_i dx &= a \qquad (for\ m = i) \\ &= 0 \qquad (for\ m \neq i) \end{aligned} \tag{5.17}$$

$$\begin{aligned} \int_0^a \psi_n \psi_k dy &= b \qquad (for\ n = k) \\ &= 0 \qquad (for\ n \neq k) \end{aligned} \tag{5.18}$$

and for the case of the characteristic beam functions only

$$\int_0^a \frac{d^2\phi_m}{dx^2}\frac{d^2\phi_i}{dx^2}dx = \frac{\lambda_m^4}{a^3} \quad (for\ m=i)$$
$$= 0 \quad (for\ m\neq i) \tag{5.19}$$

$$\int_0^a \frac{d^2\psi_m}{dy^2}\frac{d^2\psi i}{dy^2}dy = \frac{\mu_m^4}{b^3} \quad (for\ m>2\ \&\ m=i)$$
$$= 0 \quad (for\ m\neq i) \tag{5.20}$$

$$\int_0^a \left(\frac{d^2\psi_1}{dy^2}\right)^2 dy = \int_0^a \left(\frac{d^2\psi_2}{dy^2}\right)^2 dy = 0 \tag{5.21}$$

For convenience it is useful to define the following notation for the terms in Equation (5.6)

$$E_{m,i}^{(p,q)} = \int_0^a \frac{d^p\phi_m}{dx^2}\frac{d^q\phi_i}{dx^2}dx \tag{5.22}$$

$$EAX_{m,i}^{(p,q)} = \int_0^a (a-x)\frac{d^p\phi_m}{dx^p}\frac{d^q\phi_i}{dx^q}dx \tag{5.23}$$

$$F_{n,k}^{(p,q)} = \int_0^b \frac{d^p\psi_n}{dy^p}\frac{d^q\psi_k}{dy^q}dy \tag{5.24}$$

In *C5Prog1.m* the integrals, Equations (5.17) to (5.24), were evaluated using the MATLAB function *'trapz' (trapezoidal integration procedure).* The results of calculations, Tables (B1) and (B2), compare exactly with those tabulated by Young (1950). For the case where orthogonal beam functions were used, the recurrence relationships, Equations (5.14a) to (5.14e) were substituted into Equations (5.17) to (5.21) and the integrals evaluated exactly. The analytical expressions for Equations (5.17) to (5.24) are listed in Section B2 and the results of calculations are listed in Tables (B3) and (B4)

5.5 Numerical analysis

Considering the results from orthogonality conditions and following the notation from Equations (5.22) to (5.24), Equation (5.7) becomes

$$A_{mn}\left\{E_{m,i}^{(2,2)}b\delta_{n,k}+aF_{n,k}^{(2,2)}+2\nu\left[E_{m,i}^{(2,0)}F_{n,k}^{(0,2)}+E_{m,i}^{(0,2)}F_{n,k}^{(2,0)}\right]+2(1-\nu)E_{m,i}^{(1,1)}F_{n,k}^{(1,1)}\right.$$

$$\left.\frac{\rho gh}{D}EAX_{m,i}^{(1,1)}b\delta_{n,k}-\frac{\rho h\omega^2}{D}a\delta_{m,i}b\delta_{n,k}\right\}=0 \tag{5.25}$$

where $\delta_{ij} = 1$ if $i = j$ and 0 if $i \neq j$. Equation (5.25) represents $M \times N$ simultaneous equations with $M \times N$ unknowns A_{mn}. For the purpose of simplifying the analysis it is convenient to define the coefficient matrix C_{mnik} as

$$C_{mnik}=E_{m,i}^{(2,2)}b\delta_{n,k}+aF_{n,k}^{(2,2)}+2\nu\left[E_{m,i}^{(2,0)}F_{n,k}^{(0,2)}+E_{m,i}^{(0,2)}F_{n,k}^{(2,0)}\right]+2(1-\nu)E_{m,i}^{(1,1)}F_{n,k}^{(1,1)}$$

$$+\frac{\rho gh}{D}EAX_{m,i}^{(1,1)}b\delta_{n,k} \tag{5.26}$$

where C_{mnik} is a square symmetric matrix of order $M \times N$. Equation (5.26) may be written in the matrix notation

$$\left(C_{mnik}-\Omega\delta_{m,i}\delta_{n,k}\right)A_{mn}=0 \tag{5.27}$$

where A_{mi} is a column vector with components A_{mn} ($m = 1,2, \ldots M, \quad n = 1,2, \ldots N$) and $\Omega = \rho\, h\, \omega^2\, a\, b / D$. The non-trivial solution of equation (5.27) requires

$$Det\left(C_{mnik}-\Omega\delta_{m,i}\delta_{n,k}\right)=0 \tag{5.28}$$

Equation (5.28) is a polynomial in Ω of degree $M \times N$ having $M \times N$ solutions *(eigenvalues)*. The eigenvalues were evaluated using the *eig* function in MATLAB.

5.6 Summary of results

A procedure for measuring the first plate mode involved twisting the top of the blade about its vertical axis then releasing the blade from the displaced position and measuring the frequency response using the same procedure as discussed in Section 4.3.2. Figure 5.4 shows the results of this test.

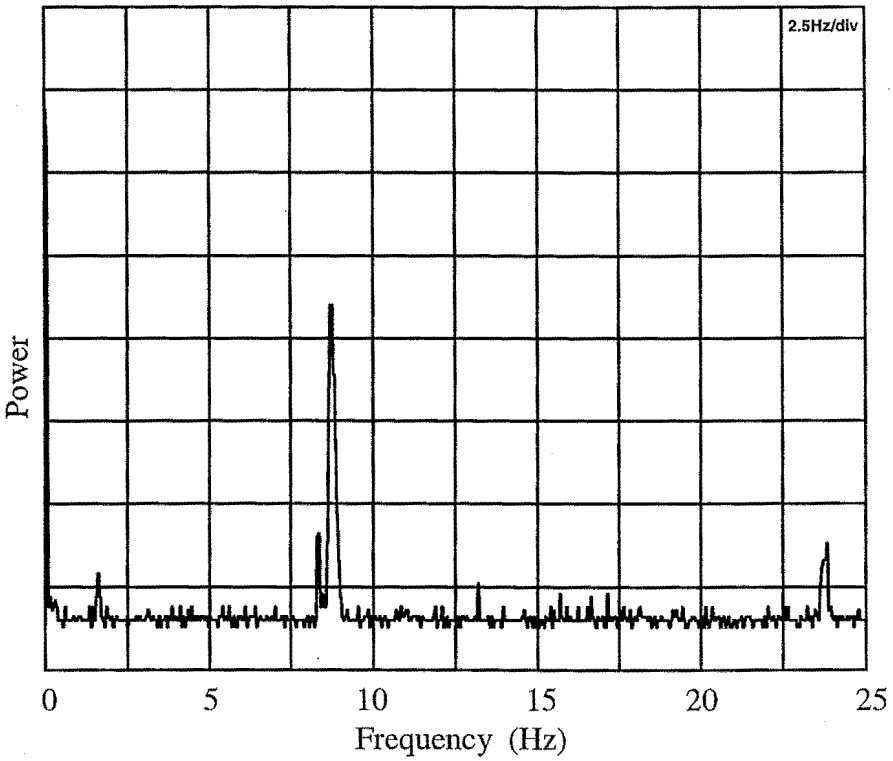

Figure 5.4 *Frequency spectrum showing first plate mode using FFT analysis*

The first four natural frequencies calculated for the original and scaled blades are listed in Table 5.5 below. These results are for the case where the first twenty characteristic functions *(in the longitudinal and transverse directions)* are used in conjunction with the Rayleigh-Ritz method.

Table 5.5 *Summary of results of calculations and experimental observations for the plate modes of vibration for the blade*

Analytical treatment of ***Blade***	Plate mode frequencies (Hz)			
	First	Second	Third	Forth
Excluding effects of gravitational acceleration				
Beam functions for the original blade	*0.584* (0.578)	*3.659* (3.620)	*9.316*	*10.263* (10.135)
Beam functions for the scaled blade	*0.384* (0.380)	*2.406* (2.379)	*6.040*	*6.746* (6.662)
Polynomial functions for the original blade	*0.583*	*3.651*	*9.324*	*10.228*
Polynomial functions for the scaled blade	*0.383*	*2.400*	*6.045*	*6.727*
Including effects of gravitational acceleration				
Beam functions for the original blade	*0.317* (0.306)	*3.475* (3.433)	*9.302*	*10.076* (9.946)
Beam functions for the scaled blade	*0.184* (0.176)	*2.273* (2.245)	*6.030*	*6.612* (6.526)
Polynomial functions for the original blade	*0.314*	*3.465*	*9.310*	*10.040*
Polynomial functions for the scaled blade	*0.182*	*2.267*	*6.034*	*6.593*
Results of experimental observations of the original blade *(FFT using the impact test)*	-	-	*8.7*	-

(NB. the numbers in the brackets in Table 5.5 are the calculated exact bending frequencies as listed in Table 4.3)

The mode shapes corresponding to the first four plate frequencies are shown in Figure 5.5

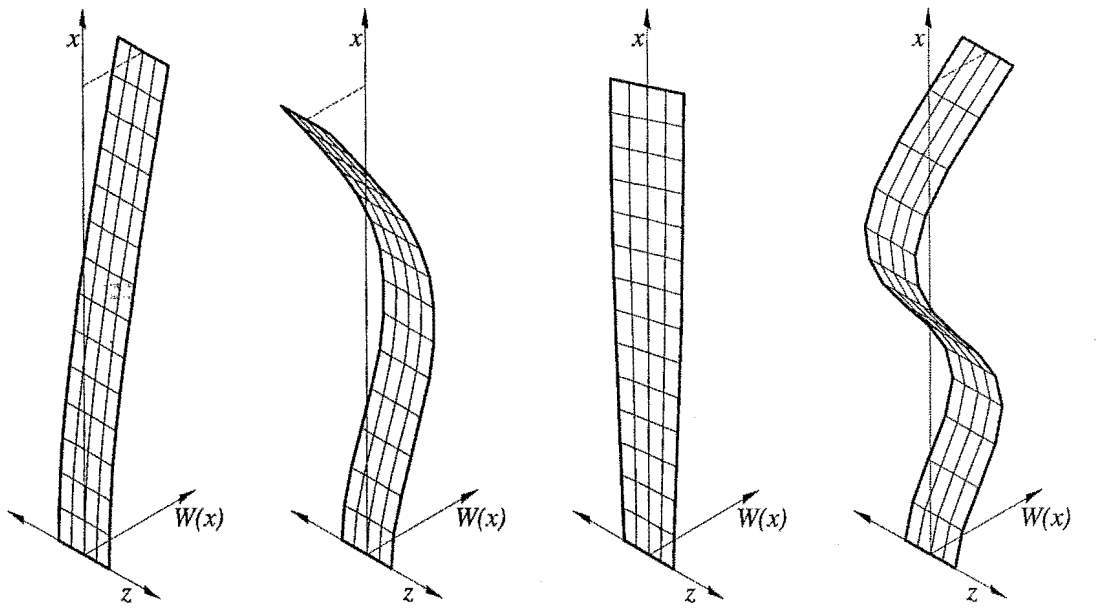

Figure 5.5 *The first four plate modes*

5.7 Discussion

The results of calculated mode frequencies and mode shapes have been found to be in good agreement with experimental observations.

The calculated bending frequencies using the Rayleigh-Ritz method are slightly higher than those given by the exact solutions in Chapter 4. This is expected because the Rayleigh-Ritz method gives an upper bound on vibration frequencies [Leissa (1973)]. It was found that increasing the number of functions in the Rayleigh Ritz procedure resulted in lower calculated frequencies i.e. increased accuracy

The '*orthogonal polynomial functions*' were found to give more accurate results for the bending frequencies than those obtained using the beam functions. This result is consistent with the conclusions of Bhat (1985a) and Dickinson and Di Blasio (1986).

5.8 Conclusion

The first, second, and fourth plate modes correspond with the first, second and third beam bending modes respectively.

Len Lye's shimmering frequency corresponds with the third plate mode of vibration

Because the third plate mode is not, by design, excited on the original sculpture, the energy required for Lye's shimmering frequency is the result of out-of-balance mechanism forces and motion.

6

Mathematical model for the forced damped vibration of Blade

6.1 Introduction

Lye's objectives were to maintain a vertically stable symmetric standing wave pattern for *Blade* vibrating at either the ***single*** or ***double harmonic*** frequencies [Webb (Jan 1996 – Dec 1998)].

Observations of the original *Blade* identified an undesirable swinging phenomenon that develops when the blade base motion frequency is set to coincide with the third natural blade bending frequency. The swinging frequency is lower than the third natural blade bending frequency and in the performance of the original sculpture was found to increase in amplitude with time.

The purpose of this chapter is to develop a mathematical model for the forced damped vibratory response of Blade and thus identify the significant factors contributing to this lower frequency swinging phenomenon. The mathematical model, once verified using observations from the original Blade, will be used to specify a suitable system configuration for the scaled Blade.

Preliminary observations of original *Blade* showed that the lower frequency swinging phenomenon shown in Figure 6.1a, not only increases in amplitude with time but will eventually dominate the blade shape as in Figure 6.1b. After considering the limits imposed on the maximum bending stresses for the blade, from Chapter 3, then at the scaled size this swinging phenomenon is expected to reduce blade life significantly and may even cause the blade material to yield.

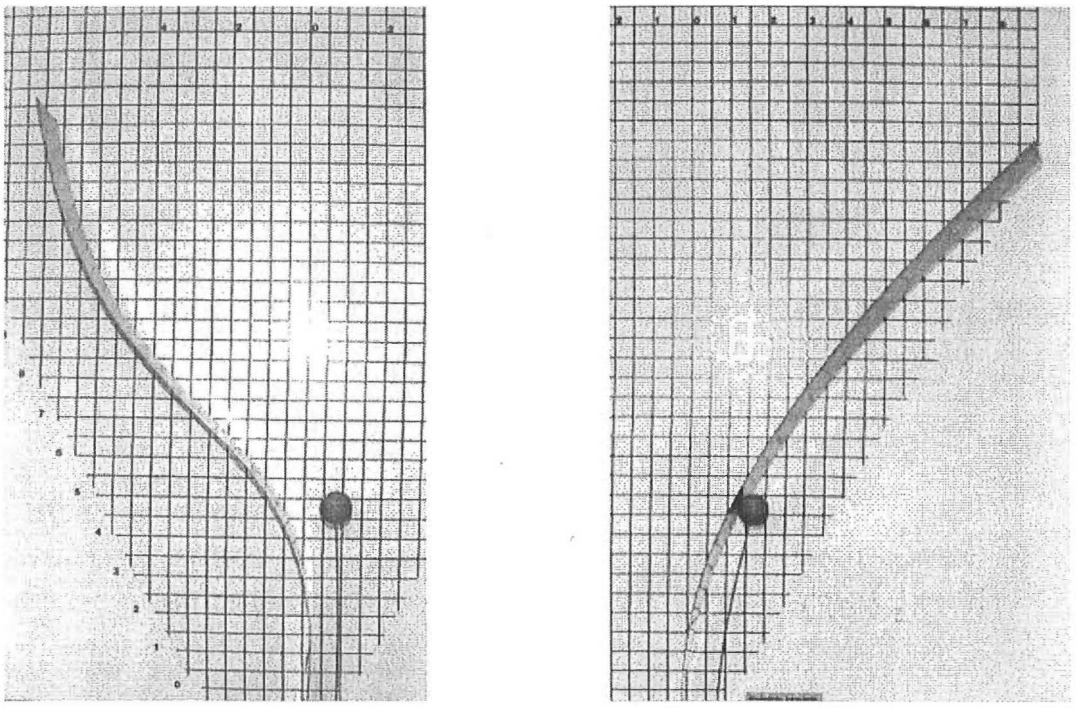

(a) (b)

Figure 6.1 *The swinging phenomenon at the third natural bending frequency*
(a) large amplitude swinging phenomenon
(b) swinging phenomenon dominates the third mode shape

The sign convention and nomenclature used in this analysis is consistent with that used in Chapter 4. For convenience, the co-ordinate system, geometry, and mass properties for the blade and the wand are illustrated in the schematic diagram in Figure 6.2.

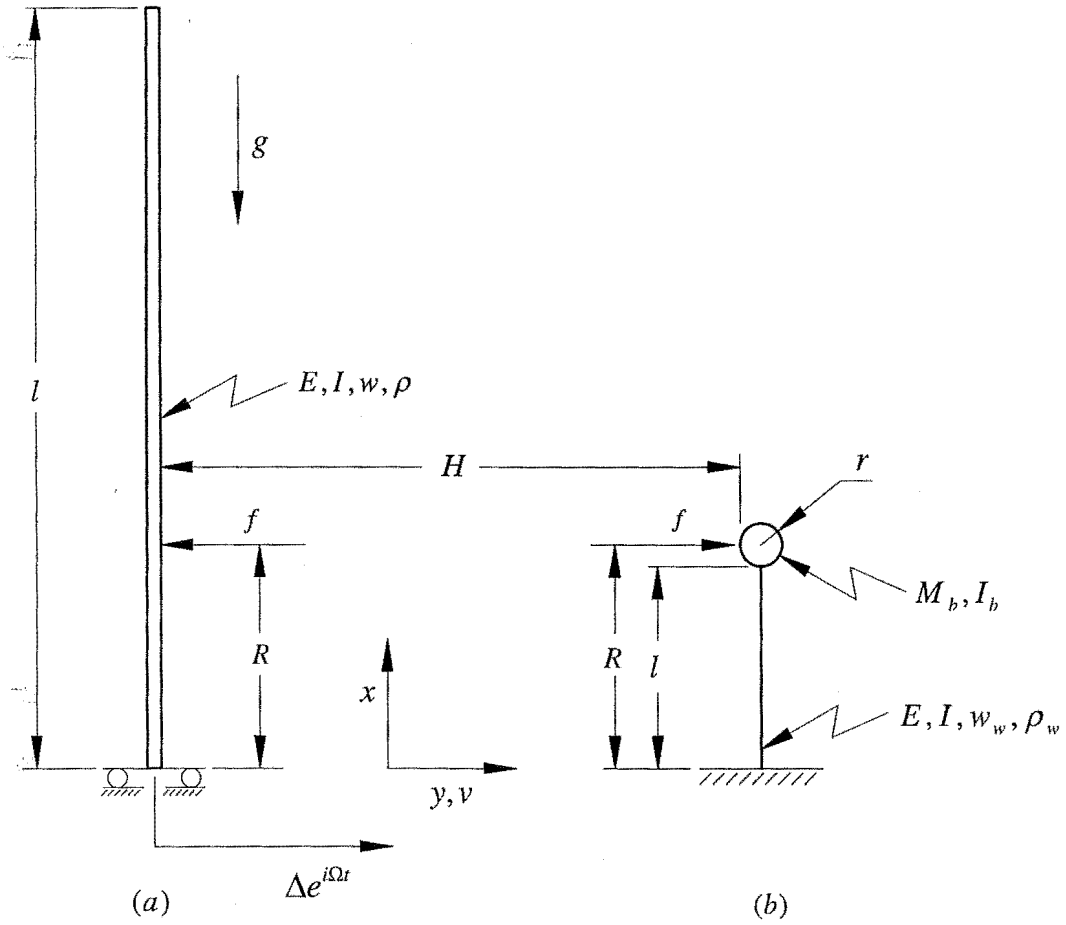

Figure 6.2 *The co-ordinate system, geometry, and mass properties used in the mathematical model (a) for the blade*
(b) for the wand

6.2 The equations of motion for the blade

The equation of motion for the free undamped vibration of the blade and the wand stem was derived in Chapter 4. For the case of the blade, the equation of motion, Equation (4.7), can be reduced to

$$EI\frac{\partial^4 v(x,t)}{\partial x^4}+wg(l-x)\frac{\partial^2 v(x,t)}{\partial x^2}-wg\frac{dv(x,t)}{\partial x}+w\frac{\partial^2 v(x,t)}{\partial t^2}=0 \tag{6.1}$$

The aim of this analysis to introduce damping, the rigid body clamp motion, and the wand contact force into the equation of motion.

6.2.1 The forced damped vibration of blade

Assuming damping to be proportional to velocity, the equation of motion for the forced damped vibration of the blade is

$$EI\frac{\partial^4 v(x,t)}{\partial x^4}+c\frac{\partial v(x,t)}{\partial t}+wg(l-x)\frac{\partial^2 v(x,t)}{\partial x^2}-wg\frac{dv(x,t)}{\partial x}+w\frac{\partial^2 v(x,t)}{\partial t^2}=-f(x,t) \tag{6.2}$$

To simplify later calculations, it is useful to define $\hat{V}_r$ as the principal modes scaled so that the values of $\hat{V}_r$ at the ball height are equal to unity i.e. $\hat{V}_r(R)=1.0$. The scaled modes $\hat{V}_r(x)$ were calculated in Section C6prog1.3 of *C6prog1.m* using

$$\hat{V}_r(x)=\frac{V_r(x)}{V_r(R)} \tag{6.3}$$

where V_r is one of the flexible beam modes derived in Chapter 4.

The built-in end of the blade is subject to a reciprocating harmonic ground motion. The blade displacement is assumed to take the form

$$v_r(x,t) = \sum \hat{V}_r(x) q_r(t) + \Delta e^{i\Omega t} \tag{6.4}$$

where $\sum \hat{V}_r(x) q_r(t)$ represents the scaled flexible beam modes, and $\Delta e^{i\Omega t}$ is the rigid body ground motion. By substituting Equation (6.4) and derivatives of Equation (6.4) into Equation (6.2), the equation of motion for the forced motion of the blade becomes

$$\begin{aligned} &EI \sum \frac{d^4 \hat{V}_r(x)}{dx^4} q_r(t) + c \sum \hat{V}_r(x) \frac{dq_r(t)}{dt} + ci\Omega \Delta e^{i\Omega t} + wg(l-x) \sum \frac{d^2 \hat{V}_r(x)}{dx^2} q_r(t) \\ &- wg \sum \frac{d\hat{V}_r(x)}{dx} q_r(t) + w \sum \hat{V}_r(x) \frac{d^2 q_r(t)}{dt^2} - w\Omega^2 \Delta e^{i\Omega t} = -f(x,t) \end{aligned} \tag{6.5}$$

By collecting like terms, Equation (6.5) may be expressed more clearly in the following standard form

$$\begin{aligned} &w \sum \hat{V}_r(x) \ddot{q}_r(t) + c \sum \hat{V}_r(x) \dot{q}_r(t) + \sum \left[EI \frac{d^4 \hat{V}_r(x)}{dx^4} + wg(l-x) \frac{d^2 \hat{V}_r(x)}{dx^2} \right. \\ &\left. - wg \frac{d\hat{V}_r(x)}{dx} \right] q_r(t) = (w\Omega - ci)\Omega \Delta e^{i\Omega t} - f(x,t) \end{aligned} \tag{6.6}$$

6.2.2 Separating the modes of vibration for the blade

When the reciprocating ground motion frequency is equal to one of the natural frequencies of the blade, the shape of the vibrating blade is expected to be consistent with the blade mode corresponding to the ground motion frequency. The final motion will, however, be a superposition of all the blade modes.

Although the principle modes are expected to be orthogonal, orthogonality of the calculated modes was tested as a check for the numerical procedures so far.

For the modes to be orthogonal, for a blade of uniform properties along its length, the kinetic energy function gives

$$\int_0^l \hat{V}_r(x)\hat{V}_s(x)dx = 0 \qquad r \neq s \tag{6.7}$$

and the potential energy function gives

$$\int_0^l \left[EI\frac{d^4\hat{V}_r(x)}{dx^4} + wg(l-x)\frac{d^2\hat{V}_r(x)}{dx^2} - wg\frac{d\hat{V}_r(x)}{dx} \right]\hat{V}_s(x)dx = 0 \qquad r \neq s \tag{6.8}$$

or alternatively

$$\frac{1}{2}\int_0^l EI\left(\frac{\partial^2 v(x,t)}{\partial x^2}\right)^2 dx - \frac{1}{2}\int_0^l wg(l-x)\left(\frac{\partial v(x,t)}{\partial x}\right)^2 dx = 0 \qquad r \neq s \tag{6.9}$$

For convenience, the terms *E11nm* & *E22nm* are defined to represent the normalised integrals, Equations (6.7) & (6.8) respectively. These were calculated in *C6Prog1.m* and as expected, the blade modes are orthogonal. The off-diagonal terms in *E11nm* & *E22nm* approach zero as the accuracy of the numerical integration procedure increases.

$$E11nm_{r,s} = \begin{bmatrix} 1.00000000 & -0.00000077 & 0.00000116 & -0.00000156 \\ -0.00000077 & 1.00000000 & -0.00000156 & 0.00000196 \\ 0.00000116 & -0.00000156 & 1.00000000 & -0.00000235 \\ -0.00000156 & 0.00000196 & -0.00000235 & 1.00000000 \end{bmatrix} \quad (6.10a)$$

&

$$E22nm_{r,s} = \begin{bmatrix} 1.00000000 & -0.00000006 & 0.00000004 & -0.00000002 \\ -0.00000864 & 1.00000000 & -0.00000054 & 0.00000034 \\ 0.00003767 & -0.00000453 & 1.00000000 & -0.00000119 \\ -0.00010009 & 0.00001121 & -0.00000466 & 1.00000000 \end{bmatrix} \quad (6.10b)$$

6.2.3 The equivalent blade system

It was assumed that in the matrix form, a purely diagonal dissipation function would represent velocity dependent damping on the blade; this would not cross-couple modes and hence the modal equations of motion remain independent and may be separated as follows

$$w\int_0^l \hat{V}_r(x)\hat{V}_s(x)dx\,\ddot{q}_r + c\int_0^l \hat{V}_r(x)\hat{V}_s(x)dx\,\dot{q}_r + \int_0^l \left[EI\frac{d^4\hat{V}_r(x)}{dx^4} + \right.$$

$$\left. wg(l-x)\frac{d^2\hat{V}_r(x)}{dx^2} - wg\frac{d\hat{V}_r(x)}{dx}\right]\hat{V}_s(x)dxq_r = \int_0^l \left[(w\Omega - ci)\Omega\Delta e^{i\Omega t} - f(t)\right]\hat{V}_s(x)dx \quad (6.11)$$

As the modes are orthogonal this gives

$$w\int_0^l \hat{V}_r^2(x)dx\,\ddot{q}_r + c\int_0^l \hat{V}_r^2(x)dx\,\dot{q}_r + \int_0^l \left[EI\frac{d^4\hat{V}_r(x)}{dx^4} + wg(l-x)\frac{d^2\hat{V}_r(x)}{dx^2}\right.$$

$$\left. - wg\frac{d\hat{V}_r(x)}{dx}\right]\hat{V}_r(x)dxq_r = (w\Omega + ci)\Omega\Delta e^{i\Omega t}\int_0^l \hat{V}_r(x)dx - f(t)\hat{V}_r(R) \quad (6.12)$$

For convenience it is useful to introduce the following notation

$$\left.\begin{aligned} M_r &= w\int_0^l \hat{V}_r^2(x)dx \\ C_r &= c_r\int_0^l \hat{V}_r^2(x)dx \\ S_r &= \int_0^l \left[EI\frac{d^4\hat{V}_r(x)}{dx^4} + wg(l-x)\frac{d^2\hat{V}_r(x)}{dx^2} - wg\frac{d\hat{V}_r(x)}{dx}\right]\hat{V}_r(x)dx \end{aligned}\right\} \quad (6.13)$$

where M_r, C_r, and S_r may be regarded as the equivalent mass, damping, and stiffness for the r^{th} mass, damper, and spring system.

Considering the notation from above, and noting that $\hat{V}_r(R)=1.0$, then the modal equations of motion take the form

$$\begin{aligned} M_r\ddot{q}_r + C_r\dot{q}_r + S_r q_r &= (w\Omega + c_r i)\Omega\Delta e^{i\Omega t}\int_0^l \hat{V}_r(x)dx - f(R,t) \\ M_s\ddot{q}_s + C_s\dot{q}_s + S_s q_s &= (w\Omega + c_s i)\Omega\Delta e^{i\Omega t}\int_0^l \hat{V}_s(x)dx - f(R,t) \\ &\vdots \\ M_{p_{max}}\ddot{q}_{p_{max}} + C_{p_{max}}\dot{q}_{p_{max}} + S_{p_{max}}q_{p_{max}} &= (w\Omega + c_{p_{max}} i)\Omega\Delta e^{i\Omega t}\int_0^l \hat{V}_{p_{max}}(x)dx - f(R,t) \end{aligned} \quad (6.14)$$

where p_{max} is the highest blade frequency considered.

6.3 The equations of motion for the wand

Using energy functions the equivalent masses, stiffnesses, and damping terms for the equations of motion for a set of equivalent wands may be formulated as for the blade.

6.3.1 Energy functions

The kinetic energy of the system in Figure 6.2 (b) is

$$T = \frac{1}{2}\int_0^l w\left(\frac{\partial v(x,t)}{\partial t}\right)^2 dx + \frac{1}{2}M_{cb}\left(\partial\left(v(l,t) + r\frac{\partial v(l,t)}{\partial x}\right)\Big/\partial t\right)^2 + \frac{1}{2}I_{cb}\left(\partial\left(\frac{\partial v(l,t)}{\partial x}\right)\Big/\partial t\right)^2 \tag{6.15}$$

The first term in Equation (6.15) represents the sum of the kinetic energies of all of the wand stem elements of length dx summed over the interval from $x=0$ to $x=l$. The second term in Equation (6.15) is associated with the kinetic energy of the ball due to linear motion in the v direction and the third term is associated with rotary motion in the x-y plane.

The potential energy of the wand is of the form

$$V = \frac{1}{2}\int_0^l EI\left(\frac{\partial^2 v(x,t)}{\partial x^2}\right)^2 dx - \frac{1}{2}\int_0^l (P_l + wg(l-x))\left(\frac{\partial v(x,t)}{\partial x}\right)^2 dx - \frac{1}{2}P_l r\left(\frac{dv(l,t)}{\partial x}\right)^2 \tag{6.16}$$

The first term in Equation (6.16) represents the strain energy of all of the wand stem elements, of length dx, summed over the interval from $x=0$ to $x=l$, and is due to bending. The second term represents the work done by the weight of the ball and of the stem due to the shortening of the stem in the gravitational field. The third term allows for the extra work done due to the rigid body motion of the centre of mass of the ball.

The built-in end of the wand is stationary, therefore the wand displacement may be assumed to take the form

$$v_w(x,t) = \sum V_w(x) q_w(t) \tag{6.17}$$

where $V_w(x)$ is one of flexible beam modes for the wand stem as derived in Chapter 4.

Using the approach adopted for the blade, it is useful at this stage to define $\hat{V}_w$ as the wand modes scaled so that the modal displacements are equal to unity at the wand/blade contact height. i.e. $\hat{V}_w(R) = 1.0$. The scaled wand modes, $\hat{V}_w(x)$ were calculated in Section C6Prog1.3 of *C6Prog1.m* using

$$\hat{V}_w(x) = \frac{V_w(x)}{V_w(l) + r dV_w(l)/dx} \tag{6.18}$$

6.3.2 Separating the modes of vibration for the wand

In a procedure similar to that for the blade, it was checked that the calculated modes for the wand were orthogonal. Hence, the total displacement may be found by linear superposition.

6.3.3 The equivalent system for the wand

The kinetic and potential energy functions, Equations (6.15) & (6.16) may be written in terms of the principal modes giving

$$T = \frac{\omega_n^2}{2}\left[\int_0^l w \sum_n^\infty \left(\hat{V}_n(x)\right)^2 dx + M_{cb} \sum_n^\infty \left(\hat{V}_n(l)\right)^2 + 2r \sum_n^\infty \hat{V}_n(l) \frac{d\hat{V}_n(l)}{dx} + r^2 \sum_n^\infty \left(\frac{d\hat{V}_n(l)}{dx}\right)^2 + I_{cb} \sum_n^\infty \left(\frac{d\hat{V}_n(l)}{dx}\right)^2\right] \tag{6.19}$$

&

$$V = \frac{1}{2}\int_0^l EI \sum_n^{\infty}\left(\frac{d^2\hat{V}_n(x)}{dx^2}\right)^2 dx - \frac{1}{2}\int_0^l (P_l + wg(l-x))\sum_n^{\infty}\left(\frac{d\hat{V}_n(x)}{dx}\right)^2 dx - \frac{1}{2}P_l r\sum_n^{\infty}\left(\frac{d\hat{V}_n(l)}{dx}\right)^2 dx \quad (6.20)$$

After considering the kinetic energy of the system, Equation (6.19), the equivalent mass for the w^{th} mode may be expressed as

$$M_w = \int_0^l w\left(\hat{V}_w(x)\right)^2 dx + M_{cb}\left[\left(\hat{V}_w(l)\right)^2 + 2r\hat{V}_w(l)\frac{d\hat{V}_w(l)}{dx} + r^2\left(\frac{d\hat{V}_w(l)}{dx}\right)^2\right] + I_{cb}\left(\frac{d\hat{V}_w(l)}{dx}\right)^2 \quad (6.21)$$

The equivalent modal stiffness for the w^{th} mode may be obtained from Equation (6.20) as

$$S_w = \int_0^l EI\left(\frac{d^2\hat{V}_w(x)}{dx^2}\right)^2 dx - \int_0^l (P_l + wg(l-x))\left(\frac{d\hat{V}_w(x)}{dx}\right)^2 dx - P_l r\left(\frac{d\hat{V}_w(l)}{dx}\right)^2 \quad (6.22)$$

Assuming damping not to couple the modes and to be proportional to velocity, the modal equations of motion for the forced damped vibration of the wand will take the form

$$\begin{aligned} M_w\ddot{q}_w + C_w\dot{q}_w + S_w q_w &= f(R,t) \\ M_x\ddot{q}_x + C_x\dot{q}_x + S_x q_x &= f(R,t) \\ \vdots \quad\quad \vdots \quad\quad \vdots \quad\quad \vdots & \\ M_{pw_{max}}\ddot{q}_{pw_{max}} + C_{pw_{max}}\dot{q}_{pw_{max}} + S_{pw_{max}} q_{pw_{max}} &= f(R,t) \end{aligned} \quad (6.23)$$

Where pw_{max} is the highest wand mode considered.

6.4 System damping

The damping mechanisms for *Blade* are very complex. The approach adopted here is to derive realistic values for the damping constants using simple experimental procedures.

6.4.1 Damping considerations for the blade modes

The predominant damping mechanism for the blade is expected to be due to aerodynamic drag. Other damping mechanisms present dissipate energy due to internal material friction or by transmitting sound.

In an experimental procedure, the base motion frequency was set to coincide with the each of the first three natural undamped bending frequencies *($_1\Omega$, $_2\Omega$, and $_3\Omega$)* for the original blade. The maximum vibrating blade displacement was measured at the ball contact height for each of these natural frequencies. The observed blade displacements were 0.025m, 0.095m, & 0.070m for the first, second, and third bending frequencies respectively. These observed blade displacements were the vector sum of the contributions from each of the modes.

Considering the case where the base excitation frequency coincides with r^{th} blade bending frequency *(i.e. $_r\Omega = {}_r\omega$)*, the r^{th} displacement vector $_rq_r$, is perpendicular to the forcing function vector due to damping, as shown in Figure 6.3. Components of force f from lower modes of vibration than the exciting frequency have negative real parts and those from modes higher than the exciting frequency have positive real parts. In this particular case, where $_r\Omega = {}_r\omega$ the contributions to the total blade displacement, from the s^{th} mode may be calculated from

$$M_s\ {}_r\ddot{q}_s + C_s\ {}_r\dot{q}_s + S_s\ {}_rq_s = \left(w\ {}_r\Omega - c_s i\right)_r\Omega\Delta e^{i\,{}_r\Omega t}\int_0^l \hat{V}_s(x)dx = {}_rf_s \qquad (6.24)$$

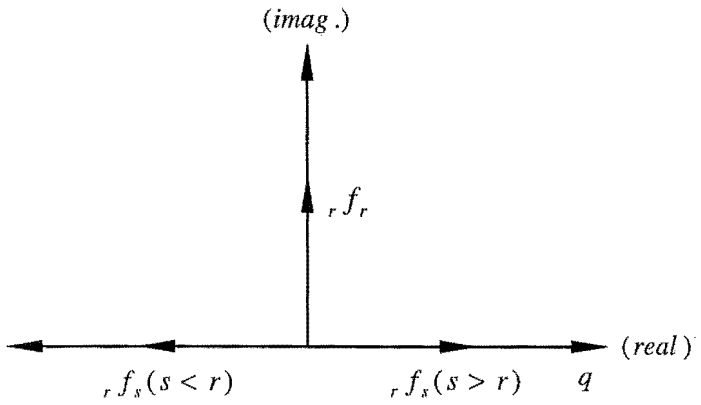

Figure 6.3 *Relationship between force and displacement vectors for the forced vibration of the blade*

Equation (6.24) may be rearranged to give the steady state displacement $_rq_s$ for the s^{th} mode as

$$ {}_rq_s = \frac{\left(w\ {}_r\Omega - c_s i\right)_r \Omega \Delta e^{i_r \Omega t} \int_0^l \hat{V}_s(x)dx}{M_s\left[-{}_r\Omega^2 + \frac{iC_s}{M_s}{}_r\Omega + \frac{S_s}{M_s}\right]} \tag{6.25} $$

Considering the relationships in Equations (6.13), and noting that $S_s/M_s \approx {}_s\Omega^2$, Equation (6.25) may be written as

$$ {}_rq_s = \frac{\left(w\ {}_r\Omega - c_s i\right)_r \Omega \Delta e^{i_r \Omega t} \int_0^l \hat{V}_s(x)dx}{w\int_0^l \hat{V}_s^2(x)dx\left[-{}_r\Omega^2 + \frac{ic_s \int_0^l \hat{V}_s^2(x)dx}{M_s}{}_r\Omega + {}_s\Omega^2\right]} \tag{6.26} $$

When $r \neq s$ the imaginary components of Equation (6.26) may be assumed to be small compared with the real components giving

$$ {}_rq_s \approx \frac{{}_r\Omega^2 \Delta \int_0^l \hat{V}_s(x)dx}{\int_0^l \hat{V}_s^2(x)dx\left[{}_s\Omega^2 - {}_r\Omega^2\right]} \qquad r \neq s \tag{6.27} $$

and when $r = s$ the real component may be assumed to be small compared with the imaginary component giving

$$ {}_rq_r = \frac{w\ {}_r\Omega\ \Delta \int_0^l \hat{V}_r(x)dx}{ic_r \int_0^l \hat{V}_r^2(x)dx} \tag{6.28} $$

or

$$ ic_r = \frac{w\ {}_r\Omega\Delta \int_0^l \hat{V}_r(x)dx}{{}_rq_r \int_0^l \hat{V}_r^2(x)dx} \tag{6.29} $$

These actual displacements are calculated in Sections C6Prog2.4 & C6Prog2.5 of Procedure *C6Prog2.m.* For the original blade the calculated displacement amplitudes are tabulated in Table 6.1.

Once the major components of the displacements from the s^{th}, t^{th}, & u^{th} modes have been calculated, the r^{th} amplitude of displacement corresponding to ${}_r\Omega$ may be found

$$ {}_rq_r = \sqrt{{}_rq_T^2 - \left({}_rq_s + {}_rq_t + {}_rq_u\right)^2} \tag{6.30} $$

Table 6.1 *Predicted maximum modal blade displacements at the ball contact height for the original blade*

	modal blade displacements coinciding with clamp frequency Ω (m)			
blade modes	$\Omega = {}_1\Omega$	$\Omega = {}_2\Omega$	$\Omega = {}_3\Omega$	$\Omega = {}_4\Omega$
$\omega = \omega_1$	0.025000	-0.001263	-0.001254	-0.001253
$\omega = \omega_2$	0.000022	0.094995	-0.003149	-0.002861
$\omega = \omega_3$	0.000002	0.000303	0.069879	-0.003007
$\omega = \omega_4$	0.0000002	0.000026	0.000282	0.029143

6.4.2 Prediction of the damping constant for the wand stem

An experimental procedure was used to determine the damping constant for the wand stem. This procedure involved releasing the wand from an initial displacement of 110mm and recording the decay in amplitude using a video. From the results of the video, the maximum wand amplitude was found to attenuate down to 48mm after 12 cycles.

The initial conditions for the experimental procedure in programs *C6Prog3.m* and *C6Prog4.m* were set as *(bwmdl=4, Ω=0, H=0.5, & qwf = 110)*, and program *C6Prog7.m* was run to simulate the time-history response for the wand displacement. The results of the time-history plot were compared with the video recording from the experimental procedure above. The damping constant for the wand stem, C_w in Equation (6.23), was adjusted in *C6Prog2.m* until the simulated results were consistent with the experimental observations. For the original cork ball the numerical value determined for C_w was 0.15N-m/sec.

6.4.3 Prediction of the stiffness & damping properties for the cork ball

6.4.3.1 Contact indentation stiffness for the original cork ball

An experimental procedure was conducted to measure the contact indentation stiffness of the original cork ball. This experimental procedure involved applying a series of loads to compress the cork ball between a hydraulic ram and flat plate *(two flat surfaces)* on a calibrated tensile testing machine. A schematic diagram of the system is shown in Figure 6.4. The results of this test are plotted in Figure 6.5

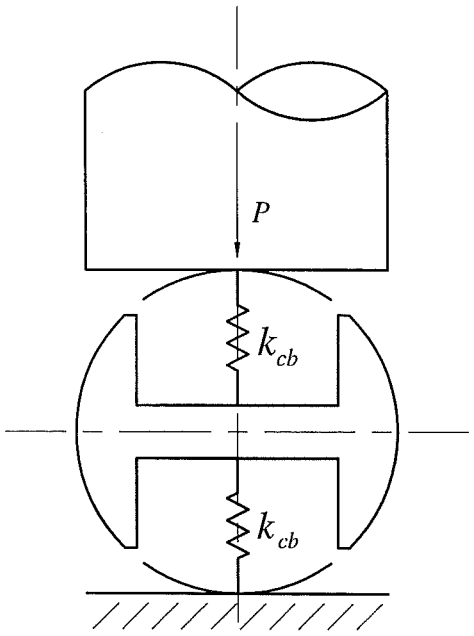

Figure 6.4 *The contact indentation test*

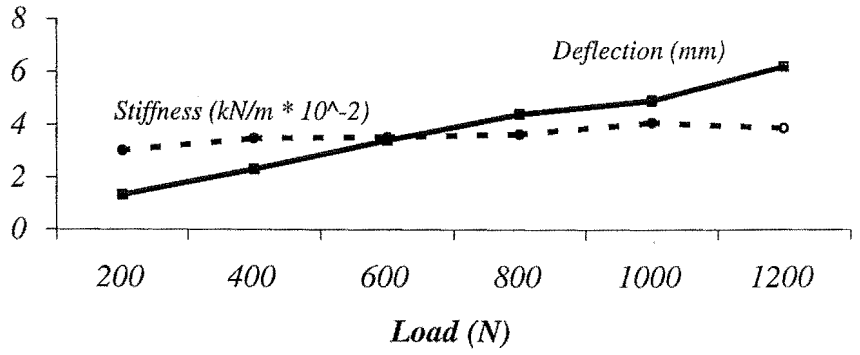

Figure 6.5 *Stiffness properties for the original cork ball*

From inspection of Figure 6.5 the stiffness of the original cork ball is relatively constant over the range of loads from 200 – 1200N. The contact indentation stiffness constant, k_{cb}, for the original cork ball was set at 360kN-m.

6.4.3.2 Contact indentation for the scaled cork ball

This analysis uses simple scaling rules to predict the stiffness properties of the scaled cork ball based on the experimental observations of the original size.

For the case of a sphere normally loaded by a flat plate, the relative motion of approach along the axis of loading of two points, remote from the contact zone, one in the sphere and one in the plate, is given by the expression [pg 650 Young (1989)]

$$\delta = 1.040\left(\frac{P^2}{2r}\left(\frac{1-\upsilon_1^2}{E_1}+\frac{1-\upsilon_2^2}{E_2}\right)\right)^{\frac{1}{3}} \tag{6.31}$$

where δ is the relative displacement, P is the contact force, r is the ball radius, ν is Poisson's ratio, E is Young's modulus, and subscripts 1 and 2 refer to each of the bodies

The differences in elastic properties between the original and the scaled blades are not expected to make a significant difference to the term in the inner brackets of Equation (6.31) because the elastic modulus for the blade material is still much greater than that for the cork ball. For the purpose of scaling we may therefore simplify Equation (6.31) to the form

$$\delta = C_1 \frac{P^{\frac{2}{3}}}{r^{\frac{1}{3}}} \tag{6.32}$$

For the case where the ball is subject to an additional much smaller load p, then the relative movement will be

$$\delta + \varepsilon = C_1 \frac{(P+p)^{\frac{2}{3}}}{r^{\frac{1}{3}}} = C_1 \frac{P^{\frac{2}{3}}\left(1+\frac{p}{P}\right)^{\frac{2}{3}}}{r^{\frac{1}{3}}} \tag{6.33}$$

Expanding Equation (6.34) using the binomial theorem and noting that $p << P$ gives

$$\delta + \varepsilon = C_1 \frac{P^{\frac{2}{3}}}{r^{\frac{1}{3}}}\left(1+\frac{2}{3}\frac{p}{P}\right) \tag{6.34}$$

In this case the contribution to the relative displacement ε may be extracted from (6.34) to give

$$\varepsilon = C_2 \frac{p}{P^{\frac{1}{3}} r^{\frac{1}{3}}} \tag{6.35}$$

For the case where the mean normal load is held constant then a linearised stiffness, S_L, may be defined as

$$S_L = \frac{p}{\varepsilon} = C_3 r^{\frac{1}{3}} \tag{6.36}$$

and the effect of ball radius on contact indentation stiffness is

$$\frac{{}_1S_L}{{}_2S_L} = \frac{{}_1r^{\frac{1}{3}}}{{}_2r^{\frac{1}{3}}} \tag{6.37}$$

Using Equation (6.37) the contact indentation stiffness of the scaled cork ball was calculated as 452kN-m.

6.4.3.3 Contact indentation damping for the original cork ball

Dropping the ball from a predetermined height onto a hard flat surface and then measuring the rebound height established the damping constant for the original cork ball. Figure 6.6 shows how stiffness and damping were modelled for such a test. The acceleration, velocity, and displacement of the ball, shown in Figure 6.6, when not in contact with the ground will be

$$\ddot{x}_1 = -g, \quad \dot{x}_1 = -gt + a, \quad x_1 = -gt^2 + at + b \tag{6.38}$$

where a & b are constants.

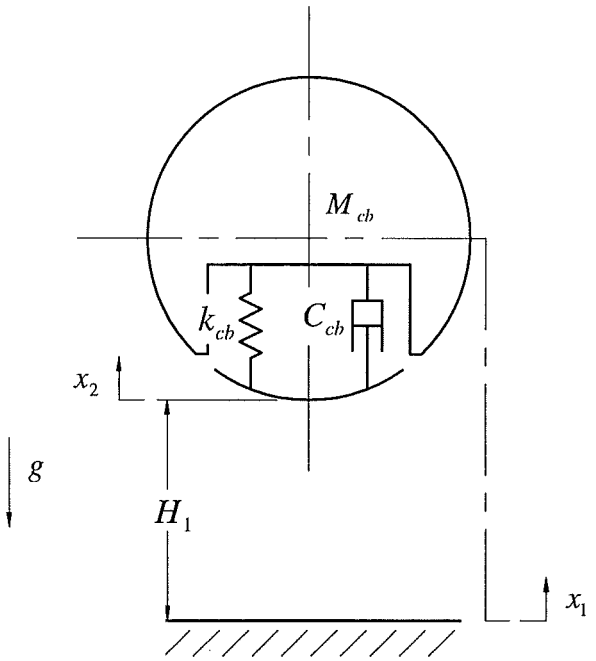

Figure 6.6 *Schematic diagram of the model for the bouncing cork ball test*

The initial conditions for the test were

$$\begin{aligned} &\dot{x}_1 = 0 \quad when\ t=0 \quad \rightarrow a=0 \\ &\&\ x_1 = H_1 \quad when\ t=0 \quad \rightarrow b=H_1 \end{aligned} \tag{6.39}$$

When the ball first made contact with the ground, $x_1 = 0$. Substituting in the initial conditions from Equation (6.39) into Equation (6.38) gives the time and the ball velocity at the instant of initial contact between the ball and ground, thus

$$t=\sqrt{\frac{2H_1}{g}}, \qquad \dot{x}_1 = -\sqrt{2gH_1} \tag{6.40}$$

When in contact the equation of motion for the ball is

$$M_{cb}\ddot{x}_1 + C_{cb}\dot{x}_1 + k_{cb}x_1 = 0 \tag{6.41}$$

The general solution to Equation (6.41) is of the form

$$x_1 = \exp^{-\alpha t}\left(A\sin(\omega t) + B\cos(\omega t)\right) \tag{6.42}$$

$$where \quad \alpha = \frac{C_{cb}}{2M_{cb}} \;\&\; \omega = \sqrt{\left(\frac{C_{cb}}{2M_{cb}}\right)^2 - \frac{k_{cb}}{M_{cb}}}$$

Setting the initial contact time to zero, and using the final displacement and velocity from the non-contact condition, the solution to Equation (6.41) is

$$x_1 = -\exp^{-\alpha t}\frac{\sqrt{2gH_1}}{\omega}\sin(\omega t)$$

$$\dot{x}_1 = \exp^{-\alpha t}\sqrt{2gH_1}\left(\frac{\alpha}{\omega}\sin(\omega t) - \cos(\omega t)\right) \tag{6.43}$$

The condition for contact is that the force on the ball surface must be greater than zero, i.e.

$$C_{cb}\dot{x}_1 + k_{cb}x_1 \geq 0 \qquad (for\ contact) \tag{6.44}$$

Setting Equation (6.44) equal to zero and substituting in the solutions for the contact displacement and velocity functions from Equations (6.43), the contact time is given by

$$t_{contact} = \frac{1}{\omega}\tan^{-1}\left(\frac{C_{cb}\omega}{C_{cb}\alpha - k_{cb}}\right) \tag{6.45}$$

The MATLAB procedure *C6Prog2a.m* solves Equations (6.38) & (6.41) for a specified number of bounces of the cork ball. The indentation damping constant, C_{cb}, was adjusted in *C6Prog2a.m* until the dynamic simulation for the bouncing cork ball was found to be a good approximation to the results from the

experimental test. The damping constant determined for indentations of the original cork ball using the simulation program was 78 N-m/sec.

6.4.3.4 Contact indentation damping for the scaled cork ball

From Figure 3.3, it can be seen that the cork material has a very high loss coefficient. Therefore in this case much of the energy absorbed by the ball is expected to be due to internal friction *(i.e. sliding along shear planes)* and will be a function of the volume affected by the deformation of the surface.

For the case of a normally loaded sphere on a flat plate, as discussed in Section 6.4.3.1, the radius, a, of the circular contact area is [pg650 Young (1989)]

$$a = 0.721\left(\Pr\left(\frac{1-\upsilon_1^2}{E_1}+\frac{1-\upsilon_2^2}{E_2}\right)\right)^{\frac{1}{3}} \tag{6.46}$$

For purposes of scaling the elastic properties between the original and scaled works are assumed to be similar and Equation (6.47) may be simplified to

$$a = C_4 P^{\frac{1}{3}} r^{\frac{1}{3}} \tag{6.47}$$

The maximum shear stress is [Young (1989)]

$$\tau = \frac{P}{\pi a^2} \tag{6.48}$$

The maximum shear stress will be on the load line at a point $a/2$ from the contact surface [Young (1989)]. From photo-elastic stress patterns [Johnson (1985)] there is spheroidal zone centred on the point of maximum shear stress of approximate radius $\sqrt{5}a/2$, which contains the most highly stressed material.

For the purpose of this analysis, this most highly stressed zone as shown in Figure 6.7, will be defined as being the effective volume for the damping model.

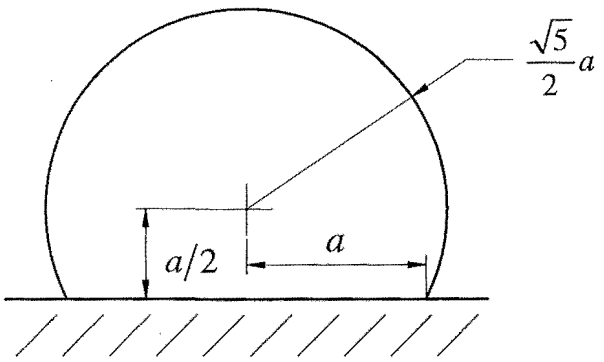

Figure 6.7 *Assumed form for the effective shear stress zone*

The volume of the sphere with a spherical sector removed, as shown in Figure 6.7, is of the form [pg 66 Oberg et al. (1992)]

$$V = a^3 C_5 \tag{6.49}$$

Combining Equations (6.47) & (6.49), the effective volume may be written as

$$V = C_6 \Pr \tag{6.50}$$

If the damping varies as the product of shear stress and affected volume, then substituting Equation (6.47) into (6.48) and multiplying by Equation (6.50) gives the ratio of the damping constants between the original and scaled cork ball as

$$\frac{{}_o C_{cb}}{{}_s C_{cb}} = \frac{{}_o P^{\frac{4}{3}} \, {}_o r^{\frac{1}{3}}}{{}_s P^{\frac{4}{3}} \, {}_s r^{\frac{1}{3}}} \tag{6.51}$$

Therefore for a constant contact force, the scaling ratio for contact indentation damping is the same as was predicted for the contact indentation stiffness. The damping constant for the indentation of the scaled cork ball was calculated as 98N-m/sec.

6.5 The contact condition

The schematic diagram in Figure 6.8 shows how the blade and wand were modelled for simulating their dynamic interaction in the kinetic sculpture *Blade.*

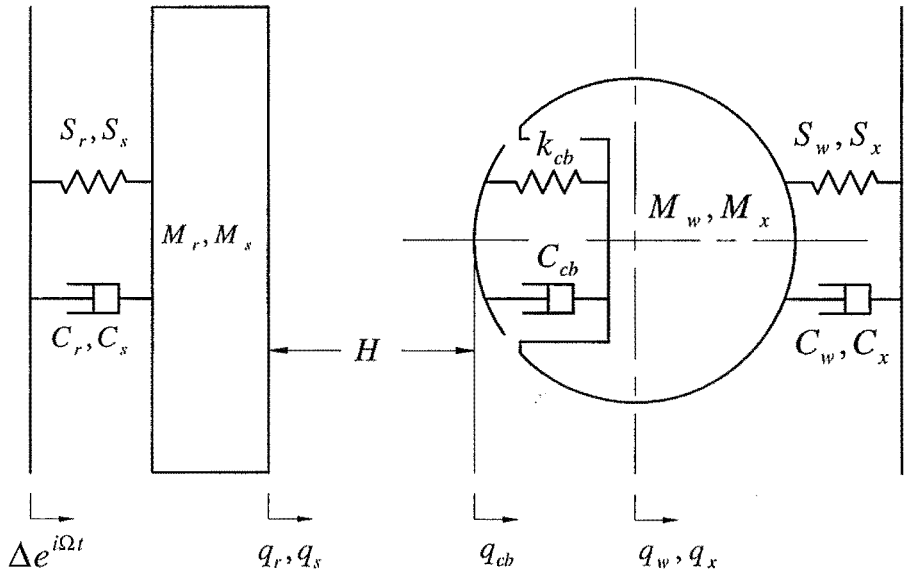

Figure 6.8 *Schematic diagram for the interaction between the blade and the wand*

Considering the coordinate system in Figure 6.8, if the *blade* and *wand* are in contact, the position of the surface of the cork ball may written as the sum of the modal *blade* displacements and the initial rest separation distance, namely

$$q_{cb} = \left(q_r + q_s + \ .... \ q_{p_{\max}}\right) - H \qquad (6.52)$$

Similarly, the following relationships for the velocity and acceleration of the surface of the cork ball can be defined

$$\dot{q}_{cb} = \dot{q}_r + \dot{q}_s + \ .... \ \dot{q}_{p_{\max}} \qquad (6.53)$$

$$\ddot{q}_{cb} = \ddot{q}_r + \ddot{q}_s + \ .... \ \ddot{q}_{p_{\max}} \qquad (6.54)$$

6.5.1 The equation of motion for the blade when in contact

Considering the principal blade modes, Equations (6.14), then the free body diagram for the r^{th} mode may be shown schematically as in Figure 6.9(a)

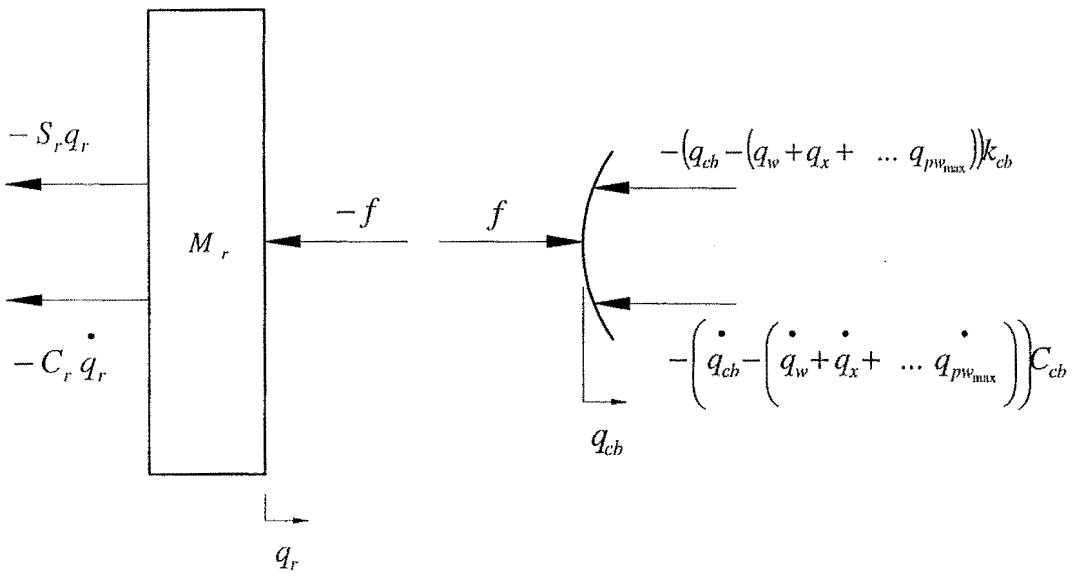

Figure 6.9 *Contact forces*

(a) Free body diagram for the blade in its r^{th} principal mode

(b) Free body diagram for the surface of the ball

If the surface segment of the ball, shown schematically in Figure 6.9(b), is assumed to have negligible mass, the contact force, f, is

$$f = \left(q_{cb} - \left(q_w + q_x + \ .... \ q_{pw_{\max}}\right)\right)k_{cb} + \left(\dot{q}_{cb} - \left(\dot{q}_w + \dot{q}_x + \ .... \ \dot{q}_{pw_{\max}}\right)\right)C_{cb} \tag{6.55}$$

Considering the displacement and velocity relationships for the contact condition, Equations (6.52) & (6.53), the contact force in Equation (6.55) may be expressed in terms of the total blade displacement giving

$$\begin{aligned} f = &\left(\left(q_r + q_s + \ .... \ q_{p_{\max}}\right) - H - \left(q_w + q_x + \ .... \ q_{pw_{\max}}\right)\right)k_{cb} \\ &+ \left(\left(\dot{q}_r + \dot{q}_s + \ .... \ \dot{q}_{p_{\max}}\right) - \left(\dot{q}_w + \dot{q}_x + \ .... \ \dot{q}_{pw_{\max}}\right)\right)C_{cb} \end{aligned} \tag{6.56}$$

Substituting the force from Equation (6.56) into the modal equations of motion for the blade modes, Equations (6.14), gives

$$M_r \ddot{q}_r + (C_r + C_{cb})\dot{q}_r + (S_r + k_{cb})q_r = \left(\left(\dot{q}_w + \dot{q}_x + \ .... \ \dot{q}_{pw_{\max}}\right) - \left(\dot{q}_s + \dot{q}_t + \ .... \ \dot{q}_{p_{\max}}\right)\right)C_{cb}$$

$$+ \left(\left(q_w + q_x + \ .... \ q_{pw_{\max}}\right) - \left(q_s + q_t + \ .... \ q_{p_{\max}}\right)\right)k_{cb} + (w\Omega - c_r i)\Omega\Delta e^{i\Omega t}\int_0^l \hat{V}_r(x)dx + k_{cb}H$$

$$M_s \ddot{q}_s + (C_s + C_{cb})\dot{q}_s + (S_s + k_{cb})q_s = \left(\left(\dot{q}_w + \dot{q}_x + \ .... \ \dot{q}_{pw_{\max}}\right) - \left(\dot{q}_r + \dot{q}_t + \ .... \ \dot{q}_{p_{\max}}\right)\right)C_{cb}$$

$$+ \left(\left(q_w + q_x + \ .... \ q_{pw_{\max}}\right) - \left(q_r + q_t + \ .... \ q_{p_{\max}}\right)\right)k_{cb} + (w\Omega - c_s i)\Omega\Delta e^{i\Omega t}\int_0^l \hat{V}_r(x)dx + k_{cb}H$$

$$\vdots \quad \vdots \quad \vdots \quad \vdots \quad \vdots \quad \vdots \quad \vdots \quad \vdots \quad \vdots \quad \vdots \quad \vdots \quad \vdots \quad \vdots$$

$$\vdots \quad \vdots \quad \vdots \quad \vdots \quad \vdots \quad \vdots \quad \vdots \quad \vdots \quad \vdots \quad \vdots \quad \vdots \quad \vdots \quad \vdots$$

$$\begin{aligned} M_{p_{\max}} \ddot{q}_{p_{\max}} + \left(C_{p_{\max}} + C_{cb}\right)\dot{q}_{p_{\max}} + \left(S_{p_{\max}} + k_{cb}\right)q_{p_{\max}} = &\left(\left(\dot{q}_w + \dot{q}_x + \ \ldots\ \dot{q}_{pw_{\max}}\right)\right. \\ -\left(\dot{q}_r + \dot{q}_s + \ \ldots\ \dot{q}_{p_{\max}-1}\right)&\Big)C_{cb} + \left(\left(q_w + q_x + \ \ldots\ q_{pw_{\max}}\right)\right. \\ -\left(q_r + q_s + \ \ldots\ q_{p_{\max}-1}\right)&\Big)k_{cb} + \left(w\Omega - c_{p_{\max}} i\right)\Omega\Delta e^{i\Omega t}\int_0^l \hat{V}_r(x)dx + k_{cb}H \end{aligned} \tag{6.57}$$

6.5.2 The equation of motion for the wand when in contact

The free body diagram for the w^{th} principal wand mode as shown by the schematically in Figure 6.10

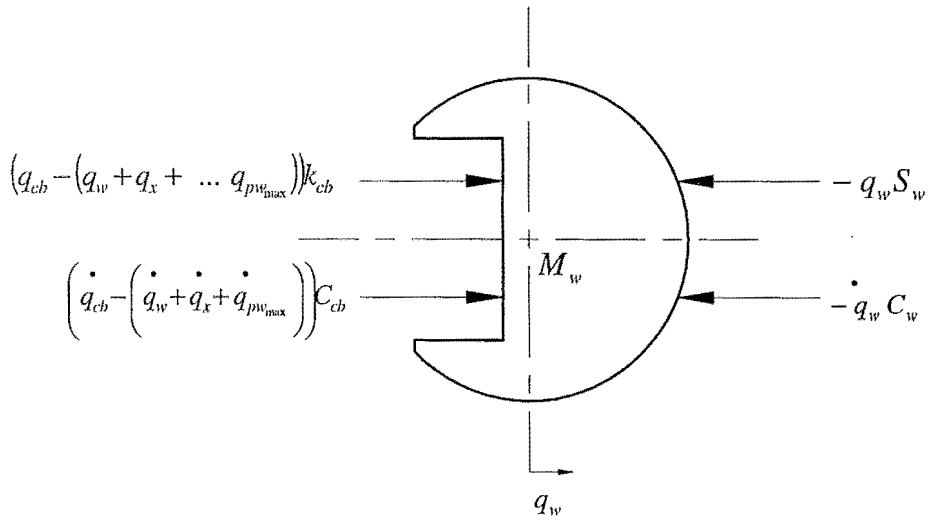

Figure 6.10 *Free body diagram for the wand in its w^{th} principal mode*

Substituting Equations (6.52) & (6.53) into the modal equations of motion for the wand, Equations (6.23), gives

$$M_w \ddot{q}_w + (C_{cb} + C_w)\dot{q}_w + (k_{cb} + S_w)q_w = \left(\dot{q}_r + \dot{q}_s + \ldots. \dot{q}_{p_{\max}} - \left(\dot{q}_x + \dot{q}_y + \ldots. \dot{q}_{pw_{\max}}\right)\right)C_{cb}$$

$$+ \left(\left(q_r + q_s + \ldots. q_{p_{\max}}\right) - H - \left(q_x + q_y + \ldots. q_{pw_{\max}}\right)\right)k_{cb}$$

$$M_x \ddot{q}_x + (C_{cb} + C_x)\dot{q}_x + (k_{cb} + S_x)q_x = \left(\dot{q}_r + \dot{q}_s + \ldots. \dot{q}_{p_{\max}} - \left(\dot{q}_w + \dot{q}_y + \ldots. \dot{q}_{pw_{\max}}\right)\right)C_{cb}$$

$$+ \left(\left(q_r + q_s + \ldots. q_{p_{\max}}\right) - H - \left(q_w + q_y + \ldots. q_{pw_{\max}}\right)\right)k_{cb}$$

$$\vdots \quad \vdots \quad \vdots \quad \vdots \quad \vdots \quad \vdots \quad \vdots \quad \vdots \quad \vdots \quad \vdots \quad \vdots \quad \vdots \quad \vdots$$

$$M_{pw_{\max}} \ddot{q}_{pw_{\max}} + \left(C_{cb} + C_{pw_{\max}}\right)\dot{q}_{pw_{\max}} + \left(k_{cb} + S_{pw_{\max}}\right)q_{pw_{\max}} = \left(\dot{q}_r + \dot{q}_s + \ldots. \dot{q}_{p_{\max}} -\right.$$

$$\left.\left(\dot{q}_w + \dot{q}_x + \ldots. \dot{q}_{pw_{\max}-1}\right)\right)C_{cb} + \left(\left(q_r + q_s + \ldots. q_{p_{\max}}\right) - H - \left(q_x + q_y + \ldots. q_{pw_{\max}-1}\right)\right)k_{cb}$$

(6.58)

6.6 Discussion of simulation results for the forced damped vibratory response of the original *Blade*

The computational procedures discussed in Appendix C were used to simulate the forced damped vibration of the original *Blade*. The results of this study are discussed in this section.

The time-history plots, Figures 6.11a & 6.11b, show the modal blade and wand displacements at the blade-wand contact height for the case where the blade is subject to the constant acceleration ground motion *(i.e. constant acceleration of motor speed)* characteristics illustrated by the dotted line in Figure C2.

Figure 6.11a shows the contributions from the first four blade bending modes as the ground motion frequency accelerates up to match the third natural bending frequency for the blade. From inspection of Figure 6.11a the dominant contribution to the total blade shape is from the third natural blade bending frequency. It can be noted that there is also a significant contribution to the total blade shape from the first blade bending mode, and that the all the other modal displacements are relatively small.

Figure 6.11b shows the results of the simulation as the clamp frequency accelerates up to the second natural bending frequency for blade *(Lye's single harmonic)* and then progressing through the *Blade* performance to the third bending mode *(Lye's double harmonic)*.

Figures 6.11a & 6.11b show that when the clamp frequency coincides with one of the blade bending modes, the dominant contribution to the total blade shape corresponds to the blade bending mode that matches the ground motion frequency. Figures 6.11a & 6.11b show that for the case where the blade is vibrating either the second or third natural bending frequencies, there is a significant contribution to the total blade shape by the first blade bending mode.

The results of the movie *(from the mathematical simulation)* were used to verify the mathematical model. The blade motion in the movie was found to be good likeness to the blade motion observed in the original sculpture. Figure 6.12 shows a sample frame from the movie. The swinging phenomenon was therefore successfully modelled using a superposition of all of the blade bending modes. The swinging phenomenon is attributed to the vibration of the first bending mode.

Figure 6.13 shows the mathematical simulation of the time-history response for the displacement of the original *Blade.* In this case the blade and wand were separated and no interaction occurred. From inspection of Figure 6.13, the abrupt end points of the acceleration periods initiate an impulse causing a disturbance to the first blade bending mode.

From a comparison of the results of Figures 6.11 & 6.13 it is clear that the wand interaction has a significant influence on the behavior of the blade. The most obvious effect is that the wand interaction causes an increase in disturbance to the first blade bending frequency when the base motion frequency matches the third blade bending frequency. This behavior is consistent with observations of the original sculpture. A second observation is that the wand interaction causes the vibrating blade shape to be asymmetric about the vertical axis. This characteristic was observed in the performance of the original sculpture.

The mathematical simulation for the wand, while predicting a similar shape to observations of the original sculpture, predicted a higher amplitude of vibration. The predicted maximum amplitude of vibration for the model scale wand, as shown in Figure 6.11b, was a factor of 2 greater than the amplitude measured in experimental observations. This discrepancy between predicted and experimental results is believed to be due to the assumptions made in the calculating the damping constant for the surface of the cork ball.

Damping assumptions in the mathematical model neglected energy dissipated due to micro slip at the cork ball – blade contact interface. In this case the energy loss is expected to be proportional to the cube of the amplitude of the contact force [Johnson (1985)]. Therefore the model clearly underestimates the part of the damping that results from micro slip at the contact interface. This underestimation is compounded by the fact that the maximum force on the surface of the cork ball predicted in the bouncing ball test, Equation (6.44), is approximately 30% (497/1507) of that predicted in the mathematical model for the original *Blade* using Equation (6.55).

Damping assumptions in the mathematical model also neglected energy dissipated by the surface macro sliding of the cork ball on the surface of the blade.

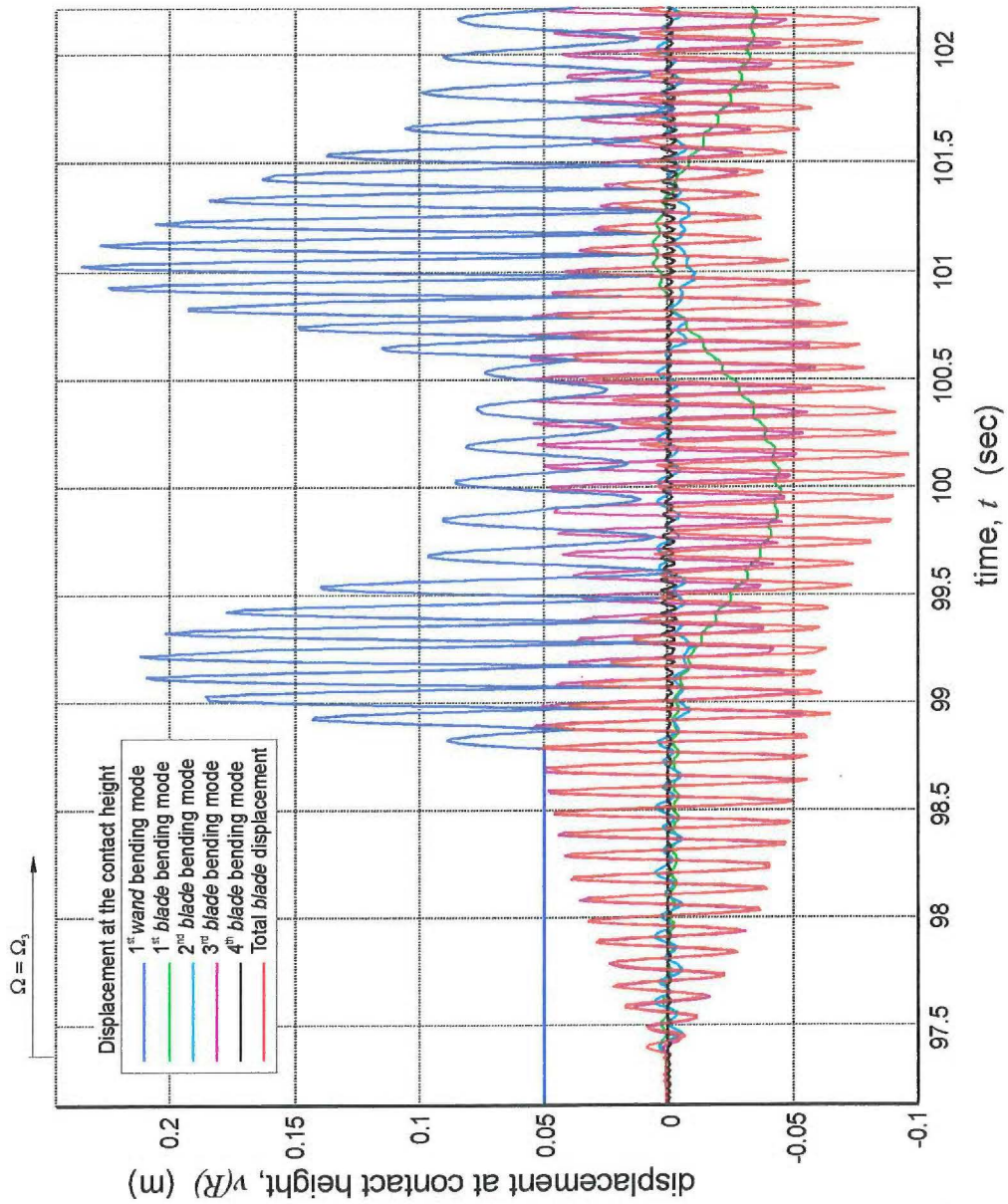

Figure 6.11a *Time history plot for the forced damped vibratory response of the original Blade showing the contributions to the total blade displacement from each of the modes*

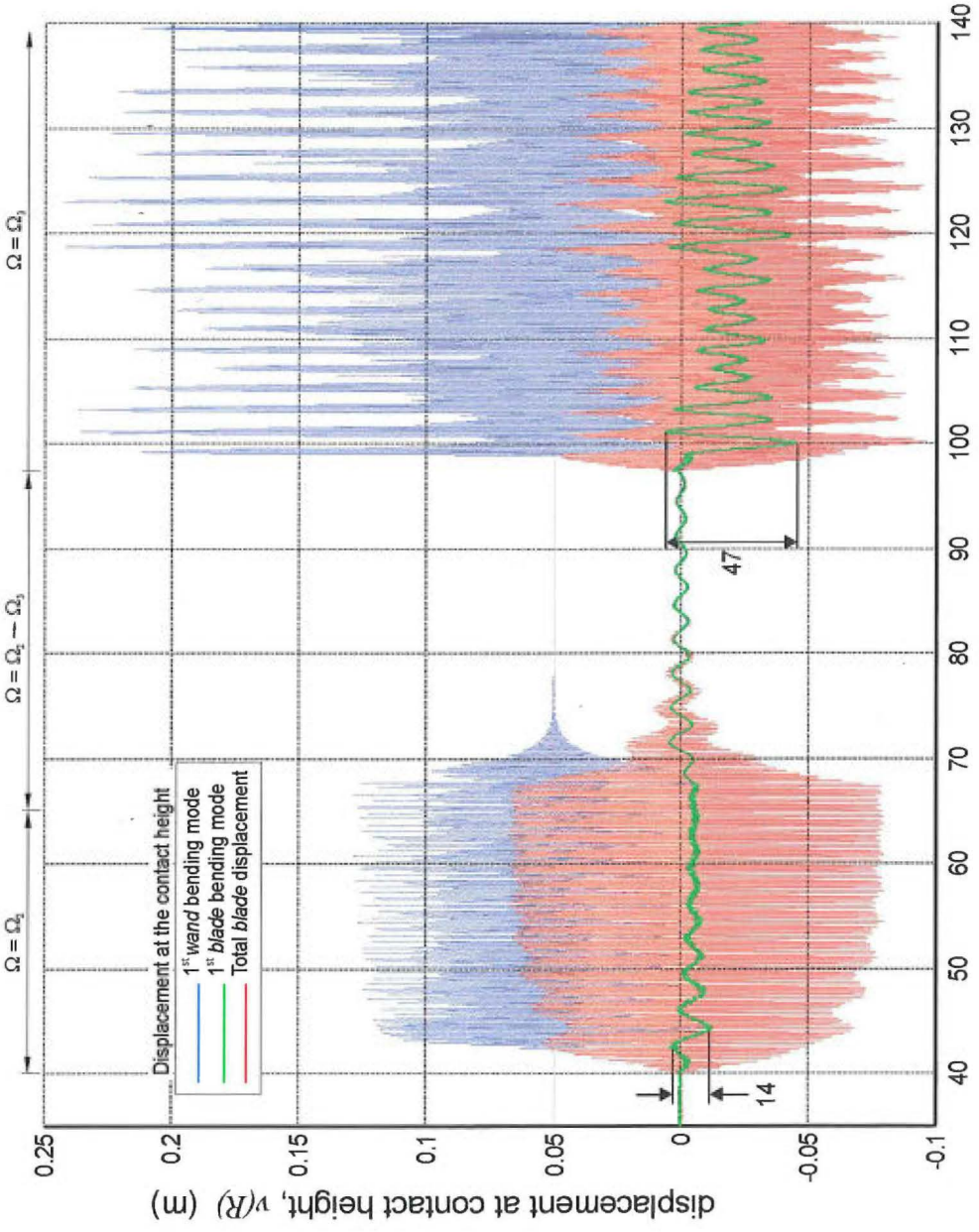

Figure 6.11b *Time history plot for the forced damped vibratory response of the original Blade*

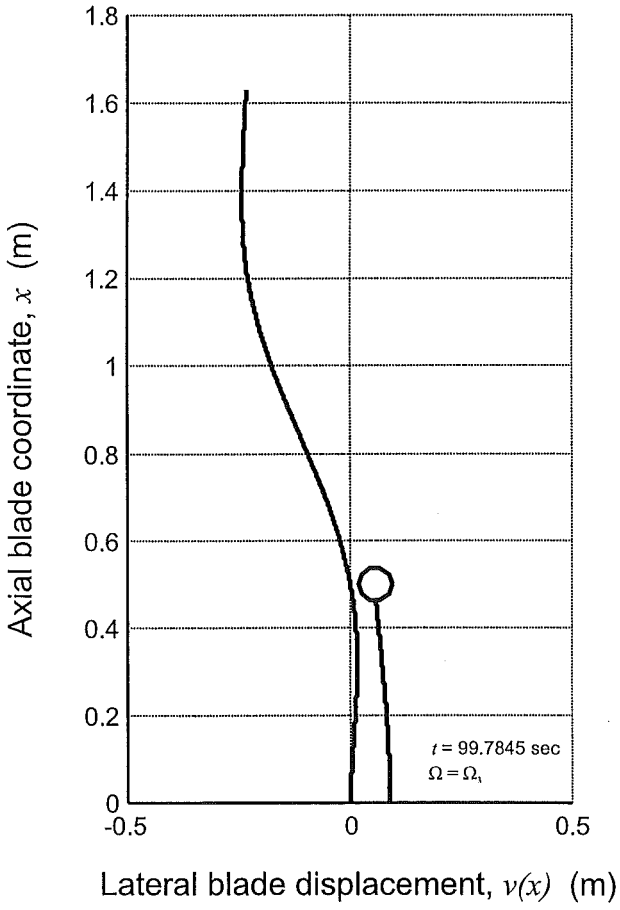

Figure 6.12 *Sample frame from the MATLAB movie*

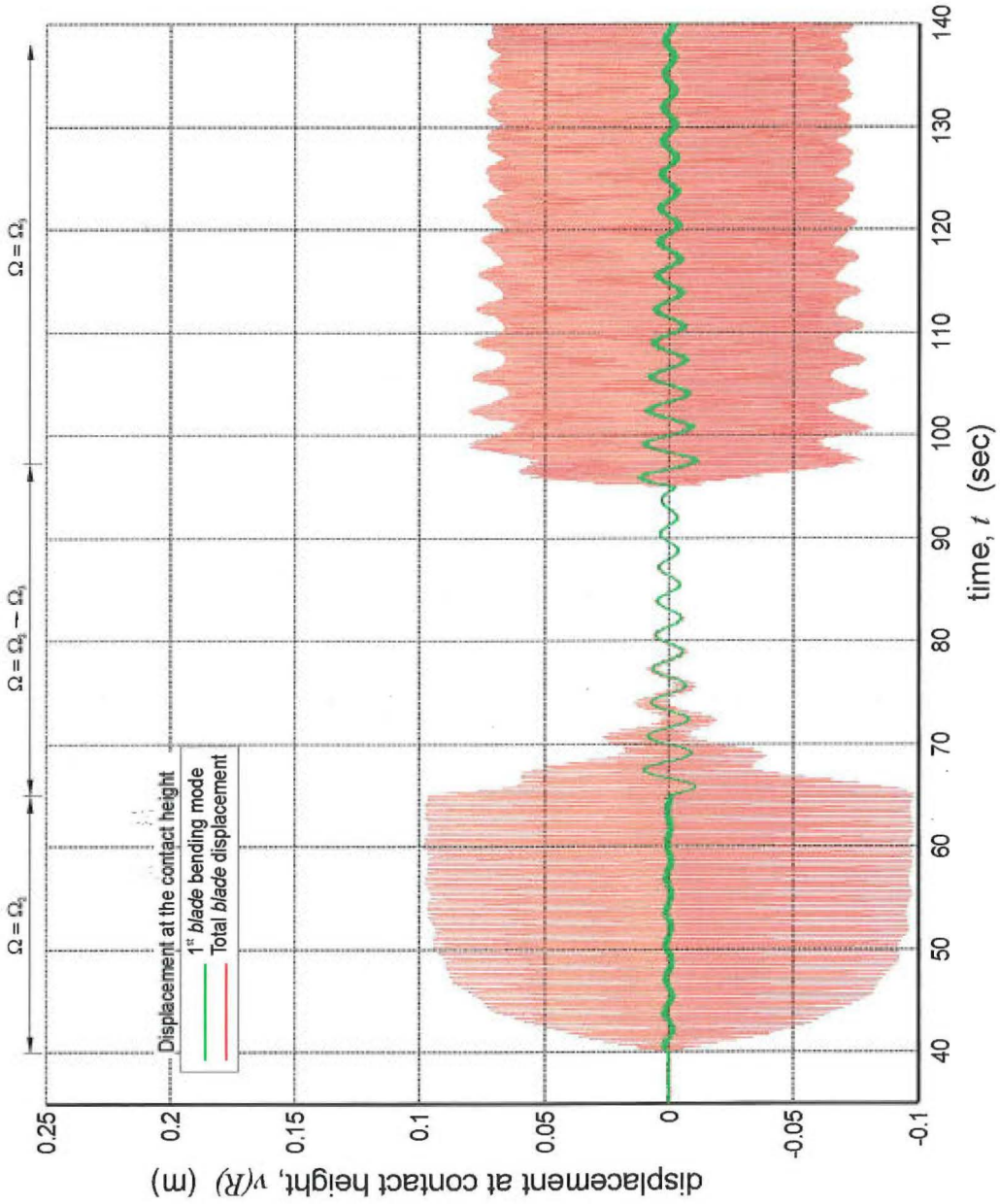

Figure 6.13 *Time history plot for the forced damped vibratory response of the original Blade for the case where no wand interaction occurs*

6.7 Discussion of results for the prediction of the forced damped vibratory response of the scaled *Blade*

In Section 6.6 blade/wand interaction was identified as a significant contributor to the swinging phenomenon. Considering a simple impact test, such as that discussed in Section 3.2.2.2, a lower mass titanium alloy blade material would be expected to be more prone to the swinging phenomenon than would a heavier steel blade.

From inspection of Figures 6.11b and 6.13 it would be expected that a wand with a lower mass cork ball and a more flexible stem would reduce the magnitude of the contact energy thus reducing the energy transmission to excite the first blade mode. Experimental investigations were conducted with the original *Blade* and confirmed that using a wand with a lower mass cork ball and a more flexible wand stem significantly reduced the swinging phenomenon.

After discussion regarding the aesthetic requirements for the work [Webb (Jan 1996 – Dec 1998)], a minimum allowable diameter for the cork ball of 140mm was established. Specifying the same wand materials as used on the original *Blade (i.e. a cork ball and a steel stem)* the wand stem thickness was reduced until the maximum amplitude of the first blade bending mode was less than the relative amplitude in the simulation of the original work. This determined the final specification for the wand, namely

Stem: 7mm diameter 4140 low alloy steel *(hardened and tempered)* 430mm long

Ball: 140mm diameter solid cork sphere with nylon threaded insert *(mass = 650g)*

Figure 6.14 shows the prediction for the forced damped vibratory response of the scaled *Blade* using the final wand specification. From Figure 6.14, the relative disturbance to the first blade mode when the base motion frequency corresponds with the third blade bending frequency $(\Omega = \Omega_3)$ is less than that for the simulation of the original *Blade* in Figure 6.11b.

A further improvement was predicted for the forced damped vibratory response of the scaled *Blade* when a cycloidal function is used to increase the velocity of the base motion between the modes. This uses the *'s-curve characteristic function'* illustrated in Figure C2. From the time-history plot for the forced damped response, Figure 6.15 shows 20 seconds of the results.

The steady state condition observed in Figure 6.15 may be unsatisfactory from the artist's perspective if the work is perceived to be too uniform and regular in motion. However from a design perspective it is desirable to have the ability to achieve a similar response to that predicted in Figure 6.15, this is because the scaled work is to operate outdoors and will be subject to other influences such as wind loads. If the work is found to be too stable and regular in motion, the control system needs to be able to introduce transients into the base motion.

Because the crank length r_c is small compared with the connecting rod length l_c $(r_c/l_c = 11/410)$, simple harmonic motion (SHM) has been assumed. A preliminary investigation considering the exact expression for SHM [Morrison and Crossland (1971)] showed that displacement, velocity, and acceleration errors are in this case small *(of the order 0.7, 1.3, and 2.5% respectively).* The exact acceleration equation from Morrison and Crossland (1971) indicates a force at twice the crankshaft speed of magnitude r_c/l_c relative to the force at crank frequency. Hence at the third bending frequency there will be a small amount of energy causing the excitation of the fourth bending frequency. An extension to the current study would be to include the exact SHM equation in the mathematical model.

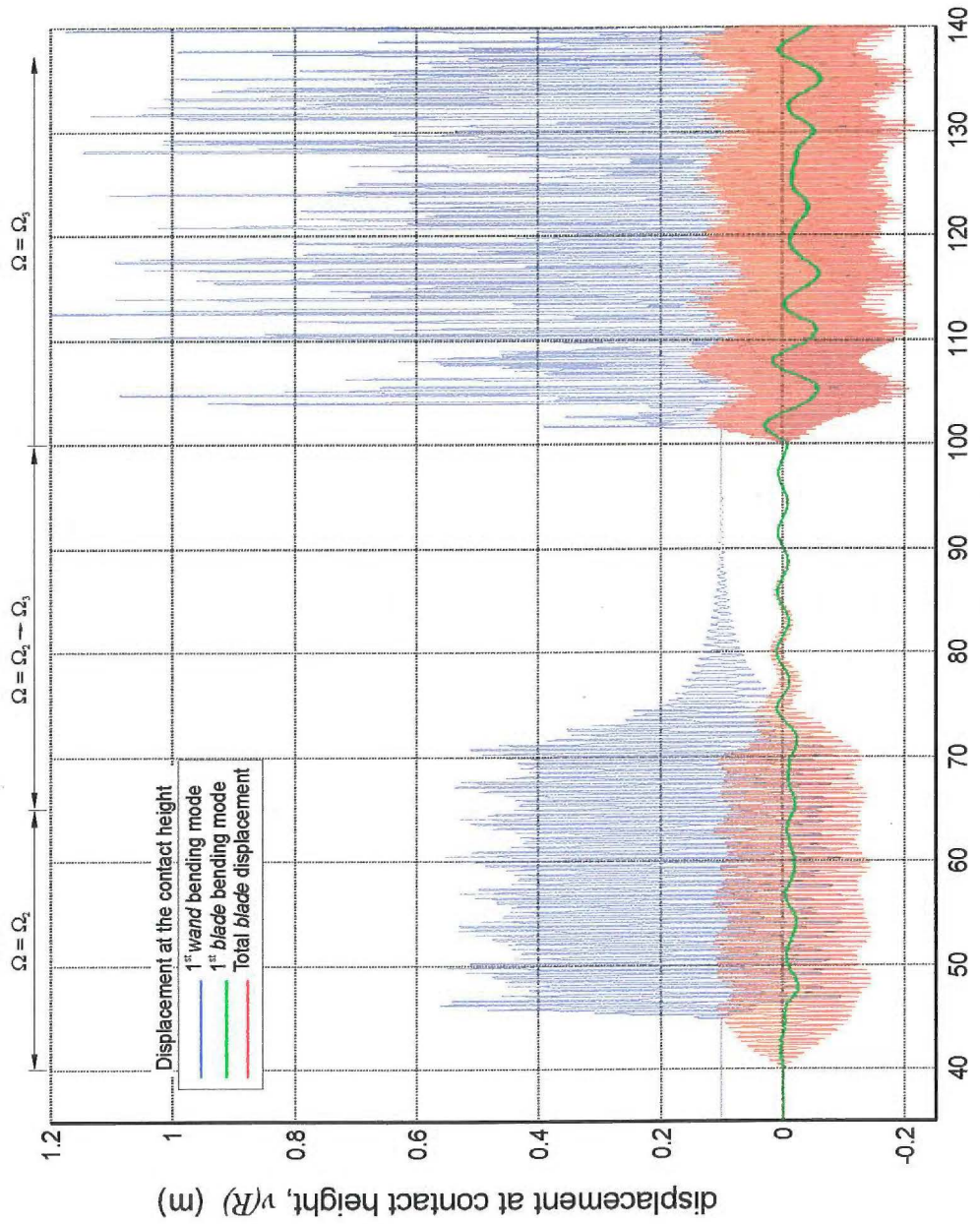

Figure 6.14 *Prediction of the forced damped vibratory response of the scaled Blade (using a constant clamp frequency acceleration rate between the modes)*

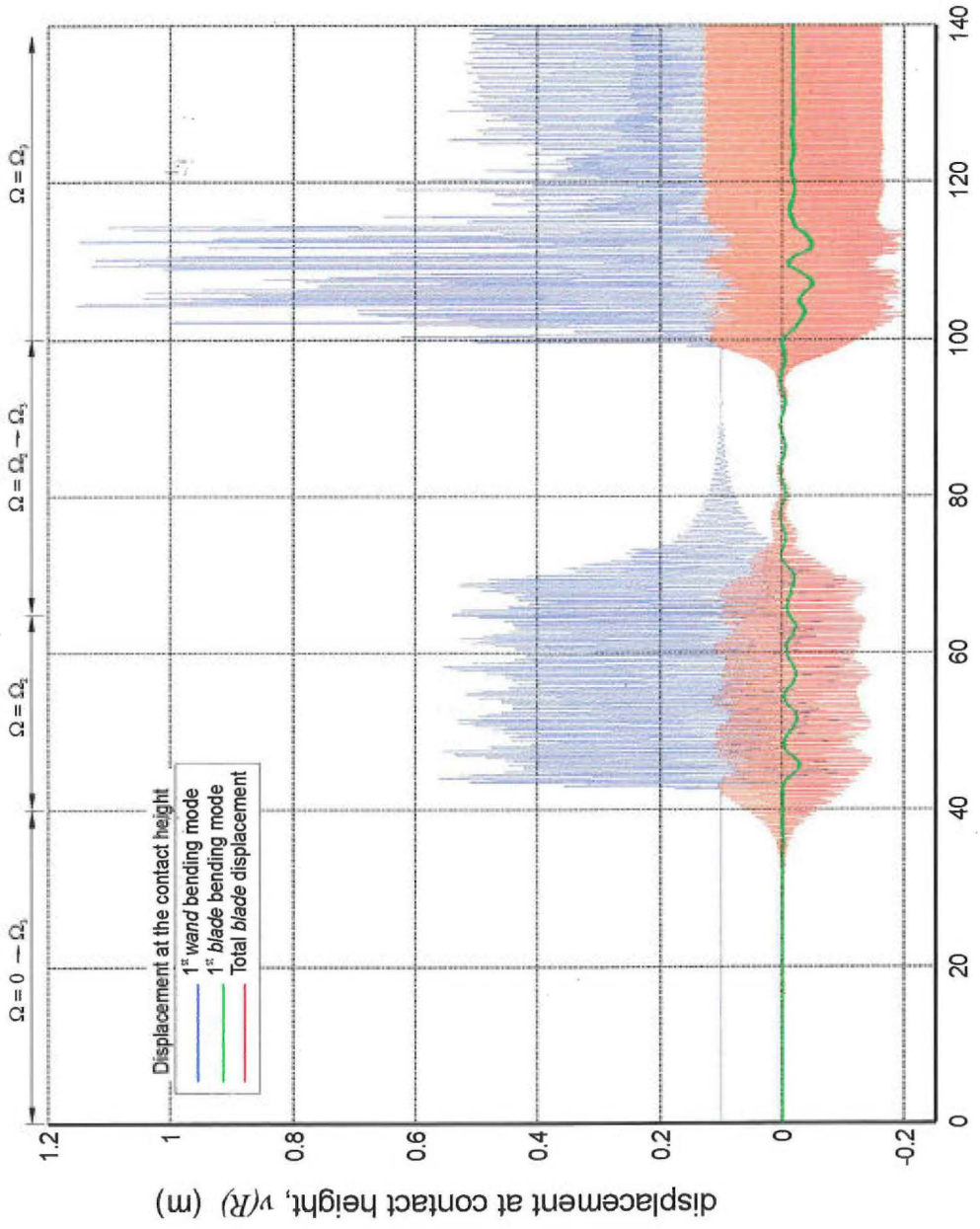

Figure 6.15 *Prediction of the forced damped vibratory response of the scaled Blade (using a cycloidal function for increasing clamp frequency between the modes)*

6.8 Conclusion

The results of this analysis show that the swinging phenomenon, when the base motion frequency corresponds with the third natural blade bending frequency, is caused by a excitation of the first natural blade bending frequency.

The significant factors affecting the excitation of the first mode blade bending frequency, and thus to promoting the swinging phenomenon, are the interaction between the blade and the wand and impulses due to abrupt changes in ground motion frequency.

For the design of the scaled Blade, a wand configuration has been specified that is expected to reduce the swinging phenomenon in the performance of the scaled Blade. An s-curve base motion acceleration characteristic has been identified as a desirable attribute for the control system of the scaled sculpture and is expected to reduce the swinging phenomenon. The drive system for the scaled work needs to have sufficient power and speed control to maintain simple harmonic ground motion. In the event that the blade becomes too stable, the control system needs to be able to introduce a number of small impulses into the ground motion and thus introduce variability in the performance, as required by the artist.

7

Design of the drive mechanism and the support structure for Blade

7.1 Introduction

The mechanism for the original *Blade,* shown schematically in Figure 1.4, incorporates slip rings that transmit electrical energy and control signals to the blade base motion drive. The performance and reliability of the slip rings are regarded as unsatisfactory.

The mathematical model identified design features that could be implemented to reduce significantly the undesirable blade swinging phenomenon.

> ***The objective of this chapter is to obtain a new improved concept for the drive mechanism eliminating problems associated with the slip rings used on the original sculpture. The design will include the embodiment for a suitable mechanism and support structure and will include features from the model that are expected to reduce the blade swinging phenomenon. The manufacturing information will be specified for the complete structure.***

The solution for the mechanism and support structure will be sought by applying a systematic approach adopted from Pahl and Beitz (1996) and Hales (1993).

7.2 Task clarification

This section defines the problem for which solutions for the drive mechanism and support structure will be established. To this end, the following problem statement was formulated to identify more clearly the design task.

> ***Problem statement:*** *To support the blade and the wand as vertical cantilever beams when at rest. To apply a base motion at the fixed end of the blade that achieves Len Lye's intended vibratory form for the blade and the intended interaction between the blade and the wand. The blade and the wand are to rotate about the vertical blade axis. The mechanism is to operate unassisted and concealed within a cylindrical cover.*

7.2.1 The design requirement specification

The design requirement specification in Table 3.1 listed the artist's *aesthetic* and *acoustic* requirements for the sculpture. Other requirements for the work may considered under the headings *functional, safety, quality, manufacturing, timing, economic, ergonomic, ecological,* and *life cycle* [Hales (1993)]. Table 7.1 lists these other requirements. The full design requirement specification, against which the proposed solutions for *Blade* will be evaluated, comprises Tables 3.1 & 7.1.

Table 7.1 *Blade design requirement specification (NB. aesthetic and acoustic requirements listed in Table 3.1)*

Demand Wish	***Blade design requirement specification (requirements under each heading are in order of importance)***
	Functional requirements for the mechanism
D	the mechanism must fit within the cylindrical space constraint of diameter $s \times 0.6\ l_o$ & and height $s \times 0.375\ l_o$ *(NB. if* $s = 2$ *then diameter* $\approx 2m$ *and height* $\approx 1.25m$*)*
D	the linear slide must be capable of reciprocating at the single and double harmonic frequencies
D	the blade clamp is to move in a linear reciprocating motion of $+/- 5.588 \times s$ millimetres in the horizontal plane.
D	the mechanical drive and the support structure to have sufficient power, strength, and rigidity to react against bending moments and shear forces due to vibration of the *Blade.*
D	the fixed end of the blade and the wand must be such that they stand vertical when at rest
D	the blade and the wand are to rotate smoothly at a nominal speed of 1 rpm about the vertical blade axis
D	adjustment of the nominal wand/blade separation distance $H > +/- s \times 10mm.$
W	adjustment of the maximum blade base motion amplitude $\Delta > +/- s \times 2.5mm$

Table 7.1 *(cont.)*

W	the reciprocating blade clamp movement to follow simple harmonic motion
W	the clamp to have adjustment for levelling the blade > +/-. 2 degrees *(may only be required if the blade has an initial curvature or set)*
W	a geometric stress concentration factor at the fixed end of the blade $k_t < 1.2$
Functional requirements for the control system	
D	accurate speed control for the shuttle drive motor *(for a double size Blade < +/- 2rpm & < +/- 3rpm at the 'single' and 'double harmonic' frequencies respectfully)*
D	control system must be capable of storing at least four set speeds and eight ramped speed changes for the shuttle drive
D	control system to allow an *'s–curve speed vs. time function'* when increasing/decreasing shuttle motor speed
D	variable speed control setting for the base rotation motor
D	include an indicator light to show the state of the *program (e.g. green for running and red for finished)*
W	the power supply and electronic control signals to be transmitted to the rotating mechanism without using slip rings
W	control system to have a very large capacity for control parameter settings during a performance
W	include a speed transducer on shuttle drive for a positive speed feedback signal

Table 7.1 *(cont.)*

W	sculpture to run from a single phase power supply
W	control system with the ability to store two preset programs *(i.e. for one full and one budget performance)*
	Safety requirements
D	include an emergency stop button to isolate power supply in the event of an emergency *(to be positioned at a clearly identified location)*
D	maintain a minimum safe spectator distance $> 2l$
	Quality requirements
D	design life for mechanism components > 10 *years*
D	wiring for electric machines to comply with NZAS 3000
D	all manufactured components to be inspected to comply with tolerances specified on manufacturing drawings
D	sculpture to be fully tested in working environment before release to end user
	Manufacturing requirements
D	mechanism to be bolted to heavy foundation *(mass* $>5t$ *when* $s = 2$*)*
W	only use manufacturing methods that allow all components to be manufactured in Mechanical Workshop at University of Canterbury.
W	ensure that all components can be assembled/disassembled using simple hand tools

Table 7.1 *(cont.)*

Ergonomic requirements	
D	allow independent on-site adjustment of control system variables
D	*'start'* and *'stop'* performance using remote control
D	display shuttle drive motor speed
D	user interface to clearly identify key performance control functions *(start / stop / program number.)*
W	allow removal of the blade without disassembly of any mechanism components
W	allow adjustment of control system variables while program is running *(helpful for tuning set frequencies)*
W	control system to be PC compatible and programmable using industry standard software
W	control system to incorporate timers to record *'total running time'* and *'total time spent operating at the double harmonic frequency'*
W	display program cycle parameters
W	check that operation of the sculpture does not cause discomfort to viewers

Table 7.1 *(cont.)*

Timing requirements	
D	allow a minimum of 1 week for in-house tests close to Mechanical Workshop before commissioning at a public venue.
D	coordinate manufacture with planning schedule at Mechanical Workshop
W	sculpture to be ready for commissioning at *'Sculpture in the Gardens'* exhibition January 1998
Economic requirements	
W	total project materials cost less than $36000
W	overall mass of the mechanism < *500kg* for a double size *Blade (this work may be air freighted to overseas exhibitions)*
Ecological requirements	
D	provide adequate protection to mechanism and electrical equipment from the outside environment *(salt air, dirt, grit, water, and temperature extremes)*
D	include fuse-able links and/or circuit breakers to protect control system from power supply surges
Life-cycle requirements	
D	service after each interval of 50 performances *(check for bearing noise, environmental damage, and loose components)*
W	obtain second use from blade material by turning end for end after the first failure

7.2.2 System structures for the Blade design

The design requirement specifications listed in Tables 3.1 & 7.1 for the drive mechanism and the support structure may be considered under the 5 sub-systems given in the organisation chart, Figure 7.1

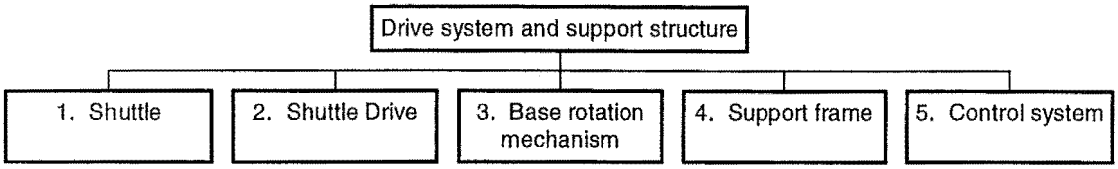

Figure 7.1 *Sub-systems for the drive system and support structure design*

7.3 Conceptual design of the drive mechanism

The purpose of this section is to establish a new concept for the drive mechanism that eliminates the need for slip rings. After considering the sub-systems in Figure 7.1 the first three sub-systems *(namely the shuttle, shuttle drive, and the base rotation mechanism)* are the critical sub-systems for which a concept will be sought. A simple support frame will be constructed from standard steel sections and hot dip galvanised. A preliminary investigation has revealed that for the case where three phase electric machines are employed, the control system can be implemented for a reasonable cost using a programmable logic controller *(PLC)* and variable frequency drives.

The approach taken is to divide each of the first three sub-systems into sub-functions and to build a morphological matrix using schematic diagrams of the solution principles considered. The solution principles for each sub-function in the morphological matrix are selected using a concept selection chart adopted from Pahl and Beitz (1996).

7.3.1 The shuttle

The function of the shuttle mechanism is to hold the fixed end of the blade, to allow for the linear reciprocating motion, and to provide an attachment point for the drive system.

The working principles considered in the development of the shuttle mechanism concept are illustrated in the morphological matrix, Figure 7.2.

The original solution for the blade support function *(solution A1)* was found to be too heavy for the scaled work. A fabricated clamp *(solution A1)* would be much lighter, however the clamp plates would be prone to distortion on welding. A clamp machined from solid plate was considered to yield a more desirable result. The excess clamp material is removed using a oxygen-acetylene profile cutting machine and the clamp is finished using a milling machine.

The preferred concept for the reciprocating mechanism support function *(row C Figure 7.2)* was to use linear motion ball bearings. Linear motion track bearings were considered *(solution B2)*, however successful attachment and location of other system components was problematic. The linear bearings were fitted in independent pedestal housings *(solution C2)*, as opposed to fitting the bearings inside the clamp *(solution C1)*, thus reducing the normal bearing reactions due to the blade reactions and bending moments. Preferably hollow linear bearing shafts should be used to reduce the reciprocating shuttles mass.

An anchor is threaded into the end of each of the linear bearing shafts and a drive bracket attached to them. The drive bracket provides the attachment point for the shuttle drive system.

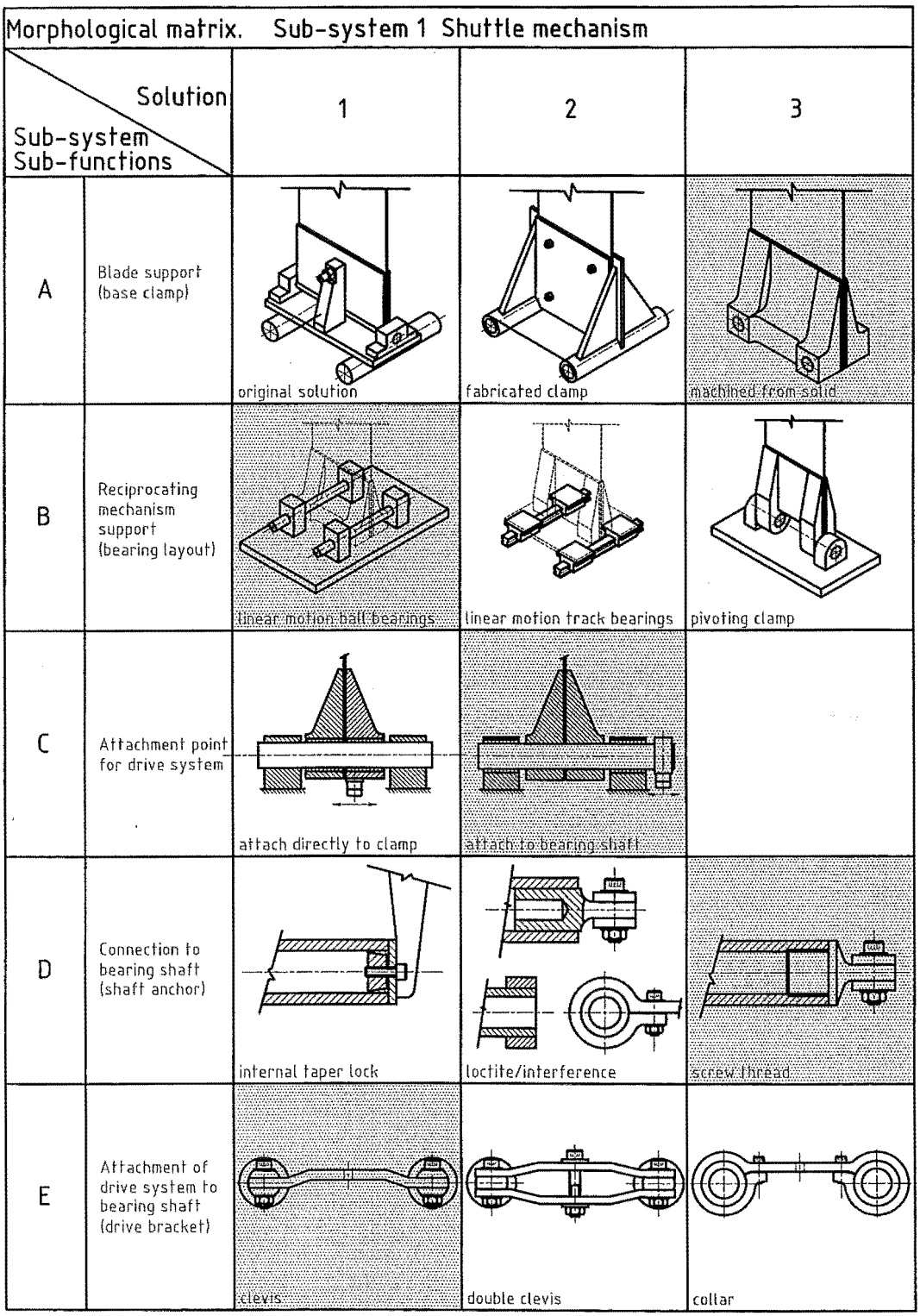

Figure 7.2 *Solution forms considered for the shuttle mechanism*

7.3.2 The shuttle drive system

The function of the shuttle drive system is to impress a linear reciprocating motion at the drive bracket attachment point.

The working principles considered in the development of the shuttle mechanism concept are illustrated in the morphological matrix, Figure 7.3.

The three configurations considered for the reciprocating mechanism were a crank, a barrel cam, and a linear actuator. The barrel cam had the advantage of being able to provide true *'simple harmonic shuttle motion'* however the concept was very complex and a simple cantilevered crank mechanism selected. The crank mechanism is connected to the drive bracket using a connecting rod. The connecting rod has self-aligning rolling element bearings.

A simple 'tee' slot concept *(solution G1)* was considered for providing adjustment for crank offset however the radial connecting rod forces were too high and a stronger *'bolted cam crank'* principle *(solution H1)* was adopted. For subsequent mechanisms and after rigorous testing a cheaper solid shaft arrangement *(solution G2)* may be feasible.

For the drive attachment sub-function *(sub-function J)* a direct drive arrangement *(solution J1)* appeared very elegant however the radial shaft load from the connecting rod required an over-sized gearbox. The central drive shaft concept *(solution J2)* can be designed to accommodate the high radial shaft load and was considered a good compromise.

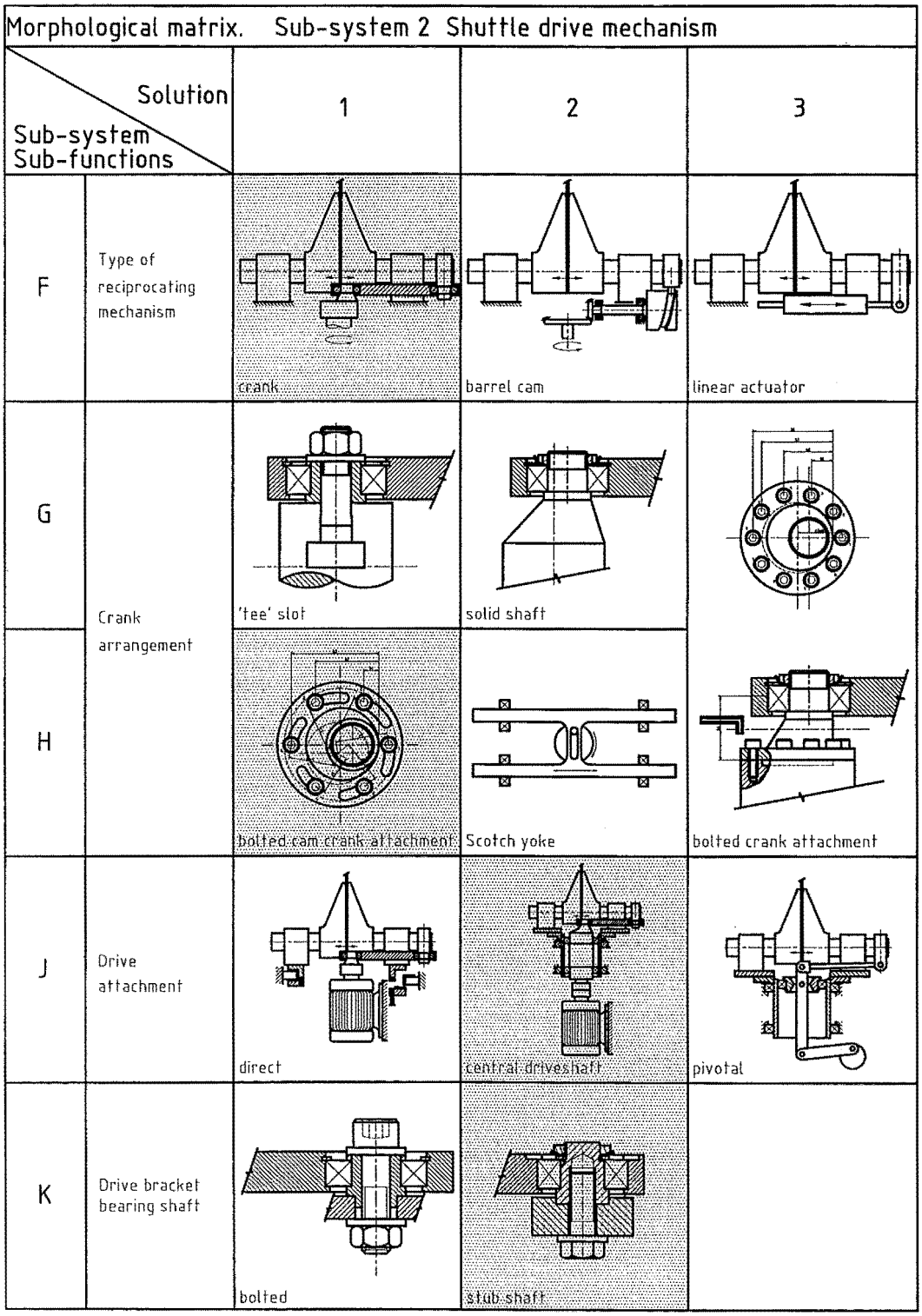

Figure 7.3 *Solution forms considered for shuttle drive mechanism*

7.3.3 The base rotation mechanism

The function of the base rotation mechanism is to provide a rotatary motion tc the blade and the wand about the vertical blade axis.

The working principles considered in the development of the base rotation mechanism are illustrated in the morphological matrix, Figure 7.4.

For the base rotation drive sub-function a worm drive *solution (L1 Figure 7.4)* was considered. The worm drive provides good speed reduction and may be designed to resists out-of-balance rotation forces. Solution L1 is expected to be relatively expensive and difficult to fit within the spatial constraints imposed by the other preferred combinations of solution principles. A simple chain or belt drive was selected.

A flat table is used as a mounting surface for the linear motion ball bearings. Plain bearings, *(solution M1),* provide a direct load path from the vibrating blade through to the support structure. A variation on the plain bearing solution is to use a slewing ring of the type commonly used for truck turn-tables, however neither of these solutions allow easy adjustment for wear. The selected concept for the table support sub-function is a set of adjustable rolling element bearings *(e.g. taper roller or angular contact bearings).*

The bearing table trunnion joint is subjected to high bending moments; also the connection method has significant implications for the manufacturing, assembly, and geometric arrangement of the base rotation and table support components. The welded connection method *(solution N2)* was selected for best strength and best sub-system component arrangement.

A friction damper was considered necessary to counteract out-of-balance forces. Combinations of base rotation drive and table support sub-functions *(row P of Figure 7.4)* led to the selection of a brake disc with mechanical spring actuated friction pads.

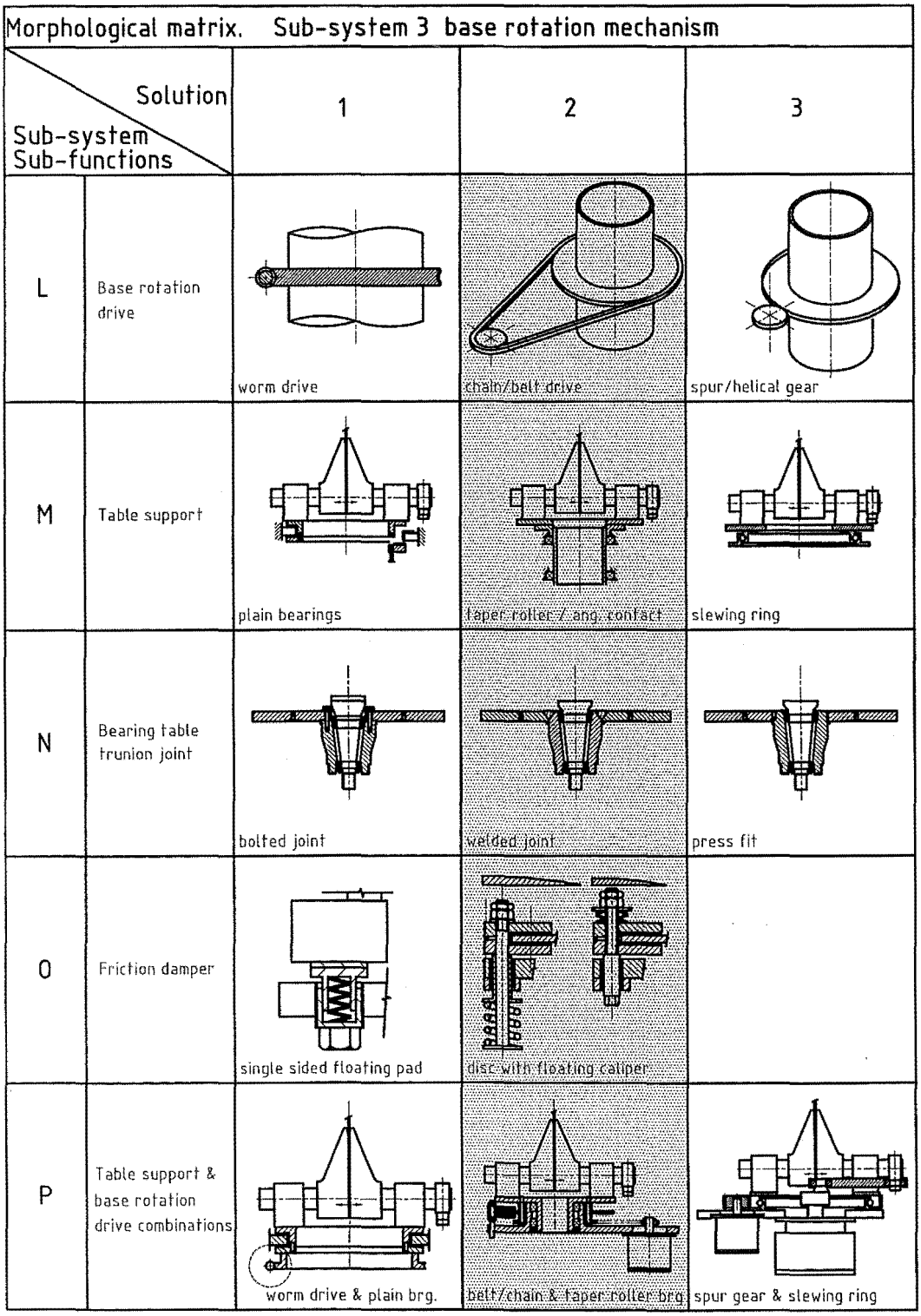

Figure 7.4 *Solution forms considered for the base rotation drive mechanism*

7.3.4 The final concept selected for the blade drive mechanism

The attributes of each of the solutions considered for the sub-system sub-functions shown schematically in Figures 7.2, 7.3, and 7.4 were evaluated in terms of the design requirement specification Tables 3.1 & 7.1.

The concept selection process is summarised by the concept selection charts, figures D1, D2, & D3, where the requirement categories (*functional, safety, quality, manufacturing, timing, Economic, Ergonomic, Ecological, aesthetic,* and *life-cycle*) were scored in terms of meeting the design requirement specification. Two further categories were included in the concept selection process: *'can it be made to work'* and *'information' (meaning is the relevant expertise and experience available).*

The selected concepts for each sub-system are assembled to give the working concept for the drive mechanism shown in Figure 7.5. The drive mechanism concept was reviewed using a conceptual design work sheet, Figure D4, from Hales (1993). The conceptual design work sheet indicates good confidence level for mechanism function and it was decided to proceed with the embodiment design where further development was expected to improve the arrangement in terms of meeting manufacturing and economic requirements.

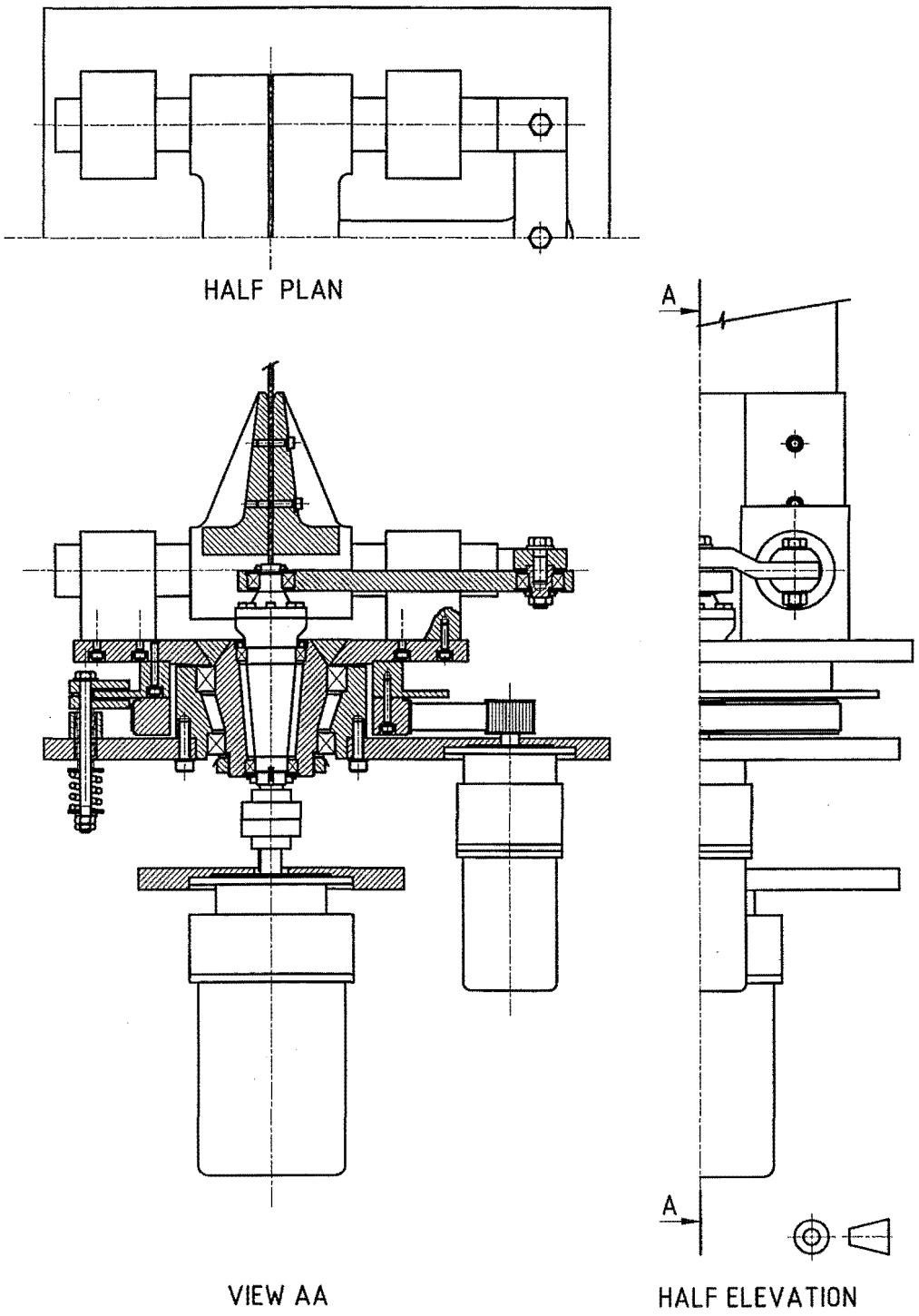

Figure 7.5 *Principal concept for the Blade drive mechanism and support structure using a combination of sub-function concepts from Figures 7.2, 7.3, and 7.4*

7.4 Embodiment for the drive mechanism and the support structure

The purpose of this section is to present the proposed solution developed for the blade drive mechanism and the support structure.

The mechanism and the support structure are designed to react against bending moments and shear forces due to the forced vibration of a steel blade, as described in Figure 3.2 *(worst case scenario)*

7.4.1 The shuttle mechanism

Objectives in the development of the shuttle mechanism, shown in Figure 7.6, were to minimise the reciprocating mass and to accommodate the central drive shaft and crank mechanism.

The blade is fixed between two half clamps and bolted together using eight M16 high tensile cap screws. The clamp is attached to two shafts using a locational transition fit and a spilt sleeve. This is a friction joint design where the securing force is achieved by tightening twelve M14 clamp anchor screws *(tightened to a torque of 52Nm).* The central clamp anchor screw on each side of each clamp half may be removed and replaced with a M16 jacking screw to release the friction joint. This arrangement allows the blade to be fitted or removed with minimal disturbance to the other mechanism components.

The clamp halves are tapered giving a relatively uniform stress distribution and include ribs for bending and torsional stiffness. The maximum clamp deflection was checked for the worst-case loads and the stress levels predict an infinite fatigue life

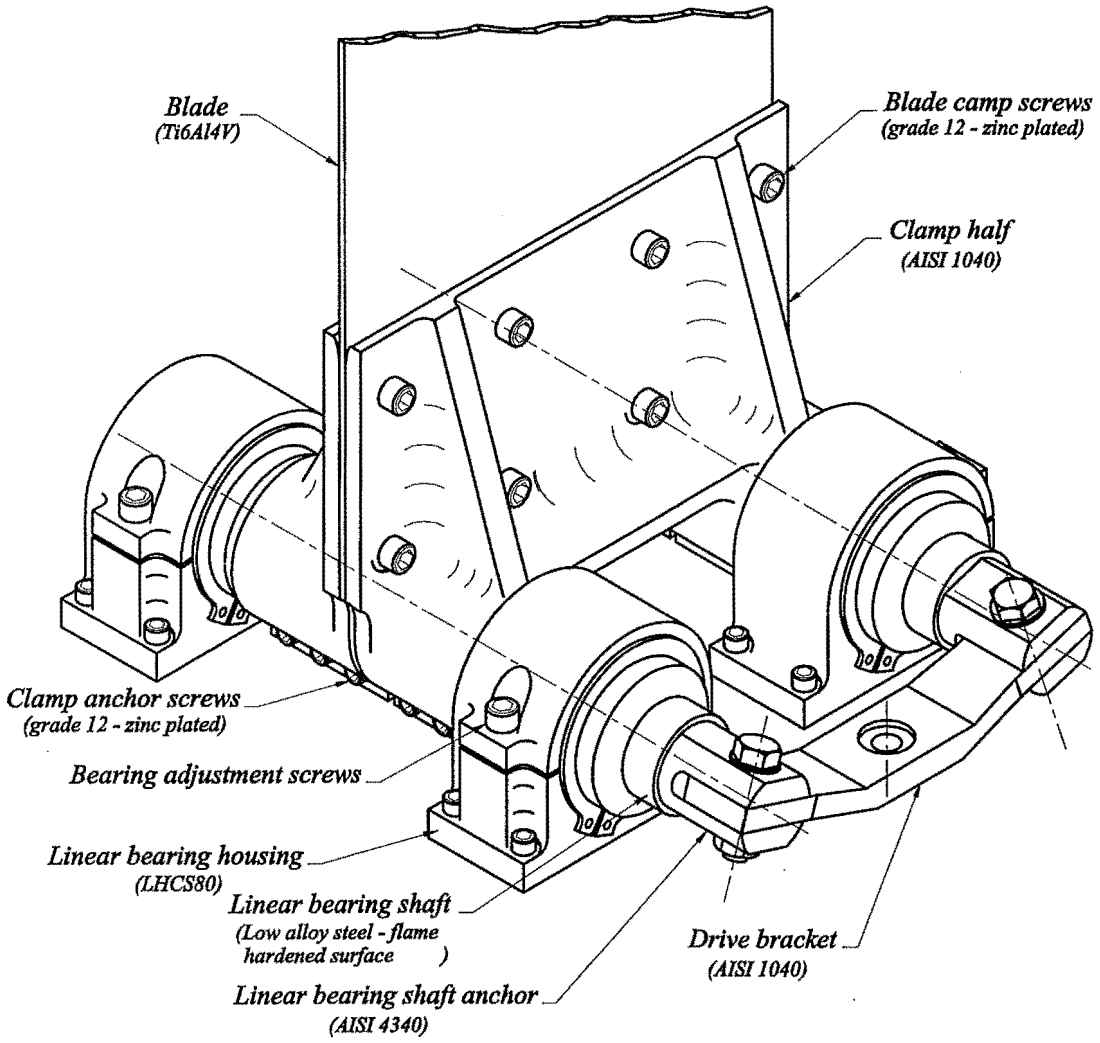

Figure 7.6 *Embodiment for the shuttle mechanism*

The clamp exit has a parabolic shape to minimise the geometric stress concentration factor experienced by the blade. The clamp exit may be modified to incorporate a levelling function should the blade have an initial curvature. This modification is shown in Figure 7.7

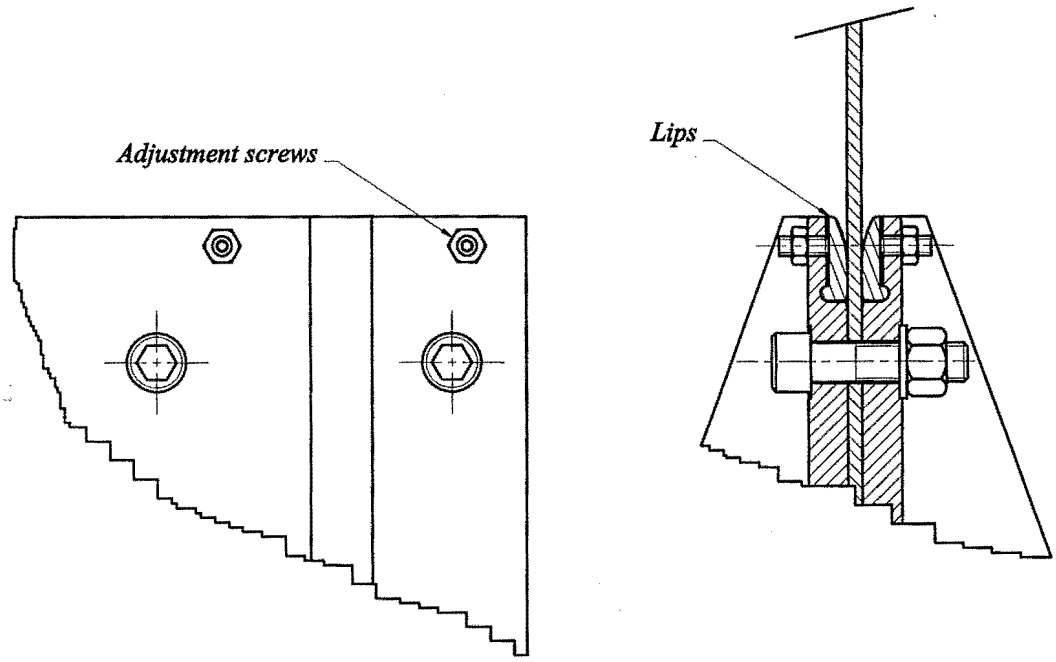

Figure 7.7 *Provision for level adjustment at the clamp exit*

The linear sliding function is provided by four linear motion ball bearings *(LBAS 80-2LS [SKF (b)])* and is designed for an expected working life of 20 years *(assumes one performance per day).* The linear motion ball bearings are fixed in cast aluminium housings *(LHCS80 [SKF (b)])* and have adjustment to accommodate wear and misalignment.

Hardened hollow bearing shafts made from low alloy steel are specified for good wear properties and a low reciprocating mass.

Two linear bearing shaft anchors and a drive bracket provide the attachment point for the drive system. The linear bearing shaft anchors are made from AISI 4340 round bar and are retained in the ends of the bearing shafts using a threaded joint and thread locking compound *(Loctite Studloc).*

The drive bracket concept shown in Figure 7.5 was simplified *(number of bends reduced from four to two)* and the connecting rod positioned at the same level as the bearing shaft centres. The drive bracket is made from AISI 1040 steel plate and is attached to the bearing shaft anchors using a clevis friction joint design, fastened together using two M20 x 1.5 grade 8.8 bolts *(tightened to a torque of 160 Nm).*

The drive bracket stub shaft is made from AISI 4340 alloy steel and fastened to the drive bracket using an M20 x 1.5 grade 8.8 bolt *(tightened to a torque of 110 Nm).*

The bearing shafts, shaft anchors, and drive bracket are designed for an infinite working life.

7.4.2 The shuttle drive system

Objectives in the development of the shuttle drive system were to provide a base reciprocation motion that is close to simple harmonic motion. Figure 7.8 shows the developed solution for the shuttle drive system.

A 3 kW 4 pole induction motor powers the shuttle drive. Speed reduction is achieved using a flange mounted helical gearbox *(GMF2D 3.27:1 [Renold Gears]).* A gear coupling provides a torsionally rigid connection from the gearbox output shaft to the drive shaft, allows the gearbox to be assembled blindly into position and accommodates parallel and angular misalignment.

The central drive shaft, machined from AISI 4340 alloy steel, is located in two taper roller bearings *(32915 and 32010X [SKF (a)]).* Taper roller bearings were used because they have a relatively high load carrying capacity, small cross-section size, and allow some adjustment for wear by tightening a locking nut *(in this case the lock-nut pre-load torque is 35 N-m).*

A general-purpose shaft seal *(CR 31530 [CR Seals])* protects the drive shaft bearings from contamination by the outside environment.

An adjustable crank attachment *(offset is 10 to 12 mm)* is bolted to the top of the drive shaft; this is a friction joint using 8 bolts tightened to a torque of 12 Nm.

The connecting rod is made from AISI 1040 steel plate and incorporates two sealed spherical roller bearings as the wearing parts.

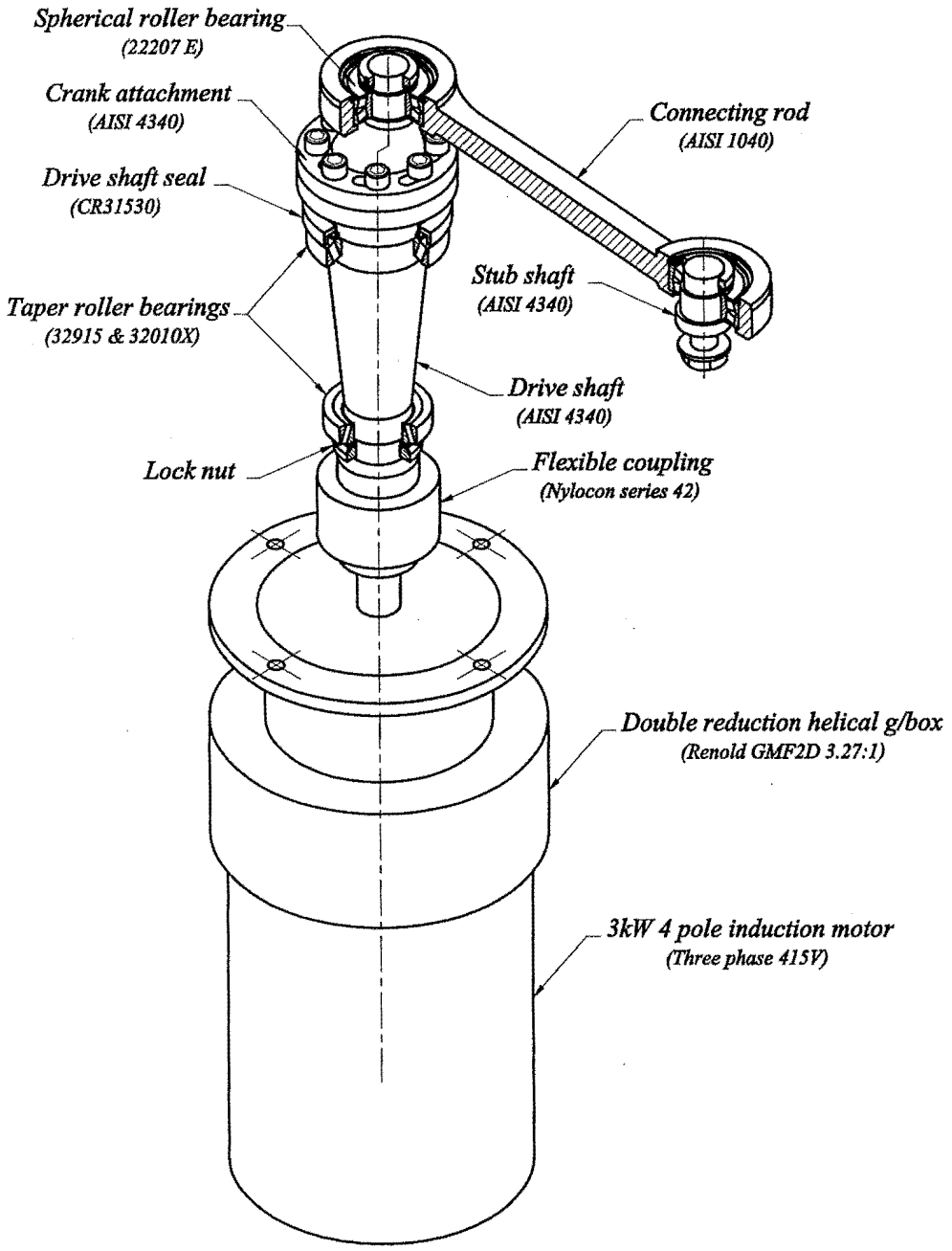

Figure 7.8 *Quater section isometric view showing the embodiment for the shuttle drive system*

7.4.3 The base rotation mechanism

Objectives of the development of the base rotation mechanism were to provide a smooth base rotation movement with minimal free-play, adjustment for wear in the bearings, and a reliable low maintenance drive. The base rotation mechanism provides a rotational drive for the sculpture and support for the shuttle bearings. Figure 7.9 shows the developed solution for the base rotation mechanism.

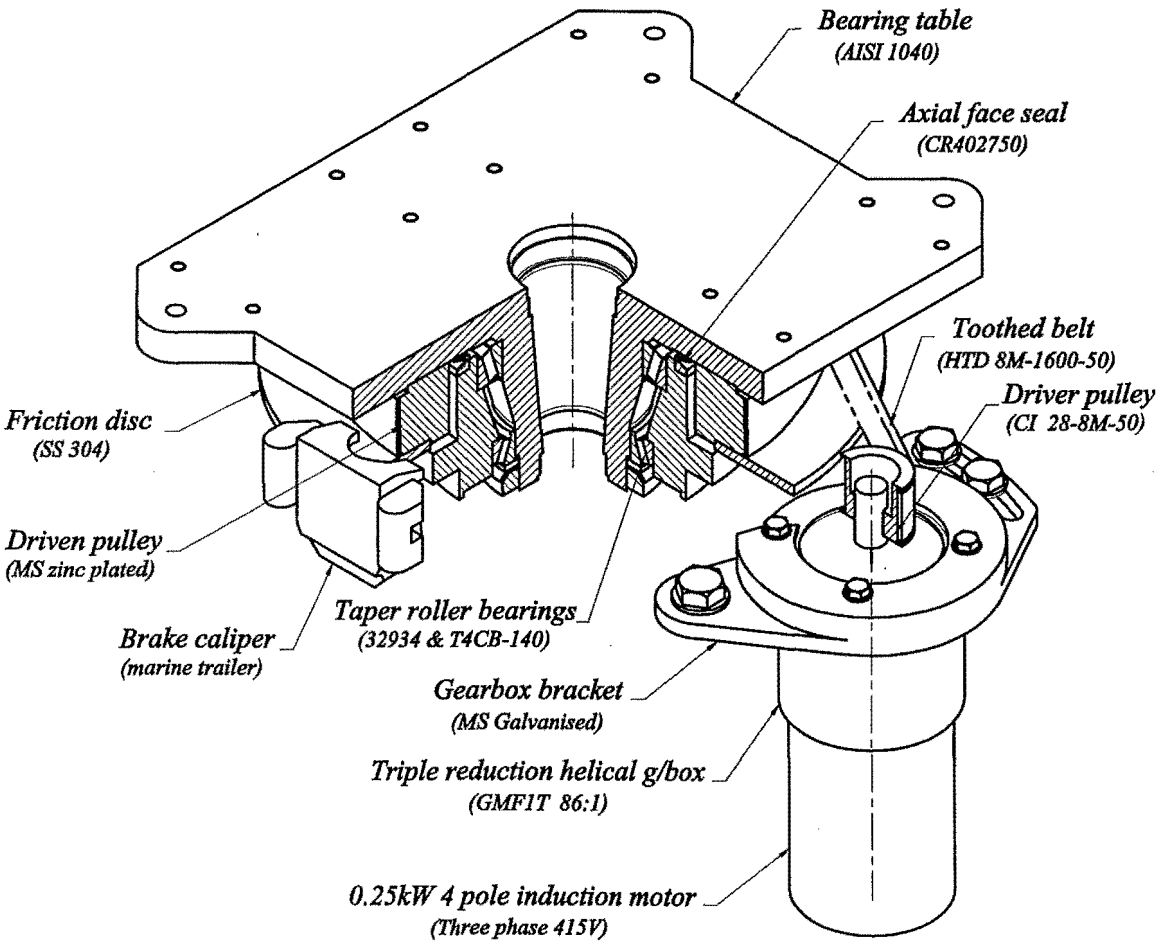

Figure 7.9 *Quater section isometric view showing the embodiment for the base rotation mechanism.*

The bearing table is, fabricated from AISI 1040 plate and bar stock and is supported on two taper roller bearings *(32934 & T4CB-140 [SKF (a)].* The bearings are protected from contamination from dust and moisture using a rubber axial face seal *(CR402750 [CR Seals])*

A 0.25 kW 6 pole induction motor powers the base rotation drive. A speed reduction of 516:1 is achieved using a flange mounted helical gearbox *(GMF1T [Renold Gears])* and a synchronous belt drive *(HTD 8M-1600-50 [Fenner]).* The driver pulley is a standard bought-out component *(cast iron 28-8M-50 [Fenner])* while the driven pulley *(168 tooth)* is machined from MS plate and electroplated with zinc to provide corrosion resistance. Belt tension is adjustable by means of a pivoting gearbox bracket *(MS hot-dip galvanised).*

A friction disc, incorporated to eliminate whipping in the drive, is machined from 304 grade stainless steel plate and has a mechanical spring actuated calliper. The calliper is the type normally used for marine trailers and is particularly suitable for use in the specified environment.

7.4.4 The support structure

The embodiment for the support structure is developed to hold the mechanism in position and to provide an anchor to the foundation. Figure 7.10 shows the developed solution for the support structure.

A base plate is cut from 32 mm MS plate and provides support and location for the base rotation bearing housing and the base rotation drive motor bracket. The base plate has ribs welded on its underside for extra stiffness and can be adjusted for level using four moveable feet.

Four pedestal type soft mounts that were incorporated following experimental observations of the original sculpture. The support frame is constructed from 350-grade box section and features a removable cross member for access to the shuttle drive motor.

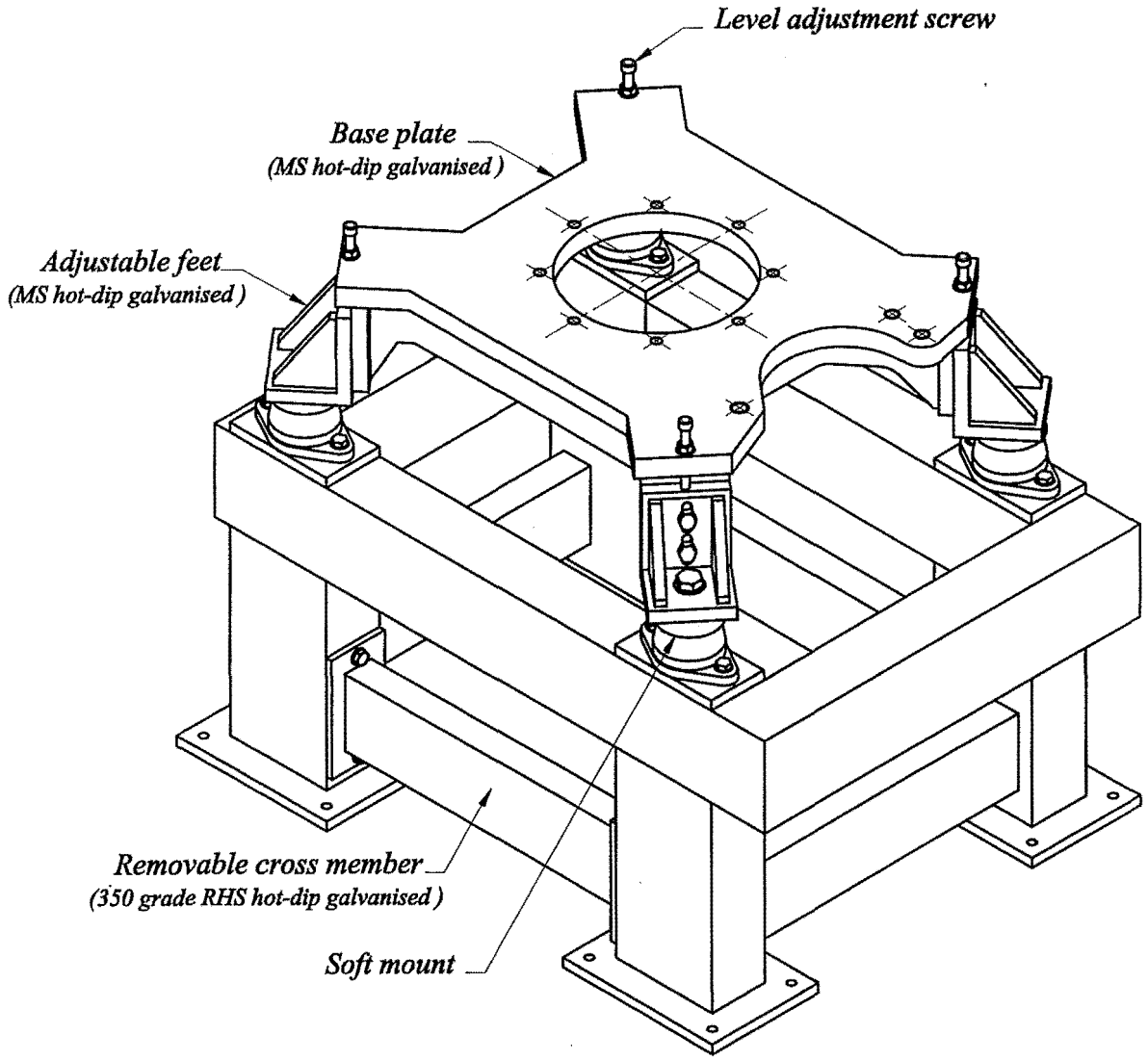

Figure 7.10 *Embodiment for the support structure*

7.4.5 The control system

The development of the control system aimed to use industry standard components with functions needed to satisfy the control requirements identified in Chapter 6.

The principal system components include a Programmable Logic Controller *(PLC)* and two variable frequency inverters. The basic wiring diagram for the proposed solution is shown in Figure 7.11

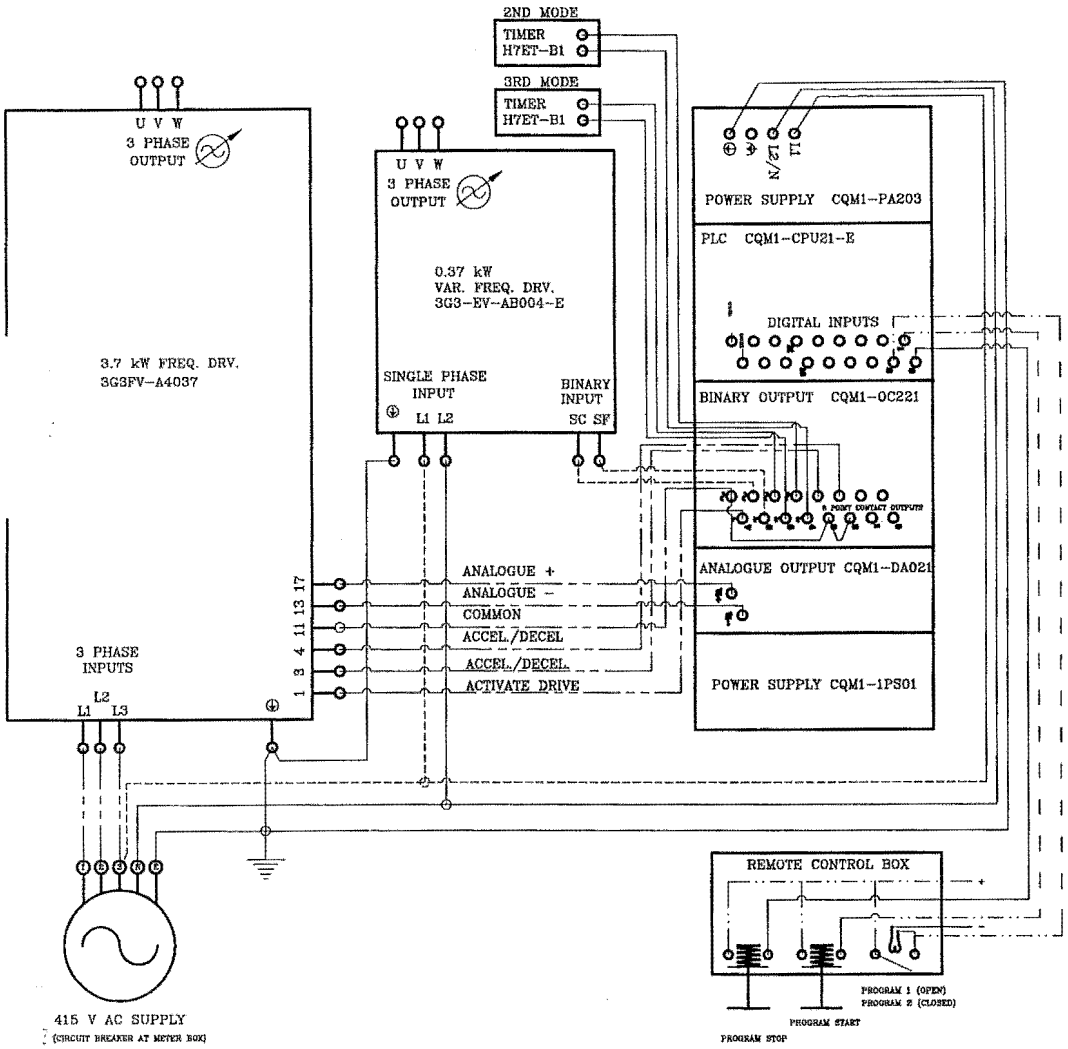

Figure 7.11 *Schematic diagram for the proposed control system*

The PLC *(CQM1 [Omron (c)])* stores program parameters for motor speed control, timing, and switching functions. The CQM1 has a single-phase 230 VAC power supply module. The CQM1 is programmed using the industry standard *'ladder logic'* control code. The control program is started or stopped by depressing a switch connected to the CQM1 binary input module and located in a remote control box. Two program options are available by either opening or closing a programme selection switch.

The 3kW induction motor is controlled using a 3.7kW variable frequency inverter *(3G3FV-A4037 [Omron (a)]).* The 3.7kW inverter measures a reference voltage from the CQM1 analogue output module to determine the drive output frequency and thus motor speed. The 3.7kW inverter features an *'s-curve characteristic function'* thus there will be no undesirable sudden changes in acceleration between set speeds that where found to cause the swinging phenomenon, best illustrated by Figure 6.13.

The speed of the 250W base rotation motor remains constant throughout the performance of the sculpture, however the pre-set speed may be adjusted using the keypad on the 0.37kW inverter *(3G3-EV [Omron (b)]).* The inverter is activated by a control signal from the CQM1 binary output module.

Battery powered digital timers are activated by the CQM1 binary output module and records both the cumulative time *Blade* spends operating at the *double harmonic* frequency and the cumulative total running time for the sculpture.

7.4.6 The general assembly

The general arrangement of the sub-systems discussed in Sections 7.4.1 – 7.4.4 is shown schematically in Figure 7.12. The general assembly drawings, Figures D8 & D9, show detailed cross sectional views.

7.4.7 Assessment of the embodiment design stage

The embodiment design stage was assessed using the embodiment design checklist, Figure D5, after Hales (1993).

Figure D5 shows confidence in meeting the functional requirements for the work. One area identified as being problematic is protection of the linear bearing shafts from the outside environment, to this end extra clearance has been allowed between the clamp and bearing so that rubber bellows may be

fitted if necessary. A second area of concern is potential noise from vibration of the gear coupling, it was decided to trial the Nylon coupling with the view that a precision coupling may be fitted if necessary. Some further work is required to include suitable protection devices in the control system, however this was not perceived to be problematic.

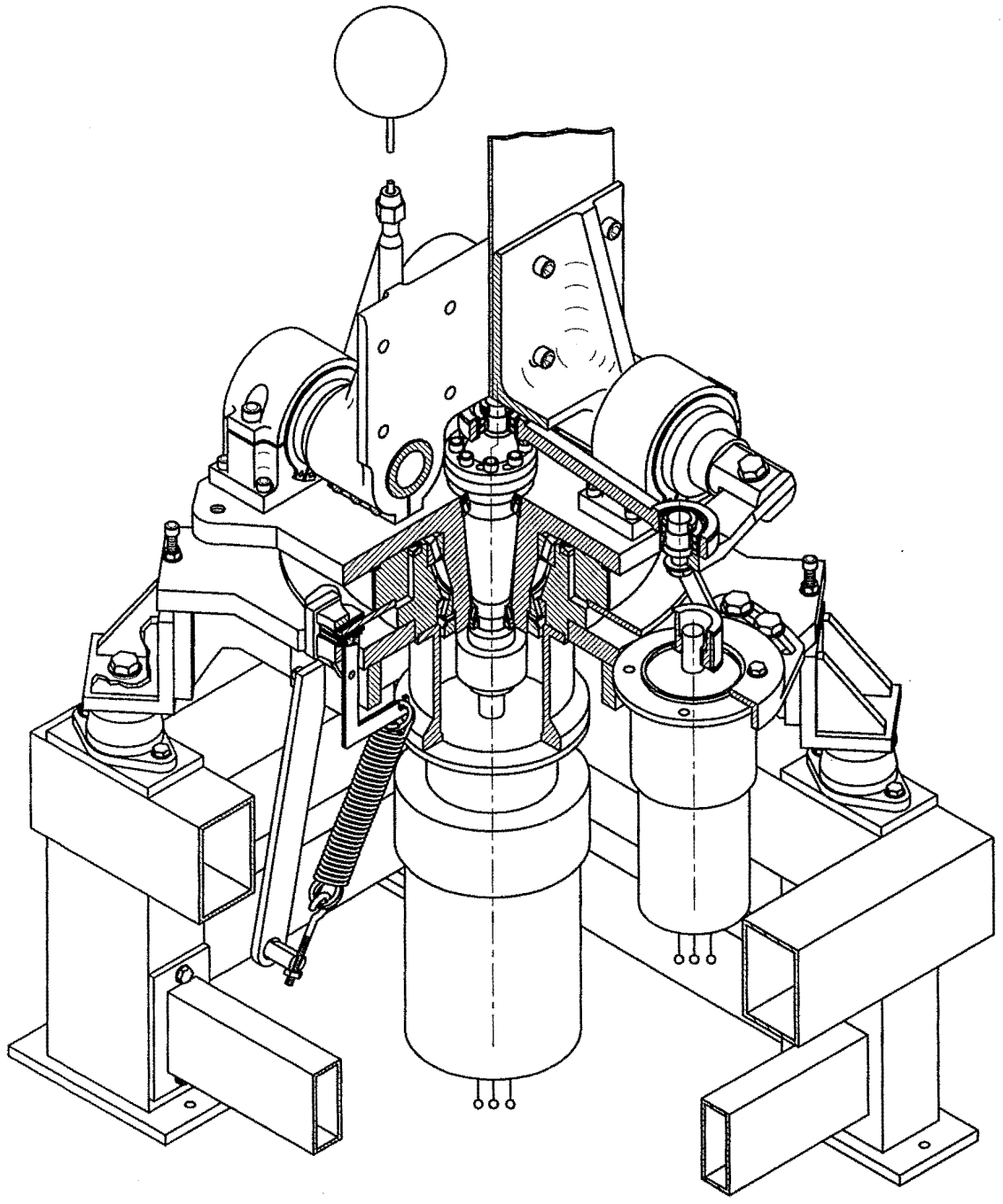

Figure 7.12 *Quarter section isometric view showing the embodiment for the drive system & the support structure*

7.5 Detailed design

The manufacturing information for the scaled *Blade* consists of a set manufacturing drawings and a detailed costing. The general assembly for the drive system and support structure following the detailed design stage is illustrated in Figure 7.13. A detailed costing is included in the EXCEL document, *parts.xls*, included on the CD-ROM. The principal manufacturing drawings are illustrated in Figures D8 – D20, the full set of manufacturing drawings are included as AutoCADr14 *.dwg* files on the CD-ROM.

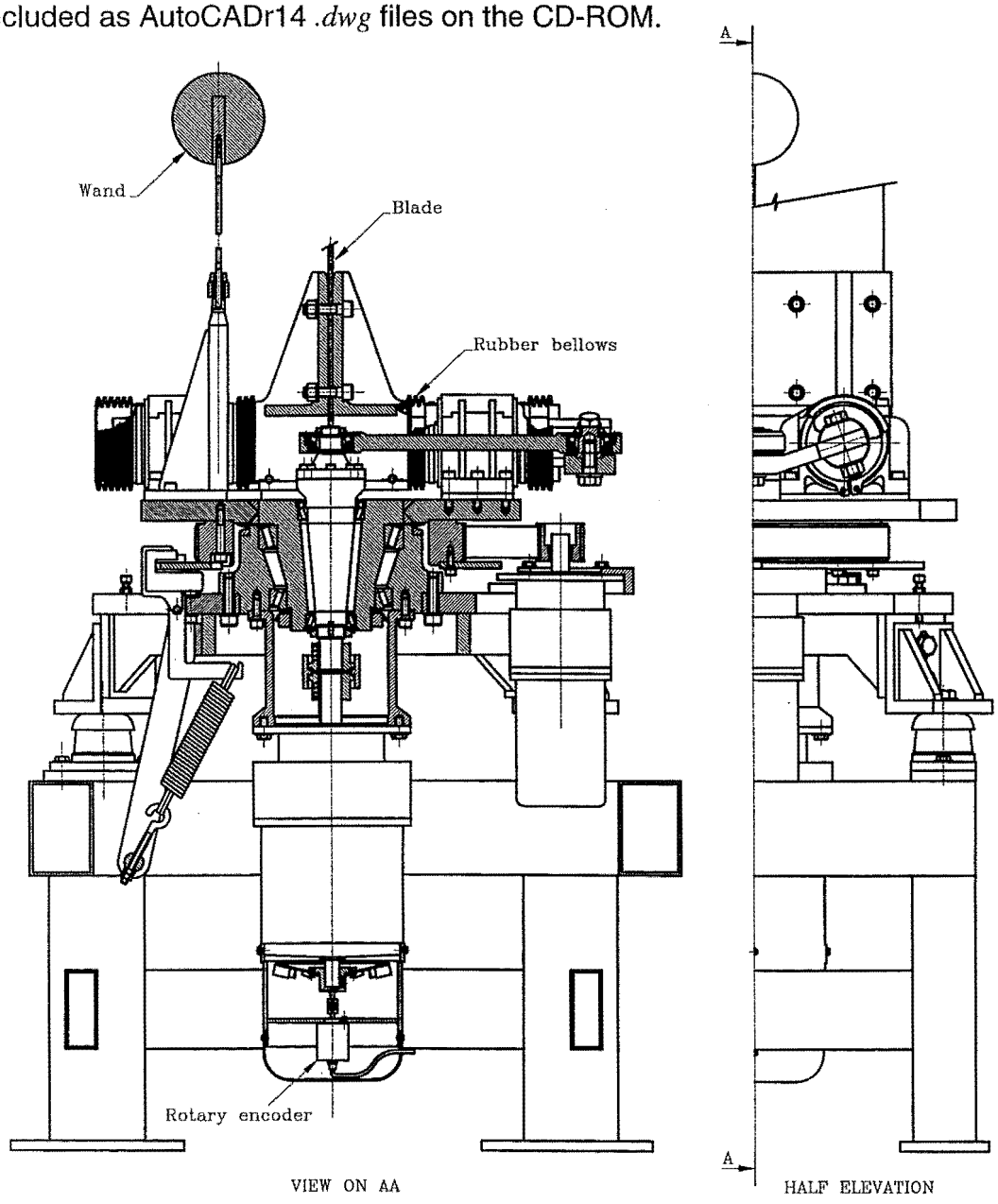

Figure 7.13 *General assembly for the scaled Blade*

This Section discusses key features in the detailed design.

Figure D10 shows the manufacturing drawings for the clamp. For a one-off design it was decided to manufacture the clamp from MS plate. The outer profile is cut from 120 mm thick MS plate using an oxygen acetylene cutting method. The machining procedure specified in Figure D10 is expected to give a satisfactory tolerance on the alignment of the linear bearing shafts.

The manufacturing information for the central drive shaft, Figure D12, specifies a machining procedure for the crank attachment that will allow manufacture using standard milling machine attachments.

For the manufacture of the bearing table, Figure D14, the trunnion shaft is firstly rough turned and then welded to the top plate. Following post weld stress relief the table is finish machined. The top surface is either surface ground or precision milled to get the required flatness.

A satisfactory solution was found to manufacture the rubber bellows and it was decided to trial the nylon gear coupling.

The fan end of the induction motor is modified to include a rotary encoder thus providing a positive motor speed feedback signal to the inverter. *(NB. an optional encoder card is fitted into the inverter)*

An emergency stop is included to activate the main circuit breaker and cut the power supply to all equipment in the control box. *(NB. after loss of system power the CQM1 program returns to the reset position)* All system components are protected by appropriate sized circuit breakers or fuse-able links.

Control system components are housed in a polyester box, which has a clear perspex lid, and is soft mounted on the support frame. The polyester box has been modified to incorporate an aluminium backing plate to conduct heat from the inverters to the outside environment.

The control system has excellent speed control *(+/- 0.3rpm at the second harmonic frequency)*

The detailed design stage was assessed using the detailed design checklist, Figure D6. Some concerns were that there may not be sufficient testing prior to the *'Sculptures in the Park'* exhibition, however this was not considered critical. The detailed design worksheet shows sufficient confidence to proceed with the manufacture.

7.6 Concluding comments

A systematic approach, adopted for the design of the mechanism and the support structure for a *Blade* at the nominally double-original size, has resulted in the manufacturing information being produced.

> ***The new drive mechanism for the scaled Blade has been designed that does not require the use of slip rings and resolves problems associated with these devices on the original work.***
>
> ***The drive mechanism for the scaled Blade has sufficient power and control to maintain the desired base motion characteristics for the blade. In addition the control system features the 's-curve characteristic function'. These features along with the wand specification in Chapter 6 will reduce the disturbances to the first blade mode.***

The control system has sufficient capacity to include additional speed changes at the second harmonic frequency, thus introducing a number of small impulses into the system should it be too stable as predicted by Figure 6.15.

8

Manufacture, testing, and commissioning the scaled Blade

8.1 Manufacture

The drive mechanism and the support structure, Figure 8.1, were manufactured at the Mechanical Workshop University of Canterbury.

The control system components were assembled as shown schematically in Figure D19; the wiring being conducted in accordance with NZAS3000.

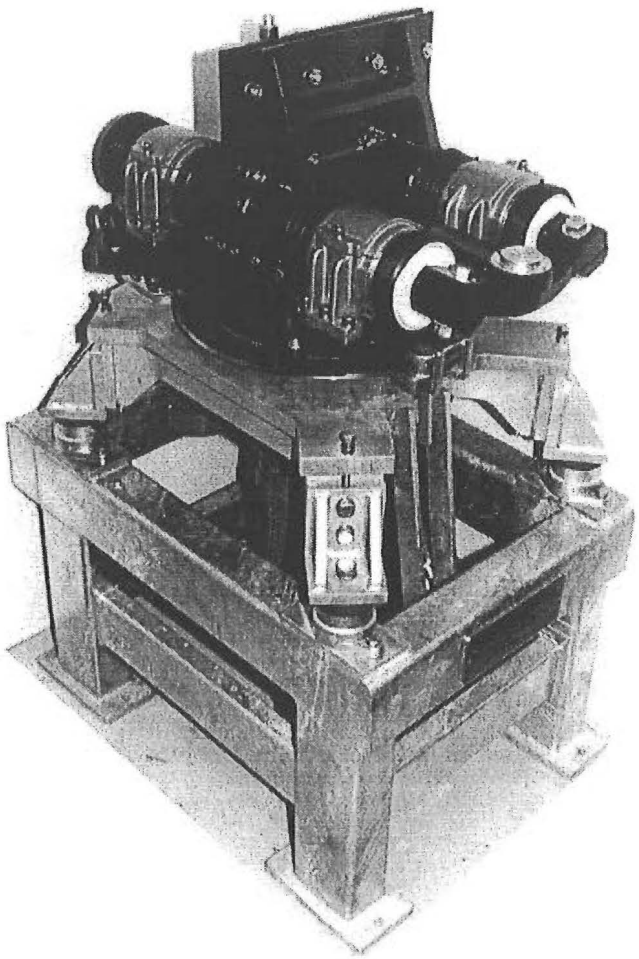

Figure 8.1 *The manufactured drive mechanism* and the support structure for Blade

8.2 Testing and commissioning the scaled *Blade*

For the initial testing the sculpture was bolted to a concrete foundation *(foundation weight = 5 tonne),* which was situated at the University of Canterbury, and the blade fitted into the rigid base clamp as shown in Figure 8.2.

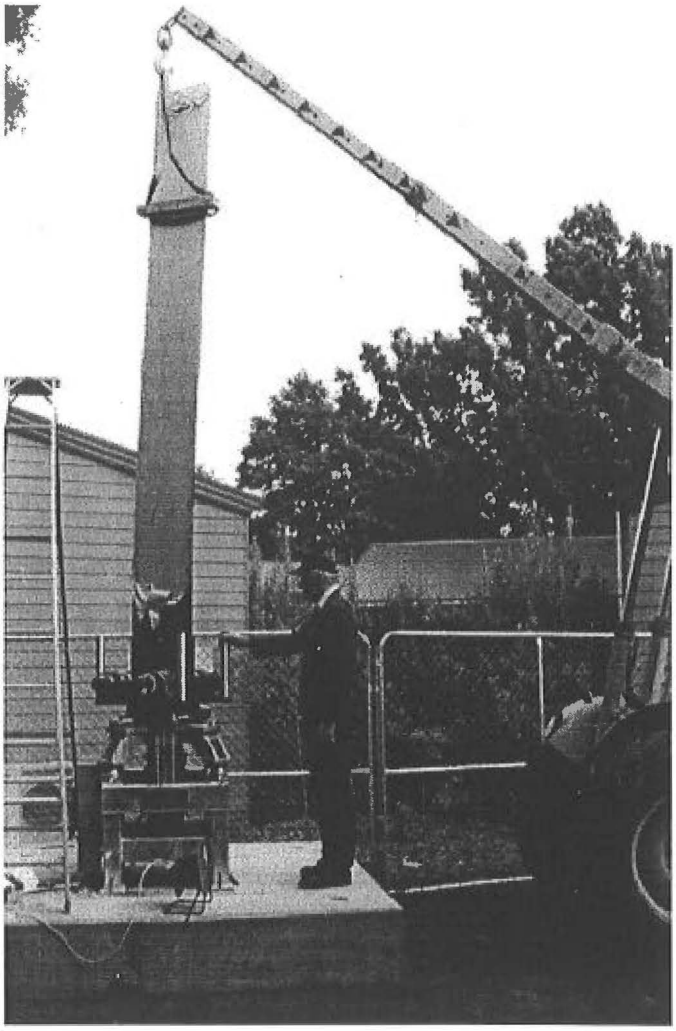

Figure 8.2 *Fitting the blade*

The blade was found to have good straightness, that is it stood vertical and straight, hence the modification anticipated in Figure 7.7 was not necessary.

The shaft speed on the 3kW induction motor was adjusted using the *'jog'* function on the 3.7kW inverter and the motor speeds corresponding to Lye's kissing, first harmonic, shimmering, and second harmonic frequencies were measured as 2.01, 2.11, 5.66, and 6.39 Hz respectively.

Following initial testing, the scaled *Blade* was commissioned at the 'Sculptures in the Park' exhibition, Figure 8.3, at the botanical gardens in Christchurch, New Zealand.

Figure 8.3 *A view of the scaled Blade at the 'Sculptures in the Park' exhibition (2 nd – 5 th February 1998)*

> *... Blade, a raw, incisive feat of research and engineering that literally dances and fascinates spectators throughout its performance ... [Christchurch Press (February 4 1998)]*

Initial testing and commissioning at the University and at the *'Sculptures in the Park'* exhibition were conducted under moderate – fresh wind conditions *(10-15 knots with occasional gusts of up to 20 knots).* Under moderate wind conditions the swinging phenomenon was observed, however the amplitude developed was not sufficient to cause the loss of the third mode shape (which occurred with the original sculpture Figure 6.1b): the performance of the work was found to be satisfactory.

Final commissioning of the scaled *Blade* was conducted at Pukekura Park, New Plymouth, New Zealand, January 30 – March 6 1999 *(images of the Pukekura Park exhibition are included on the CD-ROM).*

Wind conditions at the Pukekura Park exhibition were light - gentle *(less than 10 knots)* and the *Blade* was found to be too regular in motion at the kissing frequency. Hence further fine-tuning of the control system involving a number of step changes in clamp frequency was found necessary and resulted in the motor speed / time history shown in Figure 8.4. *(NB The ladder logic diagram for the control system program is included on the CD-ROM*

At the double harmonic frequency it was necessary to reduce the base clamp frequency in a number of small step from 6.39 to 5.81 Hz to give the maximum amplitude of vibration for the given amplitude of base motion. This requirement is consistent with the non-linear softening spring effect, Figure 4.6.

The single and double harmonic frequencies in Figure 8.4 are slightly lower than those given in Table 4.1. This is due to the softening spring effect with increasing amplitude of forced vibration.

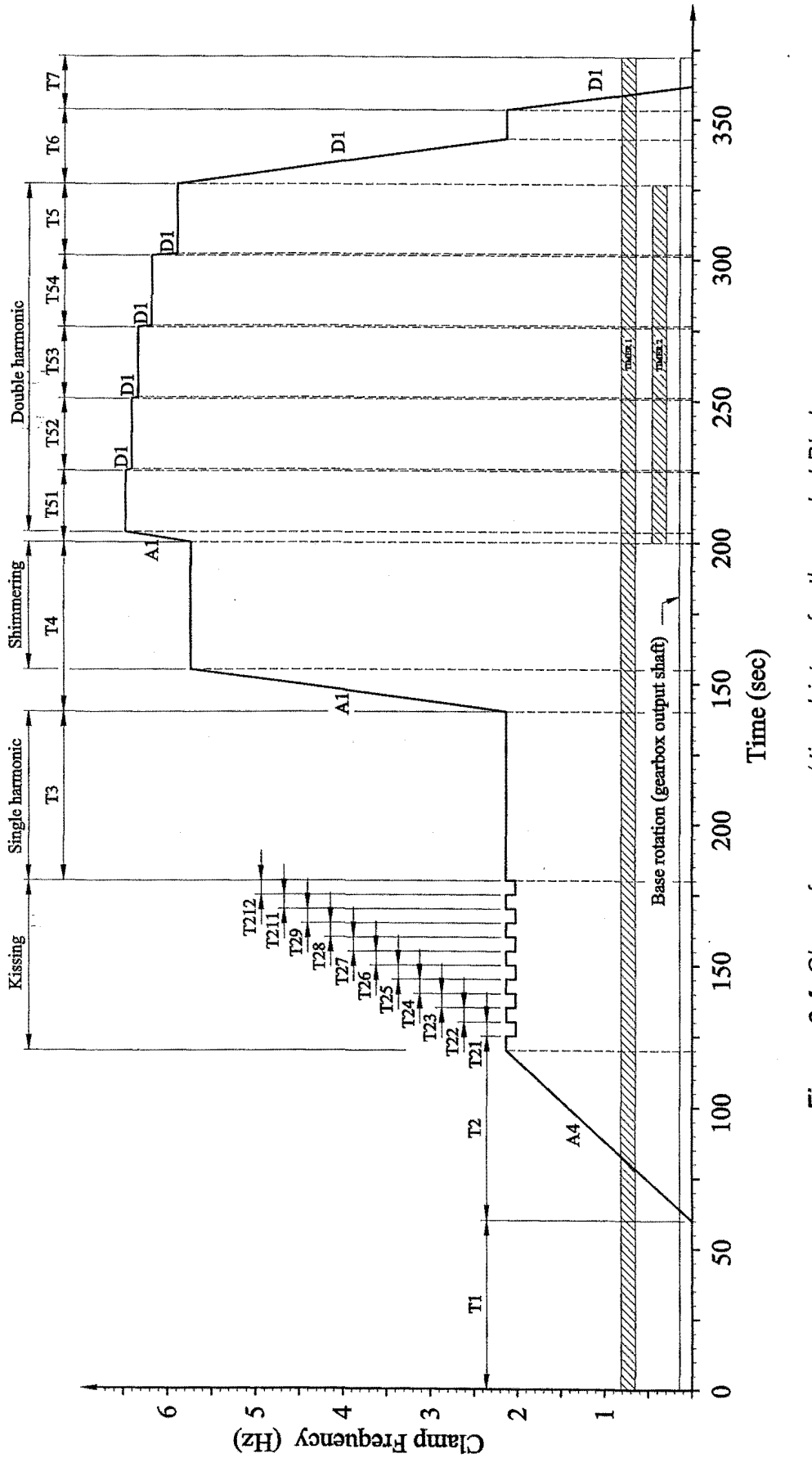

Figure 8.4 Clamp frequency / time history for the scaled Blade

The relative amplitude of Lye's shimmering vibration on the scaled work was less than that observed on the original sculpture. This relative difference is expected to be a result of finer tolerances specified on the scaled work and worn components on the mechanism for the original sculpture.

8.3 Summary and conclusions

The scaled *Blade* has been commissioned and the drive mechanism and control system were found to operate in a reliable manner.

When subject to light wind conditions, the vibrating blade has the stability characteristics predicted by the mathematical model in Chapter 6 and it is necessary to introduce step changes in the blade ground motion frequency to initiate a more irregular interaction between the blade and the wand.

In moderate winds the swinging phenomenon features in the performance of the work and has the effect of introducing a degree of irregularity in the interaction of the wand and the blade so that the step changes in ground motion frequency are not required. In moderate winds this swinging phenomenon does not result in the loss of the third mode shape which was observed on the original sculpture.

Further work may be necessary if Lye's shimmering vibration is to be observed at a greater amplitude.

If the blade is operated in strong winds *(greater than 21 knots),* loss of the vibratory form would be expected at the double harmonic frequency and damage to the blade due to yielding may occur.

9

Conclusions and recommendations

9.1 Introduction

This project has investigated the possibility of producing a structure of the form of Len Lye's kinetic sculpture *Blade* at a much larger size. This chapter summarises the research activities, the results of this study, and makes recommendations for further work.

9.2 Summary of research activities

A review of the writings of Len Lye (1901 - 1980) was conducted to establish his vision for *Blade*. This, along with an experimental investigation of the behaviour of the original *Blade,* established desirable performance characteristics and design features for the larger work.

A set of scaling rules for the blade was developed using dimensional analysis and the effect of increasing size on structural properties *(bending moments, natural frequencies and system power requirements)* was studied.

The artist's performance requirement specification *(including specifications emanating from Lye's writings)* was evolved in terms of a demands and wishes list [following the method of Pahl & Beitz (1996)]. Demands imposed by the artist's brief were formulated as either equality or inequality constraints and an

optimal solution for Blade was pursued using the method of optimal design [Johnson (1980)].

For the overall system dynamic behaviour the blade and wand stem were treated as uniform cantilever beams subject to an axial acceleration due to gravity. The natural bending frequencies and corresponding mode shapes for the blade and the wand were calculated exactly using a series solution for the mode shape differential equation *(a fourth order partial differential equation with a variable coefficient)* which was found in the literature.

The natural plate frequencies and corresponding mode shapes were also calculated for the blade to explain the shimmering motion observed by the artist. This analysis used both ordinary beam functions and orthogonal polynomials in conjunction with the Rayleigh-Ritz method.

The first four frequencies of the blade were measured experimentally.

A mathematical model was developed that that predicted the significant dynamic behaviour in the *"kinetic"* performance of *Blade*. The mathematical model included the forced damped vibration of the blade *(the blade is subject to a harmonic ground motion at its clamped end)* and the wand *(the wand is stationary at its clamped end)* and included the interaction of these two components.

A new concept was evolved for the drive mechanism using the Pahl & Beitz method. The embodiment design with complete manufacturing information was developed for a solid metal *Blade* at the largest practical size.

The sculpture was manufactured and tested at the University of Canterbury and later commissioned at public exhibitions under light to moderate wind conditions.

9.3 Conclusions of this study

Research into the writings of Len Lye found that he intended the original sculpture to be the smallest *Blade* in a larger work called *Steel Henge*. *Steel Henge* comprises twelve *Blades;* the largest to be over five times the height of the original work. In other writings he indicated that *Blade* should be built at the monumental size of 100ft tall. Lye gave vivid descriptions of how he perceived the work to look *" ...like a shinny kerosene can ... a great flash of quivering sunlight... "* *" ...the accelerating rush of the three-hundred-foot Redwood, Kurrrrash-empathy... ".*

Observations of the original sculpture found that there are four distinct segments in the vibratory performance of the blade. These are what Lye described as *kissing*, *full amplitude single harmonic*, *shimmering*, and the *double harmonic.*

The mechanism on the original work uses slip rings to transmit power and control signals to the shuttle drive. The slip rings were identified as being problematic and that a new mechanism concept was needed to overcome these associated problems.

Lye's original experimental method for establishing the blade size was found to require that static similarity exist between the original and the scaled blades. The artists' brief also required that geometric similarity of the vibrating blade at its maximum amplitude exists between the original and the scaled works. For the vibrating blade *(a damped system)* this could be achieved by adjusting the amplitude of the reciprocating harmonic ground motion.

The scaling rules showed that as *Blade* size increases the magnitudes of the drive forces, bending stresses in the blade, and system power requirements

increase at an increasing rate. Despite this it was found that a drive mechanism could provide sufficient power and support for a blade size of up to 5m and still meet the requirements imposed by the artist's brief. The optimal design solution for the Blade is found by the selection of a blade material that best meets the artist's brief. The artist's specifications form design constraints that may be considered under four sub-headings, namely; *the vibratory form, sound quality, surface finish,* and *economic availability.* The two best candidate material groups were found to be a high strength titanium alloy and low alloy steel. A variational study of the number of *Blade* performances per dollar expended, constrained by availability gave the optimum solution. The optimal design of the kinetic sculpture Blade, within the artist's brief, required the sculpture to have a titanium alloy (6Al/4V) blade with a nominal blade length of 3.355m

It is interesting to note that for a nominally double size sculpture, the titanium alloy was almost six times cheaper than low alloy steel *(based of the number of Blade performances per dollar expended).*

The scaled *Blade* is expected to fail due to reversed bending fatigue at the fixed end after *260* performances. This blade life corresponds to a blade material cost per performance of *NZ$36.* The selected titanium alloy has good reverberant properties and has particularly good resistance to attack by the specified environment.

Lye's *kissing* and *single harmonic* frequencies were found to correspond to the second bending mode of vibration for the blade while the double harmonic frequency corresponds to the third bending mode of vibration. The inclusion of gravity in the analysis was found to be significant *(the calculated first bending frequencies for the original blade were 0.306 and 0.578Hz for the cases including and excluding gravity respectively).*

At large amplitudes of vibration, the measured bending frequency was less than that calculated. This is believed to be due to a non–linear softening spring effect. Non-linearities have been found to be an important factor affecting the performance of the blade, particularly at the third bending mode of vibration.

The first, second, and fourth plate modes for blade were found to correspond with the first, second and third beam bending modes respectively. Lye's shimmering frequency corresponds with the third plate mode and is purely torsional. The third plate mode is not directly excited on the original sculpture, thus the energy required for the shimmering frequency is supplied by out-of-balance mechanism forces.

An observation made during experimental procedures was that the blade tended to develop an undesirable lower order swing while vibrating at the third bending frequency *(i.e. Lye's double harmonic frequency).* The mathematical model showed that the swinging phenomenon is caused by a disturbance to the first natural blade bending frequency. The significant factors causing this disturbance are the interaction between the blade and the wand and impulses due to abrupt changes in ground motion frequency. Specifying a lighter more flexible wand and by removing abrupt changes in ground motion frequency reduced the tendency for the blade to develop the swinging phenomenon.

A new drive mechanism for the scaled Blade was designed that did not require the use of slip rings and resolved the problems associated with these devices on the original work.

To reduce the disturbances to the first blade mode (i.e. the swinging phenomenon), a drive mechanism for the scaled Blade was specified with sufficient power to control and maintain the desired base motion characteristics and with a control system that includes an *'s-curve transition function'* to reduce

abrupt changes in ground motion frequency at the end of acceleration and deceleration periods.

While testing the scaled sculpture in light wind conditions, the blade had the stability characteristics predicted by the mathematical model but it was found to be too stable from an artist's perspective. So it was necessary to introduce step changes in the blade ground motion frequency to initiate a low amplitude swing producing more irregular interaction between the blade and the wand.

In moderate winds the swinging phenomenon features in the performance of the work and has the effect of introducing the required degree of irregularity in the interaction of the wand and the blade, and in this case the step changes in ground motion frequency were not required.

If the blade is operated in a strong breeze *(greater than 21 knots)* a higher amplitude of the swinging phenomenon should be expected and is likely to result in the blade yielding due to high bending stresses.

Allowance for the non–linear softening spring effect was included in the control system program. To get the maximum blade displacement associated with the third bending mode of vibration it was necessary to increase ground motion frequency up to the calculated natural frequency *(from the free vibration analysis)* and then reduce the ground frequency to reach the maximum amplitude of vibration.

9.4 Recommendations for further work

The swinging phenomenon and hence the interaction between the blade and the wand was found to be influenced by wind conditions. It is recommended that two programme options be available, one for light-gentle winds *(less than 10 knots)* and one for moderate-fresh winds *(up to 21 knots).*

Increasing the amplitude of vibration of the third plate mode *(i.e. Lye's shimmering vibration)* has been identified as an area that may improve the performance of the sculpture. It is recommended that the sculpture be tested at the shimmering frequency with the disc brake disengaged. If this gives a more satisfactory shimming vibration, a suitable solution would be to release the brake for this part of the performance. A second solution would be to create an out-of-balance force about the vertical blade axis to energise the shimmering vibrations.

The blade at the larger size is operating at a reversed bending stress that is above the material's endurance limit. Further work could be undertaken to study clamp configurations that reduce the bending stress experienced by the blade. A configuration believed to be worth studying is a pivotal clamp arrangement as shown schematically in Figure 9.1

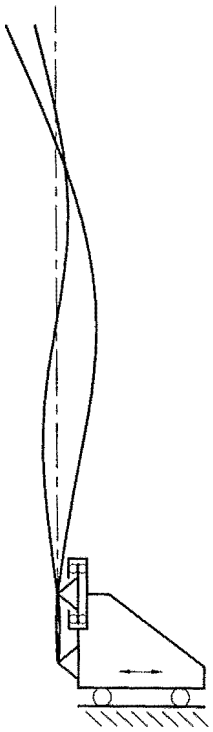

Figure 9.1 *Pivotal clamp concept*

The blade used in a pivotal clamp must have static similarity with the original blade.

References

Ashby M. F., (1992) *Materials selection in mechanical design*, Pergamon Press Inc, New York.

ASM Metals Handbook, (1992) *Properties selection: non ferrous alloys & special purpose materials,* ASM Metals Handbook, Volume 2.

Barton M. V., (1951) *Vibration of rectangular and skew cantilever plates*, Journal of Applied Mechanics 18, pp 129-134.

Bassily S. F. and Dickinson S. M., (1975) *On the use of beam functions for problems of plates involving free edges,* Journal of Applied Mechanics, 42, 858-864.

Benham P. P. and Crawford R. J., (1987) *Mechanics of engineering materials,* Longman Scientific & Technical, Harlow, Essex, England.

Bhat R. B., (1985a) *Natural frequencies of rectangular plates using characteristic orthogonal polynomials in Rayleigh-Ritz method*, Journal of Sound and Vibration, 102, 493 - 499

Bhat R. B., (1985b) *Vibration of rectangular plates using beam characteristic polynomials in the Rayleigh-Ritz method,* Proceedings of the Third International Modal Analysis Conference, Orlando, Florida, 28-31 January.

Bhat R. B., (1985c) *Vibration of structures using characteristic orthogonal polynomials in the Rayleigh-Ritz method,* Proceedings of the Tenth Canadian Congress of Applied Mechanics, London, Ontario, Canada, 2-7 June, A129-A130.

Bouhours J. M. and Horrocks R., (2000) *Len Lye*, Centre Pompidou, Paris.

Bunge Industrial Steels Pty Limited, *High strength abrasion resistant quenched and tempered Bisalloy steels,* Bunge Industrial Steels Pty Limited, P.O. Box 231, Resolution Drive, Unanderra, N.S.W. 2526, Australia.

Burden R.L., Faires J.D. and Reynolds A.C., (1981) *Numerical analysis,* Boston Massachusetts, Weber and Schmidt, 2nd edition.

Industrial Steels Pty Limited, *High strength abrasion resistant quenched and tempered Bisalloy steels,* Bunge Industrial Steels Pty Limited, P.O. Box 231, Resolution Drive, Unanderra, N.S.W. 2526, Australia.

Christchurch Press, (February 4 1998), *Mettlesome garden metaphors*, Art review by Fusco Cassandra, pg 16.

Collins, J. A., (1993) *Failure of materials in mechanical design*, 2nd edition, John Wiley & Sons, Inc., New York.

Curnow W. & Horrocks R., (1984) *Figures of motion - Len Lye – selected writings*, Auckland University Press.

Curnow W. (1980) *Len Lye*, Art New Zealand 17, pp34-41, The Art Magazine Press Limited, Auckland, New Zealand.

Denis J. & Bieringa J., (1992) *Film in Aotearoa New Zealand*, Victoria University Press.

Dickinson S. M., & Di Blasio A., (1986) *On the use of orthogonal polynomials in the Rayleigh-Ritz method for the study of the flexural vibration and buckling of isotropic and orthotropic rectangular plates,* Journal of Sound and Vibration, 108(2), 51 -62.

Dickinson S. M., (1981) *On the use of simply supported plate functions in the Rayleigh-Ritz method applied to the flexural vibration of rectangular plates,* Journal Of Sound And Vibration, 80(2), 292 - 297.

Dieter G. E., (1991) *Engineering design - a materials and processing approach,* 2nd ed., McGraw Hill, Singapore.

Diyanni M., (Jan May 1996) *Private communication with S. Gooch,* Tiernay Metals, Aerospace Products Div., Redondo Beach, California, USA.

Deutschman A. D., Michels W. J. and Wilson C. E., (1975) *Machine design theory and practice,* Macmillan Publishing Co., New York.

Duncan, R.M. and Hanson, B.H., (1980) *The selection and use of titanium,* Oxford University Press.

Forsythe G. E., Malcolm M. A. and Moler C. B., (1977) *Computer methods for mathematical computations,* Prentice-Hall, Englewood Cliffs, N.J.

Gooch S. D. and Raine, J. K., (2000) *The dynamics and limits on scaling of a flexible kinetic sculpture*, Proceedings of the Institute of Mechanical Engineers, Vol. 214, Part C, 537-548.

Gooch S. D. and Raine J. K., (1997) *A twice full scale 'Blade' - the engineering design of a kinetic sculpture, Proceedings of the IPENZ Annual Conference*, Wellington, New Zealand, 2, 247-252.

Gooch S. D., (1996) *Scaling Blade – a technical note for the engineering design of a kinetic sculpture,* I.P.E.N.Z. Proceedings of the Third New Zealand Conference of Postgraduate Students in Engineering & Technology, Canterbury University Press.

Griffiths D. V. and Smith I. M., (1991) *Numerical methods for engineers: a programming approach,* Blackwell Scientific Publications, Oxford [England]

Hales C., (1993) *Managing engineering design,* Longman Scientific & Technical, New York.

Hempel M. and Hillnhagen E., (1969) *The fatigue strength of commercial titanium alloys,* Farnborough Ministry of Technology, Royal Aircraft Establishment, Library Transaction No. 1353.

Hudson M., (Jan-May 1996) *Private communication with S. Gooch,* Timet UK, Birmingham B67UR, England.

Johnson K. L., (1985) *Contact mechanics,* Cambridge University Press, Cambridge [Cambridgeshire], New York.

Johnson R. C., (1980) *Optimum design of machine elements,* 2nd edition. Wiley New York.

Leissa A. W., (1969) *Vibration of plates (NASA SP 160),* Washington, DC: U.S. Government Printing Office.

Leissa A. W., (1973) *The free vibration of rectangular plates,* Journal of Sound and Vibration, 31, 257-293

Lye L., (1978) *Transcript of recorded discussion with J.B. Matthews*

Massey B. S., (1989) *Mechanics of fluids,* 6th Ed., Chapman & Hall, London

MathWorks, Inc., (1995) *The student edition of MATLAB, Version 4, Users guide*, Prentice Hall, Englewood Cliffs, NJ

McCallion H., (1972) *Vibration of linear mechanical systems*, Longman Group Limited, London.

McCarthy C. & Leonard R., (1991) *Composing motion - Len Lye's kinetic sculptures*, National Art Gallery, New Zealand.

Morrison J. L. M. & Crossland B., (1970) *An introduction to the mechanics of machines*, 2nd ed., Longman, London.

Naguleswaran S., (1991) *Vibration of a vertical cantilever with and without axial freedom at the clamped end,* Journal of Sound and Vibration, 146(2), 191 -198.

Naguleswaran S., (1999) *Vibration of a 'stiff' gravity pendulum with a rigid bob,* Procs. of the Asia Pacific Vibration Conf., Nanyang Technological University, Singapore (1) 84 -89.

Nayfeh S.A., and Nayfeh A.H., (1992), *Energy transfer from high - to low frequency modes in flexible structures*, DE-Vol. 50, AMD-Vol. 144, Non-linear Vibrations, ASME.

Newland D. E., (1989) *Mechanical vibration analysis & computation*, Longman Scientific & Technical, New York.

Oberg E., Jones F. D., Horton H. L. and Ryffel H. H., (1992) *Machinery's handbook 24th edition,* Industrial Press Inc., New York.

OMRON (1996a) *Sysdrive 3G3FV users manual,* Catalogue No. I516 –E1-2, Tokyo, Japan

OMRON (1996b) *General catalogue*, Catalogue No. X0-E5-3A, Tokyo, Japan

OMRON (1996c) *CQM1 operation manual*, Catalogue No. W226-E1-2D, Tokyo, Japan

Pahl G. and Beitz W., (1996) *Engineering design : a systematic approach*, 2nd edition, Springer, London; New York.

President Titanium, *Machining & technical data 6Al/4V titanium*, President Titanium, 243 Franklin St, P.O. Box 36, Hanson, Massachusetts, U.S.A., rev 12/96.

Raine J. K. and Gooch S. D., (1998) *Dynamic analysis and engineering design of kinetic sculptures*, IPENZ Transactions, Vol. 25, No. 1/Gen.

Raine J. K., Gooch S. D. and Webb E. A., (1997) *Artistic dreams, engineering limitations,* New Zealand Science Monthly, Vol. 8 Issue 9, South Pacific Information Services, Christchurch, New Zealand.

Raine J. K., Harrington J. J., Webb E. A. and Meredith Z. A., (1996) *Expanding "Universe" – design study for scaling up a kinetic sculpture*, Journal of engineering design, U.K., v&, No.4, pp 413-426

Rohde F. V., (1953) *Large deflections of cantilever beams,* Quart. Appl. Math., Vol 11, pp 337-338.

Savage G., (1993) *Carbon-carbon composites,* Chapman & Hall, London.

Shigley, J. E., (1986) *Mechanical engineering design*, McGraw Hill Book Company, New York.

Simons D. A. & Leissa A. W., (1971) *Vibrations of rectangular cantilever plates subjected to in-plane acceleration loads*, Journal of Sound and Vibration, 17(3), 407 - 422.

Steidel R. F., (1989) *An introduction to mechanical vibrations*, John Wiley & Sons, New York.

Timet, (1995) *Mill specification certificate,* Timet Morristown TN.

Timoshenko S. and Gere J. M., (1961) *Theory of elastic stability*, McGraw-Hill Book Company Inc., New York.

Timoshenko S., (1928) *Vibration problems in engineering*, D. Van Nostrand Company Inc., New York.

Webb E. A., (Jan. 1996 – Dec. 1998) *Project meetings with S.D. Gooch & J.K. Raine*, University of Canterbury.

Young W. C., (1989) *Roark's formulas for stress and strain*, 6th Edition, McGraw-Hill, New York.

Young D., (1950) *Vibration of rectangular plates by the Ritz method*, Journal of Applied Mechanics 17, pp 448-453.

A

Computation of natural frequencies and mode shapes – beam modes

The purpose of this section is to explain the numerical computation of the natural bending frequencies for the blade and the wand.

The numerical procedure is formulated as the MATLAB script file, *C4Prog1.m*, and is saved on the CD-ROM. The logical flow diagram for *C4Prog1.m*, Figure A1, summarizes the numerical procedure.

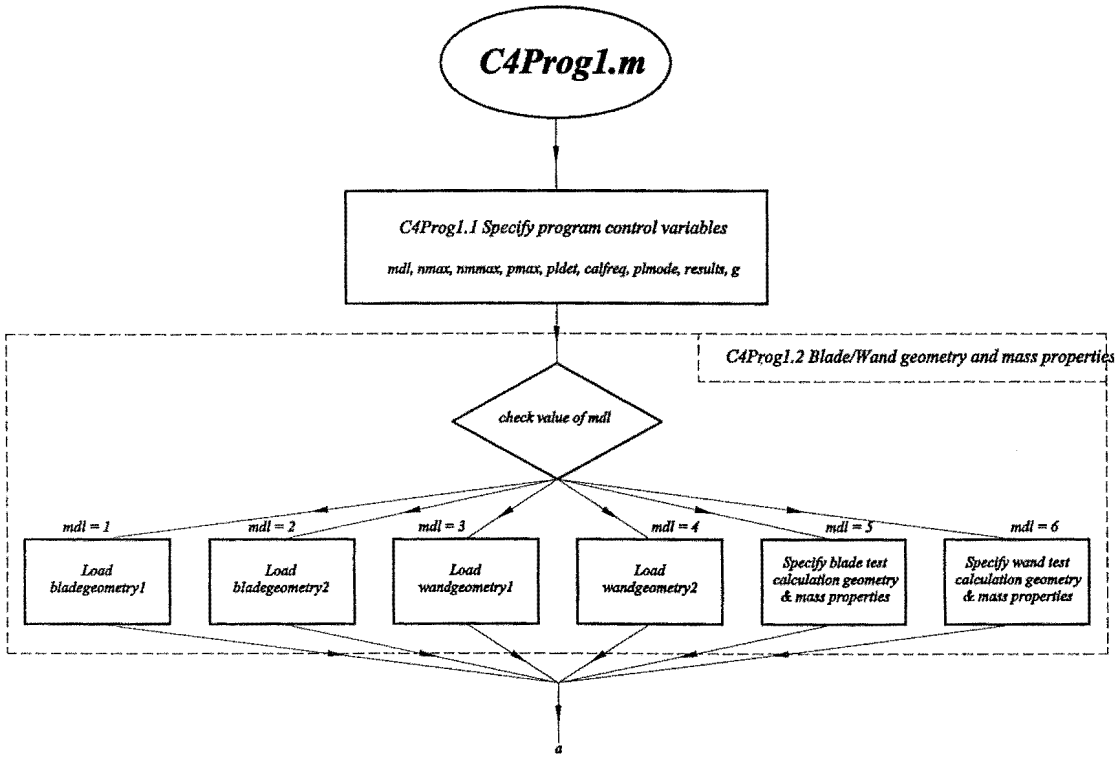

Figure A1 *Logical flow diagram for calculating bending frequencies C4Prog1.m*

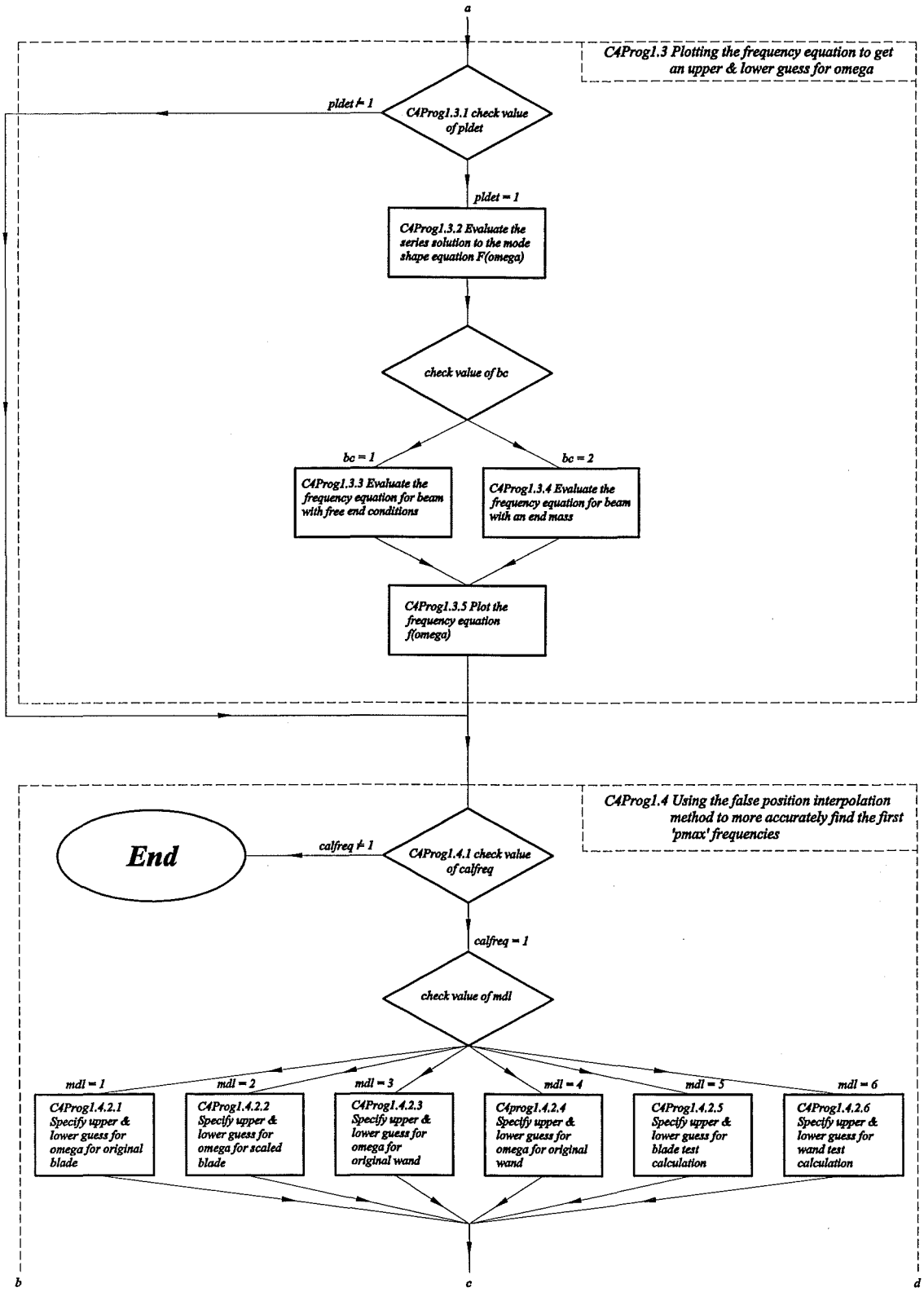

Figure A1 *(cont.)*

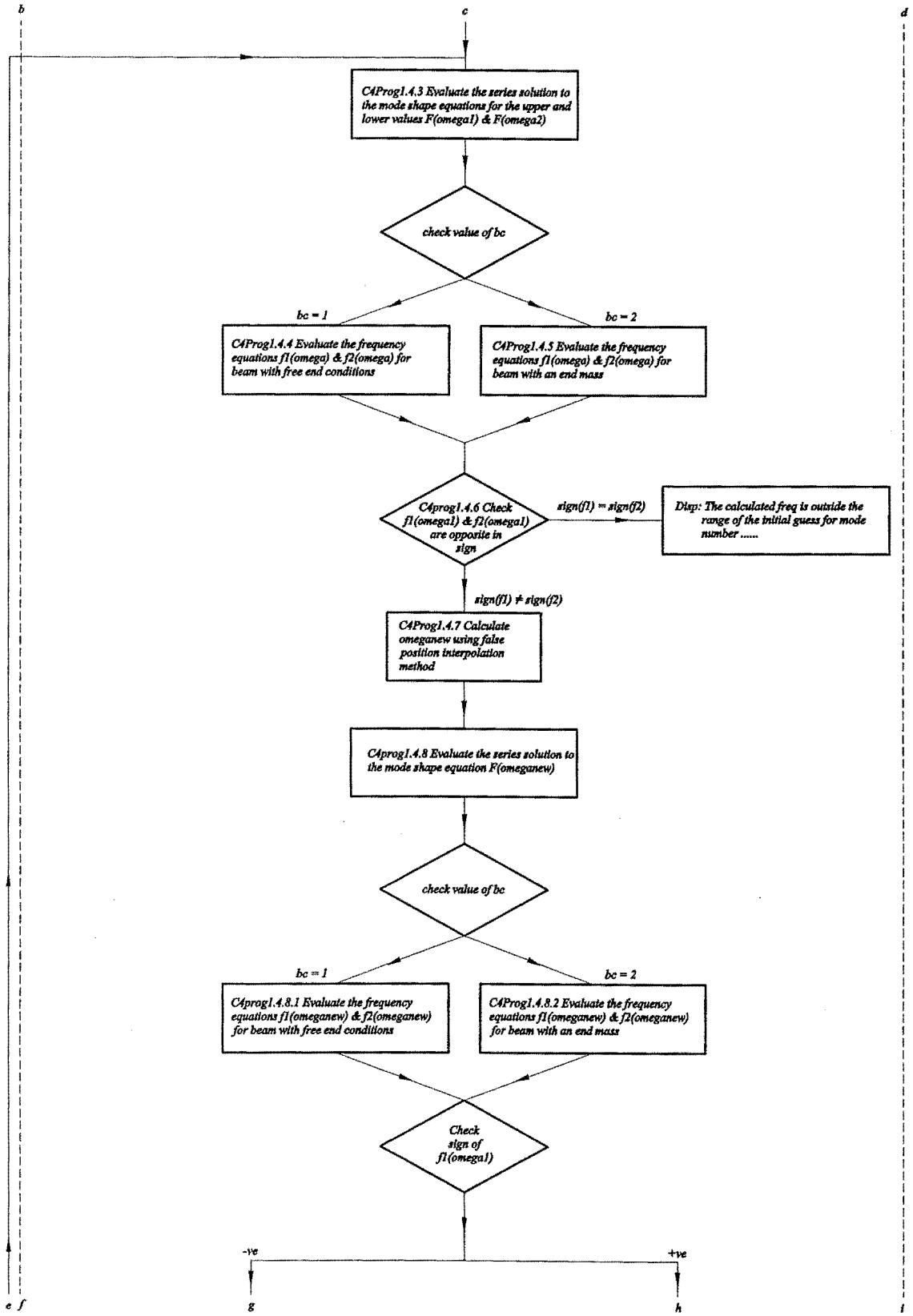

Figure A1 *(cont.)*

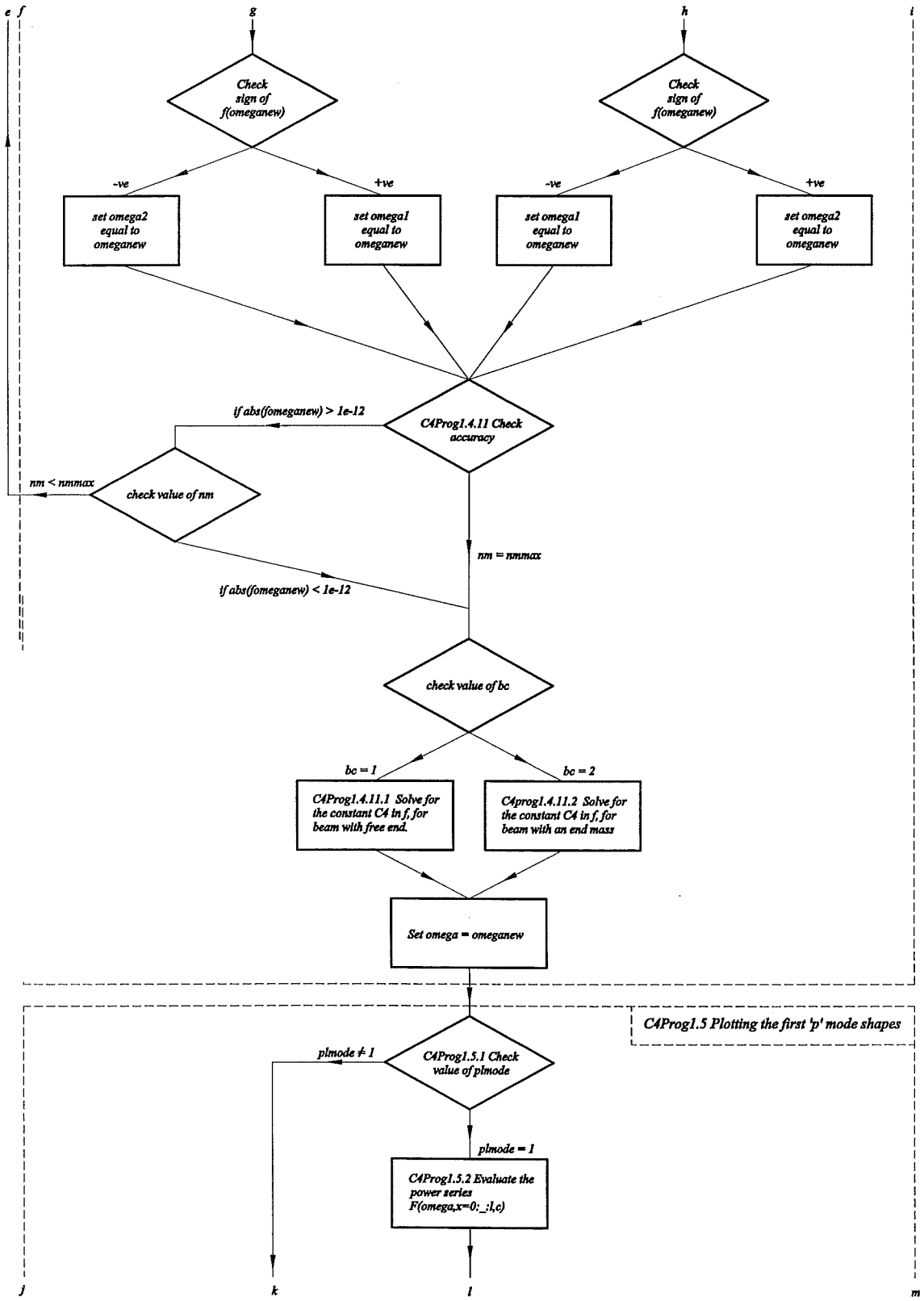

Figure A1 *(cont.)*

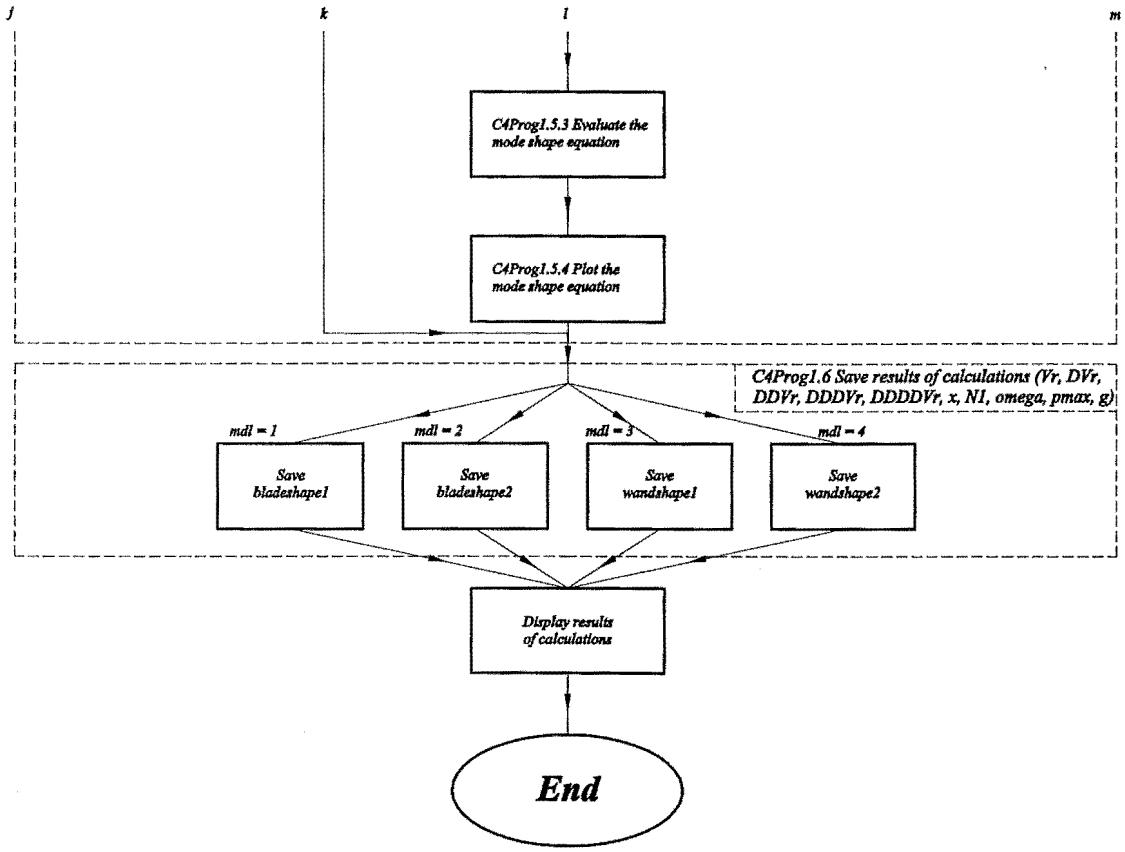

Figure A1 *(cont.)*

Section C4Prog1.1 of procedure *C4Prog1.m* specifies the program control variables *mdl, nmax, nmma, pmax, pldet, calfreq, plmode, results,* and *g*. These parameters define the model type, the number of iterations, and the number of terms generated in calculations.

Section C4Prog1.2 loads the mass and geometric properties for the blade and the wand, and defines the variables for the test calculations.

Section C4Prog1.3 plots either the frequency equation, Equation (4.36) for the case of the blade or Equation (4.45) for the wand. To solve the frequency equation, the terms in the power series $F(x,c)$, Equation (4.15) and the first four derivatives of Equation (4.15) are evaluated for the case where $x = l$ and $c = 2$ & 3. $F(x,c)$ is then assembled in the form

$$F(:,c)= \begin{array}{c} \\ 1 \\ 2 \\ 3 \\ 4 \\ n=0 \\ n=1 \\ . \\ . \\ . \\ n=nmax \end{array} \begin{array}{c} c=2 \\ \left[\begin{array}{c} F(1,1) \\ F(2,1) \\ F(3,1) \\ F(4,1) \\ F(5,1) \\ F(6,1) \\ . \\ . \\ . \\ F((nmax+5),1) \end{array}\right. \end{array} \begin{array}{c} c=3 \\ \left.\begin{array}{c} F(1,2) \\ F(2,2) \\ F(3,2) \\ F(4,2) \\ F(5,2) \\ F(6,2) \\ . \\ . \\ . \\ F((nmax+5),2) \end{array}\right] \end{array} \qquad \text{(A1)}$$

The first four rows in Equation (A1) represent the first four terms in Equation (4.15) evaluated at either the free end of the blade or at the ball end of the wand stem. The remaining rows are calculated from the recurrence relationship Equation (4.21). Equations (4.22), (4.23), and (4.24) were assembled in the same form as Equation (A1), and then the columns summed and the frequency equations, Equations (4.36) and (4.45) were plotted for a range of ω. From the plot generated in Section C4Prog1.3 an upper and lower guess for the natural frequency, ω, may defined by observing where the curve crosses the x axis. Special care is required to check that the slope of the curve changes sign at each crossing and thus a frequency has not been missed. It was interesting to note that for higher frequencies the slope of Equations (4.36) and (4.45) gets increasingly steeper.

Section C4Prog1.4 uses the lower and upper guess for ω obtained from C4Prog1.3 to assemble the matrices $F(\omega_1)$ & $F(\omega_2)$ in the same way as for Equation (A1). From the derivatives of $F(\omega_1)$ & $F(\omega_2)$, the frequency equation, Equation (4.36) or (4.45), is evaluated to give $f(\omega_1)$ & $f(\omega_2)$. After checking that

$f(\omega_1)$ and $f(\omega_2)$ have different signs then a more accurate solution to the frequency equation, ω_{new}, is obtained using the false position interpolation method [Griffiths and Smith (1991)]

$$\omega_{new} = \omega_1 + |f(\omega_1)|\left(\frac{\omega_2 - \omega_1}{|f(\omega_2)| + |f(\omega_1)|}\right) \tag{A2}$$

Using ω_{new} calculated from Equation (A2) a new value for the frequency equation $f(\omega_{new})$ was determined. If the frequency equation has a positive slope ω_1 is set to equal ω_{new} if $f(\omega_{new})$ is negative, else if $f(\omega_{new})$ is positive then ω_2 is set to equal ω_{new}.. Conversely if the frequency equation has a negative slope, then ω_2 is set to equal ω_{new} if $f(\omega_{new})$ is negative, else if $f(\omega_{new})$ is positive ω_1 is set to equal ω_{new}. This procedure is repeated until an accuracy of $|\omega_1-\omega_2| < 1e\text{-}8$ is achieved. After a final value for the system natural frequencies has been determined the constants in the general solution, Equation (4.32) are calculated. For case of the blade, if the constant C_3 in (4.35) is set equal to unity, then C_4 may be calculated as

$$C_4 = -D^3F(l,2)/D^3F(l,3) \tag{A3}$$

Similarly for the case of the wand, if the constant C_3 in Equation (4.44) is set equal to unity, then C_4 may be calculated as

$$C_4 = -ceof(2,1)/ceof(2,2) \tag{A4}$$

Section C4Prog1.5 uses the final values of ω calculated in Section C4Prog1.4 to plot the mode shapes using Equation (4.32). In the numerical procedure, a vector is defined to represent the axial blade or wand stem coordinate at evenly spaced increments. The power series $F(x,c)$, Equation (4.15), is evaluated at

each incremental step along the beam for the case where $c=2$ to evaluate $F21$ and then $c=3$ to evaluate $F31$. $F21$ & $F31$ are assembled in the form

$$
F21(:,:) = \begin{array}{c} \\ 1 \\ 2 \\ 3 \\ 4 \\ n=0 \\ n=1 \\ . \\ . \\ . \\ n=nmax \end{array}
\begin{array}{c}
\begin{array}{cccc} x=0 & x=0.001 & & x=l \end{array} \\
\begin{bmatrix}
F21(1,1) & F21(1,2) & \ldots & F21(1,N1) \\
F21(2,1) & F21(2,2) & \ldots & F21(2,N1) \\
F21(3,1) & F21(3,2) & \ldots & F21(3,N1) \\
F21(4,1) & F21(4,2) & \ldots & F21(4,N1) \\
F21(5,1) & F21(5,2) & \ldots & F21(5,N1) \\
F21(6,1) & F21(6,2) & \ldots & F21(6,N1) \\
. & . & \ldots & \\
. & . & \ldots & \\
. & . & \ldots & \\
 & & \ldots & \\
F21((nmax+5),1) & F21((nmax+5),2)\ldots & & F21((nmax+5),N1)
\end{bmatrix}
\end{array}
$$

(A5)

Equations (4.22), (4.23), (4.24), & (4.25) were assembled in the same form as Equation (A5), and then the columns summed to find the general solution, Equation (4.32), and the first four derivatives of Equation (4.32) at incremental steps along the length of the blade and the wand stem.

B

Computation of natural frequencies and mode shapes – plate modes

The purpose of this section is to explain the analytical and numerical procedures used in the computation of the natural plate frequencies for the blade.

B1 The series expansion for $W(x,y)$

Consider a series expansion for $W(x,y)$ that consists of three characteristic functions $\phi_1(x)$, $\phi_2(x)$, and $\phi_3(x)$ for the modes of vibration along the x axis of the blade and two characteristic functions $\psi_1(y)$ and $\psi_2(y)$ for modes of vibration along the y axis of the blade. Expanding Equation (5.4) will in this case give

$$W(x,y) = A_{11}\phi_1\psi_1 + A_{12}\phi_1\psi_2 + A_{21}\phi_2\psi_1 + A_{22}\phi_2\psi_2 + A_{31}\phi_3\psi_1 + A_{32}\phi_3\psi_2 \qquad \text{(B1)}$$

From Equation (B1) the components of Equations (5.1) and (5.3) will take the form

$$W(x,y)^2 = 2A_{mn}\phi_m\psi_n A_{ik}\phi_i\psi_k \qquad \text{(B2a)}$$

$$\left(\frac{\partial W(x,y)}{\partial x}\right)^2 = 2A_{mn}\phi'_m\psi_n A_{ik}\phi'_i\psi_k \qquad \text{(B2b)}$$

$$\left(\frac{\partial W(x,y)}{\partial y}\right)^2 = 2A_{mn}\phi_m\psi'_n A_{ik}\phi_i\psi'_k \qquad \text{(B2c)}$$

$$\frac{\partial W(x,y)}{\partial x}\frac{\partial W(x,y)}{\partial y} = A_{mn}\phi'_m\psi_n A_{ik}\phi_i\psi'_k + A_{mn}\phi_m\psi'_n A_{ik}\phi'_i\psi_k \tag{B2d}$$

$$\left(\frac{\partial^2 W(x,y)}{\partial x\partial y}\right)^2 = 2A_{mn}\phi'_m\psi'_n A_{ik}\phi'_i\psi'_k \tag{B2e}$$

$$\left(\frac{\partial^2 W(x,y)}{\partial x^2}\right)^2 = 2A_{mn}\phi''_m\psi_n A_{ik}\phi''_i\psi_k \tag{B2f}$$

$$\left(\frac{\partial^2 W(x,y)}{\partial y^2}\right)^2 = 2A_{mn}\phi_m\psi''_n A_{ik}\phi_i\psi''_k \tag{B2g}$$

$$\left(\frac{\partial^2 W(x,y)}{\partial x^2}\frac{\partial^2 W(x,y)}{\partial y^2}\right) = A_{mn}\phi''_m\psi_n A_{ik}\phi_i\psi'' + A_{mn}\phi_m\psi''_n A_{ik}\phi''_i\psi_k \tag{B2h}$$

Differentiating Equations (B2a) to (B2h) with respect to the coefficient A_{ik} gives

$$\frac{\partial W(x,y)^2}{\partial A_{ik}} = 2A_{mn}\phi_m\psi_n\phi_i\psi_k \tag{B3a}$$

$$\frac{\partial\left(\frac{\partial W(x,y)}{\partial x}\right)^2}{\partial A_{ik}} = 2A_{mn}\phi'_m\psi_n\phi'_i\psi_k \tag{B3b}$$

$$\frac{\partial\left(\frac{\partial W(x,y)}{\partial y}\right)^2}{\partial A_{ik}} = 2A_{mn}\phi_m\psi'_n\phi_i\psi'_k \tag{B3c}$$

$$\frac{\partial\left(\frac{\partial W(x,y)}{\partial x}\frac{\partial W(x,y)}{\partial y}\right)}{\partial A_{ik}} = A_{mn}\phi'_m\psi_n\phi_i\psi'_k + A_{mn}\phi_m\psi'_n\phi'_i\psi_k \tag{B3d}$$

$$\frac{\partial\left(\frac{\partial^2 W(x,y)}{\partial x \partial y}\right)^2}{\partial A_{ik}} = 2A_{mn}\phi'_m\psi'_n\phi'_i\psi'_k \tag{B3e}$$

$$\frac{\partial\left(\frac{\partial^2 W(x,y)}{\partial x^2}\right)^2}{\partial A_{ik}} = 2A_{mn}\phi''_m\psi_n\phi''_i\psi_k \tag{B3f}$$

$$\frac{\partial\left(\frac{\partial^2 W(x,y)}{\partial y^2}\right)^2}{\partial A_{ik}} = 2A_{mn}\phi_m\psi''_n\phi_i\psi''_k \tag{B3g}$$

$$\frac{\partial\left(\frac{\partial^2 W(x,y)}{\partial x^2}\frac{\partial^2 W(x,y)}{\partial y^2}\right)}{\partial A_{ik}} = A_{mn}\phi''_m\psi_n\phi_i\psi'' + A_{mn}\phi_m\psi''_n\phi''_i\psi_k \tag{B3h}$$

B2 Numerical procedure for generating orthogonal polynomials

Considering the form of Equations (5.14a) to (5.14e), the orthogonal polynomial functions and their derivatives may be formulated using numerical procedures. This section presents the numerical procedures adopted in this study.

B2.1 Clamped-free modes

Considering the form of the starting function, Equation (5.15) the general form of the clamped-free modes will *(for a blade length a)* be

$$\phi_m\left(\frac{x}{a}\right) = a_m \sum_{1}^{r} \hat{a}_{m,r}\left(\frac{x}{a}\right)^{r+1} \tag{B4}$$

The coefficient a_m may be appropriately chosen so as to normalise $\phi_m\left(\frac{x}{a}\right)$ such that

$$\int_0^a \phi_m^2\left(\frac{x}{a}\right)dx = a \tag{B5}$$

Substituting Equation (B4) into (B5) and integrating gives

$$a_m = \sqrt{\frac{a}{\sum_1^r \sum_1^s \frac{\hat{a}_{m,r}\hat{a}_{m,s}a}{r+s+3}}} \tag{B6}$$

It is convenient to write the normalised modes and the first two derivatives of the normalised modes in the form

$$\phi_m\left(\frac{x}{a}\right) = \sum_1^r \tilde{a}_{m,r}\left(\frac{x}{a}\right)^{r+1} \tag{B7a}$$

$$\frac{d\phi_m}{dx}\left(\frac{x}{a}\right) = \sum_1^r (r+1)\tilde{a}_{m,r}\frac{x^r}{a^{r+1}} \tag{B7b}$$

$$\frac{d^2\phi_m}{dx^2}\left(\frac{x}{a}\right) = \frac{2\tilde{a}_{m,r}}{a^2} + \sum_2^r (r^2+r)\tilde{a}_{m,r}\frac{x^{r-1}}{a^{r+1}} \tag{B7c}$$

$$where \quad \tilde{a}_{m,r} = a_m\hat{a}_{m,r}$$

Substituting Equation (B7a) into Equations (5.14d) and (5.14e) and integrating gives

$$B_m = \frac{\sum_1^r \sum_1^s \frac{\tilde{a}_{m-1,r}\tilde{a}_{m-1,s}a}{r+s+4}}{\sum_1^r \sum_1^s \frac{\tilde{a}_{m-1,r}\tilde{a}_{m-1,s}a}{r+s+3}} \tag{B8}$$

$$C_m = \frac{\sum_1^r \sum_1^s \frac{\tilde{a}_{m-1,r}\tilde{a}_{m-2,s}a}{r+s+4}}{\sum_1^r \sum_1^s \frac{\tilde{a}_{m-2,r}\tilde{a}_{m-2,s}a}{r+s+3}} \tag{B9}$$

Considering the form of Equations (B7a) to (B7c), it may be shown that the products of characteristic functions of interest *(these are in the general form of Equations (5.22) & (5.23))* may be written in the following form

$$E_{m,i}^{0,0} = \sum_1^r \sum_1^s \frac{\tilde{a}_{m,r}\tilde{a}_{m,s}a}{r+s+3} \tag{B10}$$

$$E_{m,i}^{1,1} = \sum_1^r \sum_1^s \frac{(r+1)(s+1)\tilde{a}_{m,r}\tilde{a}_{m,s}}{(r+s+1)a} \tag{B11}$$

$$E_{m,i}^{0,2} = \sum_1^r \sum_1^s \tilde{a}_{m,r}\left[\frac{2\tilde{a}_{m,1}}{a^2} + \frac{(s^2+s)\tilde{a}_{m,s}}{(r+s+1)a}\right] \tag{B12}$$

$$EAX_{m,i}^{1,1} = \sum_1^r \sum_1^s \frac{(r+1)(s+1)\tilde{a}_{m,r}\tilde{a}_{m,s}}{(r+s+1)(r+s+2)} \tag{B13}$$

$$E_{m,i}^{2,2} = \sum_1^r \sum_1^s \frac{\left(\frac{2\tilde{a}_{m,1}}{a^2} + (r^2+r)\tilde{a}_{m,r}\right)\left(\frac{2\tilde{a}_{m,1}}{a^2} + (s^2+s)\tilde{a}_{m,s}\right)}{(r+s-1)a^3} \tag{B14}$$

B2.2 Free-free modes

For free-free modes the coefficient b_1 in Equation (5.16) may be set to equal one and the general form for the free-free modes will *(for a blade width b)* be

$$\psi_n\left(\frac{y}{b}\right) = b_{n,1} + b_n \sum_2^r \hat{b}_{n,r}\left(\frac{y}{b}\right)^{r-1} \tag{B15}$$

In this case the coefficient b_n may be chosen so as to normalise $\psi_n\left(\frac{y}{b}\right)$ such that

$$\int_0^b \psi_n^2\left(\frac{y}{b}\right)dx = b \tag{B16}$$

Substituting Equation (B15) into (B16) and integrating gives

$$b_n = \sqrt{\frac{b}{\sum_1^r \sum_1^s \frac{\hat{b}_{n,r}\hat{b}_{n,s}b}{r+s-1}}} \tag{B17}$$

The first two derivatives of the normalised modes may therefore be more conveniently written in the form

$$\psi_n\left(\frac{y}{b}\right) = \sum_1^r \tilde{b}_{n,r}\left(\frac{y}{b}\right)^{r-1} \tag{B18a}$$

$$\frac{d\psi_n}{dy}\left(\frac{y}{b}\right) = \sum_2^r (r-1)\tilde{b}_{n,r}\frac{y^{r-2}}{b^{r-1}} \tag{B18b}$$

$$\frac{d^2\psi_n}{dx^2}\left(\frac{y}{b}\right) = \sum_3^r (r-1)(r-2)\tilde{b}_{n,r}\frac{y^{r-3}}{b^{r-1}} \tag{B18c}$$

$$where \quad \tilde{b}_{n,r} = b_n\hat{b}_{n,r}$$

Substituting Equation (B18a) into Equations (5.14d) and (5.14e) and integrating gives

$$B_n = \frac{\sum_{1}^{r}\sum_{1}^{s} \frac{\tilde{b}_{n-1,r}\tilde{b}_{n-1,s}b}{r+s}}{\sum_{1}^{r}\sum_{1}^{s} \frac{\tilde{b}_{n-1,r}\tilde{b}_{n-1,s}b}{r+s-1}} \tag{B19}$$

$$C_n = \frac{\sum_{1}^{r}\sum_{1}^{s} \frac{\tilde{b}_{n-1,r}\tilde{b}_{n-2,s}b}{r+s}}{\sum_{1}^{r}\sum_{1}^{s} \frac{\tilde{b}_{n-2,r}\tilde{b}_{n-2,s}b}{r+s-1}} \tag{B20}$$

Considering the form of Equations (B18a) to (B18c), it may be shown that the products of characteristic functions of interest *(from Equation (5.24))* may be written in the form

$$F_{n,k}^{0,0} = \sum_{1}^{r}\sum_{1}^{s} \frac{\tilde{b}_{n,r}\tilde{b}_{k,s}b}{r+s-1} \tag{B21}$$

$$F_{n,k}^{1,1} = \sum_{2}^{r}\sum_{2}^{s} \frac{\tilde{b}_{n,r}\tilde{b}_{k,s}}{(r+s-3)b} \tag{B22}$$

$$F_{n,k}^{0,2} = \sum_{1}^{r}\sum_{3}^{s} \frac{(s-1)(s-2)\tilde{b}_{n,r}\tilde{b}_{k,s}}{(r+s-3)b} \tag{B23}$$

$$F_{n,k}^{2,2} = \sum_{3}^{r}\sum_{3}^{s} \frac{(r-1)(r-2)(s-1)(s-2)\tilde{b}_{n,r}\tilde{b}_{k,s}}{(r+s-5)b^3} \tag{B24}$$

B3 Calculated integrals of characteristic functions

Table B1 *Evaluated integrals of characteristic beam functions for clamped/free modes*

$E^{1,1}_{m,i}$	$i = 1$	$i = 2$	$i = 3$	$i = 4$	$i = 5$
$m = 1$	4.647778	-7.379875	3.941515	-6.593389	4.591978
$m = 2$	-7.379875	32.417399	-22.352444	13.582472	-22.839532
$m = 3$	3.941515	-22.352444	77.298891	-35.648271	20.162023
$m = 4$	-6.593389	13.582472	-35.648271	142.901851	-48.71963
$m = 5$	4.591978	-22.839532	20.162023	-48.71963	228.133238
$E^{0,2}_{m,i}$					
$m = 1$	0.858244	-11.743238	27.453149	-37.390250	51.956613
$m = 2$	1.873853	-13.294285	-9.042220	30.401167	-33.709060
$m = 3$	1.564506	3.229331	-45.904227	-8.335368	36.386569
$m = 4$	1.087366	5.540642	4.253606	-98.918210	-7.828961
$m = 5$	0.914043	3.716420	11.232638	4.7359986	-171.584653
$EAX^{1,1}_{m,i}$					
$m = 1$	1.570878	-0.422320	-1.072085	-0.873137	-0.762326
$m = 2$	-0.422320	8.647142	1.890056	-3.643386	-3.062803
$m = 3$	-1.072085	1.890056	24.952112	8.338292	-7.141090
$m = 4$	-0.873137	-3.643386	8.338292	51.459102	19.019136
$m = 5$	-0.762326	-3.062803	-7.141090	19.019136	87.792320

Table B2 *Evaluated integrals of characteristic beam functions for free/free modes*

$F_{n,k}^{1,1}$	$k = 1$	$k = 2$	$k = 3$	$k = 4$	$k = 5$
$n = 1$	0	0	0	0	0
$n = 2$	0	12	0	13.856406	0
$n = 3$	0	0	49.480823	0	35.377511
$n = 4$	0	13.856406	0	108.924592	0.000002
$n = 5$	0	0	35.377511	0.000002	186.866710
$F_{n,k}^{0,2}$					
$n = 1$	0	0	18.589102	0	43.980956
$n = 2$	0	0	0	40.594484	0
$n = 3$	0	0	-12.302619	0	52.584400
$n = 4$	0	0	0	-46.050120	-0.000002
$n = 5$	0	0	1.800692	0	-98.904801

Table B3 *Evaluated integrals of characteristic orthogonal polynomials for clamped/free modes*

$E^{1,1}_{m,i}$	$i = 1$	$i = 2$	$i = 3$	$i = 4$	$i = 5$
$m = 1$	1.288147	2.327362	1.722122	2.815004	2.348916
$m = 2$	2.327362	12.738289	13.639270	13.509195	17.142711
$m = 3$	1.722122	13.639270	37.059394	35.741813	37.696283
$m = 4$	2.815004	13.509195	35.741813	78.100528	71.585567
$m = 5$	2.348916	17.142711	37.696283	71.585567	139.773849
$E^{0,2}_{m,i}$					
$m = 1$	0.214691	6.692987	20.437583	38.791768	65.670991
$m = 2$	-0.444854	-1.439086	14.118744	38.608890	68.061384
$m = 3$	0.457227	-0.558363	-4.924384	24.594463	60.943138
$m = 4$	-0.379334	1.110205	0.172711	-10.667886	38.655191
$m = 5$	0.316739	-1.142894	1.609421	2.214320	-19.123758
$EAX^{1,1}_{m,i}$					
$m = 1$	1.557692	0.246244	-0.926424	1.014645	-0.924731
$m = 2$	0.246244	8.088543	-0.891814	-2.222014	3.098498
$m = 3$	-0.926424	-0.891814	20.846998	-5.056047	-2.765336
$m = 4$	1.014645	-2.222014	-5.056047	41.381805	-13.821509
$m = 5$	-0.924731	3.098498	-2.765336	-13.821509	71.277349

Table B4 *Evaluated integrals of characteristic orthogonal polynomials for free/free modes*

$F_{n,k}^{1,1}$	$k = 1$	$k = 2$	$k = 3$	$k = 4$	$k = 5$
$n = 1$	0	0	0	0	0
$n = 2$	0	27.906977	0	42.628611	0
$n = 3$	0	0	139.534884	0	187.205691
$n = 4$	0	42.628611	0	390.69767	0
$n = 5$	0	0	187.205691	0	837.209302
$F_{n,k}^{0,2}$					
$n = 1$	0	0	62.401897	0	279.069767
$n = 2$	0	0	0	213.143056	0
$n = 3$	0	0	0	0	436.813280
$n = 4$	0	0	0	0	0
$n = 5$	0	0	0	0	0

C

The numerical computation for the mathematical model

The purpose of this section is to explain the numerical procedures developed for the solution of the mathematical model discussed in Sections 6.1 - 6.5.

The equations for the mathematical model are solved numerically using 10 procedures. These 10 procedures are formulated as script files *(sometimes referred to as M-files [MathWorks (1995)])*, and are evaluated using the MATLAB computational software program. The procedures used in the mathematical model are, *C2Prog1.m, C4Prog1.m, C6Prog1.m, C6Prog2.m, C6Prog3.m, C6Prog4.m, C6Prog5.m, C6Prog6.m, C6Prog7.m,* and *C6Prog8.m.* The script files for these procedures saved on the CD-ROM.

Data is shared between procedures using MATLAB MAT-files. MAT-files are full-precision *(16 decimal places)*, binary, MATLAB format files that store results of calculations by using the *save* command. Procedures retrieve results stored in MAT-files using the *load* command.

Successful numerical computation of the mathematical model requires the execution of the following 10 procedures and in the following order using MATLAB.

C1 Procedure *C2Prog1.m* – specifying geometric and material properties for the blade and the wand

The geometric and material properties for the blade and the wand are listed in *C2Prog1.m*. Running *C2Prog1.m* in MATLAB stores values of the geometric and material properties in the appropriate MAT-files. The values stored are

$$l,\ b,\ d,\ A,\ I,\ E,\ \rho,\ s,\ I_{cb},\ M_{cb},\ P_b,\ r,\ R$$

C2 Procedure *C4Prog1.m* – calculating the natural frequencies and mode shapes

The mathematical model uses the solution for the natural frequencies and mode shapes for the vibration of the blade and the wand as discussed in Chapter 4. *C4Prog1.m* saves the following variables that are used in the mathematical model

$$g,\ omega,\ p_{max},\ x,\ DVr,\ DDVr,\ DDDVr,\ DDDDVr,\ N1,\ Vr$$

C3 Procedure *C6Prog1.m* – scaling the mode shapes, and calculating the equivalent mass and stiffness properties

Procedure *C6Prog1.m* scales the mode shapes calculated in *C4Prog1.m* to equal unity at the contact height. The modal bending moments and shear forces corresponding to the scaled mode shapes are then calculated.

Procedure *C6Prog1.m* calculates the integrals of the products of characteristic functions. For convenience, the terms *E11* & *E22*, are defined to represent Equations (6.8) & (6.9), and V_{rshsq} & E_{vsq} are defined to represent the product terms inside the integrals in Equations (6.8) & (6.9) respectively. V_{rshsq} is equivalent to the dot product of the two mode shape vectors $\hat{V}_r(x)$ & $\hat{V}_s(x)$. For

the purpose of the numerical integration it was necessary, in Section C6Prog1.5 of *C6Prog1.m*, to assemble V_{rshsq} in the form shown in Equation (6.11)

$$V_{rshsq}(((r-1)s_{\max}+s),:) = \begin{array}{l} \\ r=1,s=1 \\ r=1,s=2 \\ r=1,s=3 \\ \vdots \\ r=1,s=s_{max} \\ r=2,s=1 \\ r=2,s=2 \\ r=2,s=3 \\ \vdots \\ r=2,s=s_{max} \\ \vdots \\ r=r_{max},s=1 \\ r=r_{max},s=2 \\ r=r_{max},s=3 \\ \vdots \\ r=r_{max},s=s_{max} \end{array} \begin{array}{c} x=0,\ x=0.001,\ x=0.002,\ \ldots\ x=l \\ \left[\begin{array}{ccc} V_{rshsq}(1,1) & \ldots & V_{rshsq}(1,l) \\ V_{rshsq}(2,1) & \ldots & V_{rshsq}(1,l) \\ V_{rshsq}(3,1) & \ldots & V_{rshsq}(1,l) \\ & & \\ V_{rshsq}(s_{max},1) & \ldots & V_{rshsq}(s_{max},l) \\ V_{rshsq}(s_{max}+1,1) & \ldots & V_{rshsq}(s_{max}+1,l) \\ V_{rshsq}(s_{max}+2,1) & \ldots & V_{rshsq}(s_{max}+2,l) \\ V_{rshsq}(s_{max}+3,1) & \ldots & V_{rshsq}(s_{max}+3,l) \\ & & \\ V_{rshsq}(2s_{max},1) & \ldots & V_{rshsq}(2s_{max},l) \\ & & \\ V_{rshsq}(((r_{max}-1)s_{max}+1),1) & \ldots & V_{rshsq}(((r_{max}-1)s_{max}+1),l) \\ V_{rshsq}(((r_{max}-1)s_{max}+2),1) & \ldots & V_{rshsq}(((r_{max}-1)s_{max}+1),l) \\ V_{rshsq}(((r_{max}-1)s_{max}+3),1) & \ldots & V_{rshsq}(((r_{max}-1)s_{max}+1),l) \\ & & \\ V_{rshsq}(r_{max},1) & \ldots & V_{rshsq}(r_{max},l) \end{array}\right] \end{array} \quad \text{(C1)}$$

E11 was evaluated using the *trapz.m* numerical integration function in MATLAB. The function, *trapz.m*, uses the trapezoidal numerical integration procedure [MathWorks (1995), Forsythe et al. (1977)]. In Sections C6Prog1.4 and C6Prog1.5 of *C6Prog1.m* each of the rows in Equation (C1) were integrated over the interval from $x=0$ to $x=l$ *(taking 1mm steps along the length dimension in the case of the original blade)* to evaluate *E11*. Adopting a similar E22 was evaluated by integrating the rows in the matrix E_{vsq}. Results of these calculations are as follows

$$E11_{r,s} = \begin{bmatrix} 21.43859567 & -0.00000419 & 0.00000454 & -0.00001192 \\ -0.00000419 & 1.38377562 & -0.00000156 & 0.00000381 \\ 0.00000454 & -0.00000156 & 0.71735879 & -0.00000330 \\ -0.00001192 & 0.00000381 & -0.00000330 & 2.73644195 \end{bmatrix} \quad \text{(C2a)}$$

$$E22_{r,s} = \begin{bmatrix} 229.72545061 & -0.00004491 & 0.00004866 & -0.00012771 \\ -0.00566216 & 1869.55250957 & -0.00210435 & 0.00514318 \\ 0.05150488 & -0.01766634 & 8136.47604093 & -0.03742364 \\ -0.52837726 & 0.16876291 & -0.14627272 & 121311.91463796 \end{bmatrix} \quad \text{(C2b)}$$

It can be seen that the diagonal terms in Equations (C2a) and (C2b) are dominant and thus the modes are orthogonal. The degree of orthogonality may be more clearly observed by normalising the matrices $E11$ and $E22$ to give $E11nm$ and $E22nm$.

$$E11nm_{r,s} = \frac{E11_{r,s}}{\sqrt{E11_{r,r}}\sqrt{E11_{s,s}}} \quad \text{(C3)}$$

The normalised matrices for integrals of characteristic functions are

$$E11nm_{r,s} = \begin{bmatrix} 1.00000000 & -0.00000077 & 0.00000116 & -0.00000156 \\ -0.00000077 & 1.00000000 & -0.00000156 & 0.00000196 \\ 0.00000116 & -0.00000156 & 1.00000000 & -0.00000235 \\ -0.00000156 & 0.00000196 & -0.00000235 & 1.00000000 \end{bmatrix} \quad \text{(C4a)}$$

$$E22nm_{r,s} = \begin{bmatrix} 1.00000000 & -0.00000006 & 0.00000004 & -0.00000002 \\ -0.00000864 & 1.00000000 & -0.00000054 & 0.00000034 \\ 0.00003767 & -0.00000453 & 1.00000000 & -0.00000119 \\ -0.00010009 & 0.00001121 & -0.00000466 & 1.00000000 \end{bmatrix} \quad \text{(C4b)}$$

In Section C6Prog1.8 the modal mass and stiffness constants, and the scaled mode shapes for the blade and wand are saved as MAT-files. The variables stored for use in other numerical procedures for the blade are

w, x, s, Err, ErSqr, ErrEr, FRQ0, FSQ0, FTQ0, FUQ0, Mrr, Mss, Mtt, Muu, MRQ0, MSQ0, MTQ0, MUQ0, N05, Srr, Sss, Stt, Suu, RQ, SQ, TQ, UQ

and for the wand are

bcx2, bcy2, k_{cb}*, xw, Mw, NLw, Sw, WQ,*

C4 Procedure *C6Prog2.m* – evaluating the damping constants

Procedure *C6Prog2.m* uses the blade displacements obtained from experimental observations of the original sculpture to calculate the damping constants for the blade and wand modes. The damping constants are stored in *dmpconst.mat* and *2xdmpconst.mat* for the original and scaled works respectively. The variables stored are

crr, css, ctt, cuu, Ccb, Crr, Css, Ctt, Cuu, Cw,

C5 Procedure *C6Prog3.m* - defining the model type

C6Prog3.m defines the model type i.e. specifies the size *Blade* to be modelled *(either the original size or the scaled size)*, sets the ground motion characteristics for the blade, defines the period in the performance routine for *Blade* to be modelled, and sets the initial blade-wand separation distance. The model parameters are stored in *model.mat,* these are

accel, bwmdl, omega, wand, DELTA, H, Ta, Tplat, TH

C6 Procedure *C6Prog4.m* – setting initial conditions for modelling

C6Prog4.m sets the initial times, displacements, velocities, and loads for the first time period in the mathematical model. These initial conditions are generally all set to zero for the blade starting at rest. The purpose of defining the initial conditions independently is so that they may be reset for debugging purposes. The variables stored are

fbmax, dqwf, dqrf, dqsf, dquf, qwf, qrf, qsf, quf, tc, ts, tsp, FVPmax, MVPmax

C7 Procedure *C6Prog5.m* - solving the equations of motion for the non-contact condition

The equations of motion for the forced vibration of the blade when not in contact, Equations (6.15), and the equations of motion for the free vibration of the equivalent wand, Equations (6.24), were solved using the *ode45* function in MATLAB. *ode45* is an automatic step-size *Runge-Kutta-Fehlberg* integration method [Forsythe et al. (1977)] and uses a fourth and fifth order pair of formulas.

Solution using the *Runge-Kutta-Fehlberg* integration method requires writing the equations of motion as an equivalent set of first order differential equations. For the case where the first *wand* mode and the first four *blade* modes are considered this requires defining

$$y_1 = q_w, \quad y_2 = q_r, \quad y_3 = q_s, \quad y_4 = q_t, \quad y_5 = q_u$$

$$\dot{y}_1 = y_6, \quad \dot{y}_2 = y_7, \quad \dot{y}_3 = y_8, \quad \dot{y}_4 = y_9, \quad \dot{y}_5 = y_{10} \qquad \text{(C5)}$$

Substituting the terms in (C5) into Equations (6.15) & (6.24) gives the following equivalent set of first order differential equations for the non-contact condition

$$\dot{y}_6 = \frac{1}{M_w}[-C_w y_6 - S_w y_1]$$

$$\dot{y}_7 = \frac{1}{M_r}\left[(w\Omega - c_r i)\Omega\Delta e^{i\Omega t}\int_0^l \hat{V}_r(x)dx - C_r\, y_7 - S_r\, y_2\right]$$

$$\dot{y}_8 = \frac{1}{M_s}\left[(w\Omega - c_s i)\Omega\Delta e^{i\Omega t}\int_0^l \hat{V}_s(x)dx - C_s\, y_8 - S_s\, y_3\right]$$

$$\dot{y}_9 = \frac{1}{M_t}\left[(w\Omega - c_t i)\Omega\Delta e^{i\Omega t}\int_0^l \hat{V}_t(x)dx - C_t\, y_9 - S_t\, y_4\right] \qquad \text{(C6)}$$

$$\dot{y}_{10} = \frac{1}{M_u}\left[(w\Omega - c_u i)\Omega\Delta e^{i\Omega t}\int_0^l \hat{V}_u(x)dx - C_u\, y_{10} - S_u\, y_5\right]$$

Equations (C6) are listed in procedure *C6Prog5.m*. *C6Prog5.m* is a *function M-file* [MathWorks (1995)] that returns the derivatives for Equations (C6) given a specified time increment and a set of initial conditions. *C6Prog5.m* loads the constants needed in Equation (C6) from the results of *C6Prog1.m*, and *C6Prog2.m*.

C8 Procedure *C6Prog6.m* - solving the equations of motion for the contact condition

Using a similar approach to that taken in Section C.7, the equations of motion for the contact condition, Equations (6.58) & (6.59), will take the form

$$\dot{y}_6 = \frac{1}{M_w}\left[\begin{array}{l}(y_7+y_8+y_9+y_{10})C_{cb}+(y_2+y_3+y_4+y_5-H)k_{cb}- \\ (C_w+C_{cb})y_6-(S_w+k_{cb})y_1\end{array}\right]$$

$$\dot{y}_7 = \frac{1}{M_r}\left[\begin{array}{l}(w\Omega-c_r i)\Omega\Delta e^{i\Omega t}\int_0^l \hat{V}_r(x)dx+(y_6-y_8-y_9-y_{10})C_{cb}+ \\ (y_1+H-y_3-y_4-y_5)k_{cb}-(C_r+C_{cb})y_7-(S_w+k_{cb})y_2\end{array}\right]$$

$$\dot{y}_8 = \frac{1}{M_r}\left[\begin{array}{l}(w\Omega-c_s i)\Omega\Delta e^{i\Omega t}\int_0^l \hat{V}_s(x)dx+(y_6-y_7-y_9-y_{10})C_{cb}+ \\ (y_1+H-y_2-y_4-y_5)k_{cb}-(C_s+C_{cb})y_8-(S_s+k_{cb})y_3\end{array}\right]$$

$$\dot{y}_9 = \frac{1}{M_r}\left[\begin{array}{l}(w\Omega-c_t i)\Omega\Delta e^{i\Omega t}\int_0^l \hat{V}_t(x)dx+(y_6-y_7-y_8-y_{10})C_{cb}+ \\ (y_1+H-y_2-y_3-y_5)k_{cb}-(C_t+C_{cb})y_9-(S_w+k_{cb})y_4\end{array}\right]$$

$$\dot{y}_{10} = \frac{1}{M_r}\left[\begin{array}{l}(w\Omega-c_u i)\Omega\Delta e^{i\Omega t}\int_0^l \hat{V}_u(x)dx+(y_6-y_7-y_8-y_9)C_{cb}+ \\ (y_1+H-y_2-y_3-y_4)k_{cb}-(C_u+C_{cb})y_{10}-(S_w+k_{cb})y_5\end{array}\right] \qquad \text{(C7)}$$

Equations (C7) are listed in the function M-file *C6Prog6.m*. *C6Prog6.m* calculates the derivatives for Equations (C7) for a specified time interval and set of initial conditions. *C6Prog6.m* loads the constants needed in Equations (C7) from the results of *C6Prog1.m*, and *C6Prog2.m*.

C9 Procedure *C6Prog7.m* - running the mathematical model

Procedure *C6Prog7.m* assembles the results of the procedures discussed in Sections C1 – C8 and calculates the time history response for the forced damped vibration of the blade and the wand. Procedure *C6Prog7.m*, summarised here, is the principal numerical procedure used to solve the mathematical model. The logical flow diagram for *C6Prog7.m* is shown in Figure C1.

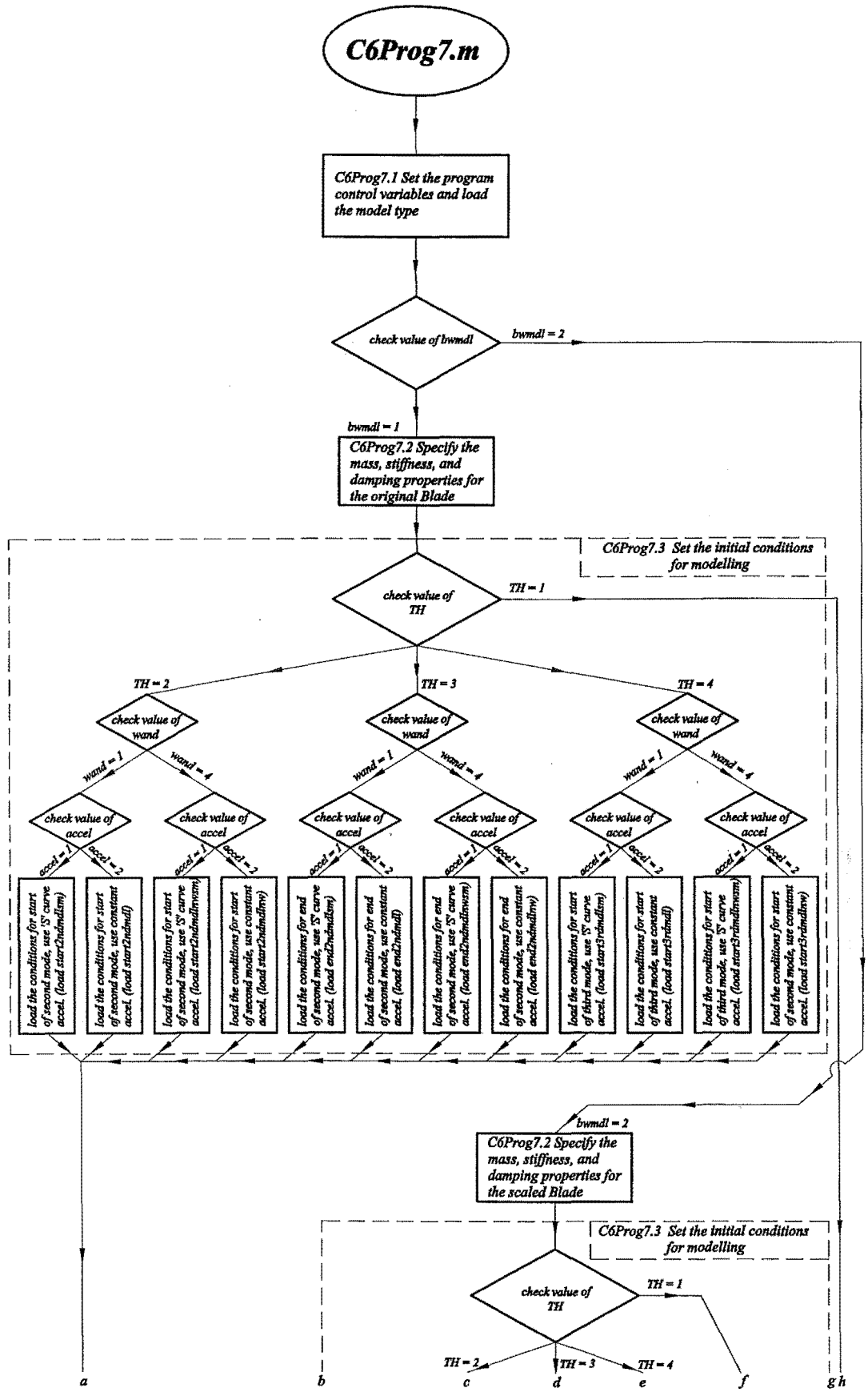

Figure C1 *Logical flow diagram for the mathematical model, C6Prog7.m*

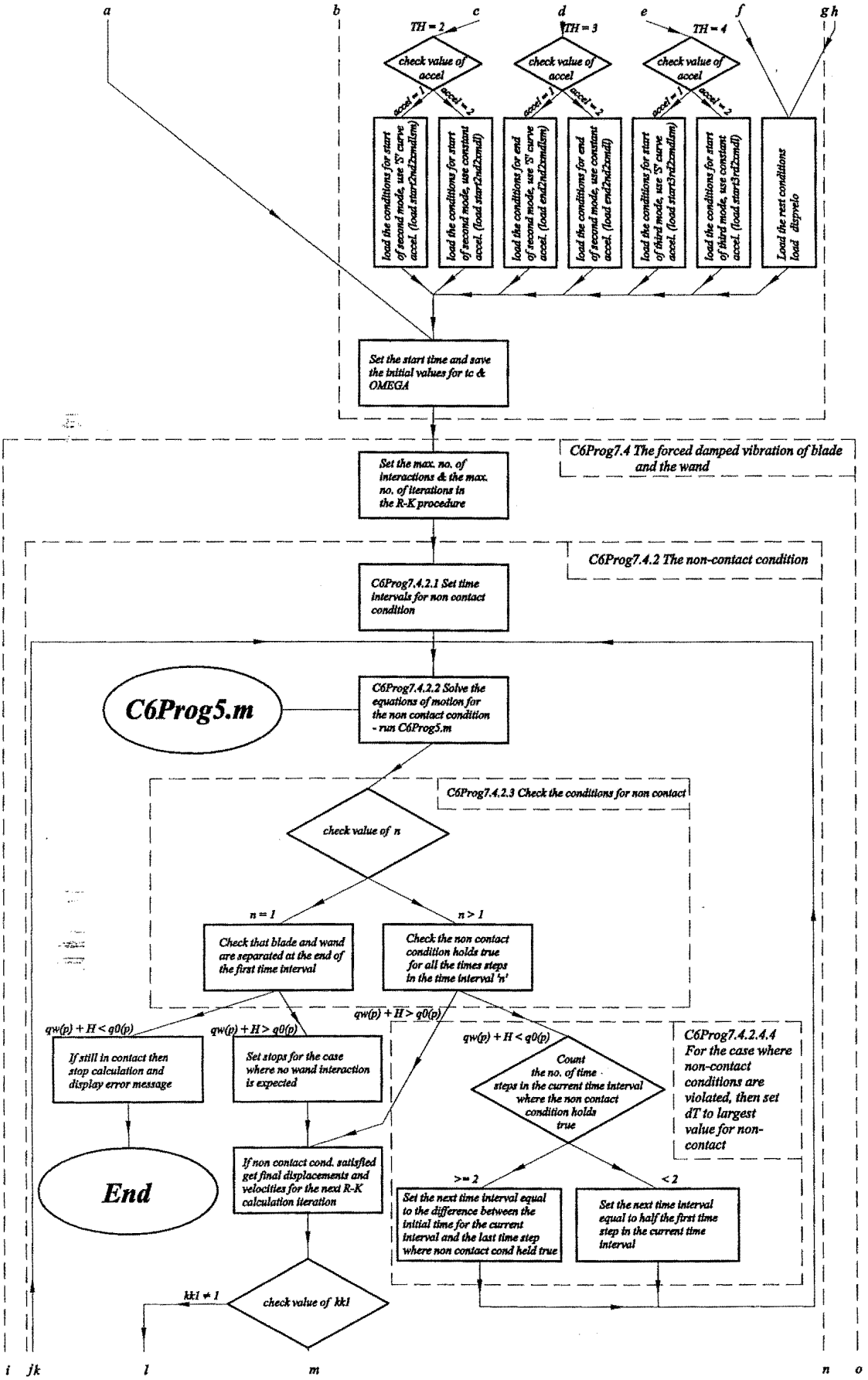

Figure C1 *(cont.)*

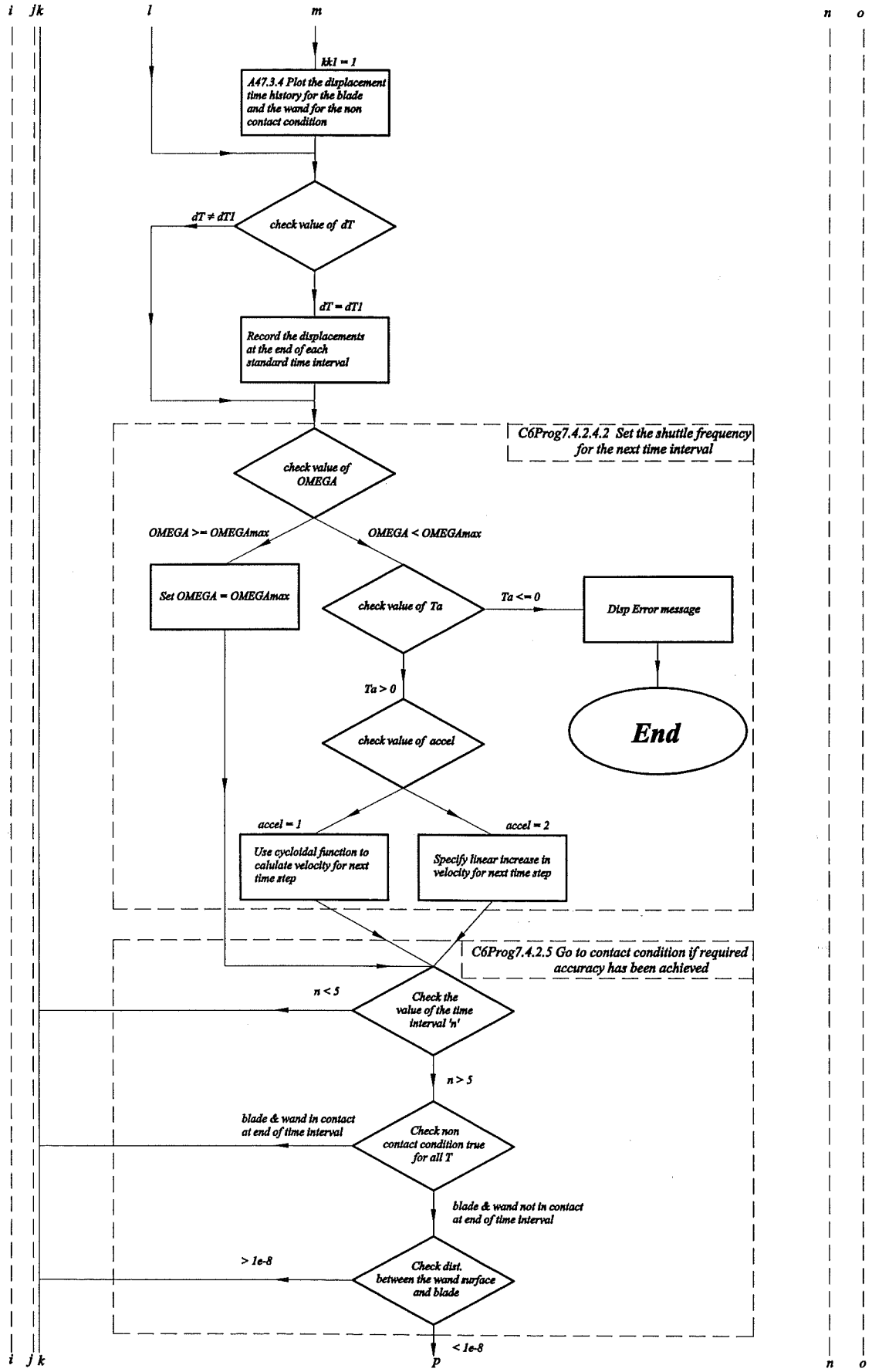

Figure C1 *(cont.)*

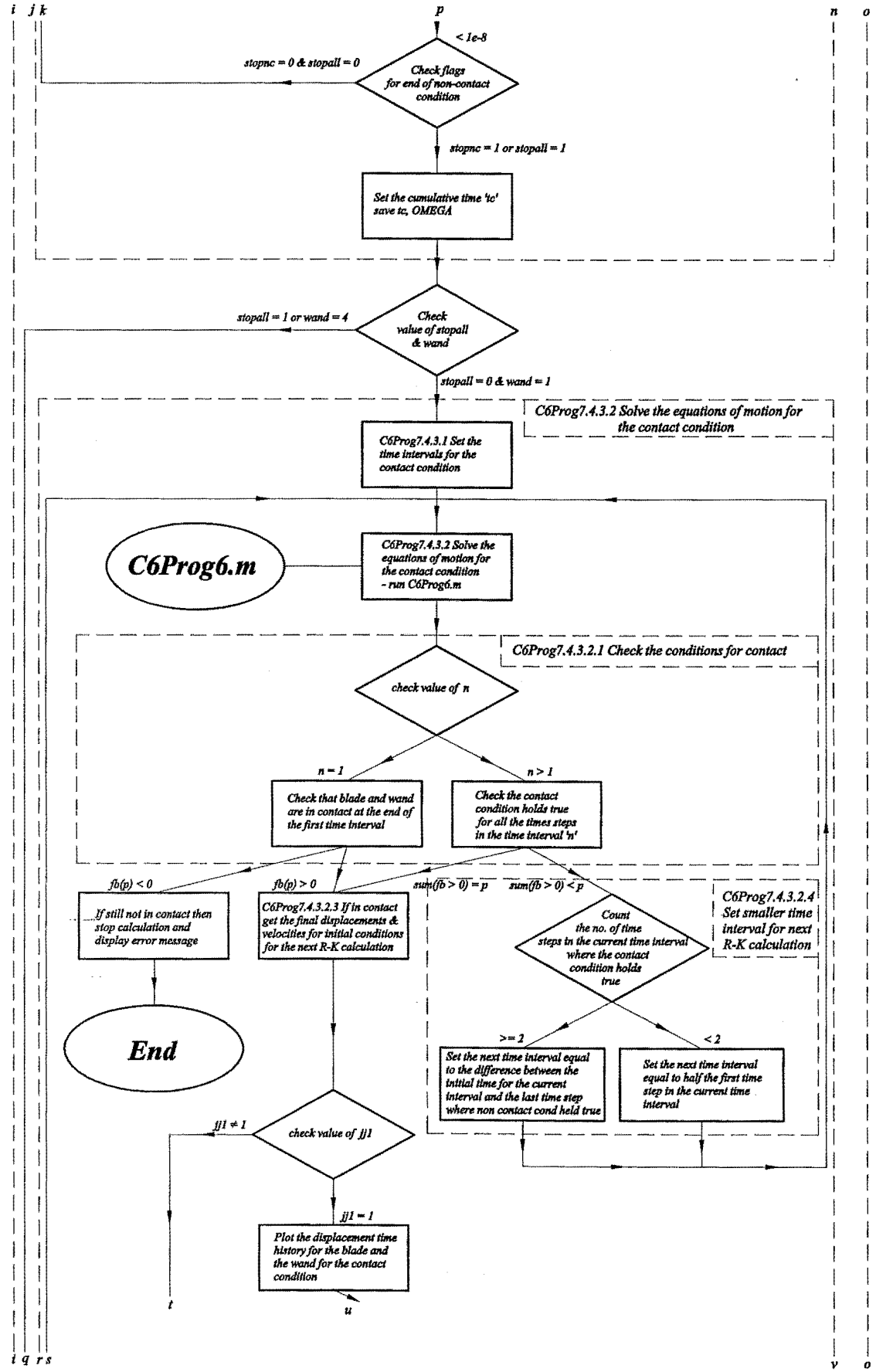

Figure C1 *(cont.)*

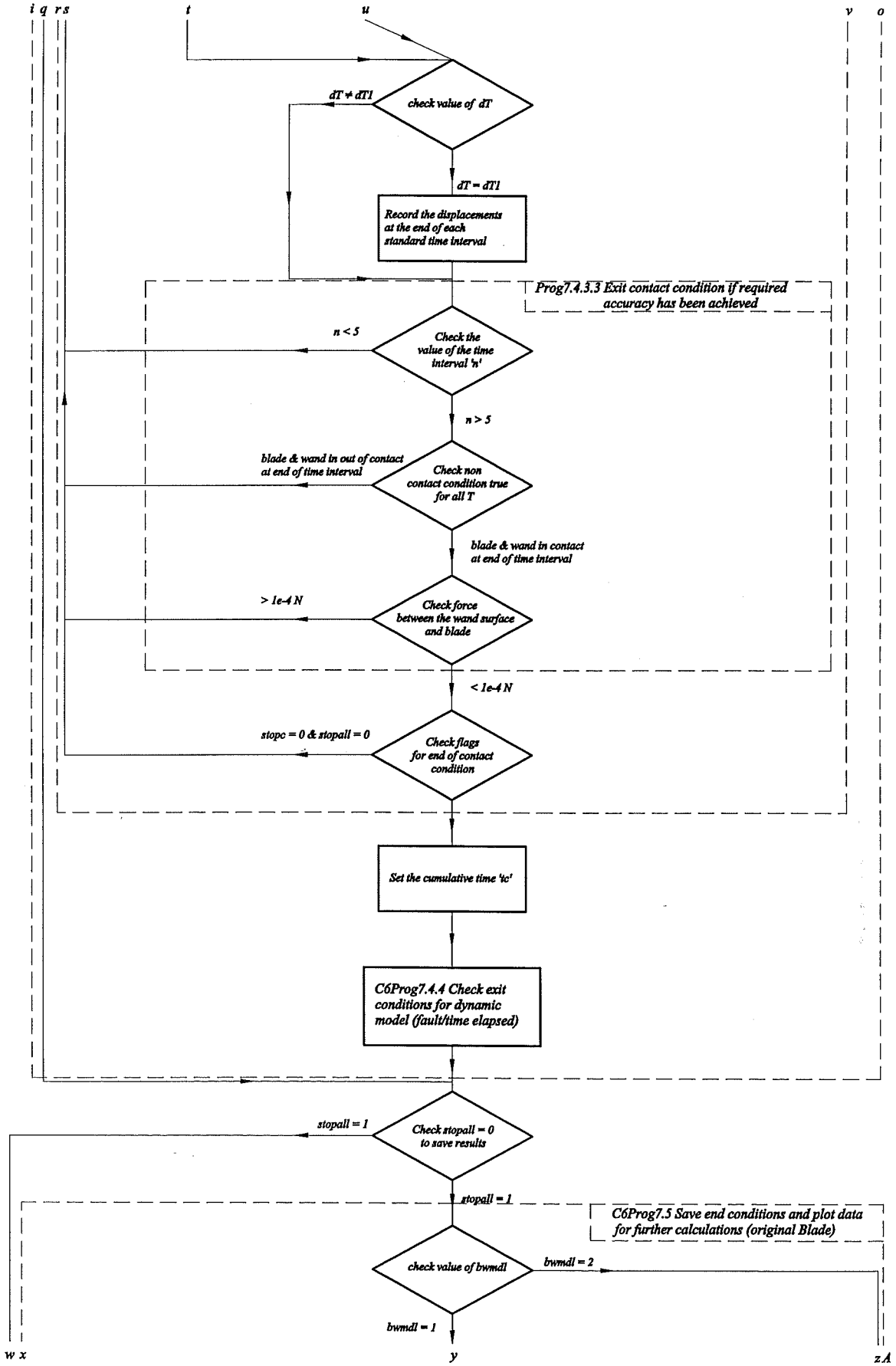

Figure C1 *(cont.)*

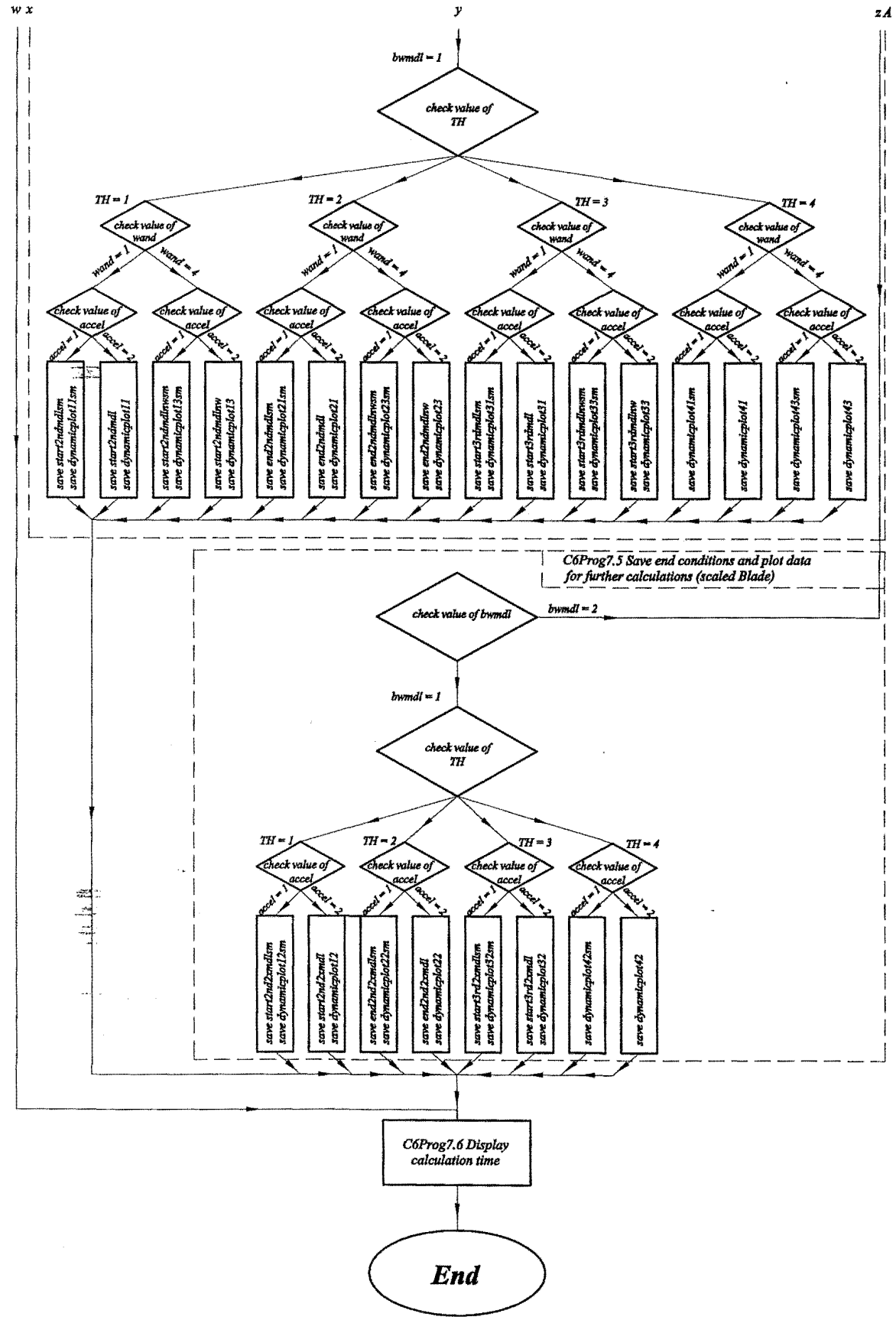

Figure C1 *(cont.)*

Section C6Prog7.1 of *C6Prog7.m* sets the flags for error messages and plotting and loads the model type specified in *C6Prog3.m.* Section C6Prog7.2 of *C6Prog7.m* loads the mass, stiffness and damping properties for the specified model type.

Because the numerical computation is time-consuming *(total computation time ranges from 7 – 60 hours depending on the model)* the computational procedure is executed in four separate calculations for the four performance intervals shown in Figure C2. The motor speed controller for the *blade* ground

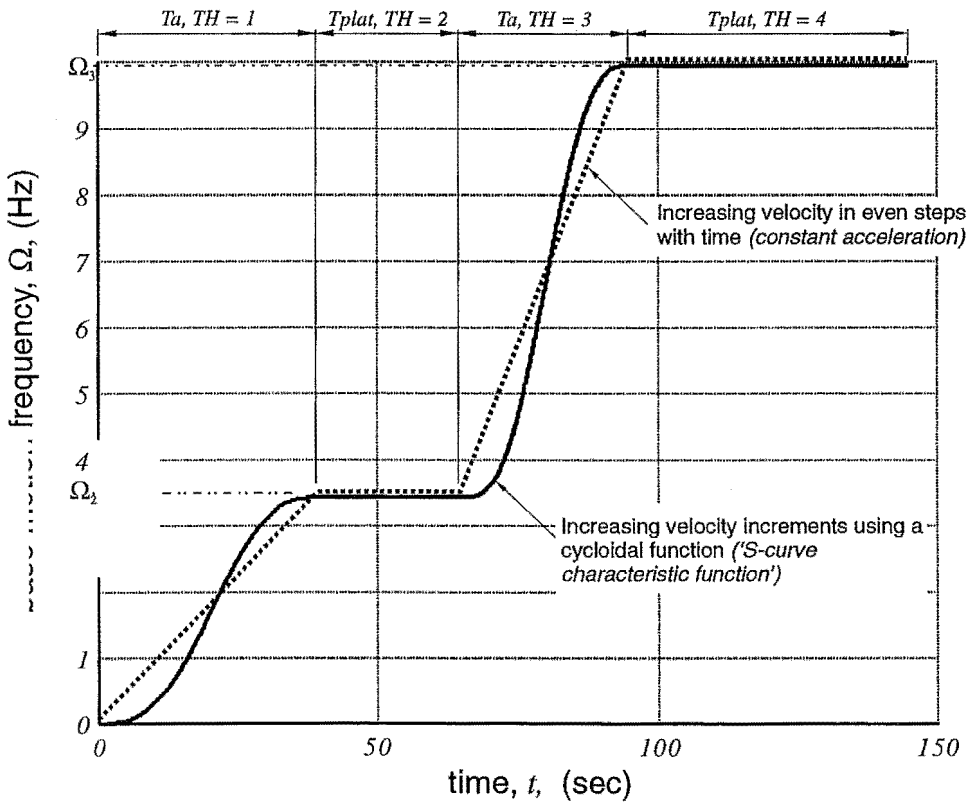

Figure C2 *Timing parameters in the mathematical model (original size Blade)*

motion on the original *Blade* uses a constant acceleration rate *(the dotted line in Figure C2)* between the set frequencies Ω_2 and Ω_3. Alternatively the mathematical model allows a cycloidal function to be used for increasing base

motion frequency between the set frequencies. This type of acceleration rate is allowed for in many modern controllers and is sometimes referred to an *'s-curve characteristic function'* [OMRON (1996)]. In Section C6Prog7.3 of *C6Prog7.m* the initial conditions for the model are loaded, these are the times, modal displacements, and modal velocities from the end of the previous performance interval.

Section C6Prog7.4 of *C6Prog7.m* manages the solution of the equations of motion for the blade and the wand. When not in contact, the initial conditions and function file *C6Prog5.m* are used to solve the equations of motion for a specified time interval dT. The conditions for non-contact are checked at the end of each time interval and the calculation repeated until the *blade* and *wand* are in contact. When contact is first detected, an iterative procedure is used *(Sections C6Prog7.4.2.4.2 and C6Prog7.4.2.4.4)* to calculate the final displacements and velocities. This iterative procedure ensures that the final separation distance between the blade and wand is very small before the procedure moves to the contact condition *(the separation distance between the blade and wand is set to* $< 10^{-8}$*m).* The final conditions from the last time interval where the blade and wand are not in contact, are used as the initial values for the contact condition. When in contact, the initial conditions and function file *C6Prog6.m* are used to solve the equations of motion for the specified time interval dT. The conditions for contact are checked after each time interval by calculating the contact force. When the contact force becomes very small then the procedure moves back into the non–contact condition. In Section C6Prog7.4 of *C6Prog7.m* the computation alternates between the contact and non-contact conditions as the wand and blade interaction is modelled. The calculation is stopped when the end of the performance interval TH is reached.

The data for displacement/time histories is recorded as the procedure is running. for the purpose of debugging, it was most convenient to plot data as the procedure was running, however this slows the calculation. It was found to be more efficient to plot the results of calculations after the procedure is finished. To this end, in Section C6Prog7.5 the data is saved in the appropriate MAT-file. The variables saved are

dqrf, dqsf, dqtf, dquf, dqwf, fbmax, q0pp, qrf, qrpp, qsf, qspp, qtf, qtpp, quf, qupp, qwf, qwpp, tc, tsp, tstart, when, OMEGA, OMEGArun, TPPP

C10 Procedure *C6Prog8.m* - displaying the results of calculations

Procedure *C6Prog8.m* processes the results of the mathematical model following the execution of *C6Prog7.m.* The output of *C6Prog8.m* may be used to generate a time history plots of the blade and wand displacements at the contact height, such as those given in Figures (6.11a) and (6.11b) and Figures (6.13) to (6.15).

To gauge similarity between the mathematical model and the original *Blade,* the blade shapes corresponding to the superposition of all of the modes may be plotted with time. These plots were saved a series of frames and compiled to make a movie using the MATLAB *movie function.*

D

Design assessment and manufacturing drawings

Concept selection chart

Sub-system 1: The shuttle mechanism

Sheet 1 of 1

Concept No.	Functional (geometry, motion, load paths, compatibility, control)	Manufacturing, quality, & life cycle (production, purchase, assembly, waste)	Ergonomic, ecological, aesthetic, & safety (user, environmental, appeal)	Can be made to work (potential, confidence, enthusiasm)	Economics & timing (materials, manufacturing, operational)	Information (cooperation, expertise, experience)	Comments	Score	Develop further	Eliminate	Get information
A1		√	√ √	√	√	√	***Pros*** *- good facility for level adjustment* ***Cons*** *- high mass & poor load path* ***Ideas*** *- move leveling function to support structure*	6		√	
A2	√ √		√	√	√ √		***Pros*** *- low mass & good load path* ***Cons*** *- machining difficult, distortion & welds prone to fatigue* ***Ideas*** *- machine from solid*	6		√	
A3	√ √	√	√ √	√ √	√	√	***Pros*** *- accuracy, aesthetics* ***Cons*** *- distortion from mach. - heat treatment reqd.* ***Ideas*** *- incorporate leveling function at exit point*	9	√		
B1	√ √	√ √	√ √	√ √	√	√	***Pros*** *- bearing shaft allows for easy location & machining* ***Cons*** *- bearings have a limited load carrying capacity* ***Ideas*** *- try hollow shaft to reduce mass*	10	√		
B2	√	√	√ √	√ √	√	√	***Pros*** *- track bearings have higher load carrying capacity* *- bigger distance between table and clamp* ***Cons*** *- results in a heavier shuttle*	8			√
B3	× ×	√ √	× ×	√	√	√	***Pros*** *- uses low cost bearings* ***Cons*** *- requires additional control functions for 'blade' at rest* *- attachment of drive system is problematic*	1		√	
C1	×	√	√	√	√	√	***Pros*** *- less reciprocating mass* ***Cons*** *- higher bearing loads* *- attachment to central drive shaft is difficult*	4		√	
C2	√ √	√ √	√	√ √	√ √	√ √	***Pros*** *- smaller radial load on linear bearings* *- allows for centrally located drive system* ***Cons*** *- higher reciprocating mass*	11	√		
D1	×	√ √	×	√	√	√	***Pros*** *- simple, low cost, easy assembly/disassembly, & low mass* ***Cons*** *- may deform bearing shaft* *- bolt load required is too high for friction joint*	3		√	
D2	√	√	√ √	√ √	√ √		***Pros*** *- simple, low cost* ***Cons*** *- difficult to disassemble bonded anchor* ***Ideas*** *- try screw thread for positive retainment*	8		√	
D3	√ √	√ √	√ √	√ √	√	√ √	***Pros*** *- easily disassembled* ***Cons*** *- care required when turning internal thread* ***Ideas*** *- specify that soft jaws must be used on lathe*	11	√		
E1	√	√ √	√ √	√ √	√ √	√	***Pros*** *- simple* ***Cons*** *- prone to twisting* ***Ideas*** *- try simplifying by rotating anchors*	10	√		
E2	√ √		√ √	√ √	√	√ √	***Pros*** *- good torsional stiffness* ***Cons*** *- bracket must be disassembled to remove connecting rod*	9		√	
E3	√	√	√ √	√	√		***Pros*** *- ease of assembly* ***Cons*** *- must be accurately machined* *- clamping may distort bracket and load bearing shaft*	6		√	

Key: (√) yes +1, (×) no -1, ( ) neutral 0, (?) not enough information

Figure D1 Concept selection for the shuttle mechanism

Concept selection chart

Sub-system 2: The shuttle drive mechanism

Sheet 1 of 1

Concept No.	*Functional (geometry, motion, load paths, compatibility, control)*	*Manufacturing, quality, & life cycle (production, purchase, assembly, waste)*	*Ergonomic, ecological, aesthetic, & safety (user, environmental, appeal)*	*Can be made to work (potential, confidence, enthusiasm)*	*Economics & timing (materials, manufacturing, operational)*	*Information (cooperation, expertise, experience)*	*Comments*	*Score*	*Develop further*	*Eliminate*	*Get information*
F1	√ √	√ √	√	√ √	√ √	√ √	***Pros*** *- simple & uses standard low cost bearing* ***Cons*** *- long con. rod needed to give S.H.M.* ***Ideas*** *- try 'tee' slot*	*11*	√		
F2	×		√	√			***Pros*** *- high blade forces may be resisted by thrust bearings* ***Cons*** *- likely to require motor position at table level* *-follower may chatter in groove*	*1*		√	
F3	×			√	√		***Pros*** *- good for resisting high blade feedback forces* ***Cons*** *- may be difficult to get S.H.M.* ***Ideas*** *- use Hydraulic , Electro-magnetic, linear ball screw*	*1*		√	
G1	√	√ √	√	√	√		***Pros*** *- proven solution with lots of crank adjustment* ***Cons*** *- requires high pre-tension on bolt* *- difficult to make fine adjustments*	*6*		√	
G2	√ √	√		√	√ √	√	***Pros*** *- simple, high strength solution* ***Cons*** *- no adjustment of crank offset* ***Ideas*** *- try replaceable cam attachment*	*7*		√	
G3	√ √	√ √		√	√	√	***Pros*** *- high strength & adjustable* ***Cons*** *- adjustment is time consuming* ***Ideas*** *- try adjustable crank using eccentric*	*7*		√	
H1	√ √	√	√ √	√ √	√	√ √	***Pros*** *- high strength & easy adjustment of crank offset* ***Cons*** *- limited adjustment*	*10*	√		
H2		√	√	√	√		***Pros*** *- S.H.M* ***Cons*** *- prone to rattle in groove* *- lubrication may be difficult*	*4*		√	
J1	√	√ √	√	√ √		√	***Cons*** *- imposes on bearing space for table rotation* *- high loads on output shaft of g/box or electric mach.* ***Ideas*** *- try custom building a g/box with heavy output shaft*	*7*			√
J2	√ √	√	√	√ √	√ √	√ √	***Pros*** *- allows space for table rotation bearings* *- shaft designed to tolerate high radial loads* ***Cons*** *- requires height*	*10*	√		
J3		×	√				***Cons*** *- mechanism is very complex* *- mechanism may be prone to binding* *- pivot rod will need high stiffness*	*0*		√	
K1		√	√ √	√ √	√	√	***Pros*** *- bolt length allows for good pre-tension* ***Cons*** *- diameter requires bigger bearing than necessary* *- bolt must be released before con. rod can be removed*	*6*		√	
K2	√	√ √	√ √	√ √	√ √	√ √	***Pros*** *- easy to disassemble con. rod* ***Cons*** *- smaller bearing may be used*	*11*	√		

Key: (√) yes +1, (×) no -1, ( ) neutral 0, (?) not enough information

Figure D2 *Concept selection for the shuttle drive mechanism*

Concept selection chart

Sub-system 3: The base rotation mechanism

Sheet 1 of 1

Concept No.	*Functional (geometry, motion, load paths, compatibility, control)*	*Manufacturing, quality, & life cycle (production, purchase, assembly, waste)*	*Ergonomic, ecological, aesthetic, & safety (user, environmental, appeal)*	*Can be made to work (potential, confidence, enthusiasm)*	*Economics & timing (materials, manufacturing, operational)*	*Information (cooperation, expertise, experience)*	*Comments*	*Score*	*Develop further*	*Eliminate*	*Get information*
L1			√ √	√			***Pros*** *- high gear ratio eliminating need for other reductions* *- friction damper not needed* ***Cons*** *- expensive & violates space constraints*	*3*			√
L2	√ √	√ √	√	√ √	√ √	√ √	***Pros*** *- low maintenance, low cost, & uses standard comp.* ***Cons*** *- chain/belt may whip due to out of balance forces* ***Ideas*** *- include friction damper*	*11*	√		
L3	√	√	√	√		√	***Pros*** *- easily incorporated with slewing ring & external gear* ***Cons*** *- lubrication containment may be difficult* ***Ideas*** *- try a simple friction wheel*	*5*			√
M1	√		√	√	√		***Pros*** *- rotary actuator can be directly coupled to shuttle* ***Cons*** *- free-play may be problematic as bearings wear* ***Ideas*** *- try using a slewing ring or truck turntable bearing*	*4*			√
M2	√ √	√ √	√ √	√ √	√ √	√	***Pros*** *- may use low cost rolling element bearings* *- facilitates the inclusion of a central drive shaft* ***Cons*** *- bearing table will need to thick to give reqd. stiffness*	*11*	√		
M3	√	√	√	√			***Pros*** *- excellent load path* ***Cons*** *- no adjustment for wear* *- expensive compared with other types of bearings*	*4*			√
N1	√	√ √			√ √		***Pros*** *- table may be disassembled* *- bearing seats are easy to machine* ***Cons*** *- water/dirt entrapment at top shaft seal*	*5*		√	
N2	√ √	√		√ √	√	√ √	***Pros*** *- good bearing & seal location tolerance* ***Cons*** *- distortion after welding*	*8*	√		
N3	√	√			√		***Pros*** *- good bearing & seal location tolerance* ***Cons*** *- difficult to get required strength*	*3*		√	
O1	√	√		√ √	√ √		***Pros*** *- simple & low cost* ***Cons*** *- results in a high load on bearings*	*5*			√
O2	√ √	√		√ √	√	√ √	***Pros*** *- springs allow for wear* ***Cons*** *- may stick if not released after use* ***Ideas*** *- try hydraulic actuation*	*8*	√		
P1	×	×	√	√		√	***Cons*** *- base rotation motor position obstructs plain bearings* *- grease containment for worm is problematic* *- difficult to give adequate support for shuttle actuator*	*2*		√	
P2	√ √	√ √	√ √	√ √	√ √	√ √	***Pros*** *- disc brake and chain/belt drive work well in same space* ***Cons*** *- chain grease may contaminate disc pads* ***Ideas*** *- investigate synchronous belt drives*	*12*	√		
P3	√	√	√ √	√ √		√ √	***Pros*** *- very simple arrangement* ***Cons*** *- requires bigger gearbox to accommodate radial load* ***Ideas*** *- try single sided floating friction pad for damping*	*8*		√	

Key: (√) yes +1, (×) no -1, ( ) neutral 0, (?) not enough information

Figure D3 *Concept selection for the base rotation mechanism*

Conceptual design work sheet

The shuttle drive mechanism

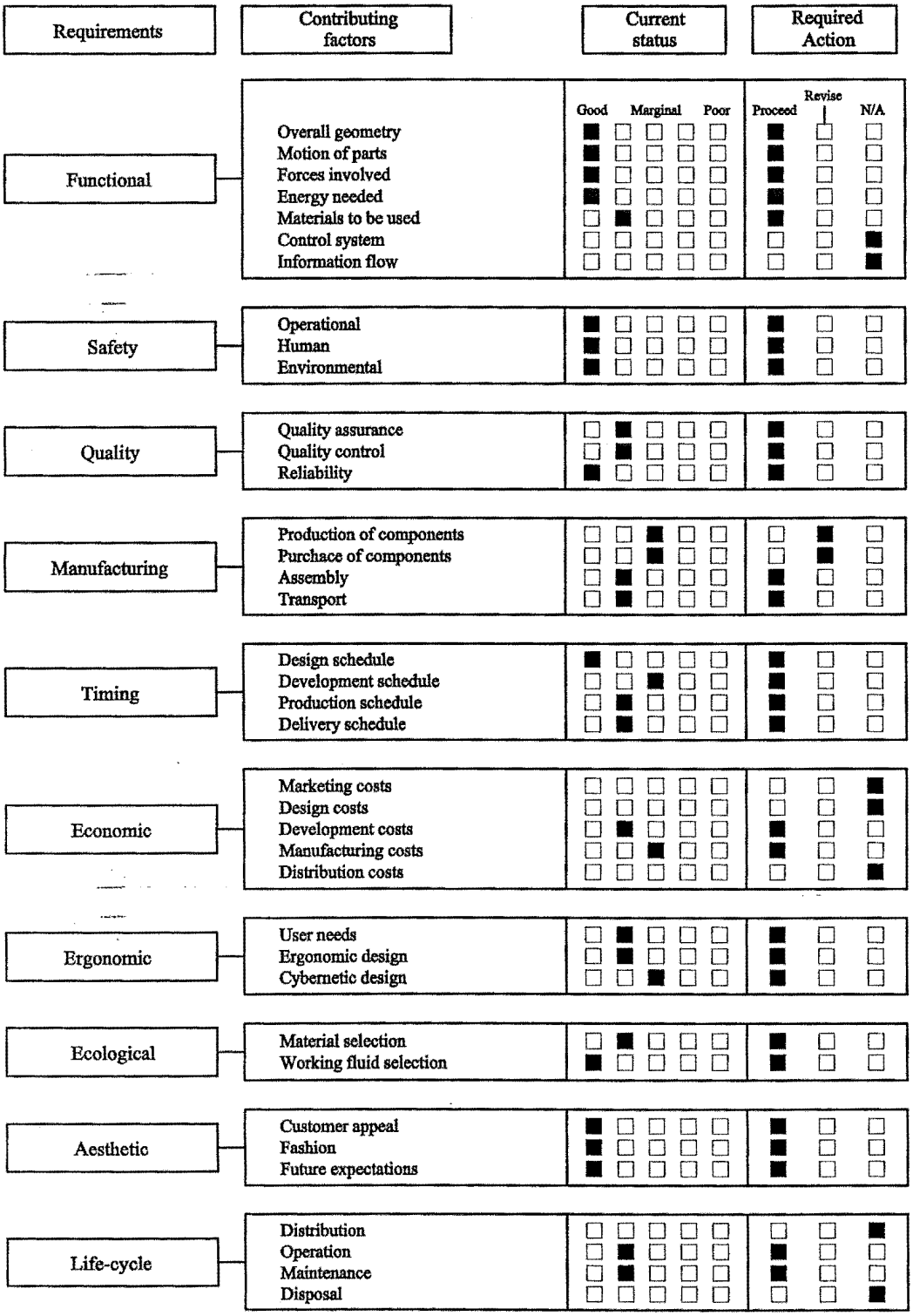

Figure D4 *Conceptual design worksheet for the drive mechanism design [after Hales (1993)]*

Embodiment design work sheet

The shuttle drive mechanism and the support structure

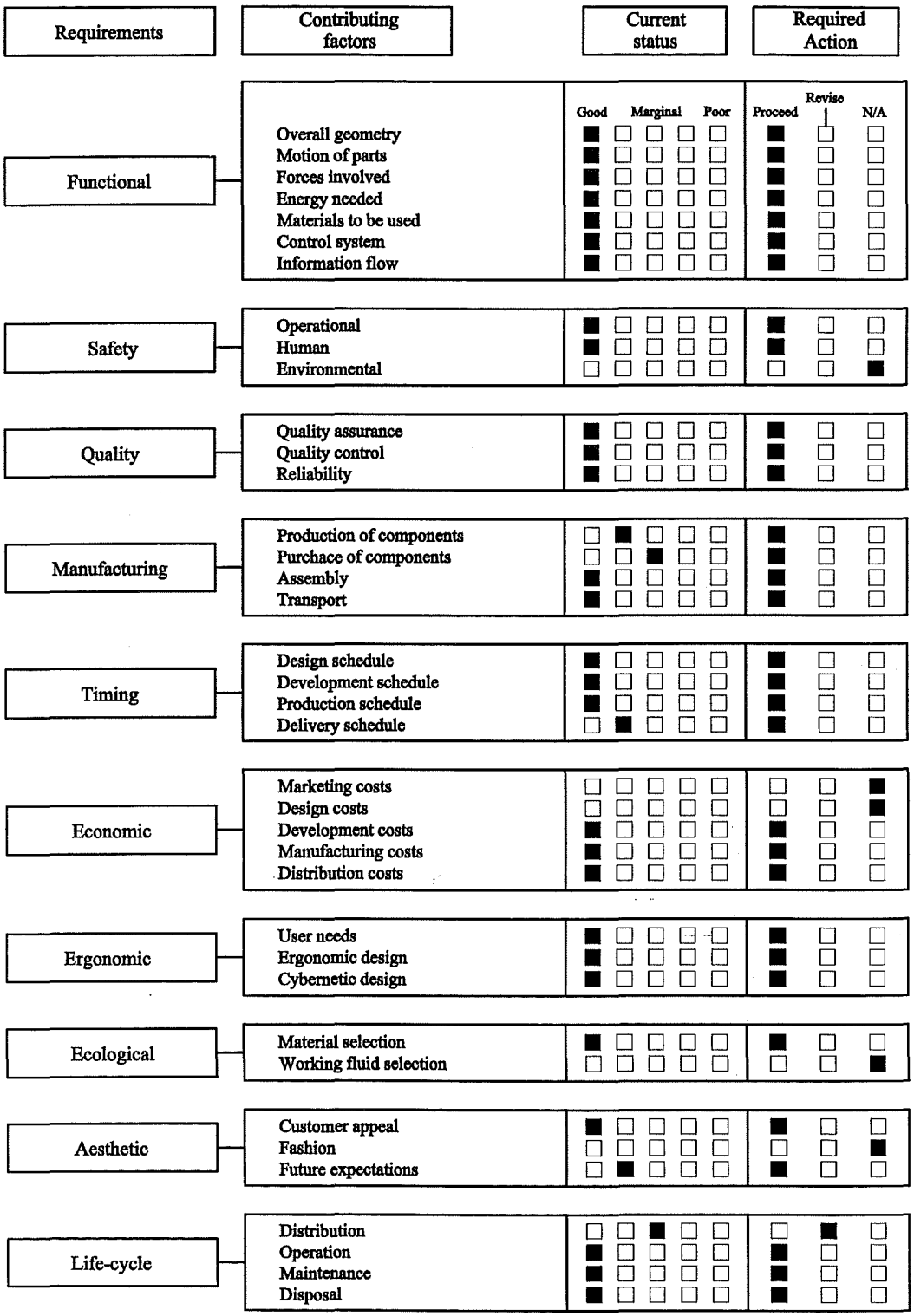

Figure D5 *Embodiment design worksheet for the drive mechanism and the support structure design. [after Hales (1993)]*

Detail design work sheet

The shuttle drive mechanism and the support structure

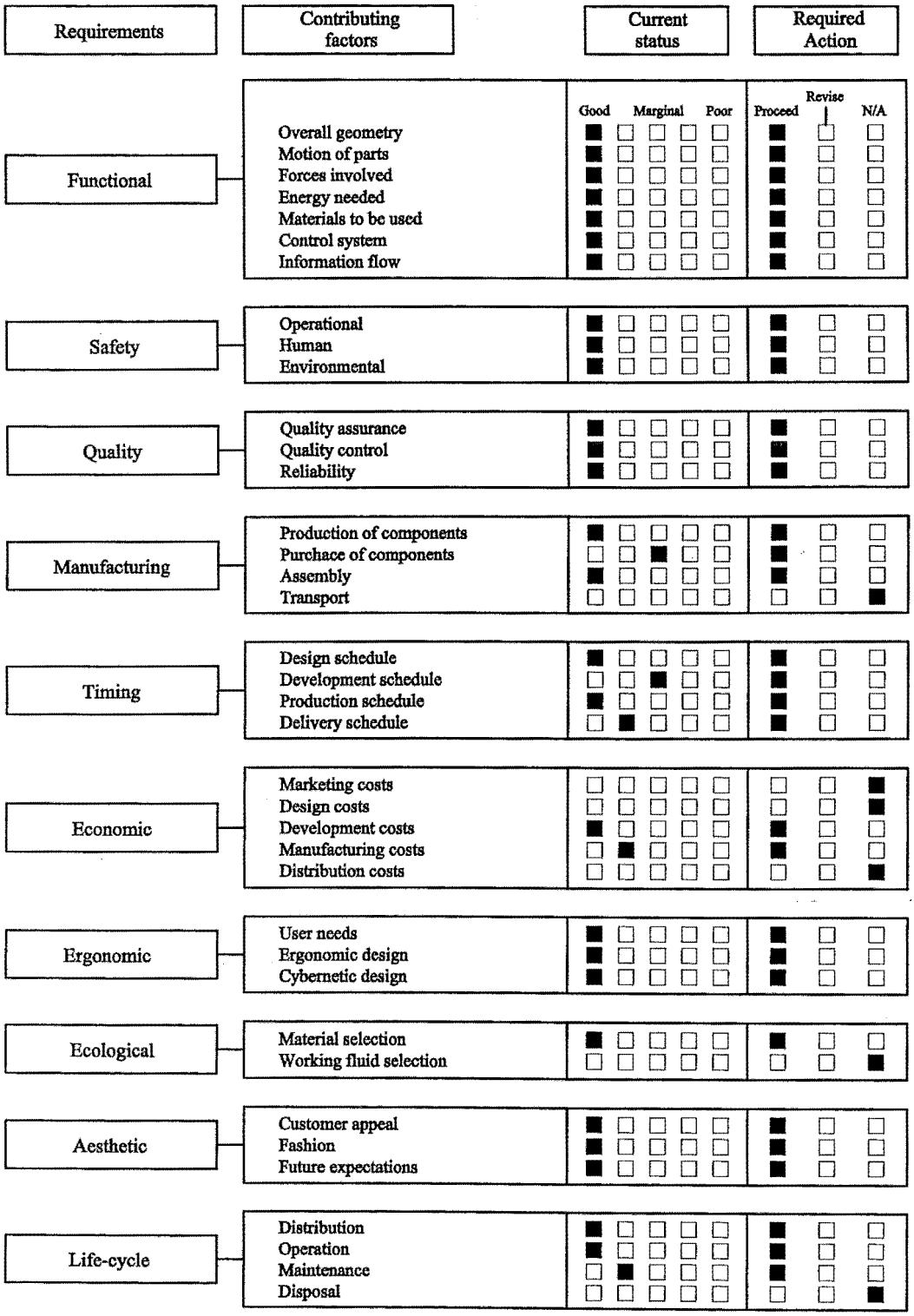

Figure D6 *Detailed design worksheet for the drive mechanism and the support structure design. [after Hales (1993)]*

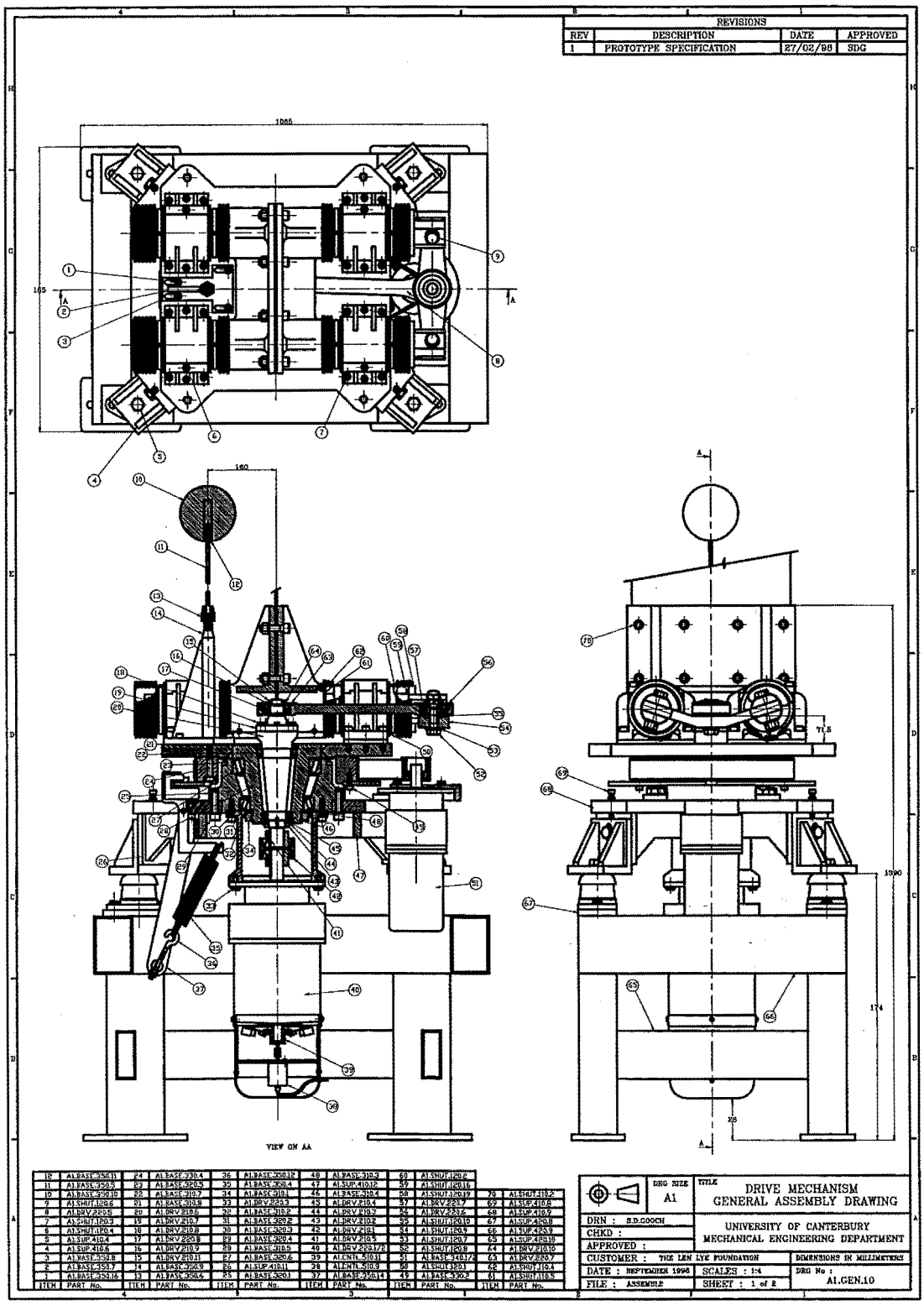

Figure D7 *General assembly drawing of the drive mechanism and the support structure for the scaled blade, Drg. No. A1.GEN.10*

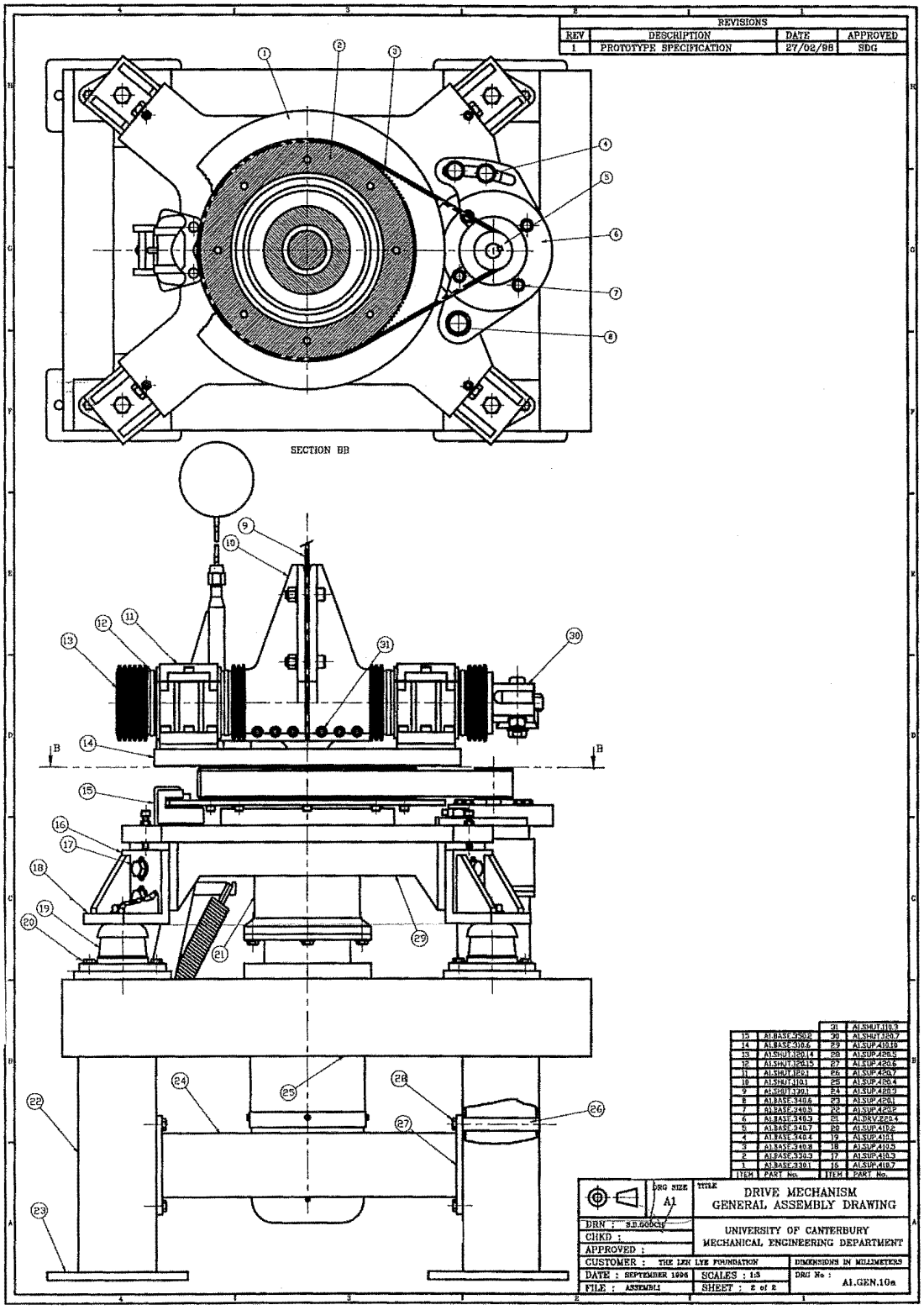

Figure D8 *General assembly drawing of the drive mechanism and the support structure for the scaled blade, Drg. No. A1.GEN.10a*

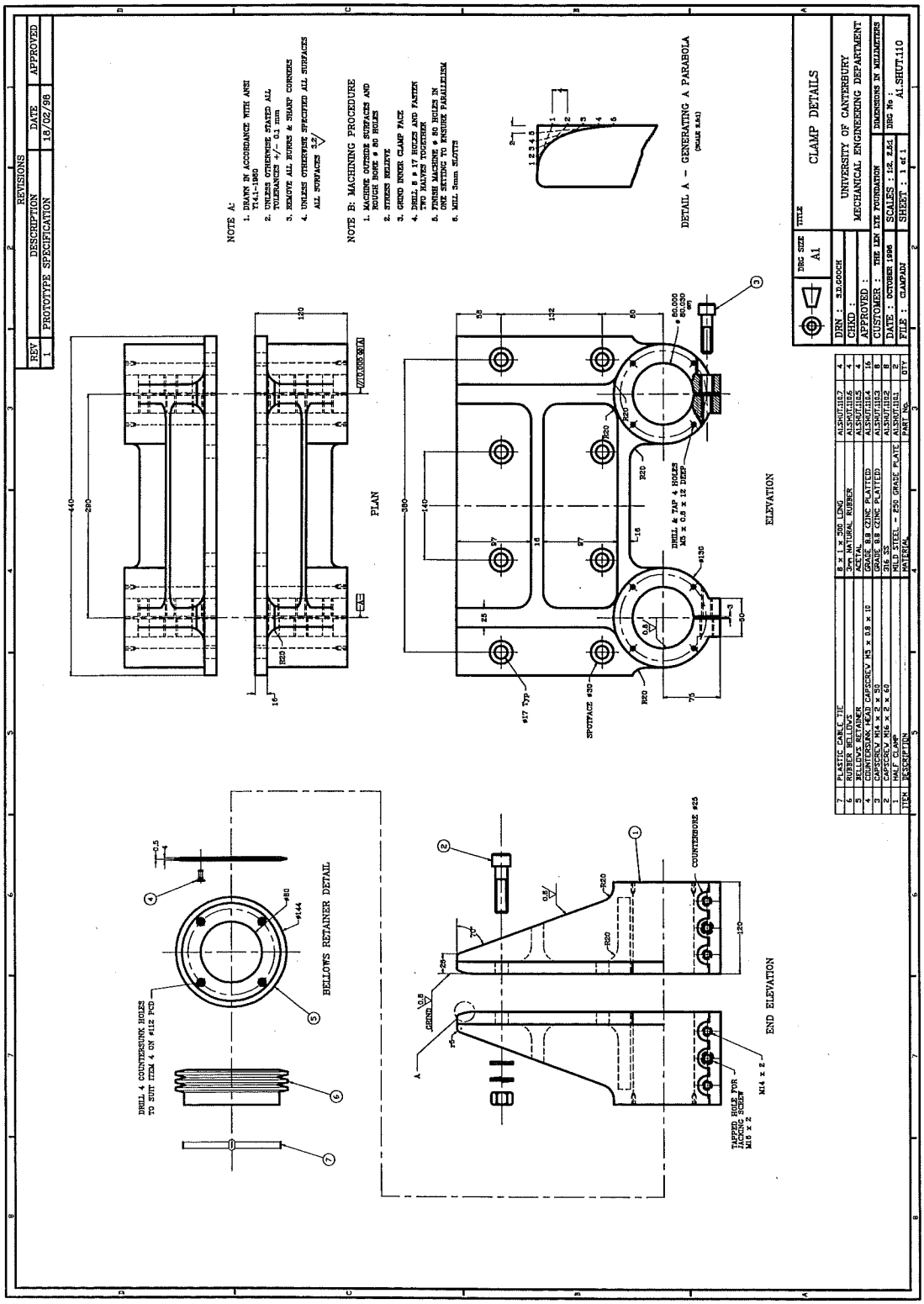

Figure D9 *Manufacturing drawing for the blade clamp at the scaled size, Drg. No. A1.SHUT.110*

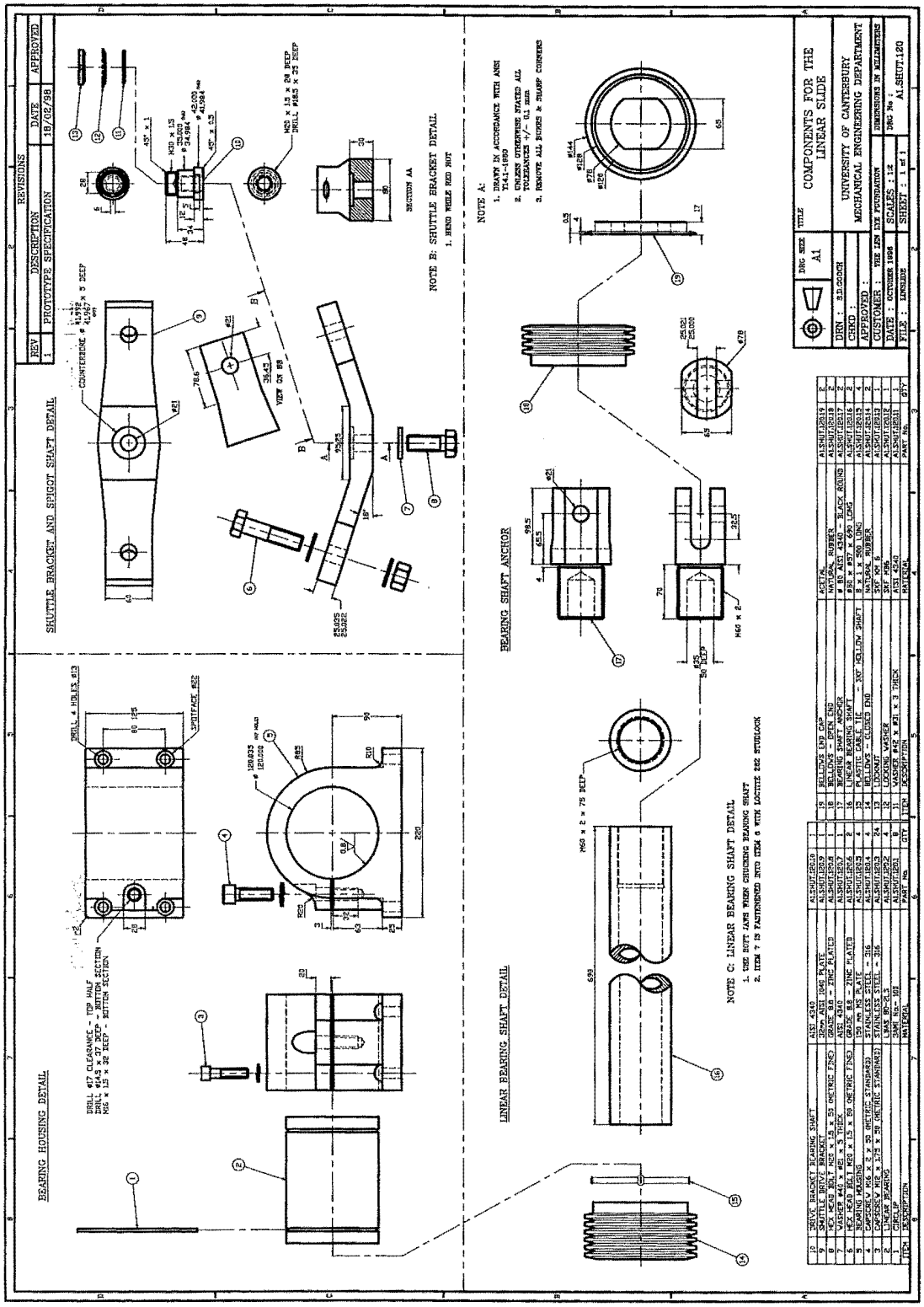

Figure D10 *Manufacturing drawing for the linear slide components at the scaled size, Drg. No. A1.SHUT.120*

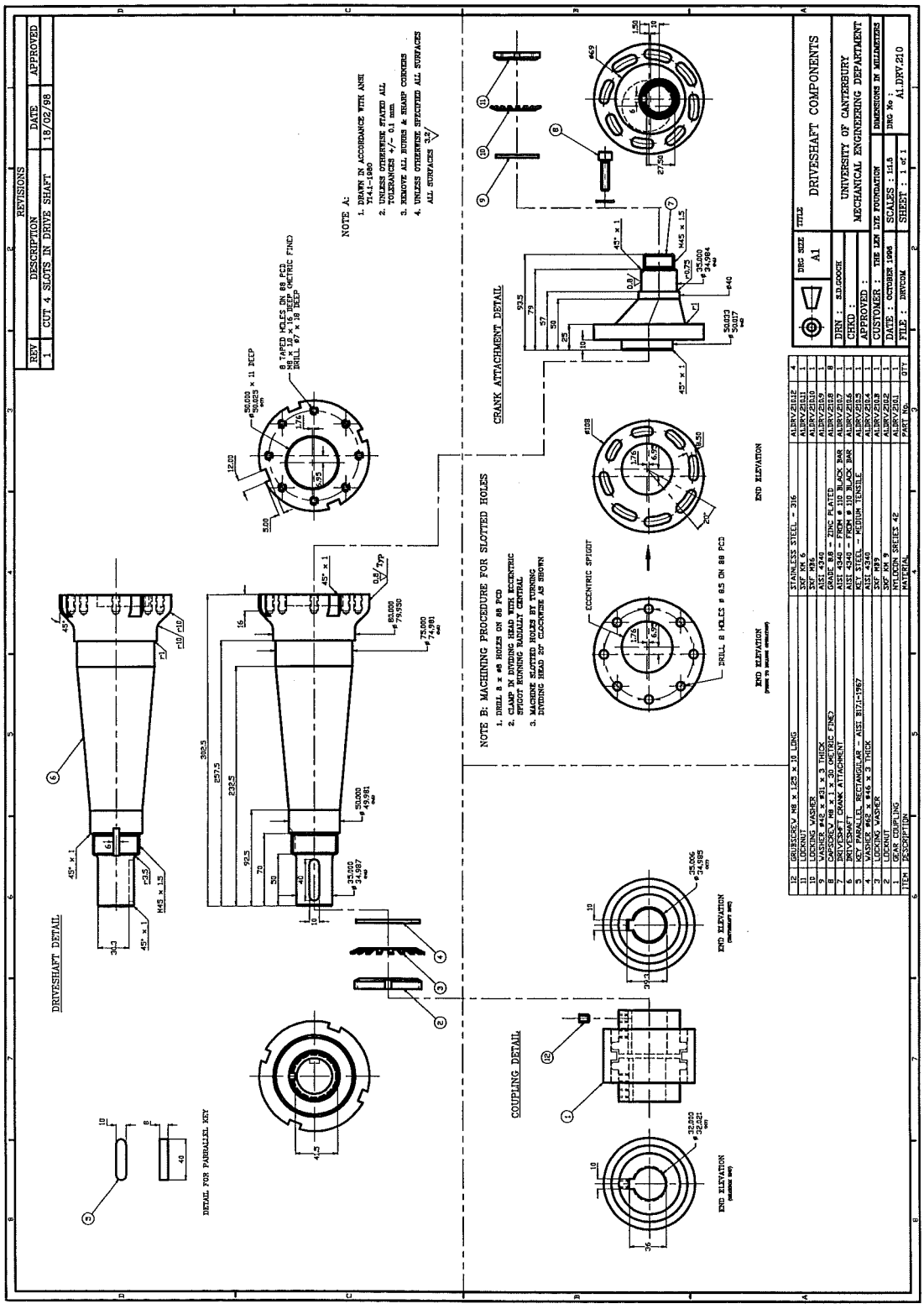

Figure D11 *Manufacturing drawing for the central drive shaft components at the scaled size, Drg. No. A1.DRV.210*

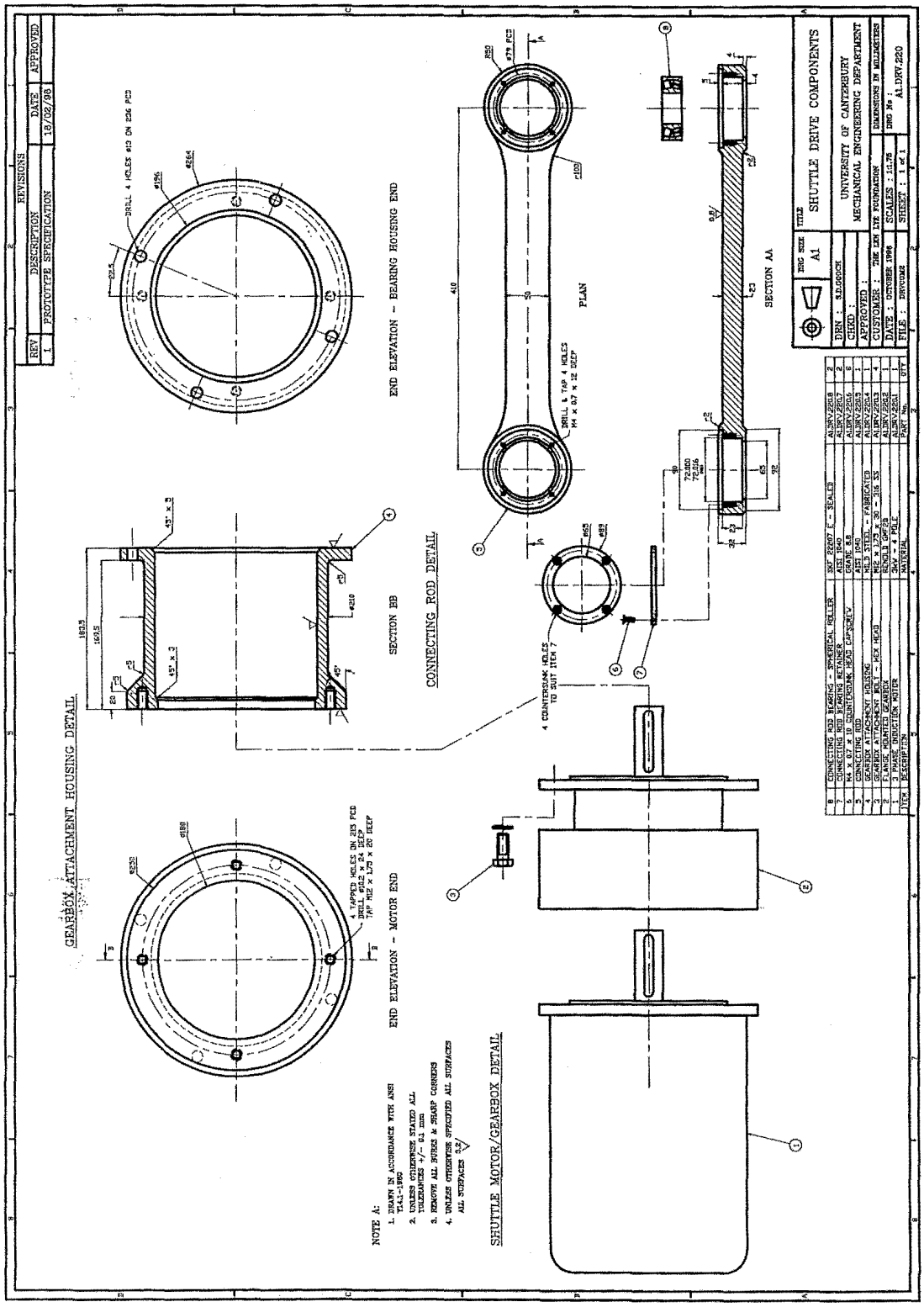

Figure D12 *Manufacturing drawing for the shuttle drive components at the scaled size, Drg. No. A1.DRV.220*

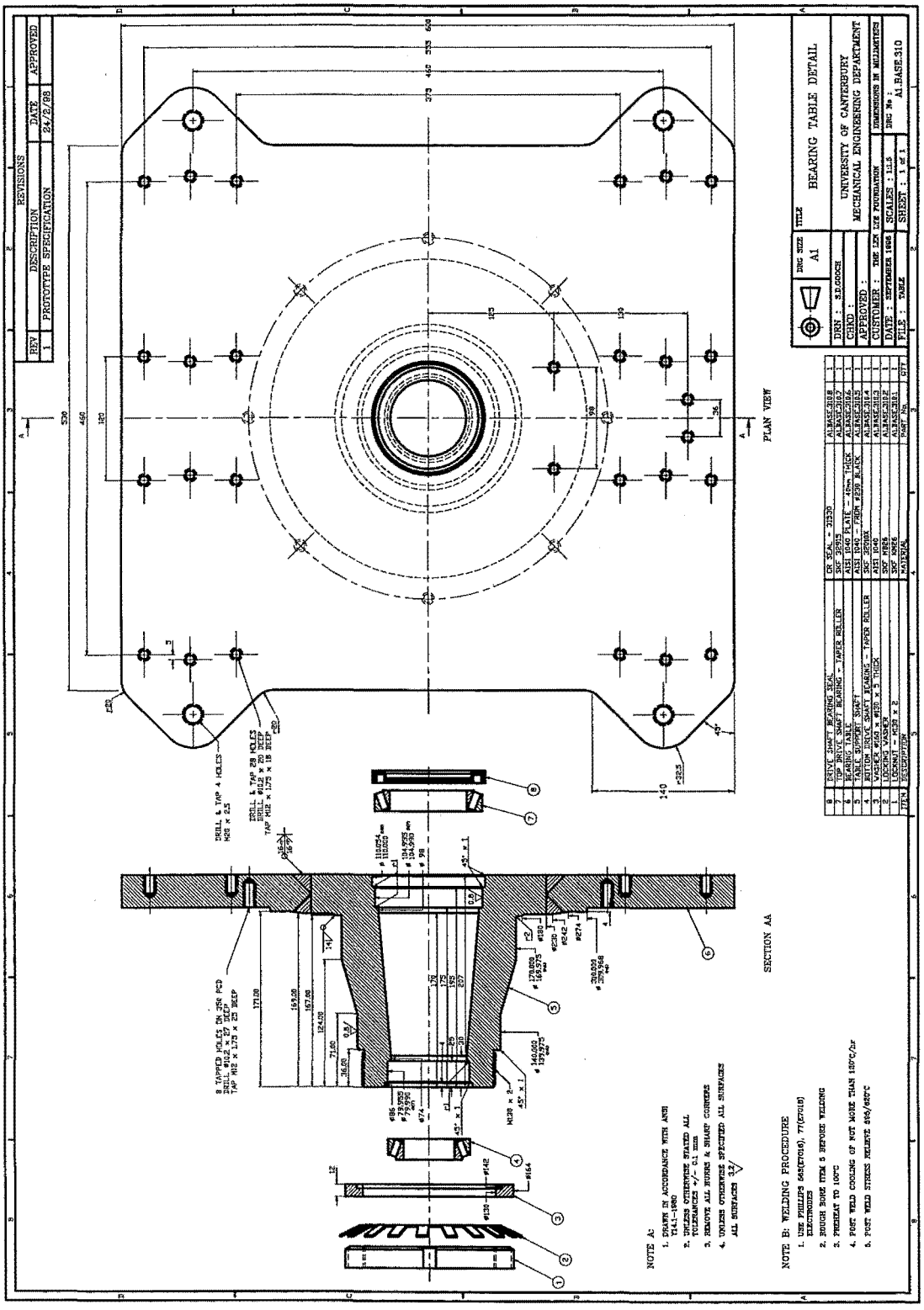

Figure D13 *Manufacturing drawing for the bearing table at the scaled size, Drg. No. A1.BASE.310*

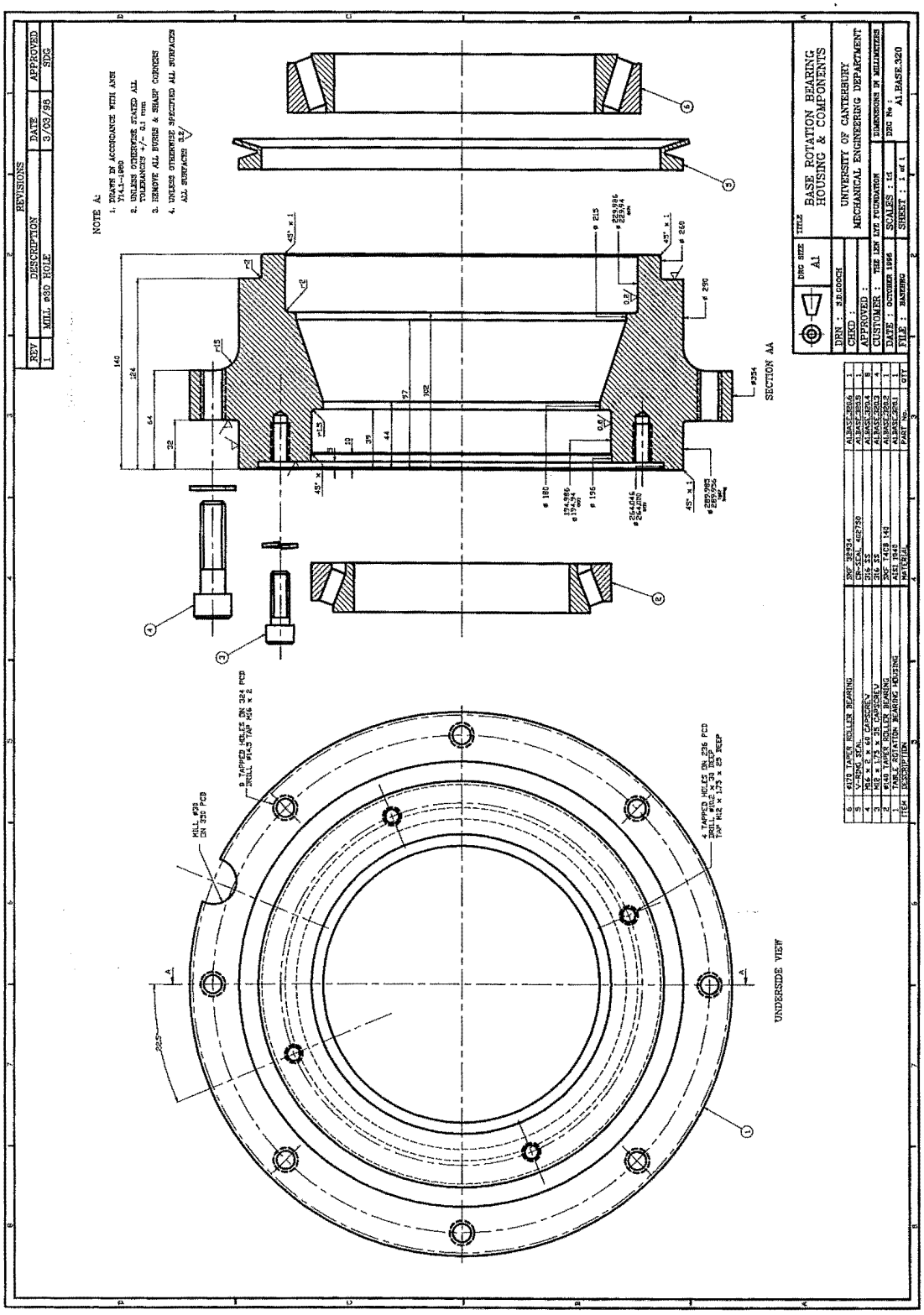

Figure D14 *Manufacturing drawing for the base rotation bearing housing at the scaled size, Drg. No. A1.BASE.320*

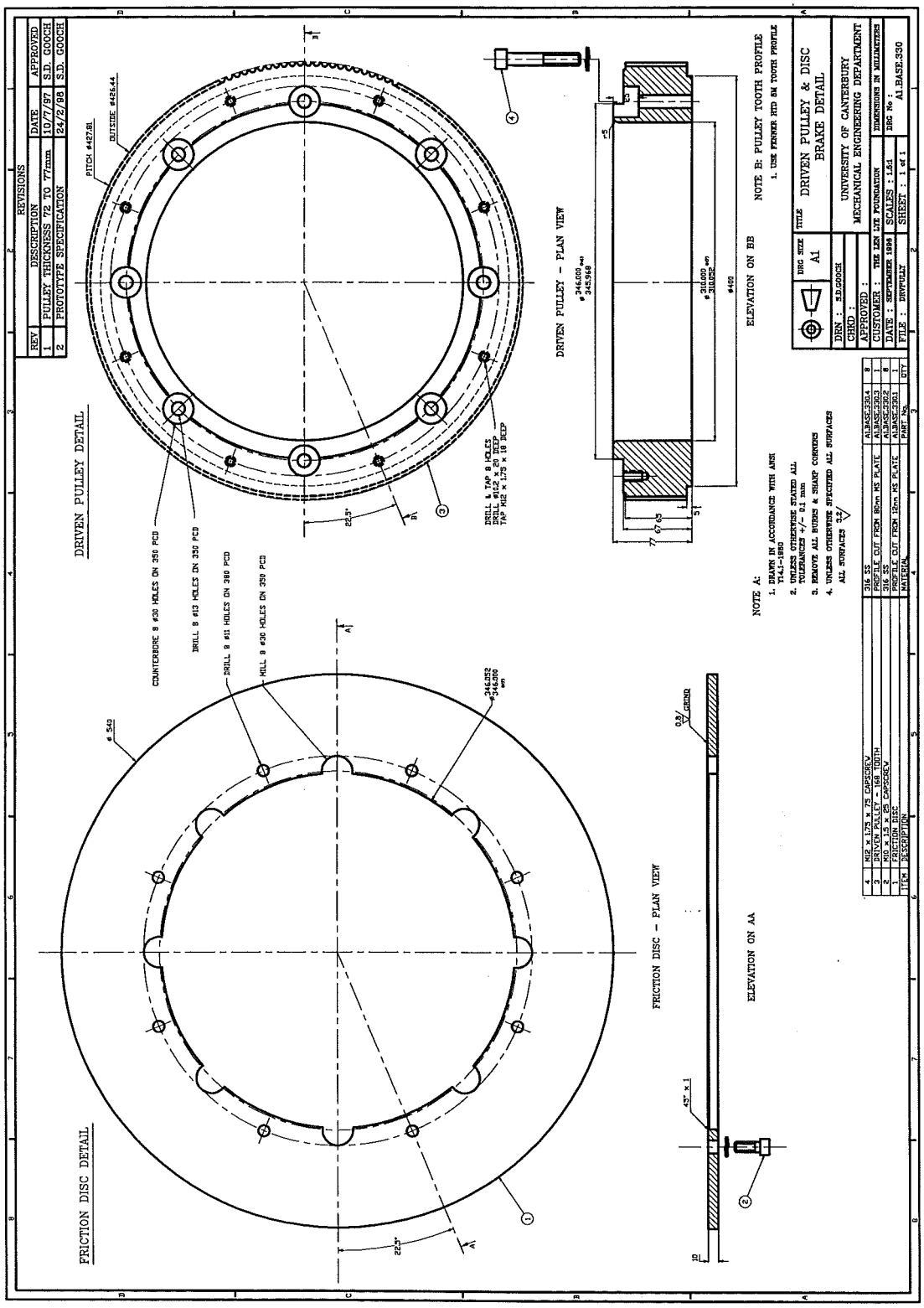

Figure D15 *Manufacturing drawing for the driven pulley and the brake disc at the scaled size, Drg. No. A1.BASE.330*

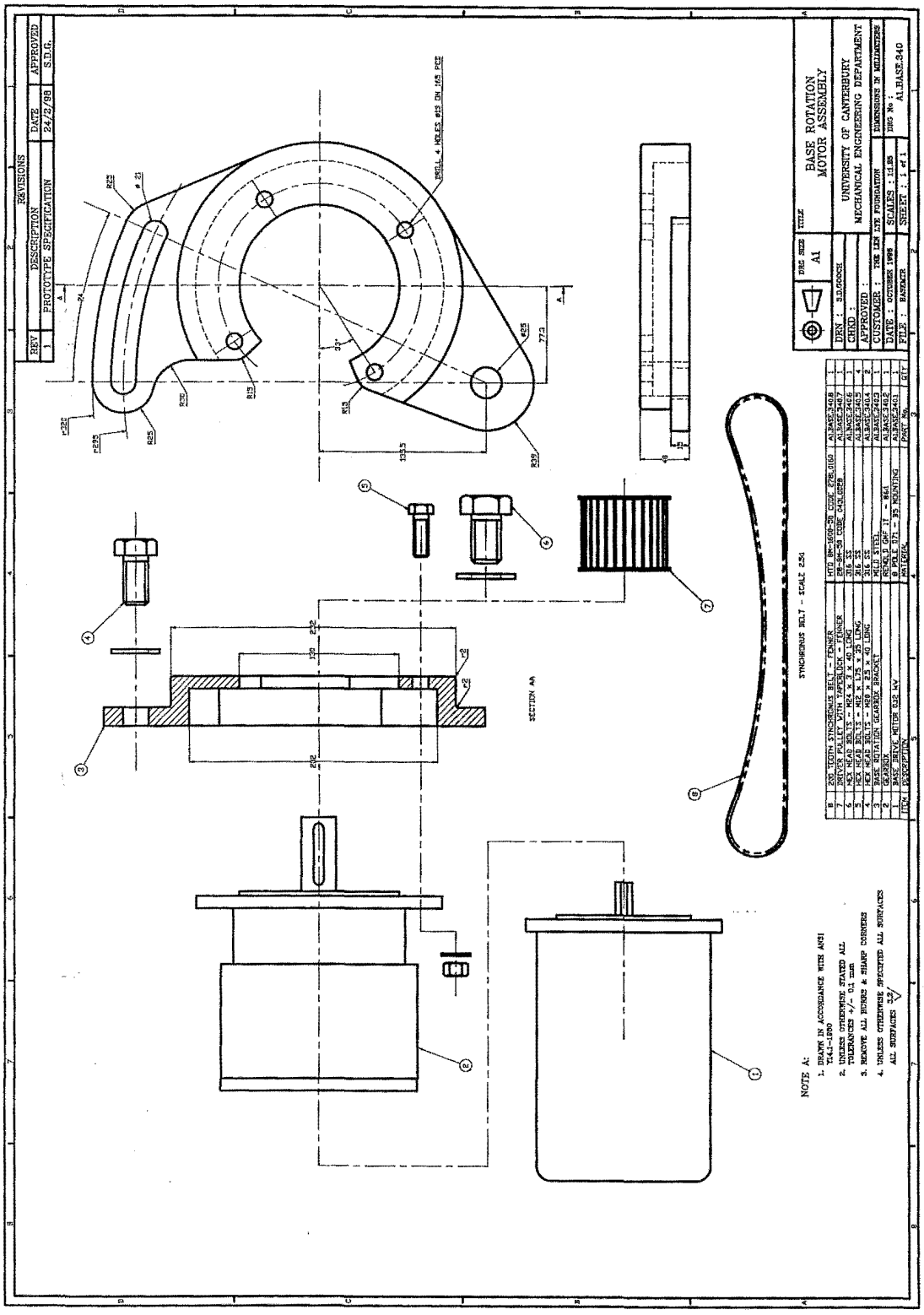

Figure D16 *Manufacturing drawing for the base rotation motor bracket, Drg. No. A1.BASE.340*

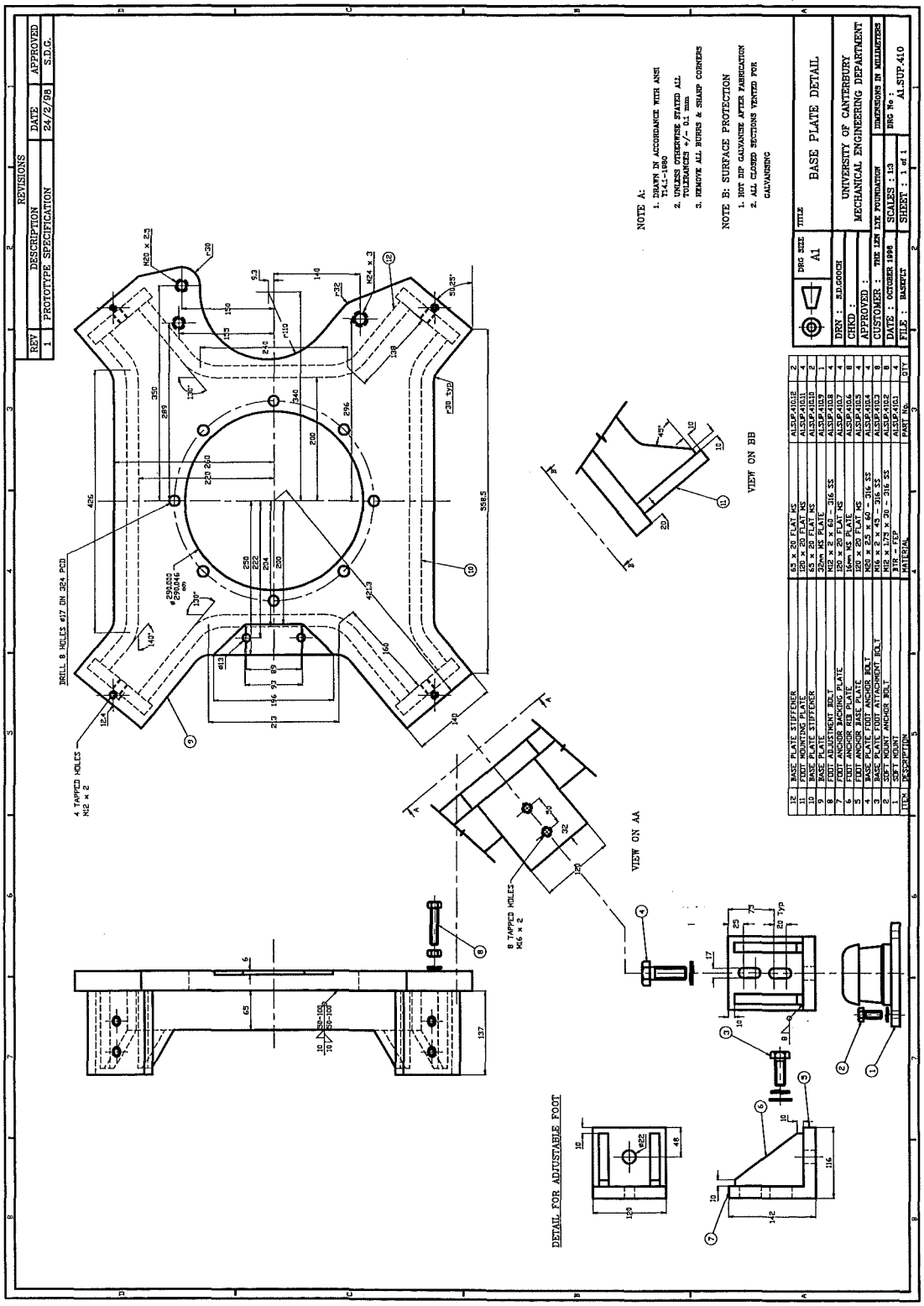

Figure D17 *Manufacturing drawing for the base plate, Drg. No. A1.SUP.410*

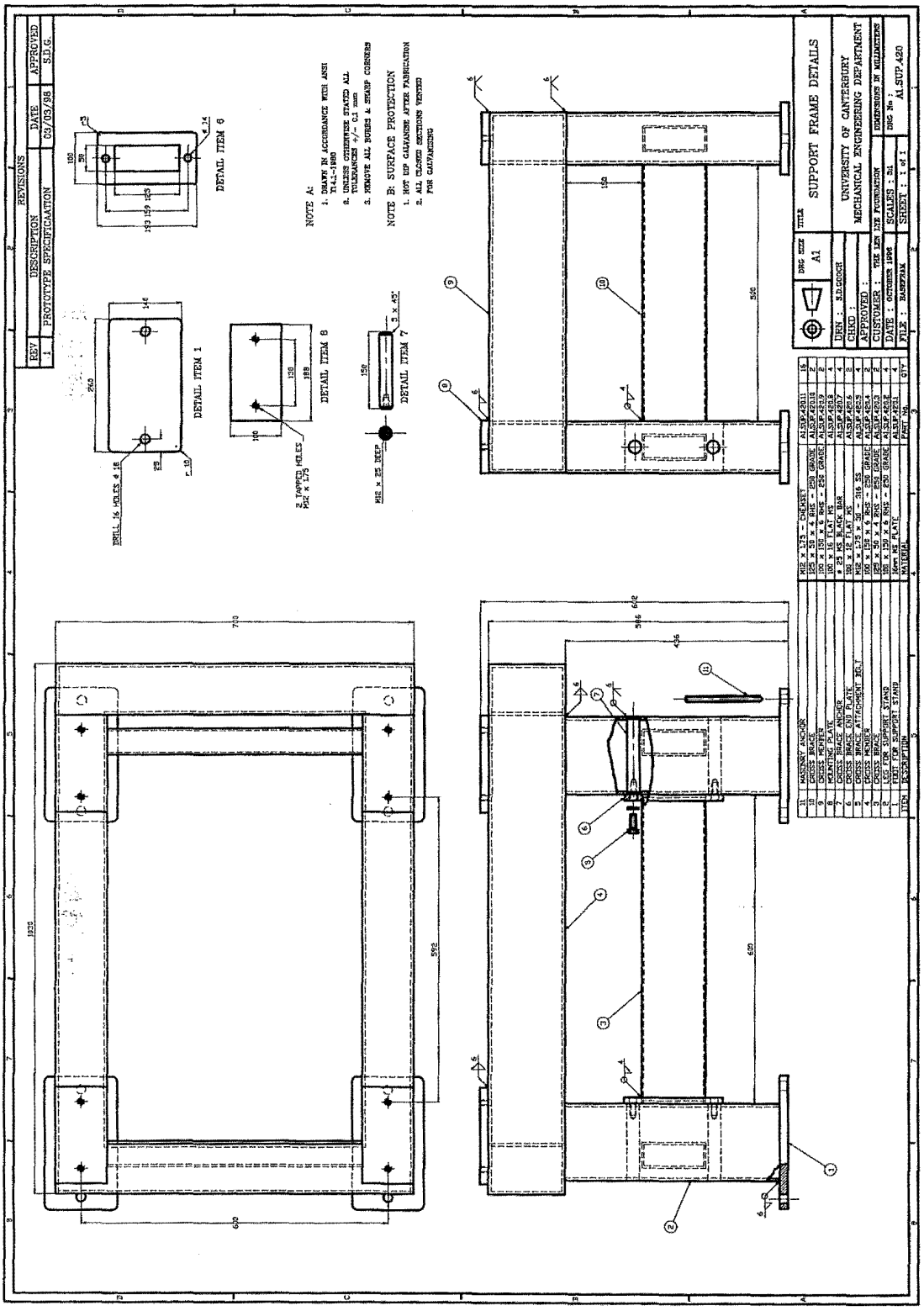

Figure D18 *Manufacturing drawing for the support frame, Drg. No. A1.SUP.420*

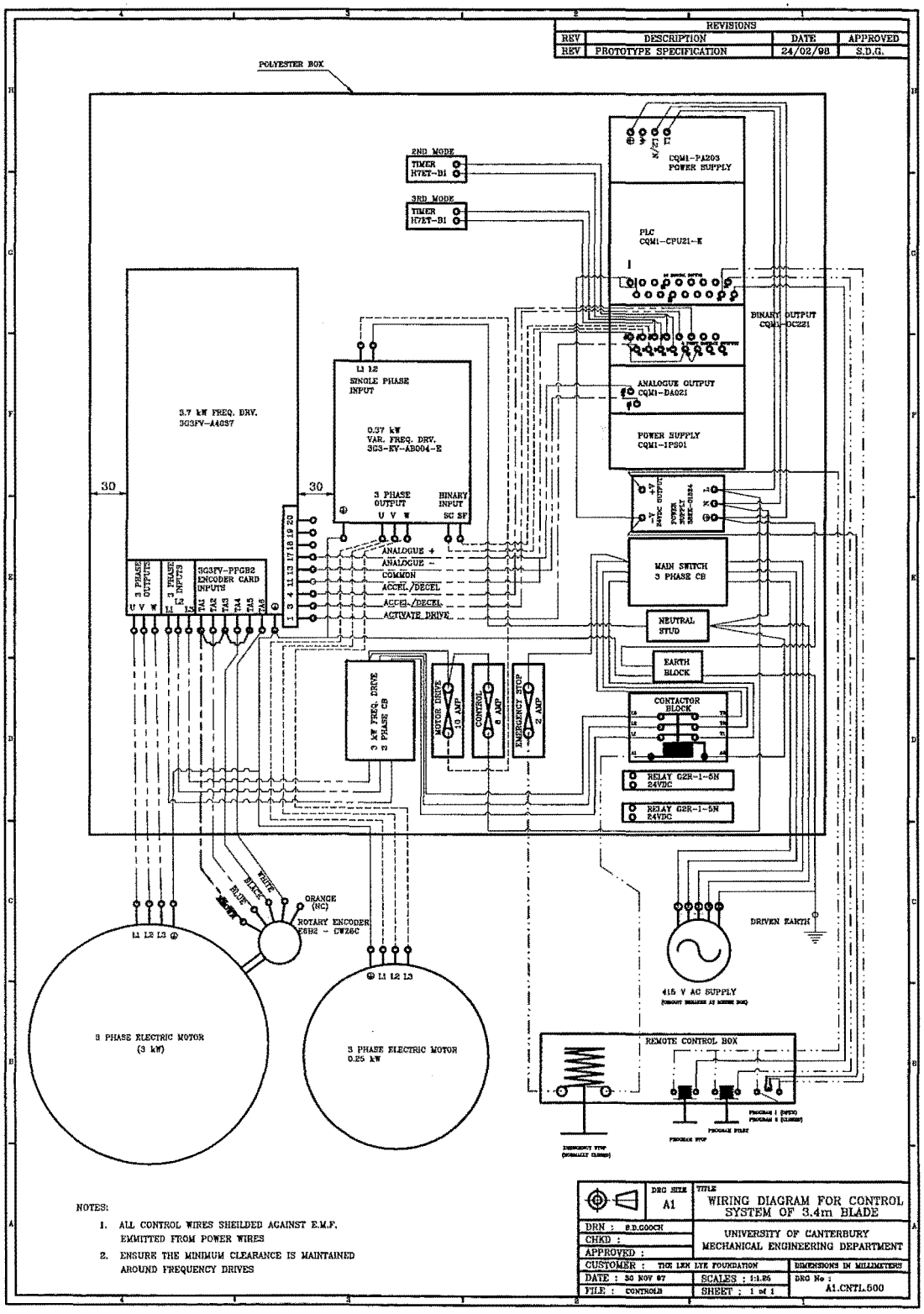

Figure D19 *General assembly and wiring diagram for the control system components Drg. No. A1.CNTL.500*